THE UNIVERSITY
of ADELAIDE

A Variational Approach to Hadron Structure in Lattice QCD

Benjamin James Owen

Supervisors: W. Kamleh and D. B. Leinweber

School of Physical Sciences
The University of Adelaide

July 2015

Abstract

In order to understand how hadrons acquire their physical properties from their constituents, we must resort to the underlying theory of the strong interaction, Quantum Chromodynamics (QCD). However, the non-perturbative nature of this theory in the relevant energy scales renders the standard perturbative methods ineffective. The formulation of QCD on a discrete space-time lattice allows for a first principles, non-perturbative approach to studying the strong interaction, in a manner well suited to numerical computation.

Over the past decade, the use of variational techniques has provided an effective framework for spectroscopic studies of the full hadron spectrum. Herein we generalise the use of the variational approach to hadron form factor calculations and examine its use in a number of different hadronic systems. As such an approach allows for the isolation of terms relevant to a single eigenstate or eigenstate transition, we show that this method is both an effective way to remove excited state contamination from the study of ground state systems and an effective framework through which one can study the structure of hadronic excitations.

We begin with an evaluation of the nucleon axial charge, g_A, to investigate the improvement offered through this method and consider the role that excited states play in the discrepancy observed between lattice determinations and experiment. This is followed by a determination of the ρ-meson electromagnetic form factors G_C, G_M and G_Q, and the corresponding radiative transition form factor G_{M1} using near physical masses. We then turn our attention to the electromagnetic form factors of the two lowest-lying negative parity nucleons, where such techniques are required to disentangle the contributions of these two near degenerate states. Here we present the first evaluation of the elastic form factors G_E and G_M for both these low-lying states.

Finally, through careful consideration of the $N\gamma \to N^*$ vertex, we develop an innovative formalism that allows one to evaluate radiative transition form factors for all spin-$1/2$ nucleon excitations. This novel formalism is implemented to provide the world's first examination of the odd-parity transitions of the nucleon in lattice QCD.

Statement of Originality

I certify that this work contains no material which has been accepted for the award of any other degree or diploma in my name, in any university or other tertiary institution and, to the best of my knowledge and belief, contains no material previously published or written by another person, except where due reference has been made in the text. In addition, I certify that no part of this work will, in the future, be used in a submission in my name, for any other degree or diploma in any university or other tertiary institution without the prior approval of the University of Adelaide and where applicable, any partner institution responsible for the joint-award of this degree.

I give consent to this copy of my thesis, when deposited in the University Library, to be made available for loan and photocopying, subject to the provisions of the Copyright Act 1968. I also give permission for the digital version of my thesis to be made available on the web, via the University's digital research repository, the Library Search and also through web search engines, unless permission has been granted by the University to restrict access for a period of time.

Benjamin James Owen

Acknowledgements

Wow, what an adventure the past four and a half years have been. Overwhelmingly the journey that has been my PhD has been a positive and enjoyable one, and for this I owe a great debt of gratitude to a great number people. So here goes!

Firstly, I would like to say a big thank you to my supervisors Derek Leinweber and Waseem Kamleh. You have always made the time for a discussion, despite your busy workloads, and through these conversations I have learnt so very much. Without your continued support, guidance and patience this thesis, and the work it embodies, would not have been possible.

During my time as a postgraduate student I have been fortunate to work alongside some great people, however two deserve particular recognition. To Ben Menadue, thanks for the countless discussions and advice, particularly on all matters coding related. These discussions were invaluable and saved countless hours and heartache. To Phiala Shanahan, I would like to say a big thanks for your friendship, both within and outside of the university over the past four and a half years. Sharing the ride with someone as talented, hard-working and enthusiastic as yourself has been a real privilege. I will particularly miss our morning coffee conversations. I wish you the best success in Boston.

Further thanks go to Adrian Kiratidis, Daniel Trewartha, Sam Thomas and Alex Chambers for all the office antics and sometimes odd and off-topic discussions, and to the Colour-singlets, namely Adrian, Daniel, Lewis, Thom, Manuel and Nathan; it was a pleasure working alongside you all, but particularly playing alongside you on the court.

To my family, particularly Mum and Dad, thank you for the continued support and encouragement, especially when times have been tough. Special thanks also go to Lorraine, Des and Emily for their contribution to this journey, as well as their continued interest in my work and life in general.

Finally, I wish to thank Emma. You have stood beside me during this whole journey, supporting me emotionally and more recently, financially, making much of what I have achieved possible. I have enjoyed every step with you by my side and look forward to the adventures that lie before us.

Contents

Chapter 1

Introduction

The confining nature of the strong interaction constrains all colour-charged particles to reside in colourless bound states. These bound states, called hadrons, present some of the most diverse and complex systems within our universe. To understand the nature of such states we must resort to the fundamental description of the strong interaction embodied within the underlying field theory, Quantum Chromodynamics (QCD). Upon examining these systems, both experimentally and through QCD, one finds that many of their physical properties, such as mass and spin, do not come directly from their underlying constituents, rather they arise from the complex interactions of these constituents, both between each other and with the physical vacuum. As hadrons form much of the observable matter within the universe, understanding their structure and subsequent dynamics from the perspective of these constituent particles, the quarks and gluons, is both an important and an interesting problem.

Hadrons exist across a wide range of energies from the pion, with a rest mass of 0.135 GeV, up to the bottomonium states with masses in excess of 10 GeV. At the fundamental level, QCD describes all of these systems; however these systems exhibit markedly different physics. Here we shall consider states which exist at the lower end of this scale, where the constituents are highly relativistic and the approximate chiral symmetry of QCD imbues these states with many interesting and non-trivial properties. At these energies, the standard method of forming perturbative series breaks down and so, in order to extract meaningful results, one must resort to other, non-perturbative techniques. To date the only *ab initio* approach to the study of QCD in this regime is to formulate the theory on a finite Euclidean space-time lattice, which acts a natural regulator for the theory. Through this formulation, one can establish a fundamental connection with statistical mechanics and consequently build a framework where the correlation functions describing the dynamics of the theory can be evaluated numerically using Monte Carlo techniques.

Given the scale and complexity of the calculation, lattice simulations require vast amounts of computing resources. Historically, in order to extract any results the earliest calculations were forced to operate with parameter sets well-removed from the physical situation. However access to ever-increasing compute power and breakthroughs in algorithmic design have allowed the community to edge ever-closer to the physical regime. Within the last decade, simulations have been

able to examine hadrons at physical quark masses and consequently produce the ground state spectrum consistent with experiment [1]. While this is an important result, these ground states represent only a small fraction of the hadron spectrum. The extended hadron spectrum presents many interesting insights into the nature of hadrons and the strong interaction. Of particular interest are those states which lie outside of the expected patterns observed generally within the spectrum, and exotic states, which are entirely permissible by QCD but have yet to be observed. The answer to such questions lies deeply within QCD, and Lattice QCD presents us with the ideal means through which to extract them.

Hadron spectroscopy on the lattice has been an active focus of the community for many years now and the techniques employed are well established. The most popular and successful of these techniques is the so-called *variational method*. The underlying principle of this approach is to access excitations via optimised operators, formed as linear combinations of basis operators determined via a variational procedure such that they effectively couple to individual energy eigenstates. Utilising the variational approach, we have been able to map out much of the hadron spectrum and consider its associated quark mass dependence. However, if we wish to gain insight into the make-up and structure of such states or the matrix elements associated with their production or decay, we must consider how the variational approach can be utilised in the context of hadron structure calculations.

As we shall see, the generalisation developed herein is effective and provides a robust and general method for the determination of hadron matrix elements. In particular, this approach provides a framework through which one can both remove excited state contributions from the determination of ground state properties and access the corresponding quantities for hadronic excitations on the lattice.

In this thesis, we examine the application of the variational method to a range of hadron structure calculations. The objective is to present a framework that provides systematic control over excited states, allowing for an accurate determination of hadronic matrix elements in the light-quark regime. Its use in the extraction of matrix elements for the excitations of the lightest QCD eigenstates, specifically the nucleon, pion and ρ meson is explored. We begin in Chapter 2 with a brief discussion of hadrons in the context of the standard model and the insights offered through the constituent quark model. This is followed by an introduction to Quantum Chromodynamics and hadron structure. In Chapter 3 we present the foundations of Lattice QCD and the basic building blocks that one requires in order to study hadrons on the lattice. Chapter 4 outlines the method for evaluating hadron correlation functions and consequently how one can access the desired information from these quantities. This leads into a discussion of the variational method and the new extensions required for its use in the evaluation of hadronic matrix elements.

We then proceed with a presentation of the calculations and subsequent results. We begin in Chapter 5 with an evaluation of the nucleon axial charge,

g_A, to examine the improvement this method offers over conventional techniques in handling excited state contamination. Chapter 6 is devoted to the evaluation of the electromagnetic form factors for the π and ρ mesons and their lightest excitations, with a particular focus on extracting these quantities for the ρ meson with near physical quark masses. We follow this up in Chapter 7 with an evaluation of the $\rho \to \pi\gamma$ transition form factor. In Chapter 8, we shall examine the electromagnetic form factors of the two lightest negative parity nucleons seen on the lattice and finally, in Chapter 9 we establish a new formalism for the extraction of the electromagnetic transition form factors for nucleon excitations, encompassing transitions between all possible parity states. The consideration of negative parity transitions in lattice QCD is novel. The formalism is implemented to provide a first look at the predictions of QCD and facilitate the interplay between theory and experiment in generating new knowledge.

Chapter 2

Quarks, Hadrons and the Strong Interaction

Our understanding of the universe on the sub-nuclear scale is embodied in the standard model of particle physics. This theory collectively describes the strong, weak and electromagnetic interactions and classifies all elementary particles into four fundamental classes: quarks, leptons, the force mediators and the Higgs Boson. Quarks and leptons, sometimes collectively called matter particles, form the basis for all directly observable[1] matter in the universe. The force mediators are responsible for facilitating the interactions between particles through the exchange of energy and momentum. The remaining ingredient, the Higgs boson, is the resultant scalar particle stemming from the spontaneous symmetry breaking of the electroweak interaction via the Higgs field (a unified description of the electromagnetic and weak interactions) through which massless fields are able to acquire mass. With the discovery of the Higgs boson in 2012 by the ATLAS and CMS experiments [2, 3], all of the elementary particles in this framework have been verified.

If we consider how we observe most matter in the universe, the vast majority of what we see is bound states. The properties and patterns observed in such bounds states can be understood from the properties of the underlying constituents and the governing interactions. As summarised in Table 2.1, the constituent particles, the quarks and leptons, are both spin-$1/2$ fermions, with six distinct types, that can be grouped according to their charge and relative mass. The key feature that differentiates quarks and leptons is in their ability to interact via the strong interaction; quarks are able to undergo such interactions while leptons are not. Remarkably, this simple defining property gives rise to the most important and notable difference between these particles: quarks are not observed in isolation. The exact mechanism for this confining property remains poorly understood; however its consequence is quite simple. In the low-moderate energy regime, quarks can only exist within colour-neutral bound states, which we call hadrons.

[1] On the basis of astrophysical observations, there is now a general consensus that Dark Matter exists in our universe. Though massive neutrinos are certainly a candidate for such matter, the number observed is insufficient to generate the required mass, thus hinting at some other, yet-to-be observed, matter in our universe. Accounting for such matter would require extensions to the Standard Model.

Table 2.1: Summary of the matter particles within the framework of the standard model. Within both the lepton and quark families, there exists a clear trend of increasing mass between identically-charged states, which further orders these states into groups called generations. Masses are quoted in units of GeV/c^2 and electric charges as multiples of the magnitude of the electron's charge $|e|$. Quark masses are quoted in the $\overline{\text{MS}}$ scheme at a scale of 2 GeV/c^2.

Quarks			Leptons		
flavour	Q	mass	flavour	Q	mass
up (u)	+⅔	0.002	electron (e)	-1	5.1×10^{-4}
down (d)	-⅓	0.005	e-neutrino (ν_e)	0	$< 2 \times 10^{-8}$
charm (c)	+⅔	1.28	muon (μ)	-1	0.105
strange (s)	-⅓	0.095	μ-neutrino (ν_μ)	0	$< 1.9 \times 10^{-4}$
top (t)	+⅔	173	tau (τ)	-1	1.78
bottom (b)	-⅓	4.18	τ-neutrino (ν_τ)	0	< 0.018

To understand the spectrum of hadrons, we label states by their total angular-momentum, parity and where possible charge conjugation (J^{PC}). In doing this one finds two fundamentally different families of hadrons, the mesons and baryons. The mesons are particles of integer spin, while the baryons are particles of half-integer spin. To truly understand the observed spectrum of hadrons requires a comprehensive understanding of how the structure and dynamics of hadrons arises from the underlying interactions of quarks. For this one needs to consider Quantum Chromodynamics (QCD), the quantum field theory that describes the strong interaction. However, many of the general features and patterns in the observed hadron spectrum can be understood in the context of constituent quark models. Before delving into underlying details of QCD, we shall take the time to consider how the hadron spectrum arises from the simple rules that govern the formation of hadrons from quarks.

2.1 The Quark Model of Hadrons

A careful examination of the lightest hadron states reveals clear patterns in the spectrum. For both baryons and mesons, one can identify distinct groupings of particles nearly degenerate in mass, differing only in their electric charge. Historically these were referred to as isospin multiplets and were understood to arise from an apparent SU(2) symmetry in the Hamiltonian of the strong interaction. Other approximate groupings can be identified where members differ in their strangeness. By combining these symmetries Gell-Mann and Neeman independently put forward the so called "8-fold way" [4, 5] which explained the observed hadron multiplets as different dimensional representations of SU(3). Fig. 2.1 highlights the lowest lying meson and baryon multiplets.

This observation was an important step forwards, however within the physical spectrum, it appeared that only a select number of representations were realised. All of this hinted at some overarching structure and it was this rationalisation that led Gell-Mann [6] to posit some fundamental entity, which he called quarks.

Within this framework, quarks are assigned to the fundamental representation of SU(3) and anti-quarks to the conjugate representation, with the elements of these vectors understood to be the quark flavours u, d and s. The observed dimensionality for the multiplets seen in the spectrum arise naturally if baryons are considered qqq states and mesons as $q\bar{q}$

$$\begin{aligned} qqq: &\quad \mathbf{3}\otimes\mathbf{3}\otimes\mathbf{3} = \mathbf{1}\oplus\mathbf{8}\oplus\mathbf{8}\oplus\mathbf{10}\,, \\ q\bar{q}: &\quad \mathbf{3}\otimes\bar{\mathbf{3}} = \mathbf{1}\oplus\mathbf{8}\,. \end{aligned}$$

However, if quarks are taken to be physical entities, the absence of free quarks leads one to conclude that the issue of select representations remains. A more troubling issue arises when one attempts to couple spin to this model. When considering the Δ^{++}, the spin-flavour wave function for this state is found to be completely symmetric, contrary to that required for fermions, which obey Fermi-Dirac statistics. A solution to this problem came from Greenberg who proposed that quarks are parafermionic [7]. If the quarks were to carry an additional quantum number, say colour charge, and the wave function were anti-symmetric in this new degree of freedom, then the Δ^{++} would be rendered anti-symmetric as required. It was further realised that if this new charge were to transform under SU(3) rotations, one could now understand why qqq and $q\bar{q}$ states are observed while others such as q and qq states are not: any combination must produce a colour-singlet representation in order to be physical. This requirement is the manifestation of the aforementioned colour confinement.

Finally, incorporating these key elements with the quark's spin, one arrives at the SU(6) quark model. Here the SU(3)-flavour symmetry group is promoted to an SU(6) spin-flavour symmetry. The vectors q now encode the spin-flavour elements $u\uparrow$, $u\downarrow$, $d\uparrow$, $d\downarrow$, $s\uparrow$ and $s\downarrow$. As highlighted by the Δ^{++}, the final requirement is that the baryon spin-flavour wave function be entirely symmetric. In this way we can completely understand the resultant ground state meson and baryon spectrum from

$$\begin{aligned} qqq: &\quad \mathbf{6}\otimes\mathbf{6}\otimes\mathbf{6} = \mathbf{56}\oplus\mathbf{70}\oplus\mathbf{70}\oplus\mathbf{20}\,, \\ q\bar{q}: &\quad \mathbf{6}\otimes\bar{\mathbf{6}} = \mathbf{1}\oplus\mathbf{35}\,. \end{aligned}$$

For the mesons, the situation becomes clearer upon writing the $\mathbf{35}$-plet in terms of flavour-spin elements,

$$\mathbf{35} = (\mathbf{8},1)\oplus(\mathbf{8},3)\oplus(\mathbf{1},3)\,, \quad \mathbf{1} = (\mathbf{1},1)\,.$$

Here we find the pseudoscalar nonet $(\mathbf{8},1)\oplus(\mathbf{1},1)$ and the vector nonet $(\mathbf{8},3)\oplus(\mathbf{1},3)$ presented in Fig. 2.1. For the baryons, the elements belonging to the $\mathbf{56}$-plet have the required spin-flavour symmetry properties. Again, expressing this

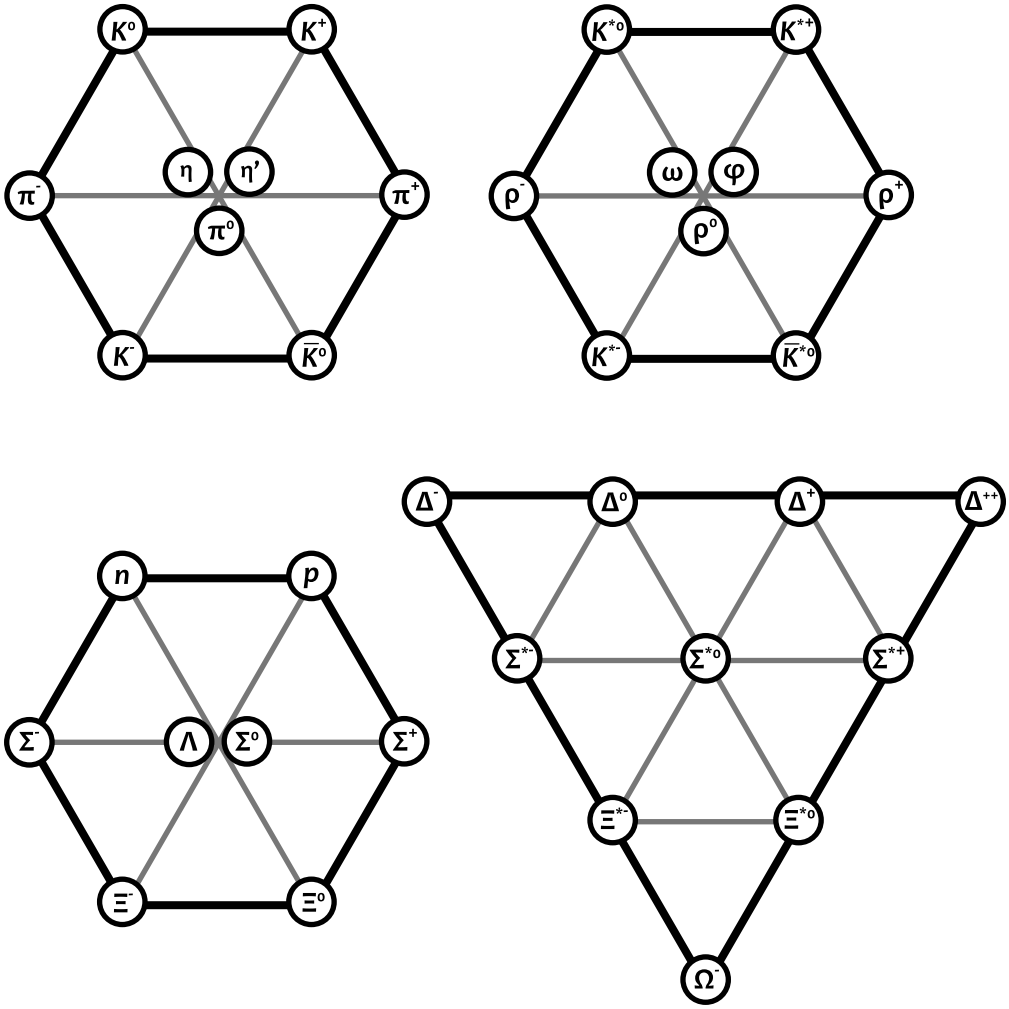

Figure 2.1: The pseudoscalar (top left) and vector (top right) meson nonets and the baryon octet (bottom left) and decuplet (bottom right). Hadrons are plotted with the third component of isospin in the horizontal direction and strangeness in the vertical direction.

representation in terms of flavour-spin elements we find

$$\mathbf{56} = (\mathbf{8}, 2) \oplus (\mathbf{10}, 4)\,,$$

which are the baryon octet and decuplet respectively, again presented in Fig. 2.1.

2.1.1 The SU(6)×O(3) Quark Model

So far we have seen how the ground state spectrum arises naturally within the SU(6) quark model, however this is only a small fraction of the observed spectrum. Given that there are six flavours of quarks, one can naturally increase

the symmetry group to include further flavours, however the remaining flavours are significantly larger and so the additions to the spectrum sit considerably higher. Much of the remaining spectrum can be understood when we recognise that the underlying quarks are interacting. Without resorting to, or historically, having QCD to completely describe these interactions one can instead place the quarks in some potential; the simplest choice being the harmonic oscillator. Through the spherical symmetry of this potential, the quarks are able to acquire orbital angular momentum, ℓ, and so the spectrum of hadrons can be built up by combining the resulting spatial and spin-flavour wave functions to form hadronic excitations. This extension is called the SU(6)×O(3) quark model [8].

For baryons, we require the flavour-spin-position wave function to be symmetric to ensure that the resulting full wave function including colour satisfies Fermi-Dirac statistics. In the case of the ground state, the spatial wave function is understood to be s-wave and so necessarily symmetric, thus permitting only the symmetric **56**-plet. For non-trivial angular momenta, non-symmetric position-space wave functions are possible providing access to other baryon spin-flavour symmetry groups. For mesons, the addition of orbital angular momentum gives rise to a strict relation between angular momentum, parity and charge conjugation,

$$\left.\begin{aligned} P &= (-1)^{\ell+1} \\ C &= (-1)^{\ell+s} \end{aligned}\right\} \qquad CP = (-1)^{1+s}\,.$$

As the only available meson spins are $s = 0, 1$, these relations induce distinct patterns in the J^{PC}. The most striking feature of the resulting meson spectrum is its inability to form particular PC combinations,

$$J^{PC} = 0^{+-}, 1^{-+}, 2^{+-}, \ldots$$

often known as forbidden, or exotic states.

2.1.2 Limitations of the Quark Model

It is clear that the quark model provides us with a natural explanation to the plethora of states that constitute the hadron spectrum. Using only qqq and $q\bar{q}$ structures we can understand the lowest lying meson and baryon multiplets. Furthermore, when coupled with orbital angular momentum, we can generate a diverse range of hadron excitations. However, examining the physical hadron spectrum one quickly finds that the quark model is far from complete. Within the excited baryon spectrum, the position of the lightest positive parity nucleon state, the $N^*(1440)$ (otherwise known as the Roper resonance) and the lightest negative parity baryon, the $\Lambda(1405)$, are much lighter than can be consistently explained using conventional quark models [9, 10]. Furthermore, the presence of light scalar mesons below 1 GeV strongly suggests the need for exotic states with quark content beyond the $q\bar{q}$ structure [11]. The existence of exotic states

has all but been confirmed with the recent discovery of the $Z^-(4430)$ at LHCb [12]. While it is possible to include extended quark content and refinements to the interaction potential such as spin-dependent effects, all fail to properly explain the small mass of the pion relative to all other hadron states. Such a shortcoming stems from the failure to properly describe the underlying dynamics of the strong interaction. For this we will need to resort to the underlying field theory that governs the strong interaction, Quantum Chromodynamics (QCD). Nonetheless, the quark model does a remarkably good job and certainly serves as a good benchmark, especially in the limit of heavy quark mass. Indeed, we will use this as a first comparison with our lattice results in the heavier quark-mass regime.

2.2 Quantum Chromodynamics

Quantum Chromodynamics (QCD) is the non-Abelian gauge theory that describes the strong interaction. This theory is formulated on the requirement of local gauge invariance for fields carrying colour charge under the non-Abelian Lie group SU(3). Through this theory, the strong interaction is understood as the interaction of quarks through the exchange of particles called gluons. In structure, this theory shares many similarities with Quantum Electrodynamics, the gauge field theory describing the electromagnetic interaction. However due to the non-Abelian nature of the underlying gauge group, the force mediators (gluons) undergo self-interactions leading to vastly different dynamics and ultimately, the non-perturbative nature of QCD. The necessary framework for non-Abelian gauge theories was first laid out by Yang and Mills [13].

The free Lagrangian density for a quark (a spin-$1/2$ particle carrying colour charge) is given by

$$\mathcal{L}_{\mathrm{F}}^{(0)}(x) = \bar{\psi}(x)\ \left(i\partial\!\!\!/ - m\right)\ \psi(x)\,, \tag{2.1}$$

where $\psi(x)$ is colour 3-vector of spinor fields (for readability we have suppressed the colour label). Under a global SU(3) transformation $\Omega = e^{i\,\theta_a\,\frac{\lambda_a}{2}}$ (θ_a is a constant phase and $\frac{\lambda_a}{2}$ the group generators),

$$\psi(x) \to \Omega\,\psi(x), \quad \bar{\psi}(x) \to \bar{\psi}(x)\,\Omega^{-1}\,,$$

and so the Lagrangian remains invariant. However, the corresponding local transformation (obtained by taking $\theta_a \to \theta_a(x)$) does not leave the Lagrangian invariant due to the non-invariance of the derivative,

$$\partial_\mu(\Omega(x)\,\psi(x)) \neq \Omega(x)\,\partial_\mu\psi(x)\,. \tag{2.2}$$

This non-invariance stems from the fact that the derivative relates fields at two different spacial locations,

$$n^\mu\partial_\mu = \lim_{\epsilon\to 0}\frac{1}{\epsilon}\{\psi(x+\epsilon n) - \psi(x)\}\,,$$

which ultimately live in separate vector spaces and so transform differently. To make sense of the derivative, we need to introduce some operator, $U(y,x)$, that will allow us to transport a vector in the vector space of point x to a corresponding vector in the vector space at point y. To achieve this, the operator will require the following transformation property,

$$U(y,x) \to \Omega(y)\, U(y,x)\, \Omega^{-1}(x)\,, \tag{2.3}$$

which ensures that $U(x+\epsilon n, x)\,\psi(x)$ transforms in the same fashion as $\psi(x+\epsilon n)$. Redefining the derivative with this addition, we obtain the covariant derivative D_μ which transforms as

$$D_\mu \to \Omega(x)\, D_\mu\, \Omega^{-1}(x)\,, \tag{2.4}$$

ensuring that $D_\mu\psi$ is consistent with ψ. The device, $U(y,x)$, that allows one to transport the field vector at x to the corresponding field vector at y is the Wilson line,

$$U(y,x) \equiv \mathcal{P} e^{i\,g\,\int_x^y A_\mu^a(z)\,\frac{\lambda^a}{2}\,dz}\,. \tag{2.5}$$

For points that are arbitrarily close we are able to make the expansion

$$U(x+\epsilon n, x) = 1_3 + i\,g\,\epsilon\, n^\mu\, A_\mu^a(x)\,\frac{\lambda^a}{2} + \mathcal{O}(\epsilon^2)\,,$$

from which it follows that the covariant derivative D_μ can be expressed as

$$D_\mu(x) = \partial_\mu - i\,g\,A_\mu^a(x)\,\frac{\lambda^a}{2}\,.$$

The required transformation property of the $A_\mu(x) \equiv A_\mu^a(x)\frac{\lambda^a}{2}$ field for D_μ to transform covariantly is

$$A_\mu(x) \to \Omega(x) A_\mu(x)\, \Omega^{-1}(x) - \frac{i}{g}\,(\partial_\mu \Omega(x))\, \Omega^{-1}(x)\,.$$

Replacing ∂_μ in (2.1) by $D_\mu = (\partial_\mu - i\,g\,A_\mu(x))$ makes the resulting Lagrangian invariant under both local and global gauge transformations, however the Lagrangian remains incomplete as there are no kinematic terms present for A_μ. As $A_\mu(x)$ is a vector field, the necessary addition is of the form $\frac{1}{2}\,\mathrm{tr}[G_{\mu\nu}G^{\mu\nu}]$ where

$$-igG_{\mu\nu} = [D_\mu, D_\nu]\,. \tag{2.6}$$

Using Eq. (2.4) and the definition of $G_{\mu\nu}$ it is easy to see that this term is gauge invariant. Thus the complete[2] QCD Lagrangian is given by

$$\mathcal{L}_{\mathrm{QCD}}(x) = \bar\psi(x)\left(i\not{D} - m\right)\psi(x) - \frac{1}{2}\,\mathrm{tr}[G_{\mu\nu}\,G^{\mu\nu}]\,. \tag{2.7}$$

[2]The term $\theta\frac{g^2}{16\pi^2}\,\mathrm{tr}[G_{\mu\nu}\,\tilde G^{\mu\nu}]$, where $\tilde G^{\mu\nu} = \frac{1}{2}\epsilon^{\mu\nu\sigma\tau}G_{\sigma\tau}$, is admissible under the requirements of renormalisability, however this term explicitly violates CP-symmetry.

To elucidate the underlying interactions encoded in Eq. (2.7), we express $A_\mu(x)$ as $A^a_\mu(x)\,\frac{\lambda^a}{2}$ in Eq. (2.6). The field-strength tensor $G_{\mu\nu}$ takes the explicit form

$$G_{\mu\nu} = \left(\partial_\mu A^a_\nu - \partial_\nu A^a_\mu + g\, f^{abc}\, A^b_\mu\, A^c_\nu\right)\, \frac{\lambda_a}{2}\,, \tag{2.8}$$

$$= \left(G^{(0)\,a}_{\mu\nu} + g\, f^{abc}\, A^b_\mu\, A^c_\nu\right)\, \frac{\lambda_a}{2}\,, \tag{2.9}$$

where $G^{(0)\,a}_{\mu\nu} = \partial_\mu A^a_\nu - \partial_\nu A^a_\mu$ is the kinetic term for A^a_ν. The quadratic terms arise from the non-Abelian nature of the Lie-Algebra for SU(3),

$$\left[\frac{\lambda^a}{2}, \frac{\lambda^b}{2}\right] = f^{abc}\,\frac{\lambda^c}{2}\,.$$

Substituting the expanded form of the covariant derivative and the field-strength tensor into Eq. (2.7), we can decompose the Lagrangian as

$$\mathcal{L}_{\rm QCD}(x) = \mathcal{L}^{(0)}_{\rm F}(x) + \mathcal{L}^{(0)}_{\rm G}(x) + \mathcal{L}_{\rm I}(x)\,,$$

where

$$\mathcal{L}^{(0)}_{\rm F}(x) = \bar\psi(x)\,\left(i\partial\!\!\!/ - m\right)\,\psi(x)\,,$$
$$\mathcal{L}^{(0)}_{\rm G}(x) = -\frac{1}{2}\,{\rm tr}[G^{(0)}_{\mu\nu}\,G^{(0)\,\mu\nu}]\,,$$

are the Lagrangians for a free quark field and massless vector boson, while the remaining terms

$$\mathcal{L}_{\rm I}(x) = +g\,\bar\psi(x)\,A_\mu\,\gamma^\mu\,\psi(x) - g\,f^{abc}\,\partial_\mu A^a_\nu\,A^{b\,\mu}\,A^{c\,\nu} - \frac{g^2}{4}\,f^{abc}\,f^{ade}\,A^b_\mu\,A^c_\nu\,A^{d\,\mu}\,A^{e\,\nu}\,,$$

encode the interaction vertices. Unlike in Quantum Electrodynamics (QED), the force mediators themselves carry charge and so are able to interact at tree level. All of the non-trivial dynamics of the strong interaction stem from these self-interactions resulting in a highly non-linear and non-trivial field theory.

Two of the most distinguishing properties of QCD are asymptotic freedom and confinement. Both give rise to distinctly different features of the strong interaction. The first of these, asymptotic freedom, is the identification that at high energies (short distance scales) the strong coupling constant is small and so perturbative methods are permissible. However, the scaling behaviour of the strong coupling constant results in an increasing value with decreasing energy and so perturbative series break down in the low energy regime. The mechanism through which this happens is well understood and stems from the anti-screening effect induced by the gluon fields. The origin of confinement on the other hand is still on open question. From our observations of the strong interaction, it is clear that there is some underlying mechanism that prohibits the existence of coloured states, at least in the realm of low energy and low density. Therefore the natural

state of a quark is to be bound. Thus treatment of the system as perturbations from a free particle state fail to properly describe the system. This argument is further enhanced with the realisation that the underlying chiral symmetry of QCD induces a change in the vacuum in which the lowest energy configuration is non-empty. It is apparent that in order to consider the underlying dynamics of a hadronic system, a non-perturbative treatment of QCD is required.

2.3 Hadron Structure and Form Factors

For a truly fundamental understanding of the hadron spectrum, we require a detailed understanding of how their underlying structure arises from quark and gluon degrees of freedom. Having arrived at the theory describing the interactions between these constituents in the previous section, one could argue that we are in a position to answer such questions. However, without a practical approach to evaluating the necessary amplitudes via QCD, it seems that we lack the machinery to work from the level of constituents to build up to a hadron. Nonetheless, it is still possible to learn a great deal by operating from the level of the hadron. Unsurprisingly, the framework and language used in mapping out hadron structure in this fashion was developed well before we had any knowledge of the underlying mechanism of the strong interaction.

The approach we take is to treat the hadron as a phenomenological quantity whose interaction with an external current is described by matrix elements of the form

$$\langle\, \alpha, p', s' \,|\, \mathcal{O}(0) \,|\, \beta, p, s \,\rangle = \bar{u}_\alpha(p', s')\Gamma(p', p)u_\beta(p, s)\,, \tag{2.10}$$

where the terms $u_\alpha(p, s)$ are relevant mathematical structures that properly describe the J^{PC} of the state α carrying momentum p and spin s. We note that in general the incoming and outgoing states need not be the same; in such a case the matrix element describes the transition amplitude between states through the current corresponding to $\mathcal{O}$. Matrix elements described by Eq. (2.10) can be represented by diagrams given in Fig. 2.2.

All of the dynamics describing the interaction with the current are encoded within the vertex function, $\Gamma(p', p)$, and so contain all the information pertaining to the hadron's underlying structure. In particular, we can identify all of the possible Lorentz covariant structures consistent with the current, and to each of these assign a scalar function called a form factor which describes the hadrons underlying structure. It turns out that the only independent scalar invariant variable is the squared momentum transfer, q^2, where $q = p' - p$. In this fashion, we can rewrite the matrix element as,

$$\langle\, \alpha, p', s' \,|\, \mathcal{O}(0) \,|\, \beta, p, s \,\rangle = \bar{u}_\alpha(p', s') \left[\sum_i \mathcal{X}_i F_i(q^2)\right] u_\beta(p, s)\,,$$

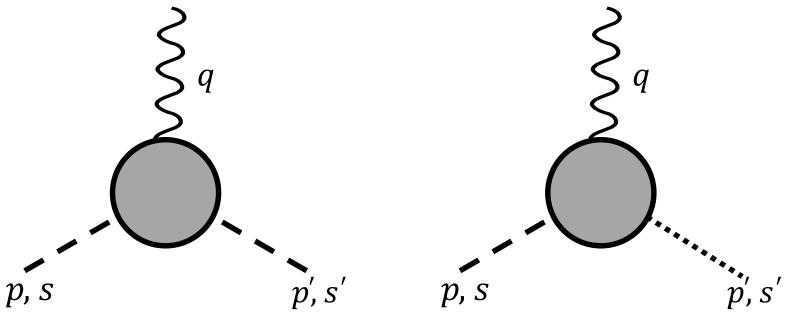

Figure 2.2: Diagrams expressing the matrix elements describing the interaction of a hadron with an external current. The diagram on the left is for elastic processes while the diagram on the right is for transitions. It is possible to describe the underlying structure and dynamics for such processes in terms of invariant scalar functions of the squared momentum transfer, called form factors. These functions can be considered as describing by how much the hadron differs from a point-like structure.

where $\mathcal{X}_i$ are the Lorentz covariant structures. In this form, it is often possible to eliminate terms through considerations of symmetries, such as parity or time-reversal, or properties required for conservation of particular quantities, such as Ward identities. A key benefit of this approach is its strong connection with experiment. As quarks are bound particles, the states experimentalists must work with are the hadrons themselves. Therefore the measurements that they make, such as cross-sections and scattering amplitudes, can be related to these form factors.

Chapter 3

Lattice QCD

For the energy scales that make up much of our universe, QCD is inherently non-perturbative. In order to extract results in this regime, we need a strategy that either re-expresses the theory in terms of the relevant degrees of freedom, the hadrons, or approach the problem in an entirely non-perturbative way. The appeal of the first method is that by re-expressing QCD as an effective theory, it is possible to perform perturbative expansions in powers of momenta when equipped with a suitable power counting scheme. These theories can provide a tremendous degree of insight into the underlying chiral dynamics of QCD and do a remarkably good job at describing QCD at low energies. However, for energy scales on the order of 0.5 GeV, the perturbative series begin to display poor convergence and render such methods useless. As the majority of hadron states lie above this threshold, accurate descriptions of such systems require non-perturbative techniques.

There exist several non-perturbative approaches to solving problems in QCD, however the only direct systematic approach that exists is that of Lattice QCD. First proposed by Kenneth Wilson [14] as a means to demonstrate the confining behaviour of QCD, the theory allows for the evaluation of observables directly from QCD. By formulating QCD on a finite, discretised piece of space-time (a lattice), the theory acquires a natural and non-perturbative regularisation scheme. Furthermore, by operating in Euclidean space, the path integrals that describe quantum process take on a form reminiscent of the Boltzmann distribution from statistical mechanics. Together these features render the phase space sampled by the path integral finite and so one can employ Monte-Carlo techniques to evaluate the observables. Given the scale of the problem, the only practical approach to this formulation is to perform such calculations numerically. In this chapter we shall consider the basic principles upon which Lattice QCD is formulated and present the simplest discretisation of the QCD action, the Wilson action. From here we shall briefly examine improvement schemes and finally consider the machinery required to probe the underlying structure of a hadronic system.

3.1 Path Integrals

An alternate prescription to the canonical formulation of a quantum field theory is that of the path integral. The underlying principle of this approach is that a quantum process can be represented as the sum over all possible field configurations, whereby each configuration's contribution to the amplitude is weighted by a phase set by the action evaluated for that configuration. It follows that the fundamental quantity is the generating functional,

$$\mathcal{Z} = \prod_i \int \mathcal{D}\phi_i \, e^{+iS[\phi_1,\phi_2,\ldots,\phi_n]} \tag{3.1}$$

which describes the make-up and evolution of the physical vacuum for the theory. Here ϕ_i are the field variables, with the action $S[\phi_1, \phi_2, \ldots, \phi_n]$ obtained from the Lagrangian density,

$$S[\phi_1, \phi_2, \ldots, \phi_n] = \int \mathcal{L}(\phi_1, \phi_2, \ldots, \phi_n; x) \, d^4x$$

and the measure defined as

$$\mathcal{D}\phi_i = \prod_x d\phi_i(x) \, .$$

To extract vacuum expectation values, one simply includes the relevant operator into the integrand and re-evaluates the normalised integral

$$\langle \mathcal{O} \rangle = \frac{1}{\mathcal{Z}} \prod_i \int \mathcal{D}\phi_i \, \mathcal{O}[\phi_1, \phi_2, \ldots, \phi_n] \, e^{+iS[\phi_1,\phi_2,\ldots,\phi_n]} \, . \tag{3.2}$$

By offering an alternate method to the evaluation of amplitudes, the path integral has furthered our understanding of field theories, especially when the canonical approach has seemed intractable. Of particular importance is the strong connection this approach provides us to statistical mechanics. Up to the fact that the exponential weight is complex, the form of Eq. (3.1) is reminiscent of the partition function from statistical mechanics. If we re-express the theory in Euclidean space through a Wick rotation,

$$t \to -it_E \, ,$$

the action is mapped to the Euclidean action,

$$S \to -iS_E \, ,$$

and the generating functional takes the correct form for a partition function,

$$Z = \prod_i \int \mathcal{D}\phi_i \, e^{-S_E[\phi_1,\phi_2,\ldots,\phi_n]} \, .$$

This in turn allows for a re-interpretation of vacuum expectation values as the weighted ensemble average over all of the allowed field configurations. From such a definition, if we wish to obtain an estimate for some vacuum expectation value, all we need do is generate a sub-ensemble of field configurations which is sampled from the full ensemble by the probability factor

$$P[\Phi_i] = e^{-S_E[\Phi_i]} ,$$

where $\Phi_i = (\phi_1^i, \phi_2^i, \ldots, \phi_n^i)$ denotes a given field configuration. The estimate for operator expectation values is then given by the average of the relevant operator evaluated over the N sub-ensembles,

$$\langle \mathcal{O} \rangle \simeq \frac{1}{N} \sum_{i=1}^{N} \mathcal{O}[\Phi_i] .$$

In the absence of an analytic approach to generating suitable gauge field configurations, the next step to a practical approach would be to perform some discretisation of space-time. In doing this for the QCD action, we arrive at Lattice QCD.

3.2 Discretising the QCD Action

Discretisation of space-time is achieved by the simple transformation,

$$x^\mu \to a n^\mu ,$$

where a is the spacing between lattice sites and n^μ are integer valued coordinates that enumerate the vertices of our lattice. We will also define e_μ to be the unit vector for a given space-time dimension specified by the index μ. We then restrict ourselves to a finite volume of space-time, $V = L^4 = (Na)^4$, where N is the number of lattice sites in a given direction. In order to solve the equations of motion one must also impose boundary conditions. For gauge field generation, periodic boundary conditions are the common choice. By limiting space-time to a finite hypercube lattice, we have rendered our field operators finite entities and reduced the phase space of possible gauge configurations from an infinite to finite number. As such, lattice field theories allows us to employ Monte Carlo sampling techniques to generate the sub-ensemble of gauge fields. In this fashion, the problem is well suited to numerical computation.

In formulating QCD on the lattice, we place the fermion fields on the lattice sites and replace derivatives by finite-differences and integrals over space-time by sums over the lattice volume,

$$\partial_\mu \psi(x) \to \delta_\mu \psi(x) = \frac{1}{2a} \left(\psi(x + a e_\mu) - \psi(x - a e_\mu) \right) ,$$
$$\int d^4x \to a^4 \sum_n .$$

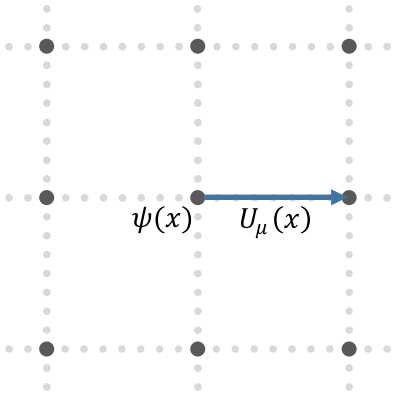

Figure 3.1: The lattice discretisation upon which Lattice QCD is formulated herein. The quark fields, $\psi(x)$, occupy the sites while the gauge fields are represented by the links between lattice sites, $U_\mu(x)$.

The final element we require is the discretised analogue of the gauge field, A_μ. In the continuum, the gauge field arose naturally through our need to restore the gauge transformation properties of the derivative. Following a similar vein, we can see that our finite difference operator fails to transform covariantly under a local gauge transformation, $\Omega(x)$, now restricted to the lattice sites. In Section 2.2 we saw that the introduction of the Wilson line was the crucial element that allowed us to relate the vector spaces at different locations and thus construct meaningful derivatives. In the continuum case we would use

$$U_\mu(x) \equiv U(x + ae_\mu, x) = \mathcal{P} e^{i\,g\,\int_x^y A_\mu^a(z)\,\frac{\lambda^a}{2}\,dz} \simeq e^{i\,a\,g\,A_\mu(x)}\,. \tag{3.3}$$

Rather than work with gauge fields A_μ, on the lattice we choose instead to work directly with the U_μ fields. In this manner we simply require these fields to satisfy the lattice analogue of Eq. (2.3),

$$U_\mu(x) \to \Omega(x)\,U_\mu(x)\,\Omega^{-1}(x + ae_\mu)\,, \quad U_\mu^\dagger(x) \to \Omega(x + ae_\mu)\,U_\mu^\dagger(x)\,\Omega^{-1}(x)\,. \tag{3.4}$$

We can then define the covariant finite difference operators as

$$\nabla_\mu \psi(x) = \frac{1}{2a}\left(U_\mu(x)\,\psi(x + ae_\mu) - U_\mu^\dagger(x - ae_\mu)\,\psi(x - ae_\mu)\right)\,.$$

This field $U_\mu(x)$ is effectively the minimal transport operator on the lattice that relates one site to an adjacent site, as shown in Fig. 3.1. For this reason, we often refer to these fields as link variables. It is useful to further define the transport operators,

$$T_\mu \psi(x) = U_\mu(x)\,\psi(x + ae_\mu)\,, \quad T_\mu^\dagger \psi(x) = U_\mu^\dagger(x - ae_\mu)\,\psi(x - ae_\mu)$$

which allow us to write the covariant finite difference operator succinctly as,

$$\nabla_\mu = \frac{1}{2a}\left(T_\mu - T_\mu^\dagger\right)\,.$$

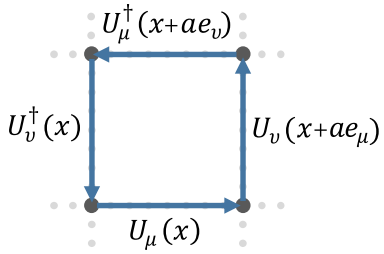

Figure 3.2: The closed product of links that give rise to the plaquette, $P_{\mu\nu}(x)$.

Having identified the lattice analogues of our continuum fermion and gauge fields, we now seek a discretisation of the QCD action which in the limit of taking the lattice spacing to zero, $a \to 0$, restores the continuum QCD action.

3.2.1 Gauge Fields on the Lattice

Here we shall consider a discretised version of the gauge field action,

$$S_{\mathrm{G}}[A] = \frac{1}{2}\int d^4x \,\mathrm{Tr}\,[G_{\mu\nu}G_{\mu\nu}]\ . \tag{3.5}$$

It is worth noting that we no longer need to delineate covariance and contravariance of terms as we are now operating in Euclidean space. In section 2.2, we arrived at this expression through considerations of gauge invariance. Following a similar motivation here, we seek a quantity composed entirely of gauge fields that satisfies gauge invariance. On the lattice, the simplest such quantity is given by the trace of the path-ordered product of links around a 1×1 loop shown in Fig 3.2,

$$P_{\mu\nu}(x) = U_\mu(x)\, U_\nu(x+ae_\mu)\, U_\mu^\dagger(x+ae_\nu)\, U_\nu^\dagger(x)\,. \tag{3.6}$$

This quantity is referred to as a plaquette. Expressing this in terms of gauge field variables we have,

$$P_{\mu\nu}(x) \simeq e^{i\,a\,g\,A_\mu(x)} e^{i\,a\,g\,A_\nu(x+ae_\mu)} e^{-i\,a\,g\,A_\mu(x+ae_\nu)} e^{-i\,a\,g\,A_\nu(x)}\,.$$

Given these are exponentials of non-Abelian objects, combing them into a single exponential requires the use of the Baker-Campbell-Hausdorf identity

$$e^A e^B = e^{A+B+\frac{1}{2}[A,B]+\ldots}\,.$$

Applying this identity and making use of the forward difference operator we can re-express the shifted gauge field as

$$A_\mu(x+ae_\nu) = A_\mu(x) + a\,\delta_\nu^+ A_\mu(x) + \mathcal{O}(a^2)\,,$$

and so arrive at

$$P_{\mu\nu} = e^{i\left(a^2\, g\, G_{\mu\nu}(x) + \mathcal{O}(a^3)\right)}\,.$$

Finally if we consider the power series definition of this exponential, we can obtain the required product of field strength tensors via

$$\left(I_3 - \frac{1}{2}\left(P_{\mu\nu} + P_{\mu\nu}^\dagger\right)\right) = \frac{a^4\, g^2}{2}\, G_{\mu\nu}\, G_{\mu\nu} + \mathcal{O}(a^6)\,. \tag{3.7}$$

We can then write down the simplest discretisation of the gluon action,

$$S_{\mathrm{G}}[U] = c \sum_x \sum_{\mu>\nu} \mathrm{Tr}\left[I_3 - \frac{1}{2}\left(P_{\mu\nu}(x) + P_{\mu\nu}^\dagger(x)\right)\right]\,, \tag{3.8}$$

with the constant c to be determined such that we obtain the correct normalisation. In this expression $\sum_{\mu>\nu}$ ensures that each plaquette contributes once only. We can promote this to a sum over all values in μ and ν provided we account for the double counting. With this adjustment and substituting Eq. (3.7) into our expression we arrive at a form that is remarkably close to Eq. (3.5),

$$S_{\mathrm{G}}[U] = \frac{g^2 c}{2}\ \cdot\ \frac{1}{2}\, a^4 \sum_x \left(\mathrm{Tr}\left[G_{\mu\nu}\, G_{\mu\nu}\right] + \mathcal{O}(a^2)\right)\,, \tag{3.9}$$

where the repeated indices are now summed over. Taking the continuum limit, we obtain the continuum expression if we choose $c = \frac{2}{g^2}$. Substituting this value into Eq. (3.9) we obtain the desired discretisation, often referred to as the Wilson gauge action. It is common practice to write this expression in the slightly modified from

$$S_{\mathrm{G}}[U] = \beta \sum_x \sum_{\mu>\nu} \left(1 - \frac{1}{3}\mathrm{Re}\,\mathrm{Tr}\left[P_{\mu\nu}(x)\right]\right)\,, \tag{3.10}$$

where the value $\beta = \frac{6}{g^2}$.

3.2.2 Fermions on the Lattice

Having arrived at a suitable discretisation for the gauge action of QCD, we now consider the fermionic portion

$$S_{\mathrm{F}}[\psi, \bar{\psi}, A] = \int d^4x\, \bar{\psi}(x)\ \left(\not{D} + m\right)\ \psi(x)\,. \tag{3.11}$$

Using the lattice analogue of the covariant derivative defined in Section 3.2, we can immediately write down a discretisation of Eq. (3.11)

$$\begin{aligned} S_{\mathrm{F}}[\psi, \bar{\psi}, U] = a^4 \sum_x \Bigg(&\frac{1}{2a}\, \bar{\psi}(x)\, \gamma_\mu\, U_\mu(x)\, \psi(x + a e_\mu) \\ &- \frac{1}{2a}\, \bar{\psi}(x)\, \gamma_\mu\, U_\mu^\dagger(x - a e_\mu)\, \psi(x - a e_\mu) + m\, \bar{\psi}(x)\, \psi(x)\Bigg)\,. \end{aligned} \tag{3.12}$$

In order to show that this takes the required form, we take the power series expansion for the links

$$U_\mu(x) = I_3 + i\,a\,g\,A_\mu(x) + \mathcal{O}(a^2)\,,$$
$$U_\mu^\dagger(x - ae_\mu) = I_3 - i\,a\,g\,A_\mu(x) + \mathcal{O}(a^2)\,,$$

and again make use of the forward difference operator, this time for the fermion fields,

$$\psi(x + ae_\mu) = \psi(x) + a\,\delta_\mu^+\psi(x) + \mathcal{O}(a^2)\,,$$
$$\psi(x - ae_\mu) = \psi(x) - a\,\delta_\mu^+\psi(x) + \mathcal{O}(a^2)\,,$$

which gives

$$S_{\mathrm{F}}[\psi, \bar\psi, U] = a^4 \sum_x \left(\bar\psi(x)\,\gamma_\mu\,\left(\delta_\mu^+ + i\,g\,A_\mu\right)\,\psi(x) + \mathcal{O}(a^2)\right)\,.$$

Though this appears to take the correct form in the continuum limit, this naïve approach has a serious flaw – it produces unphysical fermion species, often referred to as fermion doublers.

To understand the origin of these extra fermions, we consider the propagator for a free fermion field in both the continuum and lattice formulations. Beginning with the continuum case, we note that the fermion propagator being the Green's function for the fermion matrix,

$$\left(\not{p} + m\right)\,S(p) = 1\,,$$

takes the form

$$S(p) = \frac{\not{p} - m}{p^2 - m^2}\,.$$

For a massless fermion, we see that this operator has a single pole at the origin. In the case of the lattice, it suffices to consider the central difference operator in momentum space,

$$\delta_\mu\psi(x) \xrightarrow{\mathcal{F}} \frac{i}{a}\sin(ap_\mu)\,\tilde\psi(p)\,.$$

In the case of massless fermions, the zeros of this operator correspond to the poles in the lattice propagator. Once again we find zero at the origin, however we also find there now exist further zeros at $p = \frac{\pi}{a}(k_1, k_2, k_3, k_4)$ where $k_i \in \{0, 1\}$. It is these extra zeros that correspond to the spurious fermion species. So the question is how can we remove these zeros and in such a way that our discretised fermion action still recovers the continuum action in the limit that the lattice spacing tends to zero.

The solution, courtesy of Wilson, is to include extra terms to the action which will remove these unwanted zeros at finite lattice spacing and vanish in the continuum limit. By including the so called Wilson term,

$$\Delta = \frac{1}{a^2}\sum_{\mu=1}^{4} 2 - T_\mu - T_\mu^\dagger \,,$$

we arrive at the Wilson fermion action:

$$S_{\mathrm{F}}[\psi,\bar{\psi},U] = a^4 \sum_x \bar{\psi}(x)\left(\not{\nabla} + \frac{ra}{2}\Delta + m\right)\psi(x)\,, \tag{3.13}$$

where the parameter r is called the Wilson parameter and is generally set to unity. It is common practice to scale the fermion fields via

$$\psi \to \frac{\psi}{\sqrt{2\kappa}} \quad \text{where} \quad \kappa = \frac{1}{2ma + 8r}\,,$$

after which the fermion action reads

$$S_{\mathrm{F}}[\psi,\bar{\psi},U] = a^4 \sum_{x,y} \bar{\psi}(x)\mathbf{M}(x,y)\psi(y)\,,$$

with the Wilson fermion matrix

$$a\mathbf{M}(x,y) = \delta_{xy} - \kappa \sum_\mu \left[(r-\gamma_\mu)U_\mu(x)\delta_{y,x+ae_\mu} + (r+\gamma_\mu)U_\mu^\dagger(x-ae_\mu)\delta_{y,x-ae_\mu}\right]\,.$$

The parameter κ couples the fermion field at a given site to its nearest neighbours and for this reason is called the hopping parameter. To understand how this term resolves the issues of fermion doublers, we consider its Fourier transform to give its momentum space representation,

$$\Delta\psi(x) \xrightarrow{\mathcal{F}} \frac{2}{a^2}\sum_{\mu=1}^{4}\left(1-\cos(ap_\mu)\right)\,.$$

This term contains the necessary zero at the origin and remains non-zero for the remaining $p = \frac{\pi}{a}(k_1,k_2,k_3,k_4)$. Combining this with the finite difference operator we remove the unwanted zeros leaving us with a single physical fermion field. Unfortunately the addition of this term results in $\mathcal{O}(a)$ discretisation errors and explicitly breaks chiral symmetry. Though we can make improvements to the action, as will be discussed in the following section, the issue of chiral symmetry stems from the No-Go theorem of Nielsen-Ninomiya [15–17]. Here they were able to establish that when using a lattice regularisation scheme, it is not possible to formulate chirally symmetric theory that is free of fermion doublers. It is possible to invoke a generalisation of chiral symmetry on the lattice through the Ginsparg-Wilson relation [18]; however the computational expense of the resulting formulation limits its use to calculations where chiral symmetry is of particular importance.

3.2.3 Path Integrals in QCD

Here we shall consider the Euclidean definition of the path integral applied explicitly to QCD. We begin with the Euclidean definition of the QCD Lagrangian density on a lattice,

$$\mathcal{L}^{\mathrm{Eu}}_{\mathrm{QCD}}(x) = \bar{\psi}(x)\,\mathbf{M}(x,y)\,\psi(y) + \frac{1}{2}\,\mathrm{tr}[G_{\mu\nu}(x)\,G^{\mu\nu}(x)]\,,$$

where we note that the fermionic portion can be described by the operator $\mathbf{M}(x,y)$ discussed in the previous section. Integrating these densities over Euclidean space-time results in the action having two pieces,

$$S_{\mathrm{QCD}}[\psi,\bar{\psi},U] = S_{\mathrm{F}}[\psi,\bar{\psi},U] + S_{\mathrm{G}}[U]\,.$$

The fermionic portion S_{F}, is a function of both the quark fields ψ and $\bar{\psi}$, and the gluon field U^{μ}, while the gauge portion S_{G}, is a function of the gluon fields only. The corresponding QCD partition function is

$$Z[\psi,\bar{\psi},U] = \int \mathcal{D}\psi\mathcal{D}\bar{\psi}\mathcal{D}U e^{-S_{\mathrm{QCD}}[\psi,\bar{\psi},U]}\,.$$

A nice feature of the fermion fields is that to satisfy Fermi-Dirac statistics, they must behave as Grassmann variables. Grassmann numbers possess some properties that allow one to evaluate the fermionic integral explicitly. Here we will simply state the result, however a detailed discussion can be found in Ref. [19]. Performing the integration one finds

$$\int \mathcal{D}\psi\mathcal{D}\bar{\psi}e^{-\sum_{x,y}\bar{\psi}(x)\mathbf{M}(x,y)\psi(y)} = \det\left(\mathbf{M}\right)\,. \tag{3.14}$$

As a result we are able to integrate out the fermion fields reducing the partition function to

$$\begin{aligned} Z[\psi,\bar{\psi},U] &= \int \mathcal{D}U\,\det\left(\mathbf{M}[U]\right)e^{-S_{\mathrm{G}}[U]} \\ &= \int \mathcal{D}U\,e^{-S_{\mathrm{eff}}[U]}\,, \end{aligned}$$

where we can define an effective action, $S_{\mathrm{eff}}[U] = S_{\mathrm{G}}[U] - \ln\left(\det\left(\mathbf{M}[U]\right)\right)$. A similar procedure can be applied to the expression for operator expectation values, however care must be taken in the presence of operators that include fermion fields ($\mathcal{O} = \mathcal{O}[\psi,\bar{\psi},U]$) as the integrand has now changed from Eq. (3.14). For the operators considered in this work, in performing the necessary integration, we obtain effective operators, defined in terms of the gauge fields U and the inverse of the fermion matrix (the fermion propagator), $\mathbf{M}^{-1}[U]$,

$$\langle\mathcal{O}\rangle = \frac{1}{Z}\int \mathcal{D}U\,\mathcal{O}_{\mathrm{eff}}[U,\mathbf{M}^{-1}[U]]e^{-S_{\mathrm{eff}}[U]}\,.$$

Therefore if one wishes to examine hadrons using the Euclidean path integral, it suffices to generate an ensemble of gauge field configurations, evaluate the fermion propagators for these configurations and finally evaluate the expectation value of the operator over the ensemble.

3.3 Improving the Lattice Action

As with any discretisation procedure, the choice is somewhat arbitrary. Provided the continuum theory is restored in the limit that the spacing tends to zero, one has a valid discretisation. Nonetheless, the choice of discretisation has a significant impact upon the resulting discretisation error. In arriving at the Wilson action for QCD, we found that discretisation errors are $\mathcal{O}(a^2)$ for S_{G} and $\mathcal{O}(a)$ for S_{F}. In principle, one can simulate over a large range of lattice spacings a and perform the continuum extrapolation in which these discretisation effects fall out. However this is general an expensive task, particularly given the poor convergence properties of this fermion action. A more practical approach is to improve the convergence properties of the discretised theory. Generally this improvement scheme will involve the addition of higher dimensional operators which can be tuned to cancel out the leading order discretisation errors.

The Symanzik improvement scheme [20, 21] is a systematic approach in which correction terms are incorporated into the QCD action order-by-order in operator dimension,

$$S = \int d^4x \left(\mathcal{L}^{(0)}(x) + a\, \mathcal{L}^{(1)}(x) + a^2\, \mathcal{L}^{(2)}(x) + \ldots \right) .$$

Here $\mathcal{L}^{(0)}$ is the QCD Lagrangian, $\mathcal{L}^{(1)}$ the Lagrangian composed of all dimension-5 operators, $\mathcal{L}^{(2)}$ Lagrangian composed of all dimension-6 operators and so on. These higher dimensional terms are called irrelevant operators as they do not contribute to the action in the continuum limit. At a given order we can tune the coefficients of these higher order terms in such a way that we cancel out the leading order discretisation error. In the case of the Wilson gauge action, we require the addition of dimension-6 operators $U^{(i)}_{\mathrm{loop}}$ (shown in Fig. 3.3) to eliminate the leading $\mathcal{O}(a^2)$ error,

$$S_{\mathrm{G}}[U] = \frac{2}{g^2} \sum_{i=0}^{3} c_i(g^2) \sum_x \mathrm{Re}\,\mathrm{Tr} \left[I_3 - U^{(i)}_{\mathrm{loop}}(x) \right] , \tag{3.15}$$

where we impose the additional constraint $c_0(g^2) + 8c_1(g^2) + 8c_1(g^2) + 16c_3(g^2) = 1$ to ensure that S_{G} has the correct normalisation. General considerations of such an action led Lüscher and Weisz [22] to conclude that the most general choice of coefficients at tree-level are,

$$c_0(0) = \frac{5}{3} - x, \quad c_1(0) = \frac{-1}{12} + x, \quad c_2(0) = 0, \quad c_3(0) = x\,,$$

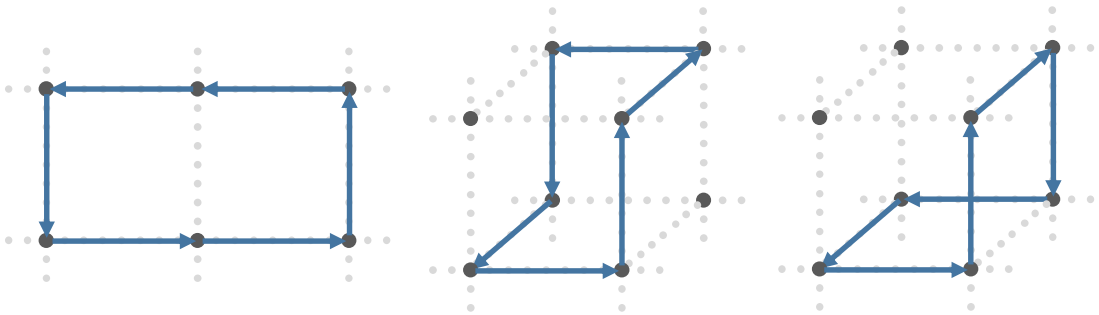

Figure 3.3: The higher order terms that contribute to the Lüscher Weisz improved action [22].

with the free-parameter x restricted to values that yield a positive action. As there are more possible orientations for the operator $U^{(3)}_{\text{loop}}$ than $U^{(1)}_{\text{loop}}$, all of which must be summed over, it is most advantageous to work with $x = 0$. This results in the Lüscher-Weisz gauge action,

$$S_{\text{G}}^{\text{imp}}[U] = \frac{\beta}{3}\sum_{x}\sum_{\mu>\nu}\left(\frac{5}{3}\text{Re}\,\text{Tr}[I_3 - P_{\mu\nu}(x)] \right. \\ \left. -\frac{1}{12}\text{Re}\,\text{Tr}[I_3 - R^{1\times 2}_{\mu\nu}(x)] - \frac{1}{12}\text{Re}\,\text{Tr}[I_3 - R^{2\times 1}_{\mu\nu}(x)]\right) ,$$

which at tree-level has $\mathcal{O}(a^4)$ discretisation error. In the presence of non-trivial gauge fields, the coefficients are renormalised away from their tree-level values, indicated in Eq. (3.15) by the fact the coefficients are functions of g^2. In order to maintain the leading order improvement, the renormalised coefficients must be used. Estimates of the renormalised coefficients $c_i(g^2)$ can be obtained perturbatively by determining the loop corrections. Alternatively, one can perform a non-perturbative determination by matching, to all orders in g^2, a given observable to its physical value.

An alternate approach to improving the action is to use Renormalisation Group Techniques. These methods use a lattice prescription of the Renormalisation Group equations to give non-perturbative estimates for the coefficients of selected irrelevant operators. This results in an action that lies closer to that on the renormalised trajectory, resulting in improved convergence properties. The Iwasaki action [23], relevant to the PACS-CS configurations [24] used in this work is one such action

$$S_{\text{G}}^{\text{iwasaki}}[U] = \beta\sum_{x}\sum_{\mu>\nu}\left(c_0\text{Tr}[P_{\mu\nu}(x)] + c_1\text{Tr}[R^{1\times 2}_{\mu\nu}(x)]\right) ,$$

where $c_0 = 1 - 8\,c_1$ and $c_1 = -0.331$. For further discussion of RG techniques, we refer the reader to Ref. [25].

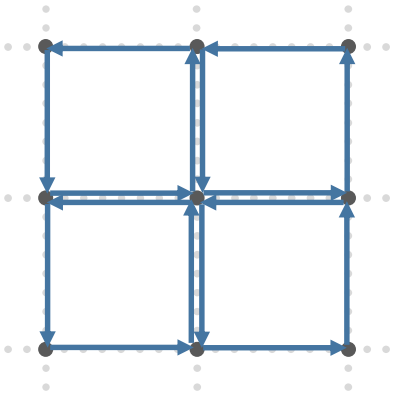

Figure 3.4: The plaquettes that contribute to the clover term, $C_{\mu\nu}(x)$ used in the evaluation of field-strength tensor $G_{\mu\nu}(x)$.

3.3.1 The Wilson Clover Action

Improvement of the fermion action is achieved in much the same way through the use of the Symanzik improvement scheme, however we are able to form operators using both fermion fields and link variables. Sheikholeslami and Wohlert [26] considered the inclusion of dimension-5 operators into the Wilson action in order to achieve $\mathcal{O}(a)$ improvement. There are five possible operators that have dimension-5, however all but one of these can be absorbed into existing terms through a redefinition of operator coefficients. Inclusion of this term into the Wilson action gives the Sheikholeslami-Wohlert, or commonly clover, action

$$S_{\mathrm{F}}[\psi,\bar{\psi},U] = S_{\mathrm{Wilson}} - \frac{iga^5 C_{\mathrm{SW}} r}{4}\sum_x \bar{\psi}(x)\sigma_{\mu\nu}G_{\mu\nu}(x)\psi(x)\,.$$

The name clover comes from the common choice for the lattice evaluation of the field strength tensor,

$$ga^2 G_{\mu\nu} = \frac{1}{2i}\left(C_{\mu\nu}(x) - C^{\dagger}_{\mu\nu}(x)\right)\,,$$

with the clover terms,

$$C_{\mu\nu}(x) = \frac{1}{4}\left(P_{\mu\nu}(x) + P_{\nu-\mu}(x) + P_{-\mu-\nu}(x)P_{-\nu\mu}(x)\right)\,,$$

depicted in Fig. 3.4. The parameter C_{SW} is tuned to remove $\mathcal{O}(a)$ errors, taking the value $C_{\mathrm{SW}} = 1$ at tree-level. Renormalised determinations of C_{SW} can be obtained in the same fashion as the gauge-field coefficients c_i, with non-perturbative determinations the preferred choice as they achieve $\mathcal{O}(a)$ improvement to all orders in g^2.

3.4 Propagators

A comprehensive picture of a hadron amounts to a complete description of its underlying quark content. As we saw in Section 3.2.3, upon integrating out the fermion fields from the path integral, one is left with an expression involving the gauge fields, U_μ, and the fermion propagator, S. Therefore the fundamental building block for hadrons on the lattice is the quark propagator. We can define the propagator as the Wick contracted correlation function

$$\langle \Omega | q_\alpha^{f,a}(x) \bar{q}_\beta^{f,b}(y) | \Omega \rangle = S_{\alpha\beta}^{f,\,ab}(x,y)\,,$$

which describes the propagation of a quark of flavour f from y, where it has colour charge b and Dirac-index β, to x where it now carries colour charge a and Dirac-index α. In order to evaluate this quantity, we make use of the Grassmann intergation result. The fermion propagator is the Green's function of the fermion matrix

$$\mathbf{M}_{\alpha'\alpha}^{a'a}(z,x)\, S_{\alpha\beta}^{ab}(x,y) = \delta^{a'b}\,\delta_{\alpha'\beta}\,\delta(z,y)\,. \tag{3.16}$$

For the Wilson discretisation of the fermion action, we found that the resulting matrix contained local and nearest neighbour interactions only. Consequently this allows us to make use of standard sparse matrix inversion methods to efficiently solve Eq. (3.16). However to obtain the full propagator that couples all lattice sites x to y, all colours a to b and spin-polarizations α to β would require $3 \times 4 \times n_V$ inversions for each gauge-field configuration, where n_V is the number of lattice sites on our discretised space-time volume. Even for a small lattice, this is prohibitively expensive. Fortunately, for our purposes it suffices to consider propagation from a single space time point, which we shall label 0 to all other lattice sites x and so reduce this down to a total of 12 inversions per gauge field configuration. [1]

3.4.1 Smeared Sources

Despite being the simplest choice, the delta function source is not a realistic representation for the distribution of a quark field within a hadron and so one finds that interpolating fields constructed with such sources tend to have a significant overlap with a large range of states. In order to study a given eigenstate, one needs to tune the interpolating field to have maximal overlap with the state in question. In Chapter 4, we shall consider the general framework for which this can be achieved for any eigenstate, however here we shall consider the standard approach to optimising ground state overlap. This can be done by generalising Eq. (3.16) to an arbitrary source vector $\eta_{\alpha'}^{a'}(z)$,

$$\mathbf{M}_{\alpha'\alpha}^{a'a}(z,x) S_{\alpha\beta}^{ab}(x,y) = \eta_{\alpha'}^{a'}(z)\,. \tag{3.17}$$

[1] In some situations, particularly when considering scattering states on the lattice, all-to-all propagators are required. In such situations, one can make use of stochastic techniques [27, 28] or the distillation method [29] to obtain an estimate of the all-to-all propagator.

To maximise the overlap of the resulting interpolator, we want a source vector that reflects the quark wave function for the system in question. In the absence of interactions, we would expect some extended, spherically symmetric source vector peaked at the origin would be an appropriate representation for the ground state wave function. One possible approach would be to take our delta function source and perform some operation which smears the source symmetrically in the spatial directions. Through repeated applications of the smearing operator, one could effectively control the width of the source to optimise overlap with the ground state. The use of Jacobi smearing in this fashion gives Gaussian shaped sources. Generalising this to a covariant formulation gives rise to the standard source smearing procedure, gauge-invariant Gaussian smearing [30]. Starting with our point source

$$\eta^{(0)a'}_{\alpha'}(z) = \delta^{a'b}\,\delta_{\alpha'\beta}\,\delta(z,y)\,,$$

we iteratively apply the operator $F(x,x')$,

$$\eta^{(i)}(x) = \sum_{\vec{x}'} F(x,x')\,\eta^{(i-1)}(x')\,, \tag{3.18}$$

where

$$F(x,x') = (1-\alpha)\,\delta_{x,x'} + \frac{\alpha}{6}\sum_{\mu=1}^{3}\left\{U_\mu(x)\,\delta_{x',x+ae_\mu} + U^\dagger_\mu(x-ae_\mu)\,\delta_{x',x-ae_\mu}\right\}\,. \tag{3.19}$$

The smearing fraction α determines the degree of smearing on each application of the operator $F(x,x')$, while the number of sweeps of smearing n determines the width of the resulting source.

3.4.2 Coupling to an External Current

To study the underlying structure of a hadron requires some external probe to interact with the underlying quark fields. On the quark level, we would need to consider correlation functions of the form

$$\langle\Omega|q^{f,a}_\alpha(x)\,j(y)\,\bar{q}^{f,b}_\beta(z)|\Omega\rangle = \hat{S}^{f,ab}_{\alpha\beta}(x,y,z)\,, \tag{3.20}$$

where we can write a general current coupling to a quark as

$$j(y) = \bar{q}_\delta(y)\,(\Gamma_\mathcal{O})_{\delta\gamma}\,q_\gamma(y)\,. \tag{3.21}$$

The choice of bilinear operator $\Gamma_\mathcal{O}$ couples the relevant spin and colour degrees of freedom of the incoming and outgoing quark fields for the corresponding interaction vertex. Substituting this into Eq. (3.20), we can perform the relevant quark contractions using Eq. (3.4) to express the correlator in terms of two-point

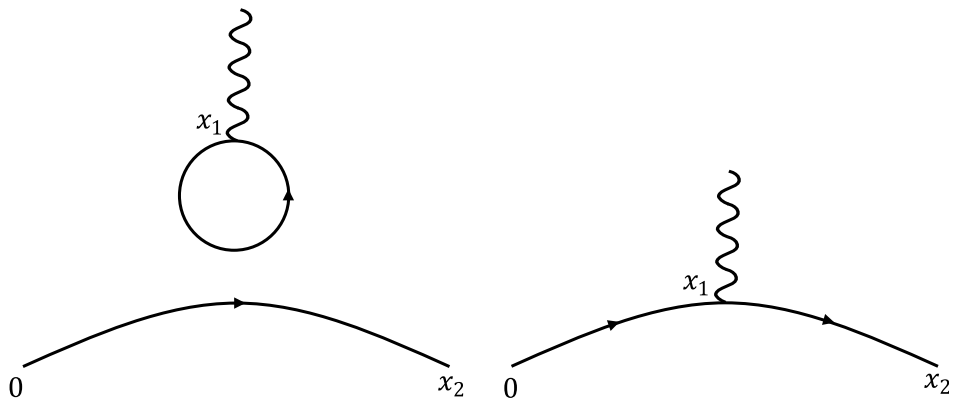

Figure 3.5: The two distinct quark flow contractions that contribute to three-point correlation functions. The term on the left is referred to as the disconnected contribution, while the term on the right is the connected contribution. These skeleton graphs are dressed by gluons. Disconnected contributions are exceptionally difficult to evaluate and so often neglected or subtracted through consideration of isovector quantities.

quark propagators. One finds two distinct contractions, which we represent diagrammatically in Fig. 3.5.

The first of these two diagrams corresponds to the external current coupling to a sea quark and contains an all-to-all two-point propagator of the form $S(x_1, x_1)$. Evaluating these disconnected contributions is a significantly challenging endeavour [31–33] requiring huge statistics to overcome the background gauge noise and for this reason are often neglected or, where possible, subtracted through consideration of isovector quantities. The second diagram represents the current coupling directly to a valence quark and it is such contributions we shall consider in this work. Expressing this explicitly in terms of two point propagators and performing a Fourier transform over x_1 to impart a momentum transfer of $\vec{q}$ through the current, we arrive at the three-point propagator,

$$\hat{S}^{f}_{\mathcal{O}}{}^{ac}_{\alpha\gamma}(x_2, x_1, 0; \vec{q}) = \sum_{\vec{x}_1} e^{i\vec{q}\cdot\vec{x}_1} \left(S^f(x_2, x_1)\, \Gamma_{\mathcal{O}}\, S^f(x_1, 0) \right)^{ac}_{\alpha\gamma} . \tag{3.22}$$

Expressed in this form, the propagator includes another all-to-all propagator and so appears beyond our reach using standard inversion techniques. Fortunately, this system can be evaluated through the use of sequential source techniques (SST) [34]. This method makes use of the Green's function properties of the propagator $S(x_2, x_1)$ to express Eq. (3.22) as

$$\mathbf{M}^{a'a}_{\alpha'\alpha}(z, x_2)\, \hat{S}^{f}_{\mathcal{O}}{}^{ac}_{\alpha\gamma}(x_2, x_1, 0; \vec{q}) = \sum_{\vec{x}_1} e^{i\vec{q}\cdot\vec{x}_1}\, \delta(z, x_1)\, (\Gamma_{\mathcal{O}})^{a'b}_{\alpha'\beta}\, S^{f}{}^{bc}_{\beta\gamma}(x_1, 0) .$$

In this form, we can treat the RHS as a source for the propagator $\hat{S}^{f}_{\mathcal{O}}{}^{ac}_{\alpha\gamma}(x_2, x_1, 0; \vec{q})$ and solve the resulting linear system. SST-propagators obtained in this manner

require us to fix the momentum $\vec{q}$, however the source and sink are left free allowing us to reuse these propagators for any number of hadron interpolators. An alternate construction in which the inversion is done through the sink requires one to fix the source and sink interpolator as well as the sink momentum. The advantage of this approach is that the current momentum is outside of the inversion allowing one to construct a range of momentum transfer $\vec{q}$, albeit for a single hadron state only. We refer the reader to Ref. [35] for a discussion and comparison of both methods.

As with any quantity determined via a quantum field theory, one must consider the issue of renormalisation in order to facilitate meaningful comparison between results, particularly with experimental measurements. To do this, we assign a factor $Z_{\mathcal{O}}$ to our quantity in order to account for the renormalisation associated with the current. In this fashion, we can define our renormalised quantities as

$$X_{\text{renorm}} = \frac{1}{Z_{\mathcal{O}}} X_{\text{latt}} \,.$$

Determination of the renormalisation constants can be estimated using lattice-perturbation theory or evaluated non-perturbatively using techniques such as the Schrödinger functional [36–38] or Rome-Southampton method [39, 40]. However, in certain situations we can invoke symmetries of continuum theory through the corresponding Ward Identities. Using a Noether construction it is possible to form currents that satisfy the Ward identities and restore the corresponding symmetry. For the electromagnetic current central to this work, one can replace the naïve vector current, $j_\mu(x) = \bar{q}(x)\gamma_\mu q(x)$, with the conserved vector current for which the renormalisation constant is unity. For our calculations, we use an $\mathcal{O}(a)$-improved conserved vector current using the method presented in Refs. [41, 42]

$$j_\mu^{CI}(x) = j_\mu^{C}(x) + \frac{r}{2}\, a \sum_\rho \partial_\rho (\bar{q}(x)\, \sigma_{\rho\mu}\, q(x)) \,,$$

where $j_\mu^C(x)$ is the conserved current for the Wilson action

$$\begin{aligned} j_\mu^C(x) = \frac{1}{4} \big(& \bar{q}(x)(\gamma_\mu - r) U_\mu(x) q(x + a e_\mu) \\ & + \bar{q}(x + a e_\mu)(\gamma_\mu + r) U_\mu^\dagger(x) q(x) \\ & + \bar{q}(x - a e_\mu)(\gamma_\mu - r) U_\mu(x - a e_\mu) q(x) \\ & + \bar{q}(x)(\gamma_\mu + r) U_\mu^\dagger(x - a e_\mu) q(x - a e_\mu) \big) \,, \end{aligned}$$

and

$$\partial_\mu (\bar{q}(x)\, q(x)) \equiv \bar{q}(x) \left(\overleftarrow{\nabla}_\mu + \overrightarrow{\nabla}_\mu \right) q(x) \,,$$

with the forwards and backwards derivatives defined as,

$$\begin{aligned} \overrightarrow{\nabla}_\mu\, q(x) &= \frac{1}{2a} \left(U_\mu(x)\, q(x + a e_\mu) - U_\mu^\dagger(x - a e_\mu) q(x - a e_\mu) \right) \,, \\ \bar{q}(x)\, \overleftarrow{\nabla}_\mu &= \frac{1}{2a} \left(\bar{q}(x + a e_\mu)\, U_\mu^\dagger(x) - \bar{q}(x - a e_\mu) U_\mu(x - a e_\mu) \right) \,. \end{aligned}$$

3.5 The $U + U^*$ trick

The invariance of the QCD action under $U \to U^*$ implies that the link variables $\{U\}$ and $\{U^*\}$ are gauge field configurations of equal weight. We can therefore account for both configurations in our ensemble without biasing the determination of our observables. Naïvely one could simply re-evaluate all the propagators across the $\{U^*\}$ configurations, however due to the nice property of the fermion matrix

$$\mathbf{M}(\{U^*\}) = \left(\tilde{C}\mathbf{M}(\{U\})\tilde{C}^{-1}\right)^* , \tag{3.23}$$

it follows that the U^* propagator can be evaluated directly from the U propagator,

$$S(x,0;\{U^*\}) = \left(\tilde{C}S(x,0;\{U\})\tilde{C}^{-1}\right)^* ,$$

eliminating the need for further inversions. We note that $\tilde{C} = C\gamma_5$. In the case of SST-propagators, care must be taken in how the current transforms when using Eq. (3.23). Applying the identity to Eq. (3.22), we have

$$\begin{aligned}
&\left(\tilde{C}\hat{S}_{\mathcal{O}}(x_2,x_1,0;\vec{q},\{U\})\tilde{C}^{-1}\right)^* \\
&\qquad = \sum_{x_1} e^{-i\vec{q}\cdot\vec{x}_1}\left(\tilde{C}S(x_2,x_1;\{U\})\tilde{C}^{-1}\,\tilde{C}\Gamma_{\mathcal{O}}\tilde{C}^{-1}\,\tilde{C}S(x_1,0;\{U\})\tilde{C}^{-1}\right)^* \\
&\qquad = \sum_{x_1} e^{-i\vec{q}\cdot\vec{x}_1} S(x_2,x_1;\{U^*\})\left(\tilde{C}^{-1}\,\tilde{C}\Gamma_{\mathcal{O}}\tilde{C}^{-1}\right)^* S(x_1,0;\{U^*\})\,.
\end{aligned}$$

In order to express this in terms of the U^* SST-propagator, we require that the operator describing the current vertex has the following properties,

$$\left(\tilde{C}\,\Gamma_{\mathcal{O}}\,\tilde{C}^{-1}\right)^* = s_C\,\Gamma_{\mathcal{O}}\,,$$

where s_C is ± 1 and is dependent upon the choice of representation of the γ-matrices. For the numerical evaluation of propagators and correlators we choose to work with the Pauli Representation used by Sakurai in Ref. [43]. For this basis, this constant is unity for the vector current and so we obtain the corresponding SST-propagator for the $\{U^*\}$ configuration from,

$$\hat{S}^{\mu}(x_2,x_1,0;+\vec{q},\{U^*\}) = \left(\tilde{C}\hat{S}^{\mu}(x_2,x_1,0;-\vec{q},\{U\})\tilde{C}^{-1}\right)^* .$$

From this expression, we can clearly see that in order to use both U and U^* configurations in the determination of three-point correlation functions, we require both $\vec{q}$ and $-\vec{q}$ SST-propagators.

An important consequence of evaluating correlators over both U and U^* is that we enforce parity symmetry onto our correlators, leading to significant

reduction in the statistical fluctuation [44]. In particular, for a correlator with parity s_P,

$$\langle G(\vec{p},t)\rangle = s_P \langle G(-\vec{p},t)\rangle \,,$$

one can show that,

$$\begin{aligned}\frac{1}{2}\left(\langle G(\vec{p},t;\{U\})\rangle + \langle G(\vec{p},t;\{U^*\})\rangle\right) \\ = \frac{1}{2}\left(\langle G(\vec{p},t;\{U\})\rangle + s_P \langle G(-\vec{p},t;\{U\})\rangle^*\right) \,. \end{aligned} \tag{3.24}$$

and consequently, as outlined in Ref. [45], renders the correlator completely real.

Chapter 4

Studying Hadrons on the Lattice

As with any field theory, the information of the system under study is contained entirely within the correlation function. It is therefore important to understand how this information is encoded within and consequently how one can extract it. On the lattice we are particularly interested in the two-point correlator

$$G(\vec{p},t) = \sum_{\vec{x}} e^{-i\vec{p}\cdot\vec{x}} \, \langle \Omega | \chi(x) \, \bar{\chi}(0) | \Omega \rangle \, , \tag{4.1}$$

which describes how the system propagates from 0 to x, and the three-point correlator

$$G(\vec{p}', \vec{p}, t_2, t_1) = \sum_{\vec{x}_2, \vec{x}_1} e^{-i\vec{p}'\cdot\vec{x}_2} \, e^{i(\vec{p}'-\vec{p})\cdot\vec{x}_1} \, \langle \Omega | \chi(x_2) \, \mathcal{O}(x_1) \, \bar{\chi}(0) | \Omega \rangle \, , \tag{4.2}$$

which describes how the system reacts to an external probe, induced through the operator $\mathcal{O}$. As we shall see, the first of these provides us with insight into the spectral and dispersive properties of the system, while the latter provides a glimpse at the underlying internal structure. In general, these correlators contain information for the full spectrum of states consistent with the quantum numbers specified by the interpolator, χ. It is thus important that we carefully examine the correlation function, both at the quark level and at the hadronic level, to understand how we evaluate the correlator on the lattice and how we can extract hadronic properties. In doing so, we will ultimately arrive at the variational method which provides us with a systematic framework for accessing any energy eigenstate.

4.1 Interpolating Fields

The starting point for the evaluation of any correlation function on the lattice is the selection of an appropriate interpolating field. Due to the complex dynamics of QCD, identifying an appropriate interpolator for a particular eigenstate *a-priori* is not possible. As we shall see towards the end of this chapter, techniques have been developed that allow one to produce "optimised" interpolators that effectively couple to individual eigenstates, however to understand this construction we must first examine the standard approach.

In general, interpolators used to access QCD eigenstates must satisfy two requirements. The first is that the interpolator be gauge invariant. This amounts to coupling the quarks so as to form colour singlet objects, ensuring there are no explicit colour degrees of freedom. The second requirement is that the interpolator carry the quantum numbers for the state of interest. Particularly, the interpolator must transform with the corresponding J^{PC} for the state in question as well as contain the same valence quark content encoded in the flavour quantum numbers.

As baryons have non-integer spin, we require that the interpolating field transform as a spinor. If we consider baryon states as simply local qqq systems, the most general choice for our baryon interpolator is a linear combination of terms of the following form

$$\chi(x) = \epsilon^{abc} \left(q_1^{aT}(x)\, C\Gamma_1\, q_2^b(x)\right)\, \Gamma_2\, q_3^c(x)\,, \tag{4.3}$$

where a, b and c are colour labels and C is the charge conjugation matrix. The operators $\Gamma_{1,2}$ are combinations of γ-matrices that couple the quark spins so as to give the desired J^{PC}. In particular, to ensure that the interpolator transforms correctly under a Lorentz transformation, we require Γ_2 to be one of either γ_5 or I. Similarly, if we treat meson states as simply local $q\bar{q}$ systems, the most general choice for our meson interpolator is a linear combination of terms of the following form

$$\chi(x) = \overline{q}_1(x)\, \Gamma_1\, q_2(x)\,. \tag{4.4}$$

These interpolators form the standard set of operators used to access ground state hadrons on the lattice.

As highlighted in our discussion of the quark model, there exist states in the hadron spectrum that do not agree with quark model predictions using just conventional qqq and $q\bar{q}$ structures. More exotic quark content such as $qqqq\bar{q}$ and $q\bar{q}q\bar{q}$ may be required to properly describe such states [46, 47]. Furthermore, there may exist states containing explicit gluonic content. Such states are able to acquire J^{PC} forbidden by the quark model and so to access them using conventional methods requires extensions to the structures above by allowing for chromoelectric and chromomagnetic fields within the Γ_1 operator of Eq. (4.4) [48]. Finally, though the above operators can have overlap with scattering states, there is strong evidence that to properly access such systems requires non-local, multi-hadron interpolators so as to project out the relative momenta for the hadron states [49–52]. Though such extensions are expected to play an important role in fully describing the hadron spectrum, for our purposes it is sufficient to limit ourselves to the standard operators defined by Eqs. (4.3) and (4.4).

4.2 Correlation Functions at the Quark Level

As QCD is a theory based on quark and gluon degrees of freedom, an examination of the correlation function at the quark level provides one with

the expressions from which to evaluate the correlation function on the lattice. Beginning from the definition given by Eq. (4.1)

$$G(\vec{p},t) = \sum_{\vec{x}} e^{-i\vec{p}\cdot\vec{x}} \, \langle\Omega|\chi(x)\,\bar{\chi}(0)|\Omega\rangle \, ,$$

we insert our interpolating field $\chi(x)$ (done here for a generic baryon field) to give

$$G(\vec{p},t) = \sum_{\vec{x}} e^{-i\vec{p}\cdot\vec{x}} \langle\Omega|\epsilon^{abc} \, \left(q_1^{aT}(x)\, C\Gamma_1 \; q_2^b(x)\right) \; \Gamma_2 \; q_3^c(x) \\ \epsilon^{a'b'c'} \, \bar{q}_{3'}^{c'}(0)\, \bar{\Gamma}_{2'} \; \left(\bar{q}_{2'}^{b'}(0)\bar{\Gamma}_{1'}\, \bar{q}_{1'}^{a'}(0)\right) \; |\Omega\rangle \, , \tag{4.5}$$

where $\bar{\Gamma}_i = \gamma_0\Gamma_i^\dagger\gamma_0$. As demanded by the Grassmann integration we then perform all possible Wick contractions of the quark fields, replacing each with the corresponding quark propagator given by Eq. (3.4). Doing this generally for the above expression gives rise to six distinct terms, each corresponding to a separate contraction

$$G(\vec{p},t) = \sum_{\vec{x}} e^{-i\vec{p}\cdot\vec{x}} \, \epsilon^{abc} \, \epsilon^{a'b'c'} \tag{4.6}$$

$$\Big\{ \Gamma_2 \; S_{33'}^{cc'}(x,0) \; \bar{\Gamma}_{2'} \; \mathrm{Tr}\left[\Gamma_1 \; S_{22'}^{bb'}(x,0) \; \bar{\Gamma}_{1'} \; (S_{11'}^{aa'}(x,0))^T\right] \; \delta_{11'}\,\delta_{22'}\,\delta_{33'} \\ + \Gamma_2 \; S_{33'}^{cc'}(x,0) \; \bar{\Gamma}_{2'} \; \mathrm{Tr}\left[\Gamma_1^T \; S_{12'}^{bb'}(x,0) \; \bar{\Gamma}_{1'} \; (S_{21'}^{aa'}(x,0))^T\right] \; \delta_{12'}\,\delta_{21'}\,\delta_{33'} \\ + \left(\Gamma_2 \; S_{32'}^{cc'}(x,0) \; \bar{\Gamma}_{1'} \; (S_{21'}^{bb'}(x,0))^T \; \Gamma_1^T \; S_{13'}^{aa'}(x,0) \; \bar{\Gamma}_{2'}\right) \; \delta_{32'}\,\delta_{21'}\,\delta_{13'} \\ + \left(\Gamma_2 \; S_{32'}^{cc'}(x,0) \; \bar{\Gamma}_{1'} \; (S_{11'}^{bb'}(x,0))^T \; \Gamma_1 \; S_{23'}^{aa'}(x,0) \; \bar{\Gamma}_{2'}\right) \; \delta_{32'}\,\delta_{11'}\,\delta_{23'} \\ + \left(\Gamma_2 \; S_{31'}^{cc'}(x,0) \; \bar{\Gamma}_{1'}^T \; (S_{22'}^{bb'}(x,0))^T \; \Gamma_1^T \; S_{13'}^{aa'}(x,0) \; \bar{\Gamma}_{2'}\right) \; \delta_{31'}\,\delta_{22'}\,\delta_{13'} \\ + \left(\Gamma_2 \; S_{31'}^{cc'}(x,0) \; \bar{\Gamma}_{1'}^T \; (S_{12'}^{bb'}(x,0))^T \; \Gamma_1 \; S_{23'}^{aa'}(x,0) \; \bar{\Gamma}_{2'}\right) \; \delta_{31'}\,\delta_{12'}\,\delta_{23'} \Big\} \, . \tag{4.7}$$

The Kroneker delta, $\delta_{ij'}$, describes which contractions are allowed for the given interpolator χ and are non-zero only when the i^{th} and $(j^{th})'$ quark fields are of the same flavour. The above expression is effectively a matrix product of propagators, γ-matrices and Levi-Cevita tensors, from which we can obtain the correlator in a practical fashion. It is worth noting that for any given expression, it may be possible to reduce the number of independent terms through the use of trace cyclicity and other similar properties or identities, thus reducing the number of terms required to evaluate the correlator. This is particularly important for systems with large quark content such as nuclear and multi-hadron systems now being considered by many groups [53, 54].

Performing the same procedure with a meson field, one finds that the correlation function

$$G(\vec{p},t) = \sum_{\vec{x}} e^{-i\vec{p}\cdot\vec{x}} \langle\Omega|\bar{q}_1^a(x)\Gamma_1\, q_2^a(x)\, \bar{q}_{1'}^{a'}(0)\bar{\Gamma}_{1'}\, q_{2'}^{b'}(0)\,|\Omega\rangle \, , \tag{4.8}$$

reduces to two terms,

$$G(\vec{p},t) = \sum_{\vec{x}} e^{-i\vec{p}\cdot\vec{x}} \Big\{ \mathrm{Tr}\left[S^{aa}_{21}(x,x)\ \Gamma_1\ \right]\ \mathrm{Tr}\left[S^{a'a'}_{2'1'}(0,0)\ \bar{\Gamma}_{1'}\right]\ \delta_{21}\,\delta_{2'1'} \\ -\mathrm{Tr}\left[S^{a'a}_{2'1}(0,x)\ \Gamma_1\ S^{aa'}_{21'}(x,0)\ \bar{\Gamma}_{1'}\right]\ \delta_{2'1}\,\delta_{21'}\Big\}\ . \tag{4.9}$$

In this case, due to the presence of both quark and anti-quark fields in the interpolator, we have contractions that result in both loop propagators, $S(x,x)$, and backwards propagators, $S(0,x)$. As is clear from the delta-function, the first term is only present in the case where both the quark and anti-quark fields for each term in the interpolator are of the same flavour. Thus by considering states that have non-zero projected-isospin (I_3), only the second term is possible. However, in the case of exact isospin symmetry one finds that the disconnected contributions only contribute to isosinglet states. In this work we shall only work with states that have non-zero isospin content and so only need consider the second term when evaluating meson correlation functions. For the backwards propagator, we are able to make use of γ_5-Hermiticity of the fermion matrix to re-express this in terms of the corresponding forwards propagator,

$$S^{ab}_{\alpha\beta}(0,x)\ = \left(\gamma_5\, S^{ba}(x,0)^{\,*}\gamma_5\right)_{\beta\alpha}\ .$$

4.2.1 Coupling to an External Current

In section 3.4, we saw how we can couple the quark fields to an external current through the use of sequential source techniques. Thus all that remains to understand is how we evaluate correlators of the form

$$G(\vec{p}',\vec{p},t_2,t_1) = \sum_{\vec{x}_2,\vec{x}_1} e^{-i\vec{p}'\cdot\vec{x}_2}\, e^{i(\vec{p}'-\vec{p})\cdot\vec{x}_1}\ \langle\Omega|\chi(x_2)\,\mathcal{O}(x_1)\,\bar{\chi}(0)|\Omega\rangle\ ,$$

at the quark level. Inserting our interpolating fields (again for a baryon) and the current defined by Eq. (3.21), we arrive at an expression that, like Eq. (4.5), is entirely in terms of quark fields and fermion bilinears,

$$G(\vec{p}',\vec{p},t_2,t_1) = \sum_{\vec{x}_2,\vec{x}_1} e^{-i\vec{p}'\cdot\vec{x}_2}\, e^{i(\vec{p}'-\vec{p})\cdot\vec{x}_1} \\ \langle\Omega|\,\epsilon^{abc}\ \left(q_1^{aT}(x_2)\,C\Gamma_1\ q_2^b(x_2)\right)\ \Gamma_2\ q_3^c(x_2) \\ \bar{q}_i^d(x_1)\,\Gamma_{\mathcal{O}}\ q_i^d(x_1)\ \epsilon^{a'b'c'}\ \bar{q}_{3'}^{c'}(0)\,\bar{\Gamma}_{2'}\ \left(\bar{q}_{2'}^{b'}(0)\,\bar{\Gamma}_{1'}\ \bar{q}_{1'}^{a'}(0)\right)\ |\Omega\rangle\ . \tag{4.10}$$

Performing the contractions now in the presence of the current, we find two topologically distinct classes. The first results when we perform the same contractions as was done for the two-point function along with the additional contraction of the current-coupled quark fields with themselves. These terms take the form of the two-point function weighted by an additional trace

$$\mathrm{Tr}\left[S^{dd}_{ii}(x_1,x_1)\,\Gamma_{\mathcal{O}}\right]\ , \tag{4.11}$$

and encode the vacuum contributions to the amplitude. These vacuum contributions are of the disconnected type discussed in Section 3.4.2 and will not be considered in this work. The remaining class are of the connected type and result from sandwiching the current-coupled quark fields between each of the paired quark fields that give rise to Eq. (4.6). It follows that the three-point correlator can be evaluated by replacing each two-point propagator in Eq. (4.6) by the corresponding SST-propagator, each in turn [42, 55]. This results in three times the number of terms in the three-point correlator relative to the two-point expression given by Eq. (4.6).

Following the same procedure for meson fields, we begin with the uncontracted expression

$$G(\vec{p}',\vec{p},t_2,t_1) = \sum_{\vec{x}_2,\vec{x}_1} e^{-i\vec{p}'\cdot\vec{x}_2}\, e^{i(\vec{p}'-\vec{p})\cdot\vec{x}_1} \\ \langle\Omega|\, \bar{q}_1^a(x_2)\,\Gamma_1\; q_2^a(x_2)\;\bar{q}_i^d(x_1)\,\Gamma_{\mathcal{O}}\; q_i^d(x_1)\,\bar{q}_{1'}^{a'}(0)\;\bar{\Gamma}_{1'}\; q_{2'}^{b'}(0)\,|\Omega\rangle\,, \tag{4.12}$$

and consider all possible contractions. We can again contract the current quark fields to themselves to obtain the vacuum contribution; once more these terms are given by the two-point expression weighted by Eq. (4.11). As was stated for the baryon case, we shall not consider such terms here. The remaining terms can all be obtained by replacing the two-point propagators in Eq. (4.9) by the corresponding three-point propagator, each in turn. Doing this for the first term, we access a new class of diagrams given by the three-point propagators

$$\left(S^{ad}(x_2,x_1)\,\Gamma_{\mathcal{O}}\; S^{da}(x_1,x_2)\right)_{\beta\alpha} \quad\text{and}\quad \left(S^{da'}(0,x_1)\,\Gamma_{\mathcal{O}}\; S^{da'}(x_1,0)\right)_{\beta'\alpha'}.$$

Such terms are connected loop contributions. Accordingly, the propagator on the right can be expressed in terms of standard two-point propagators, while the propagator on the left once again requires all-to-all propagators. Fortunately however, following the same arguments as the for the two-point correlator, such contributions only arise when considering isosinglet quantities, or when isospin symmetry is explicitly broken.

Finally, we obtain the remaining two terms by replacement of the two-point propagators in the second term of Eq. (4.9); one in which the current is coupled to the forward propagating quark, the other with the current coupled to the backwards propagating quark:

$$-\,\mathrm{Tr}\left[S_{2'1}^{a'a}(0,x_2)\,\Gamma_1\; S_{2i}^{ad}(x_2,x_1)\,\Gamma_{\mathcal{O}}\; S_{i1'}^{da'}(x_1,0)\,\bar{\Gamma}_{1'}\right],\ \text{and,} \\ -\,\mathrm{Tr}\left[S_{2'i}^{a'd}(0,x_1)\,\Gamma_{\mathcal{O}}\; S_{i1}^{da}(x_1,x_2)\,\Gamma_1\; S_{21'}^{aa'}(x_2,0)\,\bar{\Gamma}_{1'}\right].$$

For this first term, the three-point propagator is consistent with our SST-propagators and so simple to evaluate. For the second term, we could once again make use of γ_5-hermiticity to re-express the backwards propagating quark fields in terms

of forward propagating quarks. However, through considerations of charge conjugation, it is possible to express this term in a form matching the first. After some manipulation, one finds this second term can be written

$$-\mathrm{Tr}\left[S^{a'a}_{2'1}(0,x_2)\,\left(C^\dagger\,\Gamma_1\,C\right)^T\,S^{ad}_{2i}(x_2,x_1)\,\left(C^\dagger\,\Gamma_{\mathcal{O}}\,C\right)^T\,S^{da'}_{i1'}(x_1,0)\,\left(C^\dagger\,\bar{\Gamma}_{1'}\,C\right)^T\right].$$

For the vector current we have

$$\left(C^\dagger\,\gamma^\mu\,C\right)^T=-\gamma^\mu\,,\quad\text{and}\quad Q_{\bar{f}}\to Q_f\,.$$

Since $\frac{Q_{\bar{f}}}{Q_f}=-1$ the two factors combine to leave the contribution invariant. Considering quark sectors of unit charge, the d contribution to the π^- equals the $\bar{d}$ contribution to the π^+. To calculate the hadronic form factor, one need only include the charges of the quark and anti-quark composing the meson.

For the two remaining bilinears, all are eigenstates of the charge conjugation operator and encounter factors of plus or minus one.

$$\bar{q}(x)\,\Gamma_i\,q(x)\xrightarrow{C}\pm\bar{q}(x)\,\Gamma_i\,q(x)\Rightarrow\left(C^\dagger\,\Gamma_i\,C\right)^T=\pm\Gamma_i\,.$$

In the case that the source and sink interpolators are the same, the factors multiply to one.

4.3 Correlation Functions at the Hadronic Level

Having outlined how one evaluates the correlation function on the lattice, we now consider how the information pertaining to the hadron is encoded within. Once again we begin with Eq. (4.1)

$$G(\vec{p},t)=\sum_{\vec{x}}e^{-i\vec{p}\cdot\vec{x}}\,\langle\Omega|\chi(x)\,\bar{\chi}(0)|\Omega\rangle\,.$$

Taking the view point that the operator $\bar{\chi}(0)$ creates a hadron state with the relevant quantum numbers, while $\chi(x)$ annihilates a state in the same fashion, we naturally expect the two-point correlator to encode the properties governing the propagation of the hadron. Furthermore, as the operator should couple to any state consistent with the given quantum numbers, it should contain the corresponding information for all these states.

We begin by inserting the completeness relation for the QCD Hamiltonian

$$\mathbb{I}=\sum_{\alpha,\tilde{p},s}|\alpha,\tilde{p},s\rangle\langle\alpha,\tilde{p},s|\,,$$

between the operators $\chi(x)$ and $\bar{\chi}(0)$ to give

$$G(\vec{p},t)=\sum_{\alpha,\tilde{p},s}\sum_{\vec{x}}e^{-i\vec{p}\cdot\vec{x}}\langle\Omega|\chi(x)|\alpha,\tilde{p},s\rangle\langle\alpha,\tilde{p},s|\bar{\chi}(0)|\Omega\rangle\,.\tag{4.13}$$

Invoking operator translation

$$\chi(x) = e^{+iHt}\, e^{-i\vec{P}\cdot\vec{x}}\, \chi(0)\, e^{-iHt}\, e^{+i\vec{P}\cdot\vec{x}}\,,$$

the overlap $\langle\Omega|\chi(x)|\alpha, p', s\rangle$ can be simplified, reducing Eq. (4.13) to

$$\begin{aligned} G(\vec{p}, t) &= \sum_{\alpha,\tilde{p},s} \sum_{\vec{x}} e^{-i\vec{p}\cdot\vec{x}}\, \langle\Omega|e^{+iHt}\, e^{-i\vec{P}\cdot\vec{x}}\, \chi(0)\, e^{-iHt}\, e^{+i\vec{P}\cdot\vec{x}}|\alpha, \tilde{p}, s\rangle\langle\alpha, \tilde{p}, s|\bar{\chi}(0)|\Omega\rangle \\ &= \sum_{\alpha,\tilde{p},s} \sum_{\vec{x}} e^{+i(\tilde{\vec{p}}-\vec{p})\cdot\vec{x}}\, e^{-iE_\alpha(\tilde{\vec{p}})t}\, \langle\Omega|\chi(0)|\alpha, \tilde{p}, s\rangle\langle\alpha, \tilde{p}, s|\bar{\chi}(0)|\Omega\rangle \\ &= \sum_{\alpha,s} e^{-iE_\alpha(\vec{p})t}\, \langle\Omega|\chi(0)|\alpha, p, s\rangle\langle\alpha, p, s|\bar{\chi}(0)|\Omega\rangle\,, \end{aligned}$$

where in the final line we have made use of the identity

$$\sum_{\vec{x}} e^{+i(\tilde{\vec{p}}-\vec{p})\cdot\vec{x}} = \delta_{\tilde{\vec{p}}\vec{p}}.$$

Finally adopting a Euclidean time formulation

$$t_M \to -it_E\,,$$

we arrive at the following expression

$$G(\vec{p}, t) = \sum_{\alpha,s} e^{-E_\alpha(\vec{p})t}\, \langle\Omega|\chi(0)|\alpha, p, s\rangle\langle\alpha, p, s|\bar{\chi}(0)|\Omega\rangle\,. \tag{4.14}$$

Expressed in this form, it is clear that the correlator has contributions from all eigenstates consistent with the quantum numbers of the interpolating field. Each term is the product of an exponential, which encodes the time dependence, and operator overlap factors which can be parameterised as

$$\langle\Omega|\chi(0)|\alpha, p, s\rangle = Z^\alpha(\vec{p}) \times \{\text{spin-terms}\}\,,$$

with the factor $Z^\alpha(\vec{p})$ encoding the coupling strength of the operator $\chi(0)$ to the eigenstate $|\alpha, p, s\rangle$. As the argument in the exponential is the energy of the state, in the large Euclidean time limit all contributions will be suppressed relative to the ground state. Therefore by examining the correlator at large times, one is able to access the inertial properties to the lowest lying state in the channel under consideration. In particular, by forming the ratio of the correlator at successive times with the hadron at rest, we can access the eigenstates mass

$$m = \log\left(\frac{G(0, t)}{G(0, t+1)}\right)\,.$$

Following a similar process, one is able to work towards a similar expression for Eq. (4.2)

$$G(\vec{p}', \vec{p}, t_2, t_1) = \sum_{\vec{x}_2,\vec{x}_1} e^{-i\vec{p}'\cdot\vec{x}_2}\, e^{i(\vec{p}'-\vec{p})\cdot\vec{x}_1}\, \langle\Omega|\chi(x_2)\, \mathcal{O}(x_1)\, \bar{\chi}(0)|\Omega\rangle\,.$$

Again treating $\bar{\chi}(0)$ and $\chi(x)$ as creation and annihilation operators, this correlator should encode the reaction of a state to the external current $\mathcal{O}$. Thus we should expect to find somewhere in our expression matrix elements of the form $\langle \beta, p', s' | \mathcal{O}(0) | \alpha, p, s \rangle$. Again invoking the completeness relation, this time between both our pairs of operators,

$$G(\vec{p}', \vec{p}, t_2, t_1) = \sum_{\beta, \tilde{p}', s'} \sum_{\alpha, \tilde{p}, s} \sum_{\vec{x}_2, \vec{x}_1} e^{-i\vec{p}' \cdot \vec{x}_2} \, e^{i(\vec{p}' - \vec{p}) \cdot \vec{x}_1} \\ \times \langle \Omega | \chi(x_2) | \beta, \tilde{p}', s' \rangle \langle \beta, \tilde{p}', s' | \mathcal{O}(x_1) | \alpha, \tilde{p}, s \rangle \langle \alpha, \tilde{p}, s | \bar{\chi}(0) | \Omega \rangle \, ,$$

invoking operator translation and moving to Euclidean time we arrive at the corresponding expression for the three-point correlation function,

$$G(\vec{p}', \vec{p}, t_2, t_1) = \sum_{\alpha, \beta} \sum_{s', s} e^{-E_\beta(\vec{p}')(t_2 - t_1)} \, e^{-E_\alpha(\vec{p}) t_1} \\ \times \langle \Omega | \chi(0) | \beta, p', s' \rangle \langle \beta, p', s' | \mathcal{O}(0) | \alpha, p, s \rangle \langle \alpha, p, s | \bar{\chi}(0) | \Omega \rangle \, . \tag{4.15}$$

We can see that this has a form similar to Eq. (4.14), with three significant differences. Firstly, there are now two exponential terms with one dependent on the temporal separation between source and current, t_1, and the other dependent on the sink–current separation, $t_2 - t_1$. By using the completeness identity twice in the same expression, there now exists that possibility that the asymptotic states differ. And most importantly, we find the matrix element $\langle \beta, p', s' | \mathcal{O}(0) | \alpha, p, s \rangle$, as expected.

Once more, the exponential acts to suppress all terms relative to the ground state in the large Euclidean time limit. However in evaluating the SST-propagator one is required to fix either t_1 (fixed current) or t_2 (fixed sink). In order to ensure that excited state contributions are sufficiently suppressed one should work with large time separations between source, current and sink. Unfortunately, for large Euclidean times the correlator drops below the threshold of statistical noise leading to poor signal and large statistical errors. Thus one must find a window whereby excited state contributions are sufficiently suppressed while maintaining good signal quality.

Having identified a suitable regime where the correlator is dominated by ground state, extraction of the matrix element proceeds with the construction of a suitable ratio of two- and three-point correlation functions. The ratio is chosen such that all time-dependence of the correlator is completely eliminated, as well as the operator couplings $Z(\vec{p})$.We choose to work with the ratio defined in Ref. [56],

$$R(p', p) = \sqrt{\frac{\langle G(\vec{p}', \vec{p}, t_2, t_1) \rangle \langle G(\vec{p}, \vec{p}', t_2, t_1) \rangle}{\langle G(\vec{p}', t_2) \rangle \langle G(\vec{p}, t_2) \rangle}} \, . \tag{4.16}$$

This construction is a symmetrised version of that presented in Ref. [44], namely

$$R(p', p) = \sqrt{\frac{\langle G(\vec{p}', \vec{p}, t_2, t_1) \rangle \langle G(-\vec{p}, -\vec{p}', t_2, t_1) \rangle}{\langle G(\vec{p}', t_2) \rangle \langle G(\vec{p}, t_2) \rangle}} \, . \tag{4.17}$$

The benefit of Eq. (4.16) over Eq. (4.17) is that by using (p', p) and (p, p') over (p', p) and $(-p, -p')$ we do not rely on the approximate symmetry $Z(-\vec{p}) \simeq Z(\vec{p})$ in order to achieve cancellation of the overlap factors, leading to an improved statistical uncertainty of the ratio. Though this choice requires both $\vec{q}$ and $-\vec{q}$ SST propagators, if one chooses to average over the U and U^* configurations as we shall in the majority of this work, there is no additional cost. It is worth noting that if one chooses to use both U and U^* configurations working with Eq. (4.17), the symmetry $Z(-\vec{p}) = Z(\vec{p})$ is exact and so both formulations are equivalent.

4.4 The Variational Method

As we saw in the previous section, the correlation functions do not simply contain information about a single hadron, rather all hadrons consistent with the quantum numbers in question. Through sampling the correlator at sufficiently large times we are able to obtain the contributions relevant to the ground state. But if we are instead interested in a state other than the ground state, how would we go about obtaining the corresponding information from the correlator?

This question lies at the heart of hadron spectroscopy on the lattice. The simplest approach would be to perform a multi-exponential fit to the data, however such an approach is unstable. Several methods have been developed for the study of the hadron spectrum. The most robust approach is the variational method.

The variational method [57, 58] is essentially a prescription to perform a diagonalisation procedure on a basis of operators $\{ \chi_i \,|\, i = 1, \ldots, n \}$ in order to produce a new basis $\{ \phi^\alpha \,|\, \alpha = 1, \ldots, n \}$ for which operators couple to a single energy eigenstate

$$\langle \Omega | \phi^\alpha | \beta, p, s \rangle \propto \delta^{\alpha\beta} \,. \tag{4.18}$$

The way in which this is achieved is to construct the operators ϕ^α as linear combinations of the original basis operators

$$\phi^\alpha(x) = \sum_i v_i^\alpha \, \chi_i(x), \qquad \bar{\phi}^\alpha(x) = \sum_j \bar{\chi}_j(x) \, u_j^\alpha \,, \tag{4.19}$$

and then determine the weights v_i^α and u_j^α which satisfy Eq. (4.18). Beginning with the matrix of two-point correlation functions

$$G_{ij}(\vec{p}, t) = \sum_{\vec{x}} e^{-i\vec{p}\cdot\vec{x}} \, \langle \Omega | \chi_i(x) \, \bar{\chi}_j(0) | \Omega \rangle \,,$$

we can establish a recurrence relation by considering $G_{ij}(\vec{p}, t+\delta t)\, u_j^\alpha$

$$\begin{aligned}
G_{ij}(\vec{p}, t+\delta t)\, u_j^\alpha &= \sum_{\vec{x}} e^{-i\vec{p}\cdot\vec{x}}\, \langle\Omega|\chi_i(x)\, (\bar{\chi}_j(0)\, u_j^\alpha)|\Omega\rangle \\
&= \sum_{\vec{x}} e^{-i\vec{p}\cdot\vec{x}}\, \langle\Omega|\chi_i(x)\, \bar{\phi}^\alpha(0)|\Omega\rangle \\
&= \sum_{\beta} e^{-E_\beta(\vec{p})(t+\delta t)}\, \langle\Omega|\chi_i(0)|\beta, p, s\rangle\langle\beta, p, s|\bar{\phi}^\alpha(0)|\Omega\rangle \\
&= e^{-E_\alpha(\vec{p})\delta t} \left(\sum_{\beta} e^{-E_\beta(\vec{p})t}\, \langle\Omega|\chi_i(0)|\beta, p, s\rangle\langle\beta, p, s|\bar{\phi}^\alpha(0)|\Omega\rangle \right) \\
&= e^{-E_\alpha(\vec{p})\delta t} \left(\sum_{\vec{x}} e^{-i\vec{p}\cdot\vec{x}}\, \langle\Omega|\chi_i(x)\, \bar{\phi}^\alpha(0)|\Omega\rangle \right) \\
&= e^{-E_\alpha(\vec{p})\delta t} \left(\sum_{\vec{x}} e^{-i\vec{p}\cdot\vec{x}}\, \langle\Omega|\chi_i(x)\, (\bar{\chi}_j(0)\, u_j^\alpha)|\Omega\rangle \right) \\
&= e^{-E_\alpha(\vec{p})\delta t}\, G_{ij}(\vec{p}, t)\, u_j^\alpha\,,
\end{aligned}$$

where we have made use of Eq. (4.18) in order to establish that the only non-zero term in the sum is that of the state α, allowing us to factor out the exponential; an analogous expression can be obtained for $v_i^\alpha G_{ij}(\vec{p}, t+\delta t)$. It follows that the required weights to form the operators ϕ^α and $\bar{\phi}^\alpha$ are the eigenvector solutions to the following generalised eigenvalue equations

$$v_i^\alpha\, G_{ij}(\vec{p}, t_0+\delta t) \quad = e^{-E_\alpha(\vec{p})\delta t}\, v_i^\alpha\, G_{ij}(\vec{p}, t_0)\,, \tag{4.20a}$$

$$G_{ij}(\vec{p}, t_0+\delta t)\, u_j^\alpha = e^{-E_\alpha(\vec{p})\delta t} \quad G_{ij}(\vec{p}, t_0)\, u_j^\alpha\,. \tag{4.20b}$$

An important point to note is that Eqs. (4.20a) and (4.20b) are evaluated for a given 3-momentum $\vec{p}$ and so the corresponding operators satisfy Eq. (4.18) for a given momentum only. With this in mind, one can form the correlator for the state $|\alpha, p, s\rangle$ by projecting the relevant eigenvectors onto the correlation matrix

$$G(\vec{p}, t; \alpha) = v_i^\alpha(\vec{p})\, G_{ij}(\vec{p}, t)\, u_j^\alpha(\vec{p})\,.$$

Generalising to the case of three-point functions follows simply. Beginning with the matrix of three-point correlation functions

$$(G_{\mathcal{O}})_{ij}(\vec{p}', \vec{p}, t_2, t_1) = \sum_{\vec{x}_2, \vec{x}_1} e^{-i\vec{p}'\cdot\vec{x}_2}\, e^{i(\vec{p}'-\vec{p})\cdot\vec{x}_1}\, \langle\Omega|\chi_i(x_2)\, \mathcal{O}(x_1)\, \chi_j^\dagger(0)|\Omega\rangle\,,$$

we can express this in the expanded form given by Eq.(4.15)

$$\begin{aligned}
(G_{\mathcal{O}})_{ij}(\vec{p}', \vec{p}, t_2, t_1) = \sum_{\alpha,\beta} \sum_{s',s} & e^{-E_\beta(\vec{p}')(t_2-t_1)}\, e^{-E_\alpha(\vec{p})t_1} \\
& \langle\Omega|\chi_i(0)|\beta, p', s'\rangle\, \langle\beta, p', s'|\mathcal{O}(0)|\alpha, p, s\rangle\, \langle\alpha, p, s|\bar{\chi}_j(0)|\Omega\rangle\,.
\end{aligned}$$

In doing so we can see that by projecting with the eigenvector carrying the correct source/sink momenta, the overlap terms satisfy Eq. (4.18). Therefore one can obtain the projected three-point correlation function by projecting with the eigenvectors taken from Eqs. (4.20a) and (4.20b) with the required momentum,

$$G_{\mathcal{O}}(\vec{p}', \vec{p}, t_2, t_1; \alpha) \equiv v_i^{\alpha}(\vec{p}')\, (G_{\mathcal{O}})_{ij}(\vec{p}', \vec{p}, t_2, t_1)\, u_j^{\alpha}(\vec{p})\,.$$

This applies equally well to hadron transitions ($\alpha \xrightarrow{\mathcal{O}} \beta$) where one simply projects with the relevant eigenvectors for differing source (α) and sink (β) eigenstates

$$G_{\mathcal{O}}(\vec{p}', \vec{p}, t_2, t_1; \alpha \to \beta) \equiv v_i^{\beta}(\vec{p}')\, (G_{\mathcal{O}})_{ij}(\vec{p}', \vec{p}, t_2, t_1)\, u_j^{\alpha}(\vec{p})\,.$$

Having obtained the correlators relevant to the particular eigenstate, extraction of the desired information follows in the same fashion as in the case of the ground state, where one now works with the projected correlators.

4.4.1 Interpolating Fields Again

The key to the successful use and application of the variational approach stems from the initial choice for the basis of operators. Ideally one requires operators that have a range of overlaps with the states of interest so as to ensure that they sufficiently span the eigenspace. For the standard operators discussed in Section 4.1, different choices of the Γ matrices in Eqs. (4.3) and (4.4) which maintain the desired J^{PC} gives rise to different operators. In the case of the nucleon, there are three independent operators that one can form, these being

$$\begin{aligned}
\chi_1(x) &= \epsilon^{abc} \left(u^{aT}(x)\, C\gamma_5\, d^b(x)\right)\, I\, u^c(x)\,, \\
\chi_2(x) &= \epsilon^{abc} \left(u^{aT}(x)\, C\, d^b(x)\right)\, \gamma_5\, u^c(x)\,, \\
\chi_4(x) &= \epsilon^{abc} \left(u^{aT}(x)\, C\gamma_5\gamma_0\, d^b(x)\right)\, I\, u^c(x)\,.
\end{aligned}$$

Each of these will have different overlap with the nucleon and its excitations. For example, the quark fields in the brackets for $\chi_1(x)$ and $\chi_4(x)$ couple to form a scalar di-quark structure while those in $\chi_2(x)$ form a vector di-quark structure, and so we expect them to have very different overlap with a given eigenstate.

Unfortunately, there are only a finite number of operators formed in this way with each J^{PC} limited to around 2 or 3 independent operators which in turn limits us to the lowest couple of eigenstates. To perform comprehensive and robust studies of the hadron spectra, one must consider alternate ways of forming new operators. There are many ways in which one can go about doing this, however two methods in particular have grown in popularity: displaced operators and smeared interpolators. The first of these methods is to work with operators that can couple quark fields at different spatial locations [59]. This can be achieved replacing one or more quark fields in Eqs. (4.3) and (4.4) by spatially-displaced quark fields,

$$T_i\, \psi(x) = U_i(x)\, \psi(x + a e_\mu)\,.$$

From this basis, operators with the desired quantum numbers are then formed as linear combinations with the relevant Clebsch-Gordon coefficients [60]. Unfortunately, by working on a lattice, the full 3-dimensional rotational symmetry is reduced down a cubic symmetry. Consequently, due to the finite extent of the underlying symmetry group, the infinite tower of irreducible representations that correspond to distinct J^{PC} mix down into the finite irreps of the reduced symmetry group. Therefore, in order to have operators that couple to distinct J^{PC}, one must disentangle these from across the irreps of the octahedral group [50, 51, 61]. The appeal of such an approach is that by considering larger displacements, particularly in various directions, one has access to an extremely large basis of operators which can in principle access any J^{PC}. Unfortunately, using standard propagators one requires inversions for each source orientation considered. Even with two displacements, the number of possible orientations begins to get rather large. The common approach for construction of correlators that make use of these operators is to use the distillation method. Though expensive in its own right, the distillation method provides one with an effective all-to-all propagator which, once obtained, allows for consideration of any number of displacements without the need for inversion [50, 62].

The other approach and that which we choose to use in this work is that of smearing. As was discussed in section 3.4.1, smearing is used to produce a source or sink that is a truer representation of the physical state. By varying the degree of smearing assigned to the quark fields in an interpolator, one varies the overlap the interpolator has with the various eigenstates. Therefore, one can extend a basis of operators by using multiple levels of smearing for each local interpolator. For a given Dirac structure, combinations of the interpolators with increasing smearings would be expected to lead to the formation of nodes in the resultant operator. Examination of the wave functions for the nucleon and its excitations [63] using such a basis confirms this behaviour. It is thus expected that our operators should have strong overlap with radial excitations.

4.4.2 Extensions to the Variational Method

Evaluation of Eqs. (4.20a) and (4.20b) in the case of near degenerate eigenstates raises an important question: How does one properly identify eigenstates between the various sub-ensembles used in the calculation? Simply identifying states by their ordering in energy is clearly insufficient. The key is in how we form a given state. As the eigenvectors describe the operator make-up for a given eigenstate, they can be considered as a fingerprint for that state. Therefore, equipped with a suitable measure it is possible to identify eigenstates between sub-ensembles in a consistent fashion. Working with vectors, the scalar product would seem a good choice. Unfortunately however, the eigenvectors obtained from Eqs. (4.20a) and (4.20b) lack orthogonality. Thus there exists the possibility that between sub-ensembles, a given eigenvector can have large

overlap with multiple vectors in the reference basis, giving rise to a potential source for eigenstate misidentification. A second issue is that the components of the eigenvectors can differ significantly in magnitude. This stems from the potentially large variation in the overlap factors $Z_i^\alpha(\vec{p})$ for the operators in the variational basis $\{\chi_i(x)\}$. Consequently, a small number of components can dominate the scalar-product limiting its effectiveness as a discriminator between eigenvectors.

Equipped with an orthonormal basis, the scalar-product is the ideal discriminator. Therefore the key to addressing this issue lies in changing our basis in such a way as to render the eigenvectors orthonormal. As discussed in Ref. [64], through a normalisation and symmeterisation procedure, one can express Eqs. (4.20a) and (4.20b) as a real-symmertic eigenvalue problem. The first step is to work with the normalised correlation matrix defined as follows

$$\frac{1}{\sqrt{G_{ii}(\vec{p}, t_{\text{src}})}}\, G_{ij}(\vec{p}, t)\, \frac{1}{\sqrt{G_{jj}(\vec{p}, t_{\text{src}})}}\,.$$

This construction effectively normalises the operators such that their overlap factors and correspondingly their entries in the correlation matrix are rendered $\mathcal{O}(1)$. In turn, the eigenvector components become $\mathcal{O}(1)$, eliminating the second issue outlined above. In order to use these eigenvectors on the three-point correlation functions, we must normalise accordingly

$$\frac{1}{\sqrt{G_{ii}(\vec{p}', t_{\text{src}})}}\, (G_{\mathcal{O}})_{ij}(\vec{p}', \vec{p}, t_2, t_1)\, \frac{1}{\sqrt{G_{jj}(\vec{p}, t_{\text{src}})}}\,.$$

The next step is to re-express the eigenvalue equation in a symmetric form. To do this, we begin by making use of the ensemble average symmetry

$$G_{ij}(\vec{p}, t) = G_{ji}(\vec{p}, t)\,,$$

and instead work with the symmetrised two-point correlation function

$$G_{ij}(\vec{p}, t) \to \frac{1}{2}\left[G_{ij}(\vec{p}, t) + G_{ji}(\vec{p}, t)\right]\,,$$

which is an improved unbiased estimator for $G_{ij}(\vec{p}, t)$. Through this operation, the matrices $G_{ij}^{1/2}(\vec{p}, t_0)$ and $G_{ij}^{-1/2}(\vec{p}, t_0)$ are well-defined allowing us to rewrite Eq.(4.20b) as

$$G_{ij}^{-1/2}(\vec{p}, t_0)\, G_{ij}(\vec{p}, t_0 + \delta t)\, G_{ij}^{-1/2}(\vec{p}, t_0)\; G_{ij}^{1/2}(\vec{p}, t_0)\, u_j^\alpha = \; e^{-E_\alpha(\vec{p})\delta t}\, G_{ij}^{1/2}(\vec{p}, t_0)\, u_j^\alpha\,.$$

Identifying

$$w_j^\alpha(\vec{p}) = G_{ij}^{1/2}(\vec{p}, t_0)\, u_j^\alpha(\vec{p})\,, \tag{4.21}$$

and

$$H_{ij}(\vec{p}, t_0, \delta t) = G_{ij}^{-1/2}(\vec{p}, t_0)\, G_{ij}(\vec{p}, t_0 + \delta t)\, G_{ij}^{-1/2}(\vec{p}, t_0)\,, \tag{4.22}$$

we arrive at the symmetric eigenvalue equation

$$H_{ij}(\vec{p}, t_0, \delta t)\, w_j^{\alpha}(\vec{p}) = e^{-E_\alpha(\vec{p})\delta t}\, w_j^{\alpha}(\vec{p})\,. \tag{4.23}$$

Working with both $\{U\}$ and $\{U^*\}$ configurations, the correlators are rendered real, resulting in Eq. (4.23) being promoted to a real-symmetric eigenvalue problem, for which the vectors $w_j^{\alpha}(\vec{p})$ are guaranteed to be orthogonal. One can thus use this basis as a means to correctly identify eigenstates across sub-ensembles.

The need to consistently identify eigenstates extends beyond sub-ensembles. The key motivation of Ref. [64] for using an orthonormal basis was to have a solid framework which allowed for eigenstates to be tracked across different quark masses. Here they found that between successive quark masses, the vectors in respective bases had dominant overlap with a single vector only and were near orthogonal to all others in the basis. For our purposes, we require consistent ordering across different values of momenta. Ideally we seek a similar condition to that presented in Ref. [64], namely

$$w_i^{\alpha}(\vec{p}) \cdot w_i^{\beta}(\vec{p}\,') \simeq \delta^{\alpha\beta}\,. \tag{4.24}$$

Taking $\vec{p} = 0$ as a reference set, it was observed that for sufficiently large momentum $\vec{p}\,'$, Eq. (4.24) no longer held. However, the evolution of the eigenvectors away from the reference basis was slowly varying such that Eq. (4.24) holds if the reference set is kept close to the momentum under consideration. Therefore, selecting an ordering at one momentum, it is possible to have consistent ordering at all momenta by sorting against adjacent momenta in an analogous fashion to sorting against adjacent quark masses in Ref. [64].

Chapter 5

Nucleon Axial Charge

The content of this chapter is based on the publication: "Variational approach to the calculation of g_A" by B. J. Owen et al., Phys. Lett. B723, 217 (2013), [arXiv:1212.4668]

A long standing issue in the realm of hadron structure calculations has been the discrepancy between the axial charge of the nucleon measured on the lattice and the experimentally determined value. In principle, the systematics of the calculation seem relatively simple. Being an isovector quantity, disconnected loop contributions are absent and as we have direct access to $Q^2 = 0$, we circumvent the need for extrapolations in Q^2. Furthermore, both the incoming and outgoing states can be taken to be at rest leading to excellent signal to noise. Despite this, lattice determinations have been consistently lower than the experimental value by as much as 10–15% [65–67]. In the past it was hoped that as we begin to probe at or near physical quark masses, the lattice determination would rise to the experimental value. Unfortunately, as we begin to consider such masses, it appears that the discrepancy remains. In an effort to account for these discrepancies, several studies have carefully examined the systematic errors present in the calculation [35, 68–81].

There is strong evidence to suggest that finite volume effects may play a key role in this shortfall [65–67, 73, 78], however it has recently been suggested that excited state contamination may also be a significant contributing factor [65–67, 79, 82]. For this reason there has been an increased effort to understand and reduce the impact of excited states on form factor calculations. In computing these quantities, it is well understood that to ensure excited state contributions to the correlation function are sufficiently suppressed, one needs large Euclidean time separations between operators. This is made clear if we consider the time-dependence of the first few terms that contribute to the ratio used to extract the axial charge

$$R(t_2, t_1) = g_A + \mathcal{O}(e^{-\Delta^{(1)} t_1}) + \mathcal{O}(e^{-\Delta^{(1)} (t_2 - t_1)}) + \dots , \tag{5.1}$$

where $\Delta^{(i)} \equiv m^{(i)} - m^{(0)}$. To choose a suitable time separation one should identify the time slices where the correlation functions take on their asymptotic form. Using a fixed current, a suitable current insertion time, t_1, can be chosen once ground-state dominance is observed in the two-point correlator. This ensures that the exponential in the first sub-leading term of Eq. (5.1) is small enough to suppress this contribution. As the sink time is free to vary, results are

extracted once constant behaviour is observed in the ratio, indicating that $t_2 - t_1$ is sufficiently large so as to suppress the second sub-leading term. For the fixed sink method, the situation is somewhat trickier. As it is now the current insertion time that is free to vary, neither exponential is fixed and so we seek a window whereby both sub-leading terms are minimised. Effectively one requires knowledge of the asymptotic behaviour of the three-point correlator *a priori*. In order to guarantee minimisation of excited states contributions, one should work with as large a sink time as possible, but too large a value will lead to poor signal-to-noise. There is clearly a difficult balance and understandably the desire for improved precision leads one to choose the earliest sink times for which excited states appear to be sufficiently suppressed. However, in Refs. [35, 74], it has been shown that for certain matrix elements, eg. $\langle x \rangle_{u-d}$, the source-sink separations often used in the literature are not sufficiently large to suppress excited state effects. Unfortunately, as we move ever closer to the physical point one is naturally forced to consider earlier sink times, or alternately increase statistics, to achieve adequate signal to noise.

To counter this issue, new techniques are being devised to try and control the sub-leading terms to the three-point correlator. The use of the summation method [79, 82–84] has shown improvement upon the conventional approach. Rather than considering the standard ratio, one instead considers the summed ratio

$$S(t_2) = \sum_{t_1=0}^{t_2} R(t_2, t_1) \, .$$

This construction leads to a reduction in the leading order time-dependence [85]

$$S(t_2) = c + t_2 \left(g_A + \mathcal{O}(e^{-\Delta^{(1)} t_2}) \right) \, .$$

In the determination of the axial charge, this approach appears to give a value that is systematically higher than that obtained from a single ratio, however with a significant increase in uncertainty [79]. Furthermore, one requires multiple sink times, t_2, and so this construction is significantly more expensive than the standard approach.

Equipped with the variational method, we can approach this problem from an entirely different perspective. Rather than alter the time-dependence of the unwanted contributions, we are able to separate and thus remove the unwanted contributions from the calculation. From a practical perspective, for a basis of n operators $\{ \chi_i(x) \,|\, i = 1, \ldots, n \}$, we can separate out the first n eigenstates and so ratios constructed using the projected correlators should have the following asymptotic behaviour

$$R_{\text{CM}}(t_2, t_1) = g_A + \mathcal{O}(e^{-\Delta^{(n)} t_1}) + \mathcal{O}(e^{-\Delta^{(n)} (t_2 - t_1)}) + \ldots \, , \tag{5.2}$$

where we note the first eigenstate, labelled by $i = 0$, is the ground state. In order to test the improvement offered by this novel method, we shall evaluate

the nucleon axial charge using both our variational construction and the standard approach employing single correlators with smeared sources and sinks.

The remainder of this chapter is organised as follows. We begin with Section 5.1 where we briefly outline exactly how one isolates the nucleon axial charge g_A, followed by a summary of the calculation details. In Section 5.2, we carefully compare the Euclidean time-dependence for the ratios used in both methods to discern their excited state behaviour and evaluate the improvement offered through the use of the variational method. Section 5.3 is devoted to a cost-benefit discussion where we consider whether the added cost associated with this method can be justified. In the context of this discussion we also compare our variational result with other lattice determinations to ascertain the role that excited state contamination plays in the systematically low value observed on the lattice. We conclude with a summary in Section 5.4.

5.1 Calculation Details

To extract the nucleon axial charge, g_A, we are interested in the matrix element describing the weak decay of the neutron into a proton

$$\langle\, p(p',s') \,|\, A_\mu^{ud} \,|\, n(p,s) \,\rangle\,,$$

where $A_\mu^{ud} = \bar{u}\gamma_\mu\gamma_5 d$ is the flavour changing axial current. This vertex can be decomposed into two independent form factors, the axial form factor $G_A(Q^2)$ and the induced pseudoscalar form factor $G_P(Q^2)$,

$$\langle\, p(p',s') \,|\, A_\mu^{ud} \,|\, n(p,s) \,\rangle = \left(\frac{m^2}{E_{p'}E_p}\right)^{1/2} \bar{u}_p(p',s') \left[\gamma_\mu\,\gamma_5\,G_A(Q^2) + \gamma_5\,\frac{q_\mu}{2m}\,G_P(Q^2)\right] u_n(p,s)\,, \quad (5.3)$$

where $q_\mu = p'_\mu - p_\mu$ is the current four-momentum and $Q^2 = -\,q^2$, the space-like momentum transfer. For exact isospin symmetry, one can show that the matrix element for the flavour-changing current, defined above, is equivalent to that of the isovector current evaluated between proton states

$$\langle\, p(p',s) \,|\, A_\mu^{ud} \,|\, n(p,s) \,\rangle = \langle\, p(p',s) \,|\, A_\mu^{u-d} \,|\, p(p,s) \,\rangle\,,$$

where $A_\mu^{u-d} = \bar{u}\gamma_\mu\gamma_5 u - \bar{d}\gamma_\mu\gamma_5 d$. Consequently we choose to evaluate g_A using $\mathcal{O} = A_\mu^{u-d}$ as it eliminates the issue of handling the flavour-changing current.

In order to access this matrix element, we consider the following three-point function

$$\begin{aligned} G_\mu(\vec{p}',\vec{p},t_2,t_1) &= \sum_{\vec{x}_2,\vec{x}_1} e^{-i\vec{p}'\cdot\vec{x}_2}\, e^{i(\vec{p}'-\vec{p})\cdot\vec{x}_1}\, \langle\Omega|\chi(x_2)\, A_\mu^{u-d}(x_1)\, \bar{\chi}(0)|\Omega\rangle \\ &\xrightarrow{t_1,t_2\to\infty} \sum_{s',s} e^{-E_p(\vec{p}')(t_2-t_1)}\, e^{-E_p(\vec{p})t_1}\, \langle\Omega|\chi(0)|p(p',s')\rangle \\ &\quad \times\langle p(p',s')|\mathcal{O}(0)|p(p,s)\rangle\, \langle p(p,s)|\bar{\chi}(0)|\Omega\rangle\,. \end{aligned} \quad (5.4)$$

For the nucleon, the overlap factors can be expressed as

$$\langle \Omega | \chi(0) | p(p,s) \rangle = Z(\vec{p}) \sqrt{\frac{m}{E(\vec{p})}} \, u_p(p,s) \,,$$

where we note that the Dirac spinors are normalised according to

$$\sum_s u(p,s) \, \bar{u}(p,s) = \left(\frac{\not{p} + m}{2m} \right) .$$

Substituting in this expression for the overlap factors, along with the vertex given by Eq. (5.3), we obtain a general expression describing how the form factors are encoded within the three-point correlator. Here however we are interested in $g_A \equiv G_A(Q^2 = 0)$ and so it suffices to consider the case where the incoming and outgoing momenta are the same. In particular we choose to work in the nucleon rest frame as this will provide the smallest statistical uncertainties. Applying this choice of kinematics, we arrive at the following expression

$$G_\mu(0,0,t_2,t_1) \xrightarrow{t_1,t_2 \to \infty} e^{-m\,t_2} \, Z(0) \, \bar{Z}(0) \left(\frac{\gamma_0 + I}{2} \right) \gamma_\mu \, \gamma_5 \left(\frac{\gamma_0 + I}{2} \right) g_A \,,$$

where $\bar{Z}$ is the overlap factor for the interpolator $\bar{\chi}$. To construct the ratio, we also require the nucleon two-point correlator. Working through the same procedure for this two-point function, we arrive at the corresponding expression

$$G(0,t_2) \xrightarrow{t_2 \to \infty} e^{-m\,t_2} \, Z(0) \, \bar{Z}(0) \left(\frac{\gamma_0 + I}{2} \right) .$$

For both these expressions, the quantities of interest are encoded within a 4×4 matrix in Dirac space. This is a feature of all baryon correlators and stems from the fact that interpolators themselves are spinors. Therefore, to extract the desired quantities we need to project out the relevant terms using some projection operator

$$G(\vec{p},t;\Gamma) = \mathrm{Tr}\left[\Gamma \; G(\vec{p},t) \right] .$$

In the case of the two-point correlator, we use the standard positive-parity projector

$$\Gamma_0 = \left(\frac{\gamma_0 + I}{4} \right) = \frac{1}{2} \begin{pmatrix} I & 0 \\ 0 & 0 \end{pmatrix} .$$

For the three-point correlator, the projector is dependent upon the choice of current-polarisation, μ. In this calculation we choose $\mu = 3$ for which the required projector is

$$\Gamma_3 = \Gamma_0 \, \gamma_3 \, \gamma_5 = \frac{1}{2} \begin{pmatrix} \sigma^3 & 0 \\ 0 & 0 \end{pmatrix} .$$

By constructing the ratio from the parity-projected correlation functions, we obtain the axial charge

$$R = \frac{G_3(0,0,t_2,t_1;\Gamma_3)}{G(0,t_2;\Gamma_0)} \xrightarrow{t_1,t_2 \to \infty} g_A \,. \tag{5.5}$$

In the case of the variational analysis, we construct the same ratio, however this time working with the eigenstate projected correlators

$$G^{(0)}(0,t_2;\Gamma_0) = v_i^{(0)} G_{ij}(0,t_2;\Gamma_0) u_j^{(0)}(0)\,, \tag{5.6}$$

$$G_3^{(0)}(0,0,t_2,t_1;\Gamma_3) = v_i^{(0)} (G_3)_{ij}(0,0,t_2,t_1;\Gamma_3) u_j^{(0)}(0)\,, \tag{5.7}$$

giving

$$R^{\text{CM}} = \frac{v_i^{(0)}\,(G_3)_{ij}(0,0,t_2,t_1;\Gamma_3)\,u_j^{(0)}}{v_i^{(0)}\,G_{ij}(0,t_2;\Gamma_0)\,u_j^{(0)}}\,. \tag{5.8}$$

For this calculation, and those throughout the rest of this thesis, we make use of the PACS-CS (2+1)-flavour dynamical-QCD gauge field configurations [24] made available through the ILDG [86]. These configurations are generated using a non-perturbatively $\mathcal{O}(a)$-improved Wilson fermion action and Iwasaki gauge action. The value $\beta = 1.90$ results in a lattice spacing $a = 0.091$ fm, determined via the static quark potential. With lattice dimensions $32^3 \times 64$, these ensembles correspond to a physical spatial volume with a box length $L = 2.9$ fm. These 2+1 configurations are generated with five values for the light quark mass with the strange quark mass held fixed. The resulting range in pion mass extends from 702 MeV down to the near physical mass of 156 MeV. However, as the intention of this calculation is to examine whether the variational approach is an improvement upon the standard method, we limit ourselves to a single mass only. In particular, we choose to work with the second lightest mass where $m_\pi \approx 290$ MeV. The resulting value of $m_\pi L = 4.26$ is comparable to the values used by most groups for similar masses.

A fixed boundary condition is applied in the temporal direction. Our fermion sources are inserted at $t_0 = 16$ for which it has been verified that reflections from the temporal boundary are negligible. SST propagators are evaluated using a local axial current, held fixed at $t_1 = 21$ and projected onto $\vec{q} = 0$. This insertion time was determined by the onset of asymptotic behaviour for the projected two-point correlator. As we are working with the local axial current, the bare lattice quantities determined from Eqs. (5.5) and (5.8) will need to be renormalised in order to facilitate the comparison with experiment and other lattice determinations. The value we use for the the axial renormalisation constant on these ensembles, $Z_A = 0.781(20)$, was determined non-perturbatively in Ref. [38] using a Schrödinger functional scheme. To distinguish between the bare and renormalised quantities, we shall refer to them as g_A and g_A^R respectively. For our error analysis, we use a second-order, single-elimination jackknife procedure with the χ^2_{dof} obtained via covariance matrix fits.

As we are primarily interested in isolating the ground state, we choose to work with a small variational basis upon which to perform our correlation matrix analysis. This basis is comprised of smeared operators of various widths, constructed using the standard, local proton interpolator

$$\chi_1(x) = \epsilon^{abc}[u^{aT}(x) C\gamma_5 d^b(x)]\, u^c(x)\,.$$

Table 5.1: The rms radii for the various levels of smearing considered in this work.

Sweeps of smearing	rms radius (fm)
16	0.216
35	0.319
100	0.539
200	0.778

The smearing is performed using the gauge-invariant Gaussian smearing procedure outlined in Section 3.4.1. For the smearing fraction of Eq. (3.19), we use the value $\alpha = 0.7$. To construct a variety of smearing widths, we iteratively perform n sweeps of smearing via Eq. (3.18) for a range of values for n, these being 16, 35, 100 and 200, determined in Ref. [87] to give optimal span. In Table 5.1 we list the rms-radii for this choice of smearing parameters. With this basis we are able to construct correlation matrices of dimension up to 4×4. Finally, we use variational parameters $t_0 = 18$ and $\delta t = 2$, again taken from Ref. [87], where it was found that this choice produced best balance between systematic and statistical uncertainties.

5.2 Results

In Fig. 5.1 we present values for g_A as a function of Euclidean sink time t_2, using the standard single correlator method, for both point and smeared sinks, and the variational method. For the standard method we present the datasets obtained using 35 sweeps of smearing, indicative of smearing radii commonly used. Between the two methods, we can see significant differences in the overall time dependence. Beginning with the standard single source method, the Euclidean time suppression of excited state contributions manifests itself as a steady increase in the value of g_A. Between the two datasets, we see that by smearing both source and sink, there appears to be a reduction in the impact of excited states with the increase in the value of g_A immediately following the current. However the steady rise in the data remains. In the case of a point sink, it is difficult to properly identify a plateau and so we make use of the χ^2_{dof} to inform us as to a suitable fit window. In doing so we find that the earliest time-slice one should consider is $t_2 = 25$. Use of the smeared sink leads to improved plateau quality and allows for earlier fits with suitable χ^2_{dof} obtained at $t_2 = 24$.

For the variational method, we see quite a different situation. Our variational approach yields extremely clean results with rapid ground state dominance. The systematic rise in the data is no longer present and the onset of the plateau is within two time slices of the current insertion. In Fig. 5.2 we overlay the three datasets to highlight the excited state behaviour between the standard and

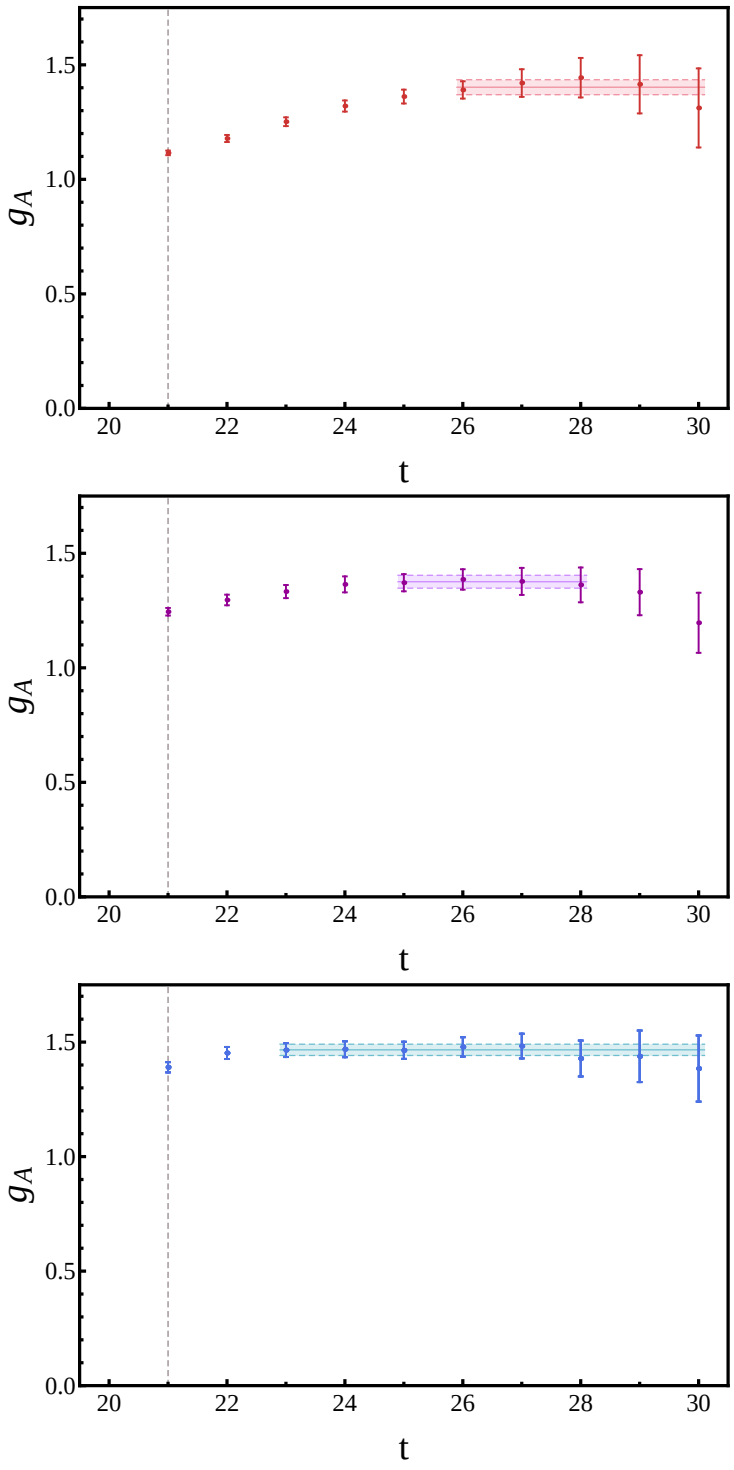

Figure 5.1: Nucleon axial charge, g_A, as a function of Euclidean sink time using the standard single correlator approach and the variational method. The red dataset (top) is for a smeared source and point sink, the purple dataset (centre) is for a smeared source and smeared sink while the blue dataset (bottom) is for the variational method. For the single correlator method, we present the data obtained using 35 sweeps of smearing, which gives a smearing radius comparable with that used by many groups. The dashed line represents the time-slice at which the current is inserted.

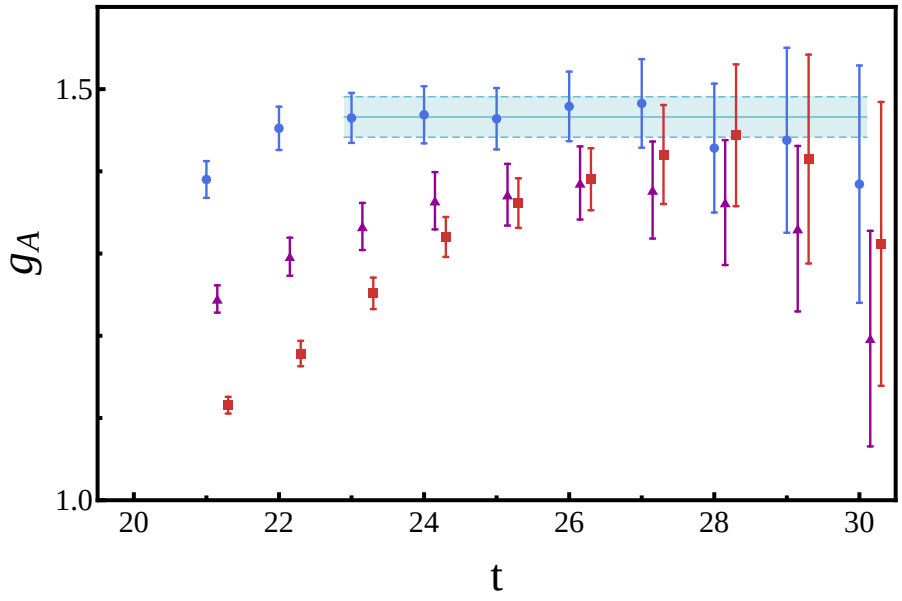

Figure 5.2: Overlay of the results presented in Fig. 5.1. The red squares (■) are for the point sink, the purple triangles (▲) for the smeared sink while the blue circles (●) are for the variational approach.

variational approach. Here it is clear that some excited state contributions remain, however this can be understood through Eq. (5.2). As we only have a finite basis, it is not possible to remove all excited state contributions, however through the larger mass splitting between the ground state and n^{th} excited state we expect these unwanted terms to be quickly suppressed. This behaviour is consistent with that observed in Fig. 5.2.

Continuing with Fig. 5.2, what is most concerning is the lack of overlap between the results of the standard single source method and those of our variational analysis in the regions identified by the χ^2_{dof} as suitable fit windows. To investigate this further, we consider all permissible fits for the three data sets with the strict criterion that the χ^2_{dof} lie between 0.800 and 1.200. These fits are listed in Table 5.2. In both data sets employing the standard approach, we can obtain good fits with small uncertainties if we choose to begin fitting around $t_2 = 25$ or 26, however these results sit significantly lower than the variational result. In the case of the point sink, moving the fit window to later times results in an increase in the central value, with a 5% variation observed in the value for g_A between 25–30 and 28–30. Fits taken at these later times are consistent with the variational result, however this is in part due to an increase in the statistical uncertainty. For the smeared sink, we find that moving the fit window to later times results in a decrease in the central value. Consequently there is no choice of fit-window that leads to a result consistent with the variational method. It is clear in either case that we have little control over the excited state systematics. In contrast to this, the variation in the extracted fits for the different fit-windows taken for the variational result, is considerably smaller than the smallest statistical uncertainty.

Table 5.2: Un-renormalized values of g_A from fit windows which give a covariance matrix based χ^2_{dof} between 0.800 and 1.200. The datasets are identified as (a) Standard approach with point sink, (b) Standard approach with smeared sink and (c) Variational approach. For the standard approach we have selected 35 sweeps of smearing. We note how the value of g_A increases for the standard approach as we move the fit window to later times. In contrast, the variational approach is stable across all windows with the desired χ^2_{dof}.

(a)

Fit Window	g_A	χ^2_{dof}
25 – 27	1.38(3)	1.168
25 – 30	1.38(4)	1.100
25 – 31	1.38(3)	0.951
26 – 27	1.40(3)	0.808
26 – 30	1.40(3)	1.077
26 – 31	1.40(4)	0.902
27 – 31	1.41(4)	1.011
28 – 30	1.42(6)	1.129
29 – 31	1.35(7)	0.994

(b)

Fit Window	g_A	χ^2_{dof}
24 – 30	1.36(3)	1.161
24 – 31	1.36(3)	1.104
25 – 28	1.38(3)	0.926
25 – 29	1.37(3)	0.812
26 – 30	1.37(4)	1.100
26 – 31	1.36(4)	0.952
27 – 31	1.33(4)	1.148
28 – 31	1.30(10)	1.082

(c)

Fit Window	g_A	χ^2_{dof}
23 – 30	1.47(3)	0.848
23 – 31	1.47(3)	0.818
24 – 29	1.47(2)	0.848
24 – 30	1.47(2)	0.988
24 – 31	1.47(4)	0.932
25 – 29	1.47(3)	0.951
25 – 30	1.47(2)	1.120
25 – 31	1.47(2)	1.040
26 – 28	1.47(2)	1.091
26 – 29	1.47(2)	1.184
26 – 31	1.47(2)	1.146

As there are multiple smearing levels required for evaluation of the correlation matrix, we can consider how the level of smearing affects the extracted value of g_A. In Fig. 5.3 we show g_A as a function of sink time t_2 using the standard method, for all of the smearing levels utilised in the variational analysis. Within the data there are some clear trends. Firstly, as was noted for 35 sweeps of smearing, the use of smeared sink leads to a reduction of the excited state contributions over the point sink method. Furthermore, the impact of excited states is reduced as we increase the level of smearing. Particularly, for the larger levels of smearing using both smeared source and smeared sink, we observe plateaus similar in nature to that of the variational analysis. Taking the fits shown in Fig. 5.3, we compare the renormalised value for g_A for all the smearing levels, both with point and smeared sinks, and compare this to the result extracted using the variational approach. This comparison is shown in Fig. 5.4 We see a clear dependence on the level of smearing used in the calculation. For low levels of smearing the extracted result can be significantly suppressed, with the smallest level of smearing differing by up to 8% from our improved, variational result. From this evidence, it is clear that if the smearing level is not properly tuned at the source and sink, then excited state effects significantly impact the extracted result for g_A. We note further that for the larger levels of smearing, though the result is still consistent with the variational result, the observed trend suggests that further smearing will result in a larger value. It is therefore entirely possible that over-smearing may also lead to systematic error in the extracted value.

In principle, one could tune the smearing so as to obtain optimal overlap with the ground state. This could be done efficiently by using a point source propagator and tuning the smearing through the sink via examination of the two-point correlator, as outlined in Ref. [88]. However, this optimal level of smearing depends entirely on the quark mass, β value, momentum or operator under consideration. Therefore one must tune the smearing level for each set of parameters one wishes to examine. Through the variational procedure we obtain operators optimised to couple to the physical eigenstates, therefore eliminating the need for tedious fine-tuning to maximise overlap with the ground state.

5.3 Cost–Benefit Discussion

A real concern with the correlation matrix approach is the increased cost. For our implementation, we require 2 inversions per configuration for every smearing we include in constructing the correlation matrix. For $n = 4$ levels of smearing we have a total of $2n = 8$ inversions per configuration, as opposed to the minimum of 2. In Fig. 5.2 we can see that, for large Euclidean times, the conventional approach is consistent with the correlation matrix approach, albeit with larger errors. Thus it is worth considering what the required increase in statistical sample would be for the conventional approach to produce results with similar error to that of our correlation matrix method.

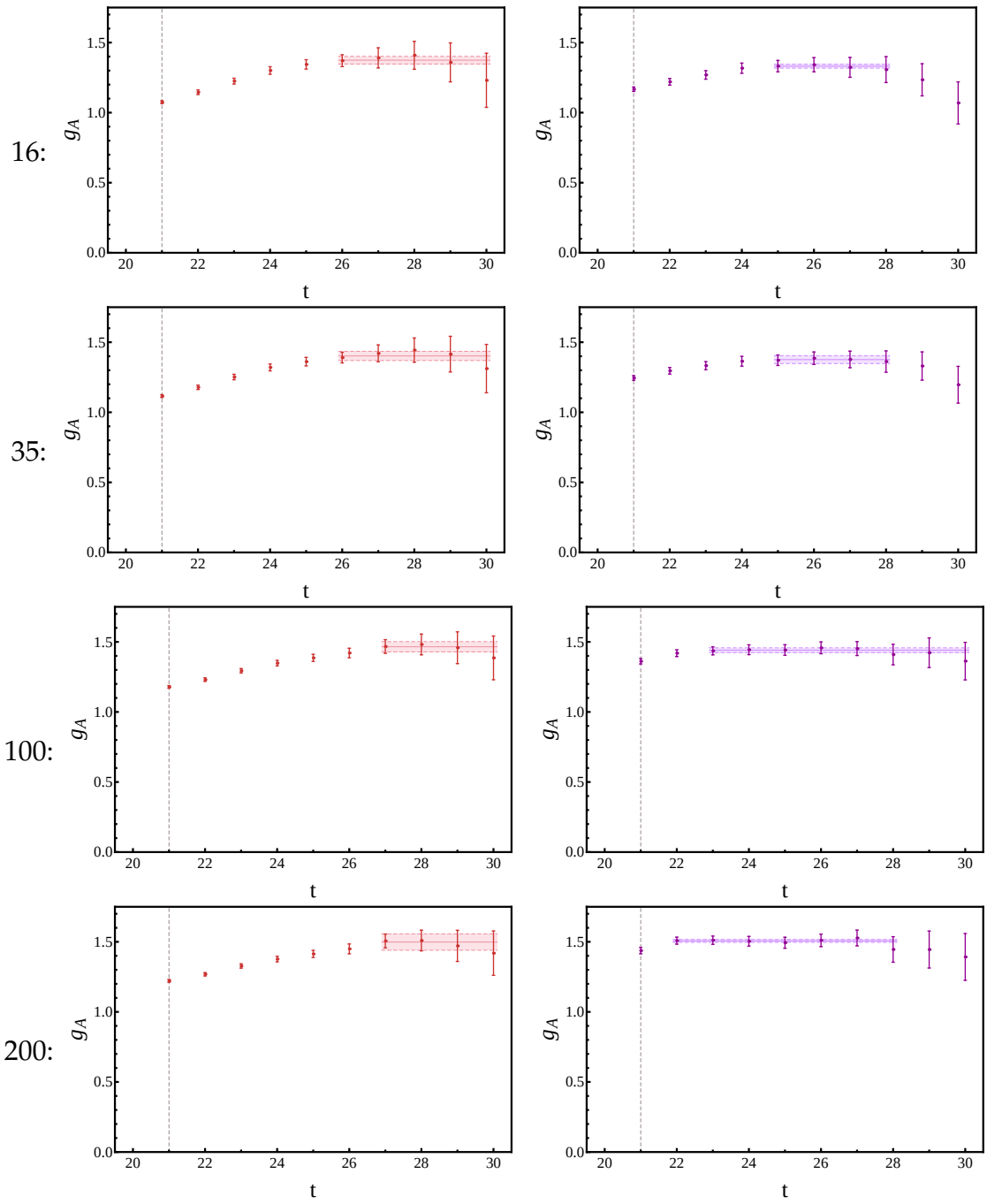

Figure 5.3: Nucleon axial charge, g_A, as a function of Euclidean sink time determined using standard techniques for the range of smearing levels presented in Table 5.1. The red dataset (left column) is for smeared source and point sink, while the purple dataset (right column) is for smeared source and smeared sink. The level of smearing increases down the column and is indicated by the row label to the left.

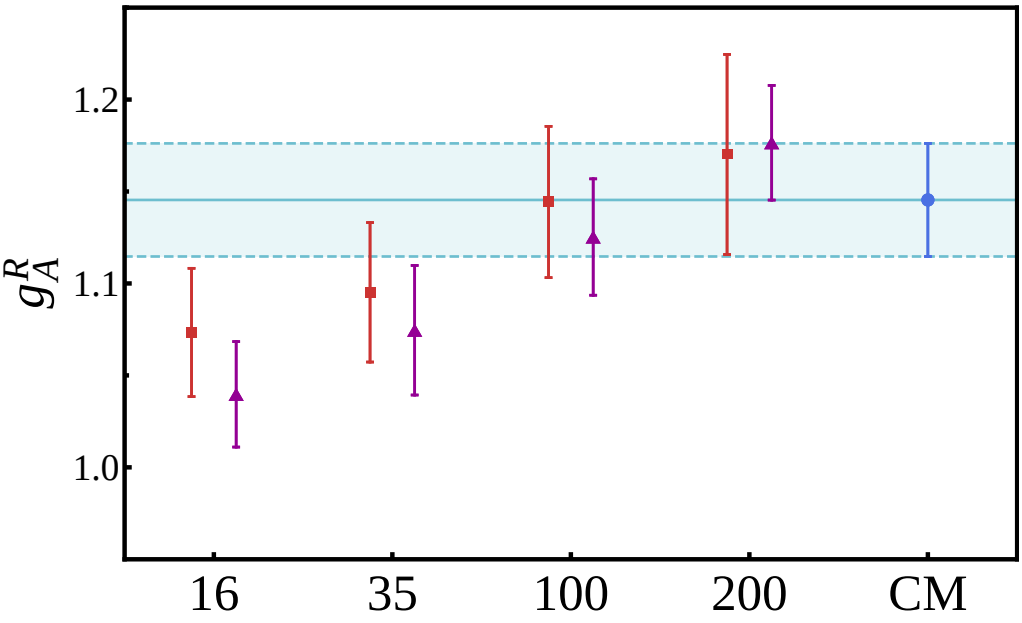

Figure 5.4: Comparison of the renormalised value of g_A. The first four pairs of points are the results for the conventional, point sink (■) and smeared sink (▲) approach with increasing levels of smearing from left to right. The rightmost point (●) is the result extracted using the variational approach.

Given the error varies with the sample size N as $\Delta g_A \propto \frac{1}{\sqrt{N}}$, then the relative increase in sample required to obtain an error $(\Delta g_A)_{\text{desired}}$ is given by

$$\frac{N_{\text{required}}}{N_{\text{current}}} = \left(\frac{(\Delta g_A)_{\text{current}}}{(\Delta g_A)_{\text{desired}}}\right)^2 = \left(\frac{(\Delta g_A)_{\text{sm-sm}}}{(\Delta g_A)_{\text{CM}}}\right)^2 ,$$

where $(\Delta g_A)_{\text{current}}$ is the error extracted with the current sample of size N_{current}. Using the leading time-slice of the associated fit-windows as indicative of the uncertainty in g_A, which for the *smeared-smeared* approach is $t_2 = 27$ and for the correlation matrix approach $t_2 = 23$, we find that

$$\left.\begin{aligned}(\Delta g_A)_{\text{sm-sm}} &= 0.059 \\ (\Delta g_A)_{\text{CM}} &= 0.030\end{aligned}\right\} \frac{N_{\text{required}}}{N_{\text{current}}} = \left(\frac{0.59}{0.30}\right)^2 = 3.87\,.$$

Naively we expect a factor 4 increase in statistics, which would require fewer inversions than our correlation matrix method. However, we note that the peak value for the *smeared-smeared* approach is at time slice 26 and so χ^2_{dof} analysis would tend to favour earlier points around times 24-25. This is consistent with Table 5.2. In the tradition of choosing the earliest possible fit-window to minimise statistical uncertainty, a more appropriate fit window would be sometime between times 24-31. Taking this into account, the best choice of fit is from times 25-28 with $\chi^2_{\text{dof}} = 0.9$ and a result $g_A = 1.38(3)$. However, it is clear that this result is systematically suppressed, relative to the correct result of $g_A = 1.47(2)$, by excited state contributions. While one could invest more super-computing resources to reduce statistical error, in this case one will only get the wrong answer very accurately if one does not take care in fine-tuning the source.

The origin of this excited state suppression stems from our choice of t_1. Using the variational approach, the onset of ground state dominance occurs earlier in Euclidean time, allowing for an earlier choice of current insertion time t_1. For this particular ensemble, ground state dominance for the nucleon occurs at time $t = 21$, so our choice for t_1 is ideal for the correlation matrix method. For the *smeared-smeared* approach with 35 sweeps of smearing, ground state dominance does not occur until time $t = 23$. Consequently, our choice of current insertion time is not sufficiently large to ensure suppression of the first sub-leading term in Eq. (5.1) and so we are therefore sampling both ground state and excited state contributions to the matrix element. This is why the peak value is systematically low for this choice of smearing. This also gives rise to the smearing dependence illustrated in Fig. 5.4. Thus for a more comprehensive comparison, one requires a new simulation with $t_1 = 23$, two time slices later. Nonetheless, we can still get some insight from our present analysis into the required increase in statistics. For the the ratio of three- to two-point functions, ground state dominance occurs 6 time slices after the current insertion, so with $t_1 = 23$ one would be considering a fit window commencing at $t_2 = 29$ as opposed to $t_s = 27$ considered earlier. Here we have

$$\left.\begin{aligned}(\Delta g_A)_{\text{sm-sm}} &= 0.101 \\ (\Delta g_A)_{\text{CM}} &= 0.030\end{aligned}\right\} \frac{N_{\text{required}}}{N_{\text{current}}} = \left(\frac{0.101}{0.030}\right)^2 \simeq 11.3,$$

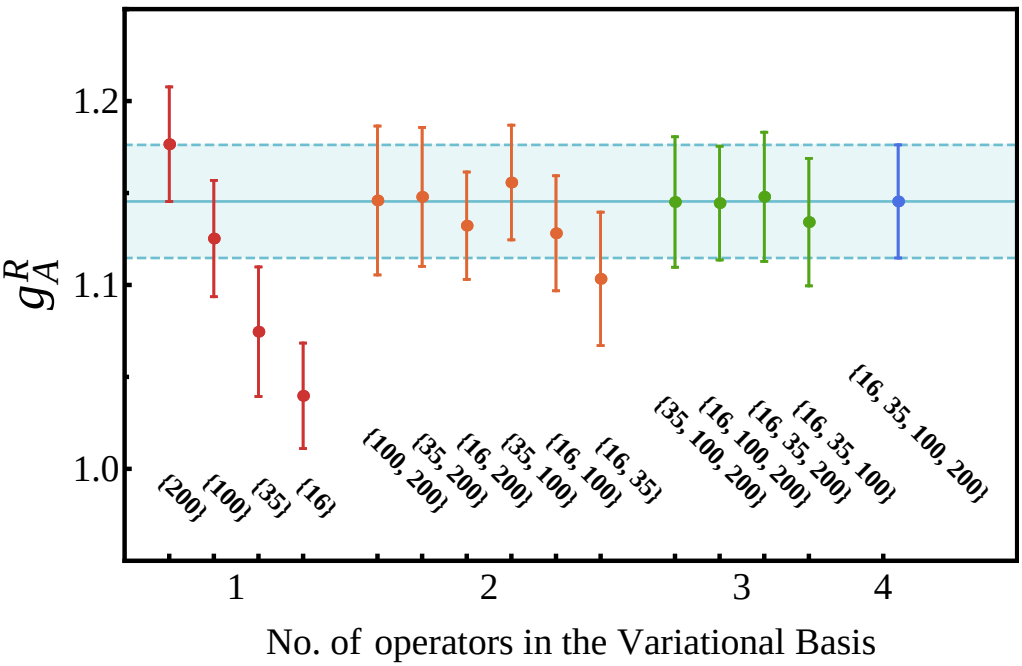

Figure 5.5: Results for g_A^R obtained with different number and combination of operators used in the variational analysis.

a factor 11 increase. As the variational approach enables one to:

1. rapidly isolate the ground state following the source, thus enabling an earlier current insertion, and

2. rapidly isolate the ground state again after inserting the current enabling an earlier Euclidean time fit,

the associated reduction in the error bar through this process outweighs the increased cost in constructing the matrix of cross-correlators.

In our implementation, due to the construction of the complete correlation matrix of three-point functions, we not only have access to the ground state, but also to the first $n-1$ excited states, where n is the dimension of our operator basis. This has been utilised in Ref. [89] to access the axial charge of nucleon excitations. In principle, if one were solely interested in the ground state properties, one could use the optimised sources generated via the two-point correlation matrix as the input for the SST inversion, providing SST propagators that couple directly with the ground state. This reduces the cost from $2n$ inversions down to $n+1$. For this calculation the cost would be reduced from 8 to 5 inversions. Further reduction in cost is demonstrated through Fig. 5.5. It was found that access to ground state properties can be achieved with 3 levels of smearing, provided the smearing radii are chosen to span the space. Therefore, we could further reduce the cost to $3+1 =$

Table 5.3: Comparison of results for g_A^R on ensembles with similar volumes and values of m_π to our calculation. For the CLS/Mainz group we have included results for the conventional ratio method (upper) and the summation method (lower). The asterisk indicates that these results include the correction of finite-volume effects and so will tend to sit slightly higher.

Group	m_π (MeV)	$m_\pi L$	$t_s - t_0$ (fm)	g_A^R	
our result	290	4.26	0.75	1.147(33)	
QCDSF '13	292	4.25	1.1	1.099(13)	
CLS/Mainz '12	277	4.25	1.1	1.137(37)	*
CLS/Mainz '12	277	4.25	0.7-1.3	1.162(95)	*
LHPC '10	293	3.68	1.2	1.154(26)	
ETMC '10	298	4.28	1.1	1.103(32)	

4 inversions per configuration, only a factor of 2 above the minimum for what is equivalent to an order of magnitude improvement in the statistics.

In Table 5.3 we present a comparison of our result for g_A^R with results by other groups on similar ensembles. The consistency between our result and those of other groups is testament to the care taken by these collaborations to minimise systematic uncertainties. Fig. 5.4 clearly shows that excited state contamination can suppress the extracted value of g_A, however the consistency of Table 5.3 leads us to conclude that the suppression observed in the literature is unlikely to stem from excited state effects. However, a key issue in the calculation of any three-point function is how large must one make their source-sink separation to ensure that excited state contaminations are sufficiently suppressed [35]. There is a general consensus within the community that source-sink separations $\lesssim 1.0$ fm will suffer from excited state contaminations without fine-tuning the source and sink to isolate the state. Indeed our results highlight this systematic effect when using the conventional approach. Here the source-sink separation of ~ 1.0 fm is too small and the extracted value for g_A suffers from excited state effects as illustrated in Fig. 5.4. The underlying issue is that there is insufficient time to isolate the ground state prior to current insertion and again isolate the ground state before annihilation. Based on our earlier arguments regarding a more suitable current insertion time, we would expect a suitable sink time would be $t_2 = 29$, increasing the source-sink separation to ~ 1.2 fm. This result is consistent with the source-sink separations used by the other groups in Table 5.3.

Using the variational approach, due to rapid onset of ground state dominance through ideal interpolators, we are able to use much smaller source-sink separations. For our variational results, ground state dominance after the current insertion occurs as early as $t_2 = 23$ resulting in a temporal separation between source and sink of only 0.64 fm. Thus, by applying the variational technique to fixed sink methods, one could consider source-sink separations ~ 0.7 fm which would result in small statistical errors.

5.4 Summary

Here we have illustrated how the variational approach can be used to eliminate excited state effects from the calculation of the nucleon axial charge, g_A. We have demonstrated , through consideration of a variety of smearing levels, that excited state effects act to suppress lattice simulation results for g_A. The use of optimised interpolators obtained via the variational approach resulted in rapid ground state dominance allowing for earlier insertion of the current and earlier fit windows resulting in smaller statistical uncertainty. The key advantage to this approach is that once a suitable basis has been chosen, optimised sources are constructed automatically, eliminating the need to tune smearing parameters. In comparing our variational result with those of other groups using similar ensembles, the observed consistency highlights the care taken by these collaborations to minimise the impact of excited state contamination. Through careful consideration of the cost versus benefit, it was found that the additional cost for this method was outweighed by the improvement in statistical uncertainty.

Chapter 6

Light Meson Form Factors

The content of this chapter is based on the publication: "Light Meson Form Factors at near Physical Masses" by B. J. Owen et al., Phys. Rev. D **91**, *no. 7, 074503 (2015), [arXiv:1501.02561]*

The fact that quarks carry electric charge makes the electromagnetic interaction an excellent probe for examining hadron structure. Mapping out the electromagnetic form factors of these states provides a direct measure of the distribution of charge and magnetism within a hadron and consequently, insight into the arrangement of the quarks within. Experimentally this can be achieved by electron scattering off the hadron target. However such measurements can only be performed with states that are stable, or decay weakly, where their lifetimes are sufficiently long to allow the necessary interactions to occur. For states that are unstable with respect to the strong interaction, direct measurements are not possible. Instead one is forced to disentangle resonant state properties from radiative processes observed during scattering experiments. Recently there has been interest in extracting magnetic dipole moments [90–92] through such methods. In particular, Gudiño *et al.* [92] have been able to provide a determination of the magnetic dipole moment of the ρ meson, the first such experimental measurement for a vector meson.

Searching through the literature to see what results lattice QCD can offer as a comparison, one finds there exist only a small handful of lattice determinations of this quantity, with the majority of these making use of the quenched approximation [56, 93–97]. Of these calculations, only three do so via direct measurement of the electromagnetic form factors and only two using dynamical quarks [95, 97]. Furthermore, their determinations of the magnetic and quadrupole moments rely upon large extrapolations to $Q^2 = 0$ due to their large value for the minimum available, non-trivial 4-momentum transfer, $Q^2_{\text{min}} \simeq 0.44$ GeV^2 and 0.28 GeV^2 respectively. Thus, there is a clear need for an evaluation of the ρ meson form factors in full QCD, with low-Q^2 and near physical quark masses, so as to allow for a direct comparison with the result of Ref. [92]. Making use of the PACS-CS configurations and our variational framework, we perform such an evaluation. We begin in Section 6.1 with an overview of the manner in which we isolate the form factors for both pseudoscalar and vector mesons from the corresponding three-point functions. This is followed by a summary of the calculation details in Section 6.2. In the remainder of the chapter, we present our results starting with

an examination of our meson spectrum followed by further considerations of the improvements offered through the use of variational techniques. We then present the form factors and corresponding moments, for both ground states and the first excitations in our spectra. We conclude with a summary in Section 6.4.

6.1 Extracting Light Meson Form Factors

As was discussed in Section 2.3, a given form factor decomposition is arrived at through general considerations of the Lorentz covariance of the matrix element and the symmetries of the system under consideration. It follows that for states within a given J^{PC}, the form factor decomposition will be the same. This is not to say that the form factors themselves will be the same, simply that the physical properties of the system can be expressed through the same set of Lorentz covariant structures. Consequently, to access the excited state form factors we consider the same combination of correlator ratios, formed with the relevant eigenstate projected correlators. Here we shall consider the correlator ratios required to isolate the Sachs electromagnetic form factors for both pseudoscalar and vector mesons. We shall begin this discussion with the pseudoscalar mesons.

Pseudoscalar mesons being spinless particles allow us to express the operator overlap as

$$\langle \Omega | \phi^{\alpha,\vec{p}}(0) | \pi_\beta(\vec{p}) \rangle = \frac{\delta^{\alpha\beta}}{\sqrt{2\, E_\alpha(\vec{p})}}\, \mathcal{Z}^\alpha(\vec{p})\,, \tag{6.1}$$

where $\phi^{\alpha,\vec{p}}$ is the optimised operator obtained through the variational analysis. Consequently the two-point function takes the form

$$G(\vec{p}, t_2; \alpha) = \frac{e^{-E_\alpha(\vec{p})\, t_2}}{2E_\alpha(\vec{p})}\, \mathcal{Z}^\alpha(\vec{p})\, \mathcal{Z}^{\alpha\dagger}(\vec{p})\,, \tag{6.2}$$

and the three-point function,

$$\begin{aligned} G^\mu(\vec{p}', \vec{p}, t_2, t_1; \alpha) = {} & \frac{e^{-E_\alpha(\vec{p}')\,(t_2 - t_1)}\, e^{-E_\alpha(\vec{p})\, t_1}}{2\,\sqrt{E_\alpha(\vec{p}')\, E_\alpha(\vec{p})}} \\ & \times \mathcal{Z}^\alpha(\vec{p}')\, \mathcal{Z}^{\alpha\dagger}(\vec{p})\, \langle \pi_\alpha(\vec{p}') | J^\mu(0) | \pi_\alpha(\vec{p}) \rangle\,. \end{aligned} \tag{6.3}$$

For a pseudoscalar meson, the matrix element is described by a single form factor $F_\pi(Q^2)$

$$\langle \pi_\alpha(\vec{p}') | J^\mu(0) | \pi_\alpha(\vec{p}) \rangle = \frac{1}{2\,\sqrt{E_\alpha(\vec{p}')\, E_\alpha(\vec{p})}}\, \left[p'^\mu + p^\mu \right]\, F_\pi^\alpha(Q^2)\,, \tag{6.4}$$

where again p and p' label the incoming and outgoing momenta and $Q^2 = -q^2$ is the space-like momentum transfer. We note that in this case the Sachs decomposition $G_C(Q^2)$ and $F_\pi(Q^2)$ are equivalent so we choose to use the

notation $G_C(Q^2)$ from here on. Substituting this expression into Eq. (6.3) and substituting correlators into the ratio given by Eq.(4.16), we have

$$R^{\mu}(\vec{p}', \vec{p}; \alpha) = \frac{1}{2\sqrt{E_\alpha(\vec{p}')\, E_\alpha(\vec{p})}} \left[p^\mu + p'^\mu\right] G_C^\alpha(Q^2)\,.$$

For this calculation we choose to work with the following kinematics

$$p' = (E_\alpha, p_x, 0, 0) \quad \text{and} \quad p = (m_\alpha, 0, 0, 0)\,,$$

where $E_\alpha = \sqrt{m_\alpha^2 + p_x^2}$. Thus the required expression through which we access the Sachs charge form factor for a pseudoscalar meson is

$$G_C^\alpha(Q^2) = \frac{2\sqrt{m_\alpha\, E_\alpha}}{E_\alpha + m_\alpha} R^0(\vec{p}_x, 0; \alpha)\,. \tag{6.5}$$

In the case of the vector meson, the situation is somewhat more complicated due to the meson's spin. In order to correctly describe the operator overlap for this state we must include a spin polarisation vector

$$\langle \Omega | \phi_\sigma^{\alpha,\vec{p}}(0) | \rho_\beta(\vec{p}, s)\rangle = \frac{\delta^{\alpha\beta}}{\sqrt{2\, E_\alpha(\vec{p})}}\, \mathcal{Z}^\alpha(\vec{p})\, \epsilon_\sigma^\alpha(p, s)\,, \tag{6.6}$$

where the polarisation vectors satisfy the spin sum relation

$$\sum_s \epsilon_\sigma^\alpha(p, s)\, \epsilon_\tau^{\alpha *}(p, s) = -\left(g_{\sigma\tau} - \frac{p_\sigma\, p_\tau}{m_\alpha^2}\right)\,. \tag{6.7}$$

An important feature of Eq. (6.6) that warrants further discussion is the presence of the Lorentz index, σ. It is not surprising that in order to correctly describe the Lorentz covariance properties of the vector meson, we require operators that in themselves transform as vectors. Accordingly we generalise the variational problem by assigning eigenvectors to each Lorentz component and forming the optimised operators as

$$\phi_\sigma^\alpha(x) = \sum_i v_{\sigma,i}^\alpha\, \chi_{\sigma,i}(x), \qquad \bar{\phi}_\tau^\alpha(x) = \sum_j \bar{\chi}_{\tau,j}(x)\, u_{\tau,j}^\alpha\,.$$

We then solve Eqs. (4.20a) and (4.20b) for each Lorentz component separately such that the resulting operators maximally isolate the spectrum observed in each Lorentz component[1]. We can then obtain the projected correlators by projecting with the relevant eigenvectors where care is taken to ensure that one uses the correct momentum and now Lorentz component for both source and sink,

$$G_{\sigma\tau}(\vec{p}, t_2; \alpha) \equiv v_{\sigma,i}^\alpha(\vec{p})\, G_{\sigma\tau,ij}(\vec{p}, t_2)\, u_{\tau,j}^\alpha(\vec{p})\,,$$
$$(G_{\mathcal{O}})_{\sigma\tau}(\vec{p}', \vec{p}, t_2, t_1; \alpha) \equiv v_{\sigma,i}^\alpha(\vec{p}')\, (G_{\mathcal{O}})_{\sigma\tau,ij}(\vec{p}', \vec{p}, t_2, t_1)\, u_{\tau,j}^\alpha(\vec{p})\,.$$

[1]We note that to account for spectral non-degeneracies induced by the finite volume of the lattice, a different approach is required.

Making use Eqs. (6.6) and (6.7), the vector meson two-point function reduces to

$$G_{\sigma\tau}(\vec{p}, t_2; \alpha) = -\frac{e^{-E_\alpha(\vec{p})\, t_2}}{2E_\alpha(\vec{p})}\, \mathcal{Z}^\alpha(\vec{p})\, \mathcal{Z}^{\alpha\dagger}(\vec{p})\, \left(g_{\sigma\tau} - \frac{p_\sigma\, p_\tau}{m_\alpha^2}\right), \tag{6.8}$$

and the three-point function

$$\begin{aligned} G^\mu_{\sigma\tau}(\vec{p}', \vec{p}, t_2, t_1; \alpha) = {} & \frac{e^{-E_\alpha(\vec{p}')\,(t_2 - t_1)}\, e^{-E_\alpha(\vec{p})\, t_1}}{2\,\sqrt{E_\alpha(\vec{p}')\, E_\alpha(\vec{p})}}\, \mathcal{Z}^\alpha(\vec{p}')\, \mathcal{Z}^{\alpha\dagger}(\vec{p}) \\ & \times \epsilon'^\alpha_\sigma(p', s')\, \langle \rho_\alpha(\vec{p}', s') | J^\mu(0) | \rho_\alpha(\vec{p}, s) \rangle\, \epsilon^{\alpha *}_\tau(p, s)\,. \end{aligned} \tag{6.9}$$

In order to reduce this further, we require an expression for the matrix element. For a spin-1 system coupled to a vector current, one finds that the matrix element can described entirely by three independent vertex functions $G_i(Q^2)$ [98–100]

$$\langle \rho_\alpha(\vec{p}', s') | J^\mu | \rho_\alpha(\vec{p}, s) \rangle = \frac{1}{2\,\sqrt{E_\alpha(\vec{p})\, E_\alpha(\vec{p}')}}\, \epsilon'^{\alpha *}_\delta(p', s')\, \Gamma^{\delta\mu\gamma}(p', p)\, \epsilon^\alpha_\gamma(p, s) \tag{6.10}$$

where

$$\begin{aligned} \Gamma^{\delta\mu\gamma}(p', p) = -\{ & g^{\delta\gamma}\, [p^\mu + p'^\mu]\, G_1(Q^2) + [g^{\gamma\mu}\, q^\delta - g^{\delta\mu}\, q^\gamma]\, G_2(Q^2) \\ & - q^\delta\, q^\gamma\, \frac{p^\mu + p'^\mu}{2m_\alpha^2}\, G_3(Q^2)\}\,. \end{aligned} \tag{6.11}$$

Taking the appropriate linear combination of these vertex functions, gives the Sachs decomposition [99, 100]

$$\begin{aligned} G_Q(Q^2) &= G_1(Q^2) - G_2(Q^2) + \left(1 + \frac{Q^2}{4m_\alpha^2}\right)\, G_3(Q^2)\,, \\ G_M(Q^2) &= G_2(Q^2)\,, \\ G_C(Q^2) &= G_1(Q^2) + \frac{2}{3}\, \frac{Q^2}{4m_\alpha^2}\, G_Q(Q^2)\,. \end{aligned}$$

Replacing the matrix element in Eq. (6.9) with the above expression and applying the spin-sum identity, the three-point function reduces to

$$G^\mu_{\sigma\tau}(\vec{p}', \vec{p}, t_2, t_1; \alpha) = \frac{e^{-E_\alpha(\vec{p}')\,(t_2 - t_1)}\, e^{-E_\alpha(\vec{p})\, t_1}}{4\, E_\alpha(\vec{p}')\, E_\alpha(\vec{p})}\, \mathcal{Z}^\alpha(\vec{p}')\, \mathcal{Z}^{\alpha\dagger}(\vec{p})\, \mathcal{A}_\sigma{}^\mu{}_\tau(\vec{p}', \vec{p}) \tag{6.12}$$

where we have grouped all covariant indices into a single term

$$\mathcal{A}_\sigma{}^\mu{}_\tau(\vec{p}', \vec{p}) = \left(g_{\sigma\delta} - \frac{p'_\sigma\, p'_\delta}{m_\alpha^2}\right)\, \Gamma^{\delta\mu\gamma}(p', p)\, \left(g_{\gamma\tau} - \frac{p_\gamma\, p_\tau}{m_\alpha^2}\right)\,.$$

We note that the placement of indices is for clarity and does not denote the covariance and contravariance of the associated quantity. Substituting our

expressions for the two- and three-point correlators into Eq. (4.16) and making use of the symmetry property $\mathcal{A}_\sigma{}^\mu{}_\tau(\vec{p}',\vec{p}) = \mathcal{A}_\tau{}^\mu{}_\sigma(\vec{p},\vec{p}')$ we obtain

$$R_\sigma{}^\mu{}_\tau(\vec{p}',\vec{p};\alpha) = \frac{1}{2\sqrt{E_\alpha(\vec{p}')\,E_\alpha(\vec{p})}} \left(\frac{p'_\sigma\,p'_\sigma}{m_\alpha^2} - g_{\sigma\sigma}\right)^{-1/2} \left(\frac{p_\tau\,p_\tau}{m_\alpha^2} - g_{\tau\tau}\right)^{-1/2} \mathcal{A}_\sigma{}^\mu{}_\tau(\vec{p}',\vec{p})\,.$$

Given our choice of kinematics, one can show that the Sachs form factors can be accessed through the following terms

$$\begin{aligned}
\mathcal{A}_1{}^0{}_1(\vec{p}_x,0) &= \frac{E}{m}\left((E+m)\,G_C(Q^2) + \frac{2}{3}\frac{p_x^2}{m}\,G_Q(Q^2)\right)\,,\\
\mathcal{A}_2{}^0{}_2(\vec{p}_x,0) = \mathcal{A}_3{}^0{}_3(\vec{p}_x,0) &= \left((E+m)\,G_C(Q^2) - \frac{1}{3}\frac{p_x^2}{m}\,G_Q(Q^2)\right)\,,\\
\mathcal{A}_1{}^3{}_3(\vec{p}_x,0) &= -\frac{E}{m}\,p_x\,G_M(Q^2)\,,\\
\mathcal{A}_3{}^3{}_1(\vec{p}_x,0) &= +p_x\,G_M(Q^2)\,.
\end{aligned}$$

As such, we isolate the form factors through the following combination of ratio terms

$$G_C^\alpha(Q^2) = \frac{2}{3}\frac{\sqrt{E_\alpha\,m_\alpha}}{E_\alpha+m_\alpha}\left(R_1{}^0{}_1(\vec{p}_x,0;\alpha) + R_2{}^0{}_2(\vec{p}_x,0;\alpha) + R_3{}^0{}_3(\vec{p}_x,0;\alpha)\right)\,, \tag{6.13}$$

$$G_M^\alpha(Q^2) = \frac{\sqrt{E_\alpha\,m_\alpha}}{p_x}\left(R_3{}^3{}_1(\vec{p}_x,0;\alpha) - R_1{}^3{}_3(\vec{p}_x,0;\alpha)\right)\,, \tag{6.14}$$

$$G_Q^\alpha(Q^2) = \frac{m_\alpha\sqrt{E_\alpha\,m_\alpha}}{p_x^2}\left(2R_1{}^0{}_1(\vec{p}_x,0;\alpha) - R_2{}^0{}_2(\vec{p}_x,0;\alpha) - R_3{}^0{}_3(\vec{p}_x,0;\alpha)\right)\,. \tag{6.15}$$

6.1.1 Extracting Static Quantities

The Sachs form factors G_C, G_M and G_Q describe the distribution of charge, magnetism and charge asymmetry within the hadron. In particular, the value of these functions at $Q^2 = 0$ define the hadron's total charge, q, magnetic moment, μ, and quadrupole moment, Q,

$$q = e\,G_C(0)\,, \tag{6.16a}$$

$$\mu = \frac{e}{2m}\,G_M(0)\,, \tag{6.16b}$$

$$Q = \frac{e}{m^2}\,G_Q(0)\,, \tag{6.16c}$$

where m is the mass of the hadron. For many quantities, such as the magnetic form factor, it is not possible to access $Q^2 = 0$ directly and so in order to obtain values for these moments, one must perform an extrapolation in Q^2. Use of fixed-current SST-propagators allows us to explore the form factors of many different hadrons using the same set of propagators. However we are limited to a single

value of 3-momentum transfer and consequently a single Q^2 for each quark mass. Motivated by the observed scaling behaviour for G_E and G_M of the proton at low Q^2 [101, 102], we shall assume the meson sector displays similar scaling within each quark sector and thus use this to extract a value for magnetic and quadrupole moments

$$G_i(Q^2 = 0) = \frac{G_i(Q^2)}{G_C(Q^2)}\,, \tag{6.17}$$

so as to facilitate a comparison with the experimental prediction of [92] and model expectations.

For the mean squared charge radius, we use the standard definition from the small Q^2 expansion of the Fourier transform of the charge distribution

$$\langle r^2 \rangle = -6\frac{d}{dQ^2}\, G_C(Q^2)\big|_{Q^2=0}\,. \tag{6.18}$$

Using a monopole ansatz

$$G_C(Q^2) = \left(\frac{\Lambda^2}{\Lambda^2 + Q^2}\right) G_C(Q^2 = 0)\,, \tag{6.19}$$

as suggested by the Vector Meson Dominance hypothesis, we have

$$\langle r^2 \rangle = \frac{6}{Q^2}\left(\frac{1}{G_C(Q^2)} - 1\right)\,. \tag{6.20}$$

6.2 Calculation Details

Here we shall consider all the available masses that comprise the PACS-CS configurations [24]. As was mentioned in Section 5.1, there are five values for the light quark masses with the resulting pion masses ranging from 702 MeV down to 156 MeV. The hopping parameters κ_{ud}, pion masses and the number of configurations for each quark mass are listed in Table. 6.1. Due to the limited number of available configurations for the lightest masses, we make use of multiple sources on each configuration. For the lightest mass, this is achieved by using two maximally separated spatial sources with relative temporal boundary shift of 8 time slices. The temporal boundary is then shifted by multiples of 16 times slices for each spatial source. This results in a total of 8 sources per configuration for this mass. For the second and third lightest masses we make use of a single spatial source and perform a single shift of 32 time slices resulting in a total of 2 sources per configuration.

The fermion source is inserted at $t_0 = 16$ relative to a fixed boundary condition at $t = 0$ and the current at $t_1 = 21$. Here we use an $\mathcal{O}(a)$-improved conserved vector current as described in Section 3.4.2. For the current 3-momentum, $\vec{q}$,

Table 6.1: Summary of the configuration details.

$\kappa_{\rm ud}$	m_π (MeV)	$N_{\rm cfg}$	$N_{\rm src}$
0.13700	702	350	350
0.13727	570	350	350
0.13754	411	350	700
0.13770	296	350	700
0.13781	156	197	~ 1600

we use the smallest non-zero momentum available, $|\vec{q}| = \frac{2\pi}{L}$ oriented in the x-direction. The current is polarized with $\mu = 3, 4$ as required by Eqs. (6.5) and (6.13)–(6.15). As was highlighted in Section 4.3, our choice of correlation function ratio requires the evaluation of both $+\vec{q}$ and $-\vec{q}$, however both are required if one wishes to use U^*-trick as we will here.

As the primary goal of this work is to cleanly extract matrix elements of the ground state, we use a small variational basis. For our interpolators, we use with the following spin-flavour structures

$$\chi_\pi(x) = \overline{d}(x)\gamma_5 u(x)\,,$$
$$\chi_\rho(x) = \overline{d}(x)\gamma_i u(x)\,,$$

for the π^+ and ρ^+ meson respectively. Our basis is composed of smeared operators formed using these interpolating structures with the four smearing widths outlined in Table. 5.1. This allows for the construction of up to a 4×4 correlation matrix. The use of the alternate bilinear forms $\gamma_0\gamma_5$ and $\gamma_0\gamma_i$ was considered, however these were found to not provide any additional basis span when used with more than two smearing levels. We considered all combinations of variational parameters t_0 and δt in range 17-20 and 1-4 respectively where a superposition of states can be used to constrain the analysis. With regard to state isolation and the stability of the analysis, the optimal choice was found to be $t_0 = 17$ and $\delta t = 3$ for the three heavier masses and $t_0 = 17$ and $\delta t = 2$ for the two remaining lighter masses. The use of an earlier t_0 value relative to baryon studies [87, 103, 104] on the same ensembles is to be expected given the larger energy gaps displayed between the ground state and first excitation in the meson sector. Eigenvectors are tracked across quark mass and momentum using the methods outlined in Section 4.4.2. Of particular importance is the need to maintain consistent orientation between bases of different momenta. In forming an orthonormal basis, one has the freedom to choose the orientation of vectors. In constructing the eigenstate projected three-point correlation, if bases are not aligned consistently, it is possible to introduce a relative sign into the correlator and consequently lead to erroneous results.

6.3 Results

6.3.1 Light Isovector Meson Spectrum

We begin the discussion of results with an examination of the spectra obtained in our variational analysis. In Figs. 6.1 and 6.2 we display the resulting spectrum below 3 GeV in the isovector 0^{-+} and 1^{--} channels, obtained from our 4×4 correlation matrix. Within these figures we also include the experimentally observed states in the respective channels. These states were taken from the summary tables prepared by the Particle Data Group (PDG) [105].

Within the pion channel we find three well separated eigenstates, consistent with the spectrum obtained in previous studies which examined the entire isovector meson sector [50, 106, 107]. At the lightest mass we find that our states are or are very nearly consistent with the those of the physical spectrum. In particular, our first excitation is consistent with the $\pi(1300)$. Reading the spectrum from right to left, we see a significant increase in the mass for the first excitation at the second lightest quark mass and a similar increase for the second excited state at the middle mass. This feature is observed across the range of variational parameters considered and corresponding 3×3 analyses formed from subsets of the variational basis. A similar feature is observed in the positive parity spectrum of the nucleon [64, 87] using the same ensembles. Examination of the wave functions for these nucleon excitations [63] show significant finite volume effects for the lightest two masses which consequently may lead to an increase in the eigenstate energy. It is certainly possible that we are observing a similar effect here.

In the ρ meson channel, we again observe three well separated eigenstates. However, in this channel we expect to see two eigenstates near 1600 MeV separated by about 250 MeV. As the mass gap between our first and second excitation is of the order of 1 GeV, our results strongly suggest that a basis of local operators is not able to isolate both of these eigenstates. A similar conclusion was found in Ref. [106]. In a subsequent study by this group [107], they found that isolation of the $\rho(1450)$ required a basis that contained displaced, derivative operators. Within the constituent quark model, these two states are identified as an S-wave dominant state and a D-wave dominant state [105]. Given the radial symmetry of our operators, it is not possible to form D-wave orbital structures and so it is not surprising that we are unable to isolate both eigenstates. Interestingly, the close agreement of our first excited state with the physical $\rho(1700)$ energy and the absence of the $\rho(1450)$ from our spectrum suggests that the $\rho(1700)$ is the S-wave state while the $\rho(1450)$ is the D-wave state. Within [61], Dudek *et al.* were able to successfully isolate both of these states. Their pion masses range from 702–396 MeV, which are comparable with our three heaviest masses. Through considerations of the operator overlaps, they show the S-wave dominated state to be the lighter of the two states for their heavier quark masses. However it appears that with decreasing quark mass the

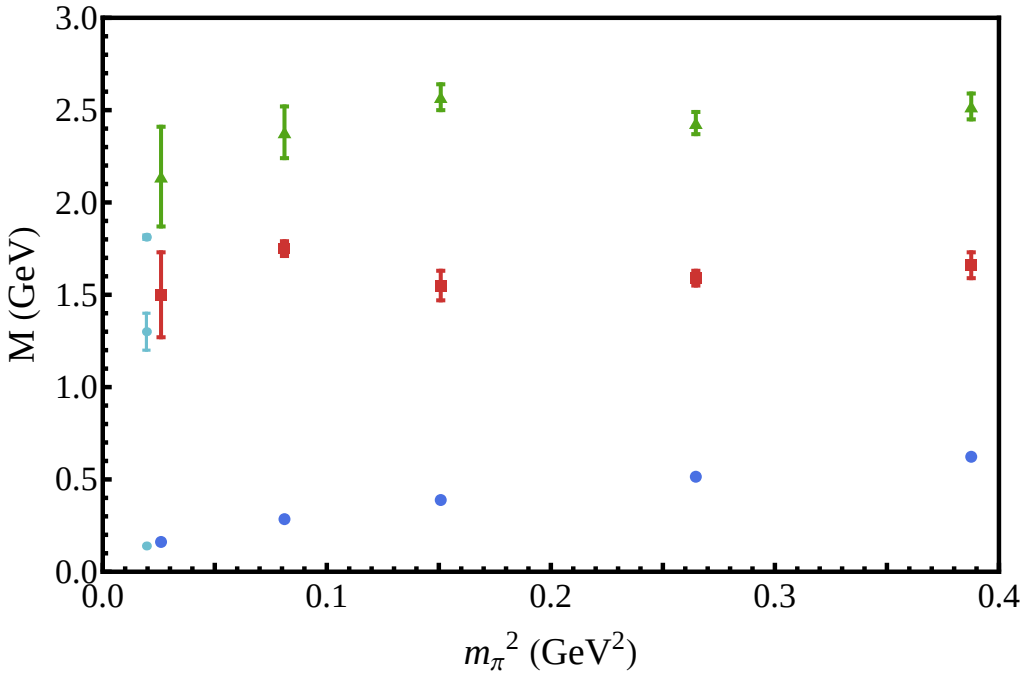

Figure 6.1: Spectrum observed in the isovector, pseudoscalar (0^{-+}) channel. The light blue data points at the far left are the experimentally observed states, taken from the PDG summary tables [105].

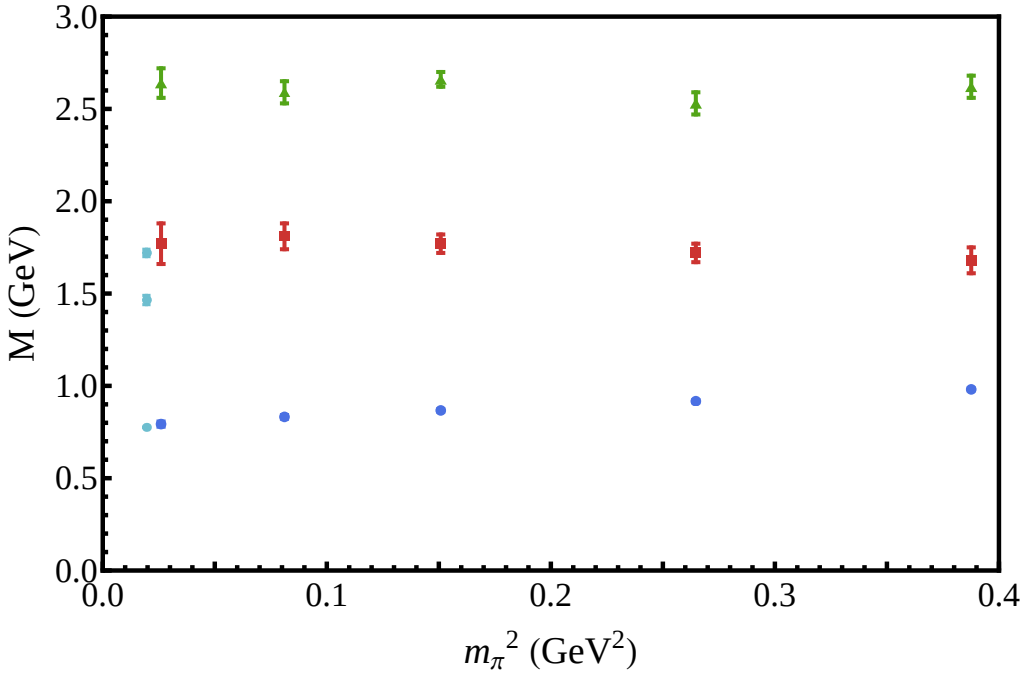

Figure 6.2: Spectrum observed in the isovector, vector meson (1^{--}) channel. The light blue data points at the far left are the experimentally observed states, taken from the PDG summary tables [105].

mass splitting between these two states became smaller, with the states nearly degenerate at their lightest mass of $m_\pi = 396$ MeV. A continuation of this trend to lighter quark masses would place the D-wave dominated state lower in mass. While this is an interesting possibility, we note that the eigenstates energies can depend heavily on the volume through the relative evolution of the allowed multi-particle dressings. Consequently if this ordering were to exist on the finite volume, there is no guarantee that it will remain in the infinite volume limit.

An important feature in the QCD spectrum is the possibility of multi-particle intermediate states. In the infinite-volume limit this renders the majority of hadrons unstable under the strong interaction. However on the finite-volume lattice, the QCD eigenstates are stable and are composed of admixtures of both single-particle and multi-particle states. Some insight into the composition of states can be taken from the physical spectrum and scattering thresholds. However, the position of these thresholds change on the finite volume. Multi-particle states are forced to overlap in the finite volume, giving rise to a volume-dependent interaction energy. Mixing with single-particle dominated states further distorts the spectrum to the point where intuition from infinite-volume scattering thresholds and the physical spectrum becomes irrelevant, particularly in volumes with lattice length $L \sim 3$ fm.

Below the finite-volume modified two-particle scattering threshold, states are generally single-particle dominated but still contain important contributions from nearby scattering channels. The position of states in the spectrum can be changed by varying the quark mass or the volume of the lattice and the eigenstates can become maximally mixed making their traditional identification as scattering states or resonant states impossible. In the case where a low-lying finite-volume scattering threshold sits well below the resonant state, then the lowest-lying state may be regarded as a two- or multi-particle scattering state and the single-particle dominated state is now the higher eigenstate.

In the case of the states under study here, particularly the ground state ρ meson, we must be careful to ensure that the state we are exciting on the lattice is in fact the single-particle dominated resonant state. Though there is strong evidence to suggest that local meson operators couple poorly to scattering states [49, 50], especially on larger volumes such as that under investigation here, we perform a check to determine whether the eigenstate isolated in our correlation-matrix analysis is single particle in nature. For all our ensembles, the ground state ρ meson at rest is well below the $\pi\pi$ threshold, and will be single-particle dominated. However, upon applying the boost to momentum $\vec{q}$, the extracted energy eigenstate on the three lightest ensembles now sits above the lowest-lying bare $\pi\pi$ energy allowed by momentum conservation. In order to determine whether the state we have isolated in the boosted case is the finite-volume ρ meson or the lower-lying $\pi\pi$ scattering state, we compare the extracted eigenstate energy against the expected energy given by the dispersion relation for a single particle.

In Figs. 6.3 and 6.4 we show the π and ρ energies extracted from the finite-momentum correlators for a range of momenta, overlaid with the dispersion relation[2] expectation for a single particle

$$E = \sqrt{m^2 + n_p |\vec{q}|^2} \quad \text{where} \quad n_p^2 = n_x^2 + n_y^2 + n_z^2 \,,$$

and m is the energy extracted with $n_p = 0$. Here we can see that the energies extracted from the boosted correlator are in excellent agreement with dispersion for small boosts, particularly for $n_p = 1$ required for our form factor analysis. For the larger momenta considered there does appear to be a slight discrepancy between the dispersion expectation and extracted energy, especially for those masses near or above threshold, however as we only use a small subset of the available momentum orientations this deviation may be due to a lack of statistics. To make a firm statement, one should average over all possibly allowed momentum orientations for a given n_p. As we are only really interested in the $n_p = 1$ case we shall not do so here.

As a further check for the ρ meson, we compare our extracted energies with the non-interacting $\pi\pi$ energies allowed by momentum and parity conservation, represented in Fig. 6.4 by the red diamonds. For the single unit of lattice momentum relevant to our form factor analysis, we find that the mass separation between the dispersion result and the non-interacting $\pi\pi$ energy is significant for all but the middle mass. Moreover, the attractive finite-volume interaction in the $\pi\pi$ system would act to further increase the separation between the single and multi-particle dominated states. As a matter of principle, we do expect a $\pi\pi$ scattering state to reveal itself in the long Euclidean-time tail of our correlation function. However, our interpolating fields have rendered this contribution to be negligible at the finite-Euclidean times considered. This indicates that our correlation functions are indeed dominated by the resonant-like state of interest and not the lower-lying finite volume scattering state. Through this process we have determined that the state we have isolated in the boosted system is in fact the state most closely related to the resonant ρ meson.

Similar considerations are given to our excited states. As these states have much larger masses, the correlator decreases more rapidly leading to earlier loss of signal. As such, any weakly coupled states can dominate the correlator at large Euclidean times [52]. Care must therefore be taken to ensure that we are probing the single particle excitation within the required Euclidean time window. To do so we consider the behaviour of our projected two-point correlator by considering where $\log(G)$ displays linear behaviour. In Fig. 6.5, we demonstrate this for the projected correlator of the π^* meson. Guided by the χ^2_{dof} we identify linear behaviour between times $t = 19 - 26$, highlighted by solid line indicating the fit. Extending this dashed line to both earlier and later times show that outside of this

[2]For the momentum we are considering in this calculation, $\sin(ap_\mu) \simeq ap_\mu$ and so the continuum dispersion relation is sufficient.

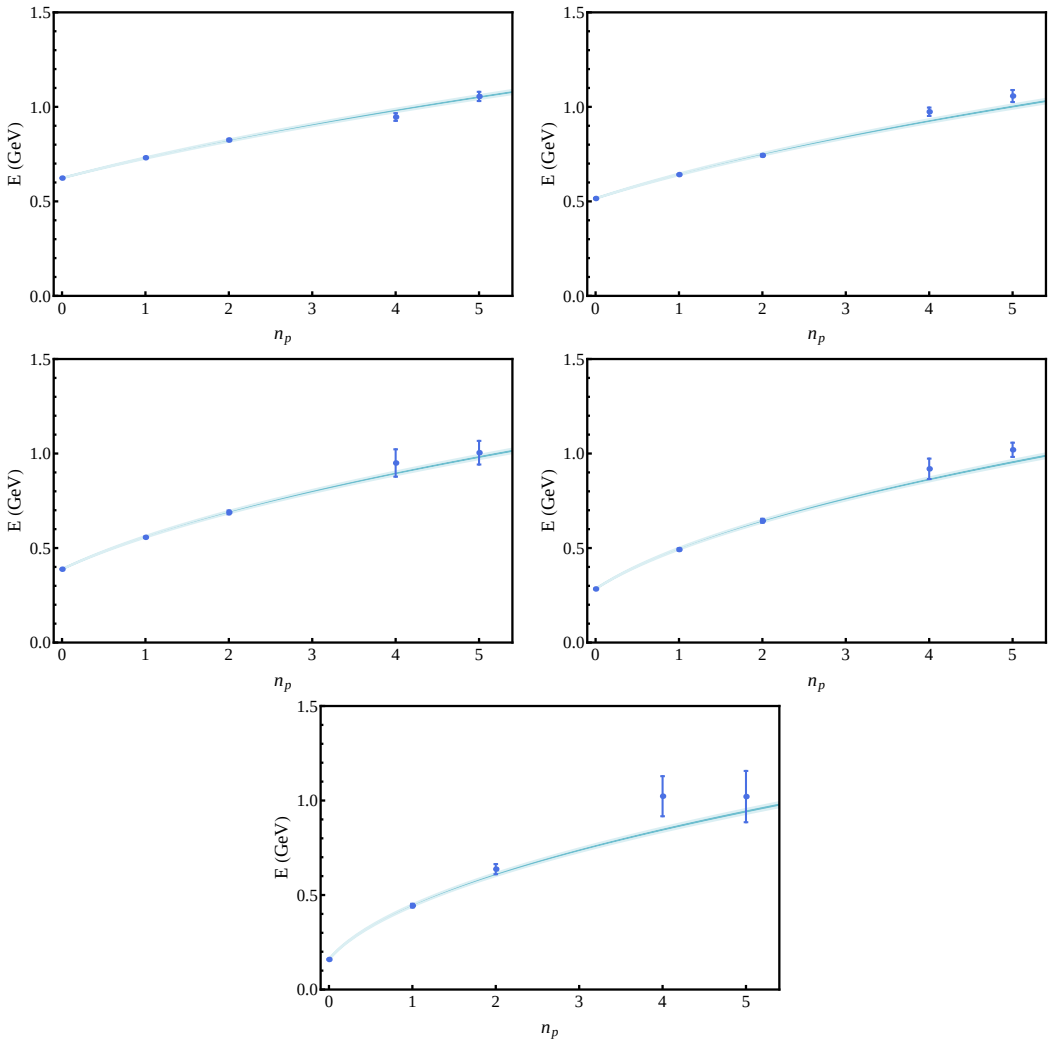

Figure 6.3: Extracted eigenstate energies for the ground state π meson against the single particle dispersion expectation. The bottom axis is the centre-of-mass momentum in units of the minimum available momentum $\frac{2\pi}{L}$. The direction of decreasing quark mass is from left to right and down the page.

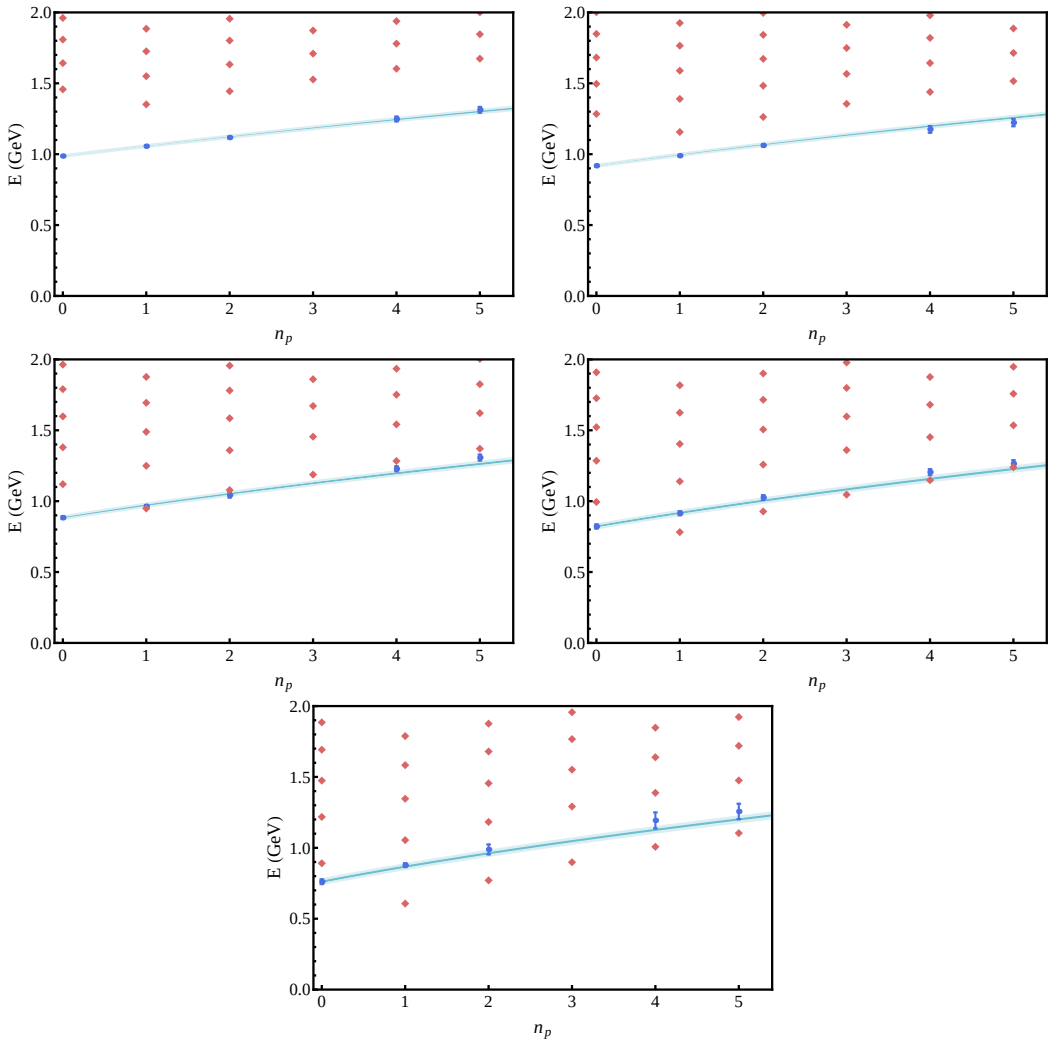

Figure 6.4: Comparison between the dispersion relation (blue line), and the energies extracted from the finite-momentum projected correlators (●) for the ρ meson over a range of momenta. The red diamonds (◆) are the corresponding non-interacting $\pi\pi$-energies allowed by momentum conservation. The bottom axis is the centre-of-mass momentum in units of the minimum available momentum $\frac{2\pi}{L}$. The direction of decreasing quark mass is from left to right and down the page.

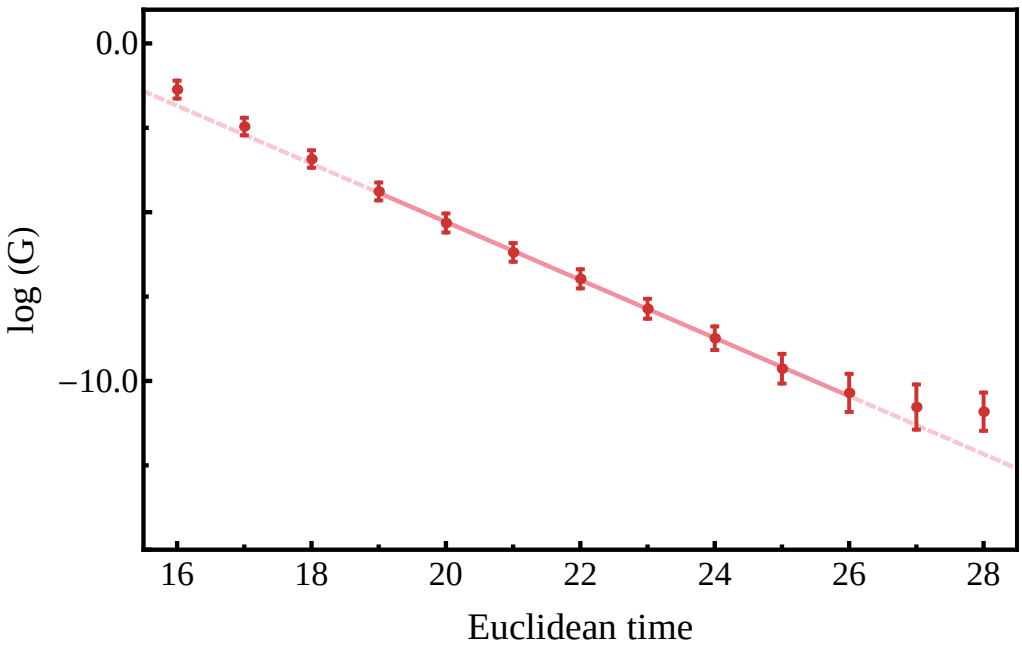

Figure 6.5: $\log(G)$ for the projected correlator of the π^* meson at m_π = 702 MeV. The solid line is the best fit highlighting the linear behaviour of the correlator indicating single state isolation. In order to examine the form factors for the excited states, we require single state isolation prior to the current at $t_1 = 21$.

window, the correlator is no longer consistent with the single particle hypothesis and so such times should not be considered in the analysis of the form factor ratios. We examine both the correlators for the state at rest and boosted to $\vec{q}$, taking the earliest time for which single state dominance is no longer observed as the limit for allowable fit windows of the form factor ratio. We further note the single state must necessarily be observed before the insertion of the current to ensure that we are sampling a single state only. For those cases where either single state dominance is observed after $t = 21$, or loss of single eigenstate dominance occurs before $t = 22$, we do not examine the form factor as we are not probing the state in question. We also compare the masses extracted from the correlator fits to the dispersion relation. These are shown in Figs. 6.6 and 6.7 for the π^* and ρ^* respectively. Here we find that for both states, all energies extracted for $n_p = 1$ are consistent within errors with dispersion expectation.

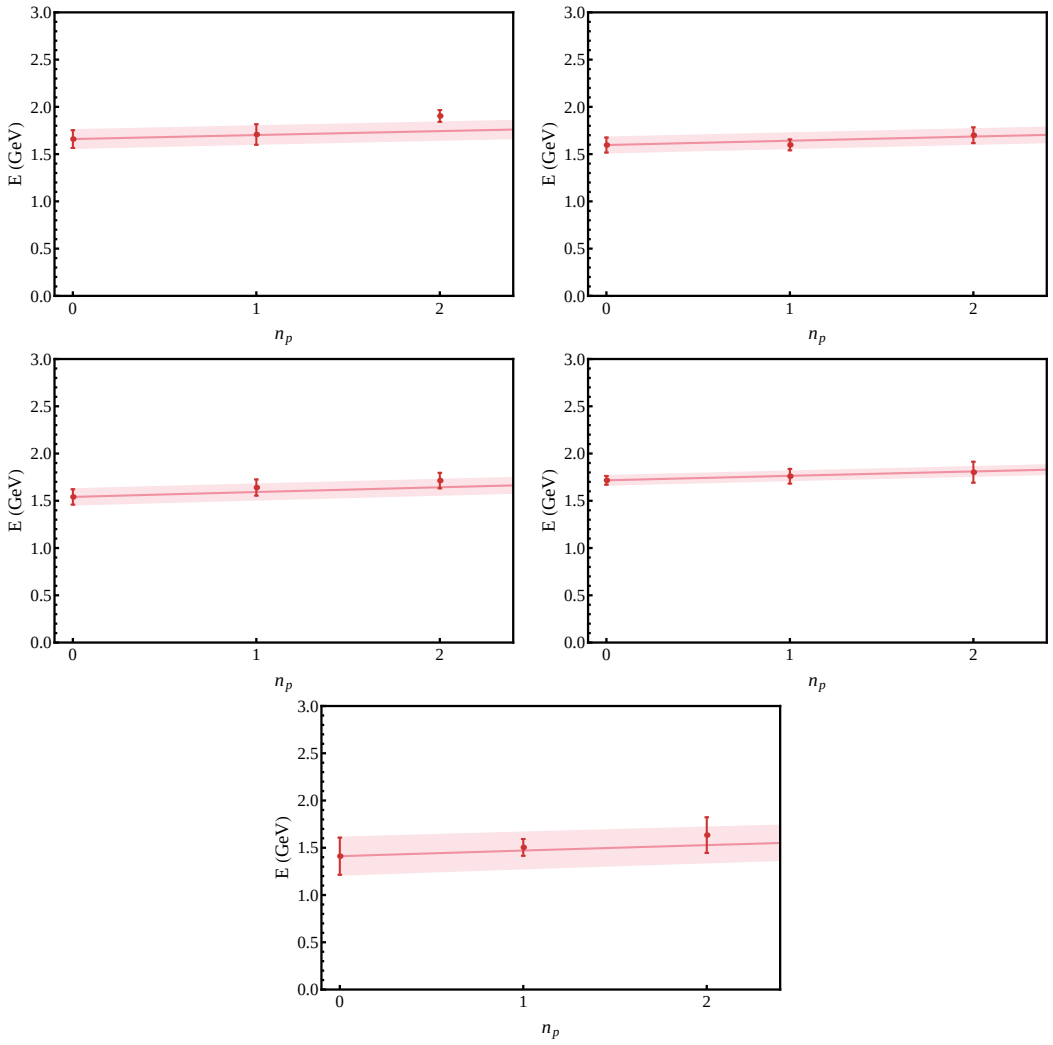

Figure 6.6: Extracted eigenstate energies for the first π^* meson against the single particle dispersion expectation. The bottom axis is the centre-of-mass momentum in units of the minimum available momentum $\frac{2\pi}{L}$. The direction of decreasing quark mass is from left to right and down the page.

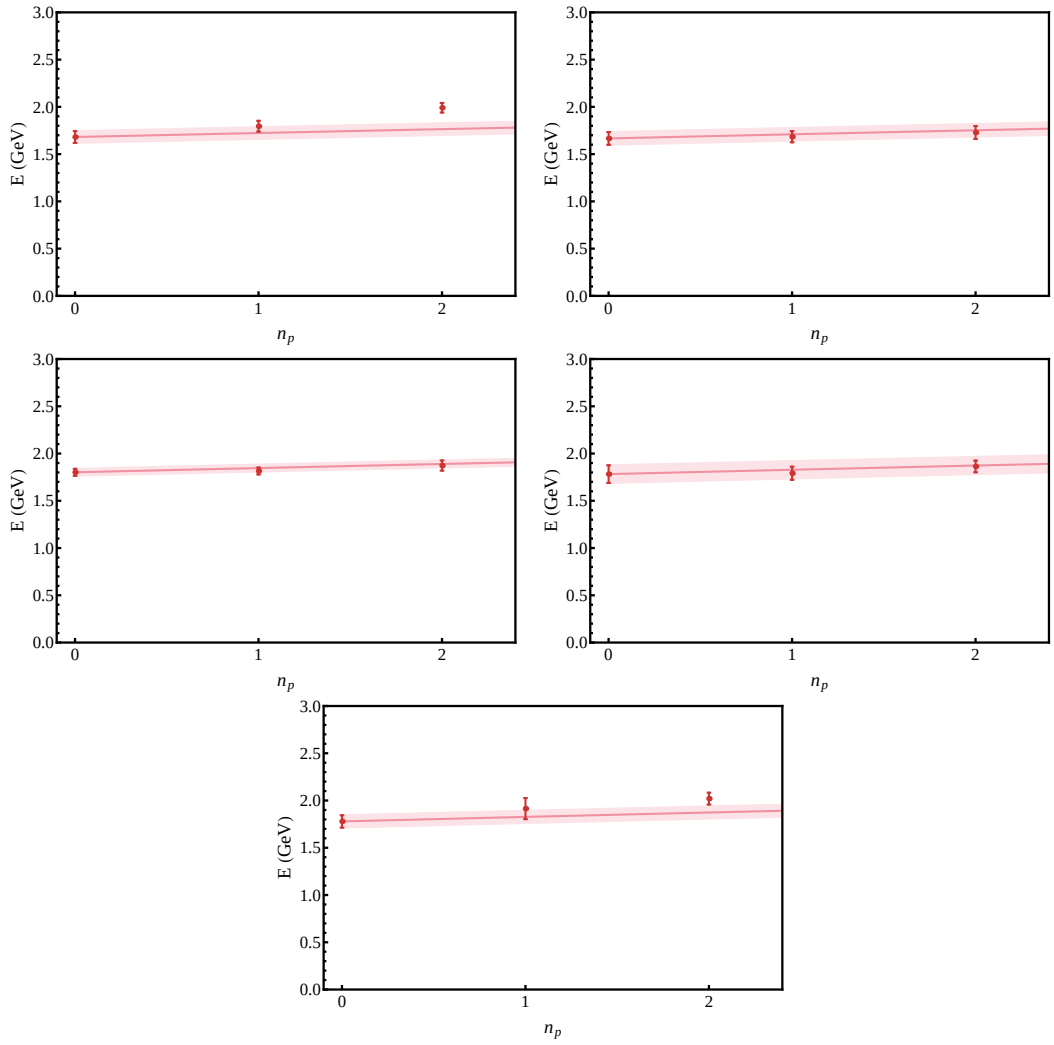

Figure 6.7: Extracted eigenstate energies for the first ρ^* meson against the single particle dispersion expectation. The bottom axis is the centre-of-mass momentum in units of the minimum available momentum $\frac{2\pi}{L}$. The direction of decreasing quark mass is from left to right and down the page.

6.3.2 Improved Excited State Systematics

As we saw in the previous chapter, use of the optimised operators obtained via the correlation matrix analysis gave rise to significant improvement in the quality and duration of the plateaus from which the matrix elements are extracted. Before we examine the form factors, we shall first consider whether similar improvement is observed here. In Fig. 6.8 we compare the ratio for the charge, magnetic and quadrupole form factor of the ground state ρ extracted using the variational method and using standard single correlator techniques utilising a modest level of smearing at the source and sink.

The improvement observed in the magnetic form factor (Fig. 6.8(b)) is by far the most striking. Here there is a clear difference in the quality of the plateau. For the correlation matrix, single-state dominance follows immediately after the current at $t_1 = 21$ allowing for fits as early as $t_2 = 22$. For the standard approach, the excited states act to suppress the value of G_M at earlier times forcing one to wait until at least $t_2 = 24$ before an adequate χ^2_{dof} is obtained. However for the standard method, the central values show a systematic upward trend following this time slice and consequently the is no clear indication that a plateau has been obtained. Similar conclusions can be drawn for the quadrupole form factor in (Fig. 6.8(c)). Here we find that both the correlation matrix and the standard approach give consistent values immediately following the current, but diverge as we move out to later time-slices. Again there is a clear systematic drift in the results obtained using the standard approach and it would be difficult to select a fit region where the form factor can be determined with confidence. Given that we seek a region where the extracted form factor is constant over successive time slices, both cases demonstrate improvement through use of the variational method. In the case of the charge form factor (Fig. 6.8(a)) the two methods are in closer agreement and display a similar quality in plateau. In either case, some Euclidean time evolution is required before a plateau is observed, but we find that the correlation matrix approach gives a systematically lower value following the current and plateaus a couple of time-slices earlier than the standard approach. Similar results are observed for the charge form factor of the ground state pion.

Though the examples presented here have been selected to highlight the improvement using the variational method, we see significant improvement across all masses and form factors considered. It is clear that through this method we are able to:

(1) Isolate an eigenstate at earlier Euclidean times,

(2) Insert the conserved vector current at earlier Euclidean times,

(3) Fit the correlation function at earlier Euclidean times,

(4) Observe robust plateau behaviour,

(5) Identify large Euclidean-time fit windows,

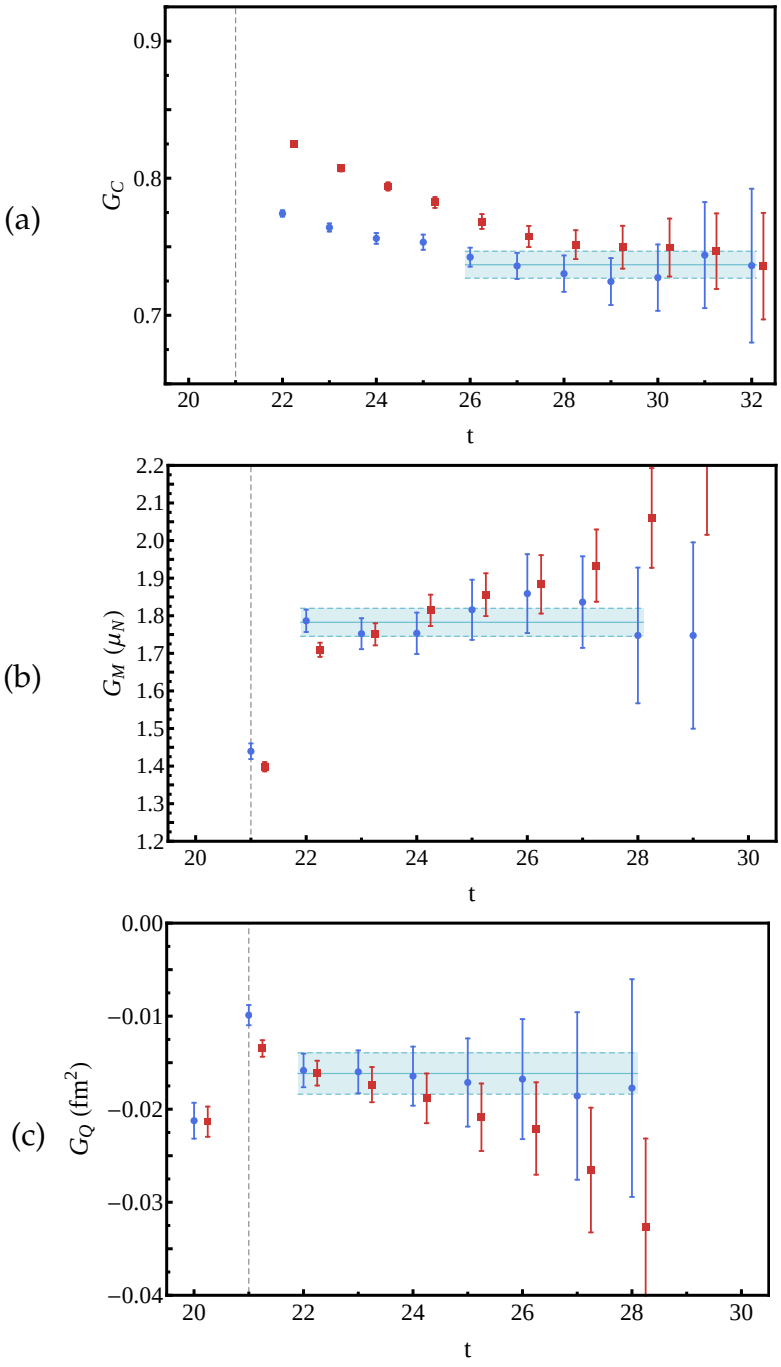

Figure 6.8: Comparison of the ρ meson form factors as a function of Euclidean sink time using the correlation matrix method (●) and the standard single correlator methods with smeared source and sink (■). For each figure we have selected the quark mass that best demonstrates the improvement offered in each channel. The upper figure is the charge form factor G_C for $m_\pi = 296$ MeV, the centre figure is the magnetic form factor G_M for $m_\pi = 156$ MeV and finally the lower figure is the quadrupole form factor G_Q for $m_\pi = 296$ MeV. The vertical dashed line indicates the position of the current insertion. The fitted value from the variational approach has been included (shaded band) to highlight where the single source approach is consistent with our improved method.

(6) Determine the form factors with significantly reduced systematic errors, and

(7) Determine the form factors with significantly reduced statistical uncertainties due to the admission of analysis at earlier Euclidean times.

6.3.3 Form Factor Results

In extracting form factors across a wide range of quark masses, it is important to note that for each mass there will be a slight change in the value of Q^2 due to the variation in the temporal component of the current four-momentum, q_0, stemming from the change in the hadron's mass. To ensure that the comparison between quark masses and furthermore eigenstates, is meaningful, we make use of the monopole ansatz to shift the extracted values for our form factors to a common Q^2. For the pion system, we shift Q^2 values to a common value of $Q^2 = 0.10$ GeV^2, while for the ρ meson system we select $Q^2 = 0.16$ GeV^2. These values are selected to minimise the shift for the form factor extractions at the lightest quark mass. We use different values to ensure that we minimise the shift for each system and given that the pion is significantly lighter than the ρ meson, a smaller value for Q^2 arises naturally. Fig. 6.9 demonstrates this shift for the pion.

Before we examine our form factor results, we note that all quantities presented are the quark sector contributions for unit-charge quarks. Here we choose to label these as the quark sector contributions to the positive-charge eigenstate of the corresponding isotriplet. That is, the quark contribution is labelled as the u-quark sector while the anti-quark contribution is labelled as the d-quark sector. Working with exact isospin symmetry, these quark sector contributions are equivalent and so we need only present the u-quark sector. In the case of meson elastic electromagnetic form factors, the invariance of the QCD action under charge conjugation forces disconnected contributions to be zero [45, 108]. This is because the "C-even" two-point function and the "C-odd" disconnected loop term give rise to a relative sign between the $\{U\}$ and $\{U^*\}$ configurations and so cancel exactly [45] in the ensemble average. Consequently in taking the charge weighted sum to give the meson form factor one finds that it is equivalent to the quark contribution

$$\begin{aligned}\langle 1_+ \rangle &= \frac{2}{3}\langle u \rangle + \frac{1}{3}\langle d \rangle \\ &= \langle u \rangle ,\end{aligned}$$

where $\langle 1_+ \rangle$ labels the positive member of the π and ρ meson isotriplets.

The Euclidean time-series data for all of our form factors, and the subsequent fits can be found in Appendix B. Here we shall simply present our extracted results.

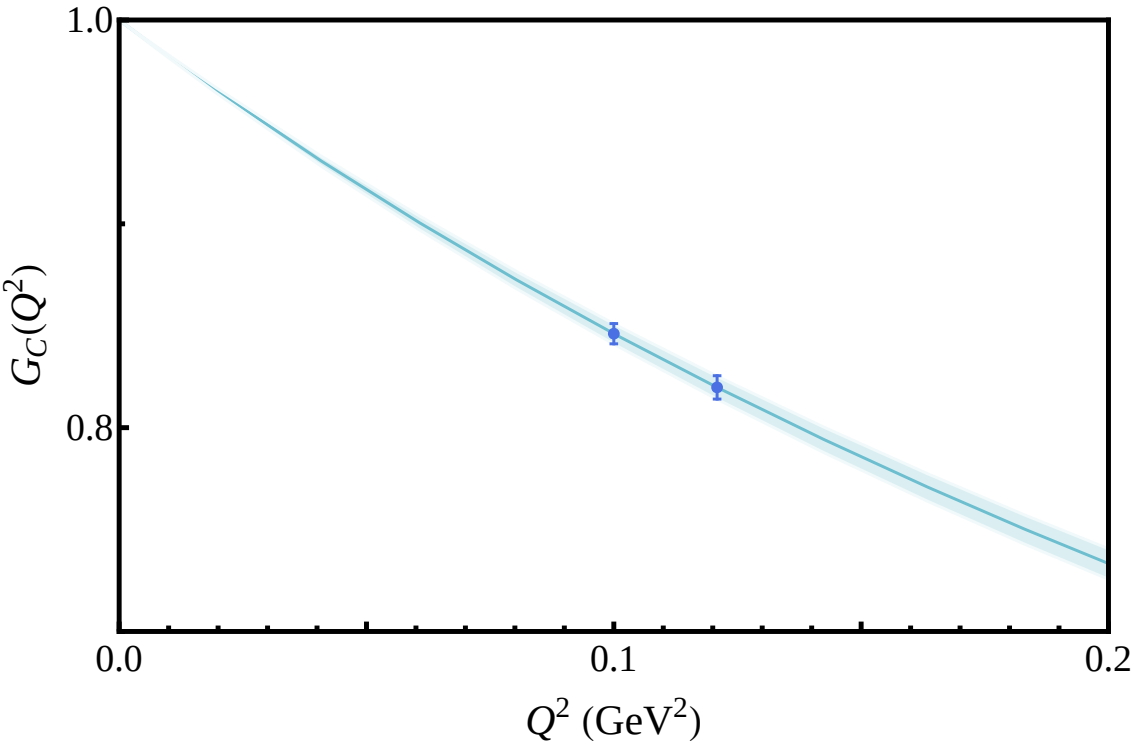

Figure 6.9: An example of the shift applied to the pion form factor to ensure that all eigenstates across all quark masses are at a common Q^2. For the pion and its excitation, this shift is to $Q^2 = 0.10$ GeV^2, while for the ρ meson and its excitation we shift to $Q^2 = 0.16$ GeV^2.

Charge Form Factor

In Figs. 6.10 and 6.11 we display the charge form factor G_C for the π and π^* mesons, and the ρ and ρ^* mesons respectively. In both channels we observe a decrease in the charge form factor for the excitation which translates to the excited states having a larger spatial extent. We note that for the excited pion, single state dominance was not achieved after $t = 21$ for the lightest two masses and so not considered.

To give us insight into the relative size of these states, we consider the mean squared charge radii, shown in Fig. 6.12. As was found in [56], the ground state vector meson is consistently larger than the corresponding pseudoscalar meson. This observation is consistent with constituent quark model expectations where a hyperfine interaction of the form $\frac{\vec{\sigma}_q \cdot \vec{\sigma}_{\bar{q}}}{m_q m_{\bar{q}}}$ acts to repel the quarks when spins are aligned and attract them when spins are anti-aligned. For the heaviest quark masses where well determined values are available for the excited states, it appears that a similar trend may exist between our ρ^* and π^* mesons. As was noted directly from the form factor itself, we see that the excited states are larger in extent through the larger value obtained for $\langle r^2 \rangle$. Again appealing to constituent quark model arguments, one would naively expect that quarks

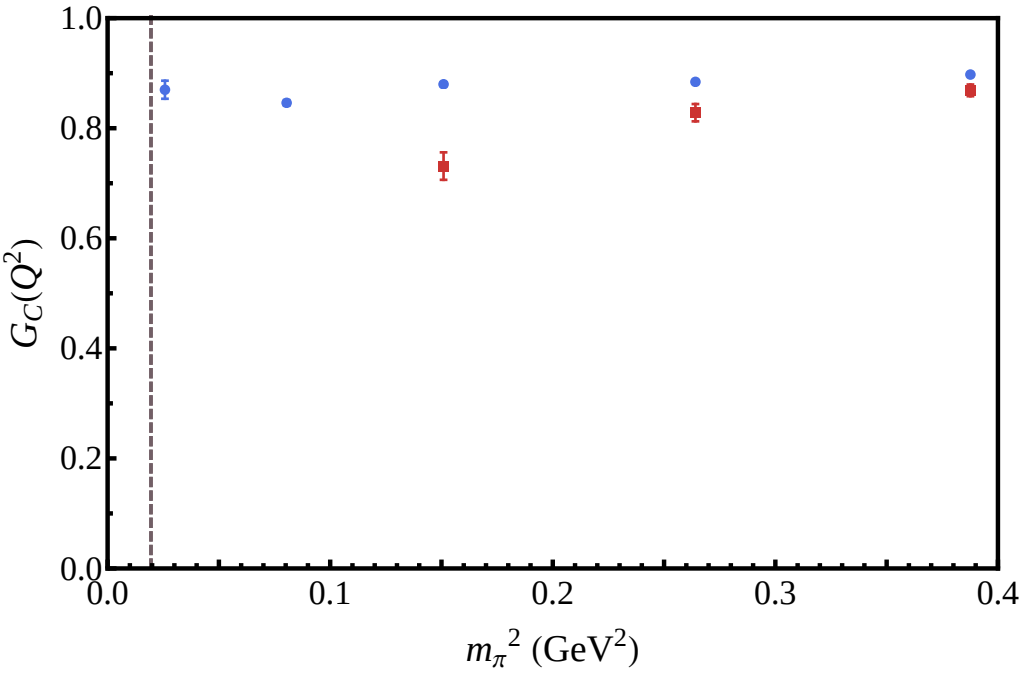

Figure 6.10: The unit-charge quark sector contributions to the charge form factor G_C of the pion (●) and its first excitation (■) at the common value $Q^2 = 0.10\,\text{GeV}^2$. The dashed line represents the physical point.

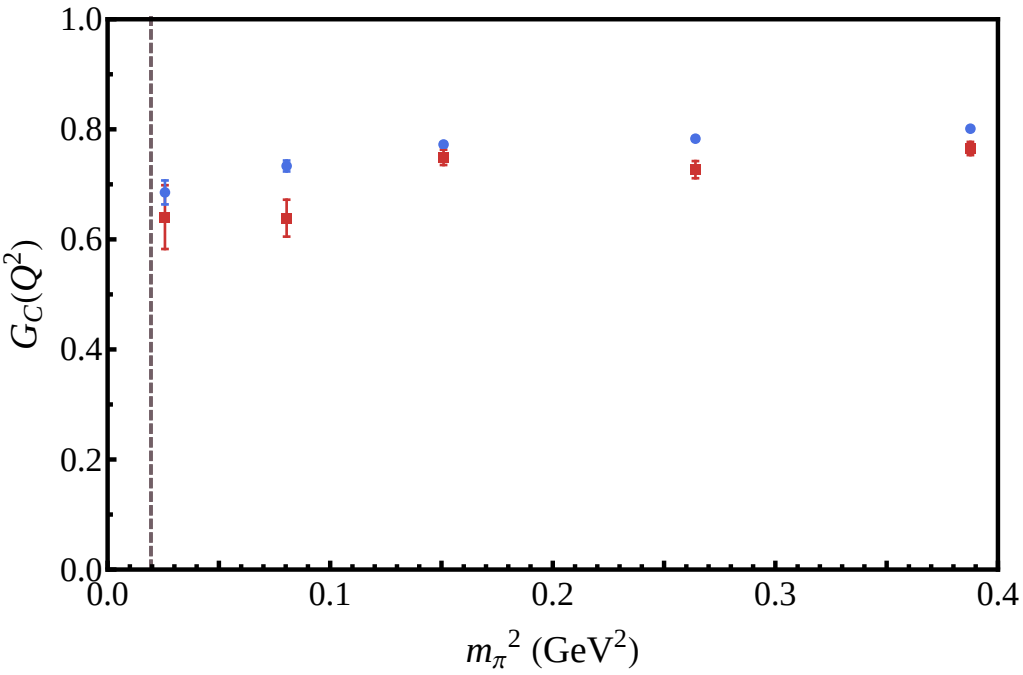

Figure 6.11: The unit-charge quark sector contributions to the charge form factor G_C of the ρ meson (●) and its first excitation (■) at $Q^2 = 0.16\,\text{GeV}^2$. The dashed line represents the physical point.

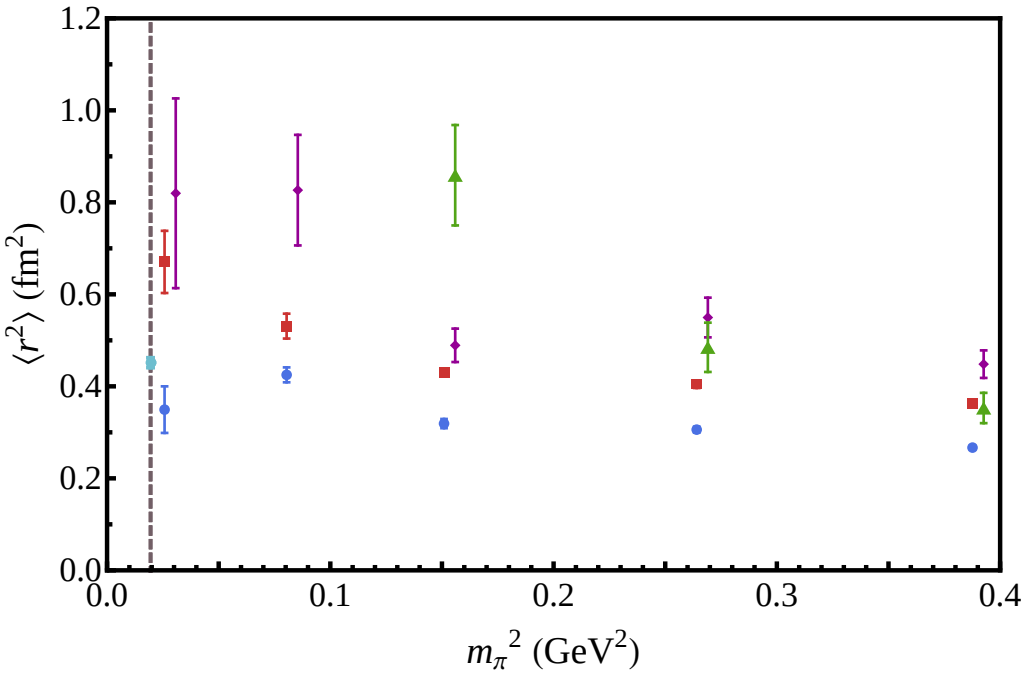

Figure 6.12: Mean squared charge radii, $\langle r^2 \rangle$, for the positive-charge states of the π (●), π^* (▲), ρ (■) and ρ^* (◆) mesons. The grey dashed line represents the physical point, while the light blue data point (●) is the experimental value for the pion obtained from the PDG summary tables [105]. The π^* and ρ^* values have been offset for clarity.

residing in a more energetic state can carry larger energies and therefore sit higher in the confining Coulomb + ramp potential, giving rise to a larger radius. In Fig. 6.12 we also include the experimental value for the pion radius [105], which compares well with our determination.

Magnetic Form Factor

The magnetic form factors for our ρ and ρ^* mesons are illustrated in Fig. 6.13. We note that at the lightest mass, the plateau for the first excitation was of insufficient duration to allow for a fit and so no value is given. For both the ground and excited state we observe very little variation in the value as we vary m_π. Comparing the results between states, we clearly observe a significantly smaller value for the excitation at this value of Q^2. Though we would expect a decrease consistent with the decrease in the charge form factor for this state, the degree of suppression suggests that the magnetic moment for this state is smaller than the ground state. In Fig. 6.14, we show the magnetic moments for these states where we invoke common scaling between the charge and magnetic form factors as discussed in Section 6.1. Here we do find a smaller magnetic moment for the ρ^*. This observation is consistent with the magnetic moments

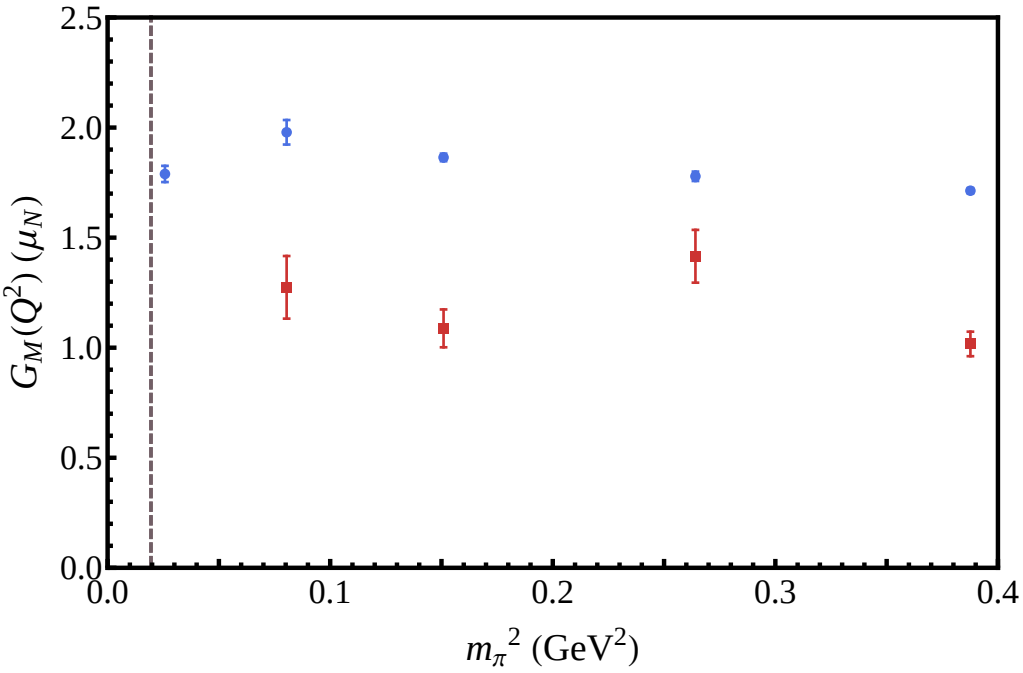

Figure 6.13: The unit-charge quark sector contributions to the magnetic form factor G_M of the ρ meson (●) and its first excitation (■) at $Q^2 = 0.16$ GeV^2. The dashed line represents the physical point.

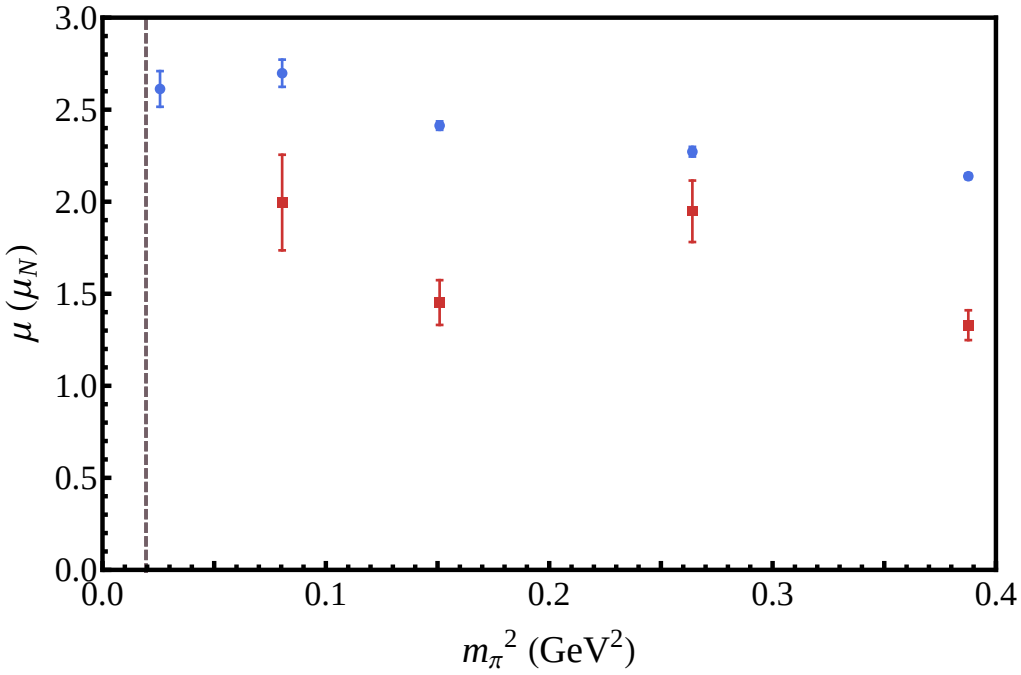

Figure 6.14: The quark-mass dependence of the ρ^+ (●) and ρ^{*+} (■) magnetic moments in units of the nuclear magneton. The dashed line represents the physical point.

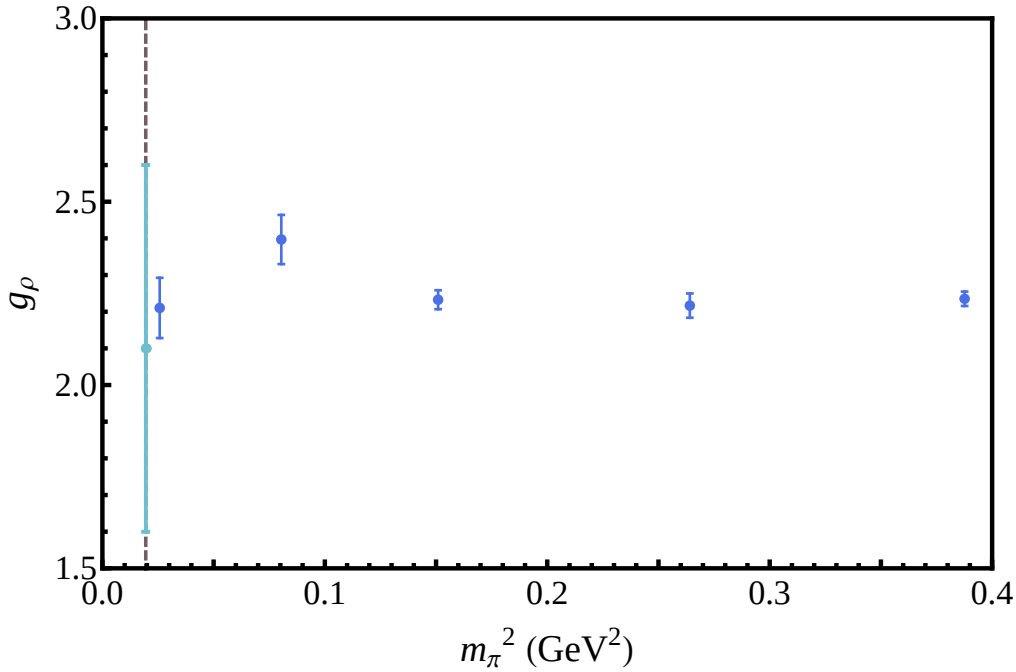

Figure 6.15: The g-factor of the ρ meson (●) is provided by the magnetic moment of the ρ meson in natural magnetons. The dashed line highlights the physical point. The light blue data point (●) is the experimental determination of Ref. [92].

extracted for excitations of the ρ meson obtained using a relativistic Hamiltonian approach [109]. Here they obtain the following values for the $1S$, $2S$ and $1D$ ρ meson systems,

$$\mu_{1S} = 2.37\,\mu_N\,, \quad \mu_{2S} = 1.71\,\mu_N\,, \quad \mu_{1D} = 0.411\,\mu_N\,.$$

Our results compare well with this determination if we identify our ρ^* as the S-wave excitation. In particular, their value for $\frac{\mu_{2S}}{\mu_{1S}} \simeq 0.7$ is consistent with our value of $\frac{\mu_{\rho^*}}{\mu_\rho} = 0.74(9)$, taken for the second lightest mass.

In Fig. 6.15 we show the g-factor for the ρ meson, provided by the magnetic moment of the ρ meson in natural magnetons. Constituent quark model expectations suggest for a pure S-wave state that,

$$\begin{aligned}
\mu_{\rho^+} &= \mu_u + \mu_{\bar{d}} \\
&= q_u\,\mu_u + q_{\bar{d}}\,\mu_d \\
&= \frac{2}{3}\left(\frac{e}{2m_{ud}}\right) + \frac{1}{3}\left(\frac{e}{2m_{ud}}\right) \\
&= \frac{e}{2m_{ud}}\,,
\end{aligned}$$

which taking $m_{ud} \simeq \frac{m_\rho}{2}$ gives,

$$\mu_{\rho^+} \simeq 2\frac{e}{2m_\rho} \quad \Rightarrow \quad g_\rho \simeq 2\,.$$

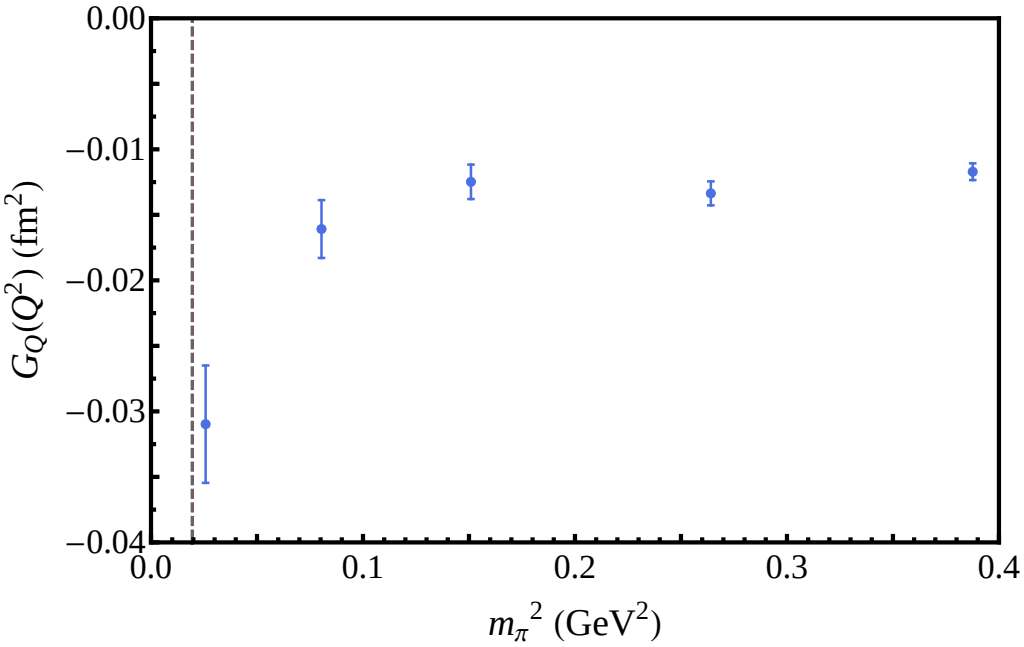

Figure 6.16: The unit-charge quark sector contributions to the quadrupole form factor G_Q of the ρ meson at $Q^2 = 0.16$ GeV^2. The dashed line represents the physical point.

Our result of $g_\rho = 2.21(8)$, taken from our lightest mass point, is larger than this expectation. A departure from $g_\rho = 2$ suggests that the ρ has a non-trivial D-wave component which in turn should give rise to a non-trivial value for the quadrupole moment induced by the asymmetry of the D-wave orbital. We observe a mild downwards trend of the g-factor with increasing quark mass suggesting that our results are compatible with the quark-model expectation of $g_\rho = 2$ in the limit of large quark mass. These results agree in value and behaviour with the previous quenched determination [56] and dynamical study using background field methods [96]. In Fig. 6.15 we include the experimental determination of Ref. [92]. Our result is in good agreement, however with a much smaller uncertainty. Within the literature, the majority of model calculations [110–116] give a value of g_ρ between 2.0 and 2.4, consistent with our determination.

Quadrupole Form Factor

The quadrupole form factor for the ρ meson is shown in Fig. 6.16. For the excited ρ^* meson, the signal was too poor to extract a result. As was found in the quenched study of Ref. [56] and the studies in full QCD [95, 97], the quadrupole form factor is negative for low-moderate Q^2. The value of G_Q varies mildly with m_π in the heavy quark regime, however displays a significant increase in magnitude as we move to the lightest mass.

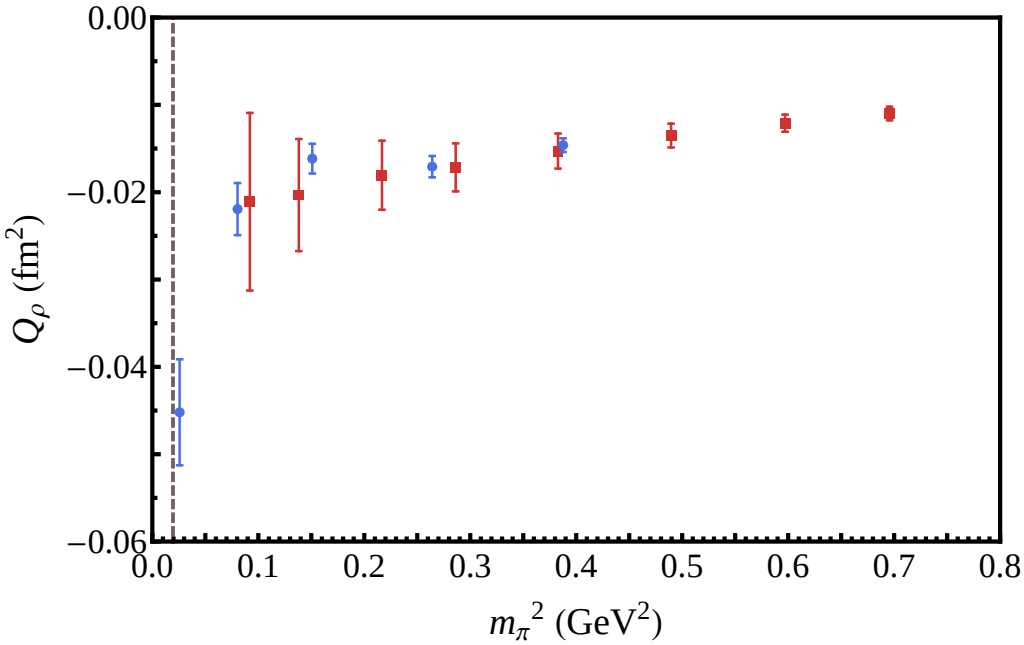

Figure 6.17: The quark-mass dependence of the ρ meson quadrupole moment. The blue circles (●) are from the current analysis, while the red squares (■) are the quenched results of Ref. [56]. The dashed line represents the physical point. We see very similar behaviour between the results at the heavier masses. However, at our lightest mass we observe a significant increase in the magnitude of the quadrupole moment indicating a significant role of the pion cloud in the underlying structure of the ρ meson.

In Fig. 6.17 we illustrate the quark mass dependence of the quadrupole moment. We also include the quadrupole moment extracted from the quenched data of Ref. [56]. At heavier masses we find consistent values and see a slight increase in the magnitude in the direction of decreasing quark mass. However, we see a rapid increase in the magnitude at our lightest mass; the value nearly doubles in comparison with the next lightest mass. This indicates the importance of light-quark dynamics to the underlying structure of the ρ meson and suggests significant contributions coming from the associated pion cloud. The dramatic variation observed warrants further investigation into the chiral dynamics of this quantity, especially into the role that finite volume effects may have on the determination.

In Ref. [117], through considerations of the most general free Lagrangian for a charged spin-1 system with minimal electromagnetic coupling, it was shown that there exists an explicit degree of freedom in the Lagrangian which can be parametrised by the g-factor. Consequently one finds that at tree-level the quadrupole moment is $Q_\rho = (1 - g_\rho)\, e/m_\rho^2$. With our value of $g_\rho = 2.21(8)$, the tree-level value for Q_ρ is $-1.21(8)\, e/m_\rho^2$. To make contact with Ref. [117], we can re-express our quadrupole moment in natural units of e/m_ρ^2, where m_ρ is the mass of the ρ meson observed on the lattice at each quark mass. Doing so for our lightest quark mass we find $Q_\rho = -0.733(99)\, e/m_\rho^2$ indicating important contributions beyond tree level, driven by the fundamental strong interactions of QCD.

As was mentioned in the discussion of the ρ meson g-factor, from the perspective of a non-relativistic quark model, the quadrupole moment arises from an admixture of S and D-wave components in the wave function. Thus our non-zero quadrupole moment, even at heavy masses, indicates an important D-wave component to the ρ meson. In our discussion of the ρ meson spectrum we noted that quark model expectations predict two excitations around 1600 GeV with one state S-wave dominant and the other D-wave dominant. As the quadrupole moment is a measure of the asymmetry of a state, we would expect such states to have very different quadrupole moments. Therefore in a next-generation calculation where excited-state signals are sufficiently precise, the quadrupole moment could be used to determine the dominant contributions to the $\rho(1450)$ and $\rho(1700)$ wave functions. Furthermore, it offers the ideal tag to track these eigenstates with varying quark mass and in this way would allow one to determine if there is a reordering of these states in the light quark regime.

6.4 Summary

As we found in the previous chapter, the use of optimised interpolators obtained from the variational approach results in a rapid isolation of the eigenstate, enabling earlier insertion of the probing current. Optimised interpolators at the sink result in a rapid onset of robust plateau behaviour enabling early and large Euclidean-time fit windows. Together these features act to reduce systematic errors through the suppression of excited state contaminations and reduce statistical uncertainties through the ability to insert the current and establish fit windows earlier in Euclidean time. This approach, coupled with the large lattice volume and light quark masses, has resulted in an accurate determination of the π and ρ meson electromagnetic form factors at low Q^2.

Our light quark-mass determination of the ρ meson g-factor, $g_\rho = 2.21(8)$, compares well with the experimental result of Ref. [92], but with significantly smaller uncertainty. This value is consistent with earlier lattice and model evaluations, which collectively prefer a g-factor slightly larger than the simple quark model estimate of 2. As was found in the quenched calculation of Ref. [56], we obtain a negative value for the quadrupole form factor. The onset of significant chiral non-analytic behaviour in the light quark-mass regime is also observed.

Finally we have for the first time measured the electromagnetic form factors for a light meson excitation. We find that the charge form factors for these states are smaller than their ground state counterparts, consistent with expectations that these states should be larger in size. For the ρ^* meson, we observed a significantly smaller value for the magnetic form factor and a smaller magnetic moment. Our observation of $\mu_{\rho^*}/\mu_\rho = 0.74(9)$ supports the model prediction of Ref. [109].

Chapter 7

Meson Transitions on the Lattice

The content of this chapter is based on the paper: "Transition of $\rho \to \pi\gamma$ in Lattice QCD" by B. J. Owen et al., arXiv:1505.02876 [hep-lat].

So far we have examined how the variational approach can be utilised in the evaluation of elastic form factors where the incoming and outgoing hadron are the same. Though such quantities can provide valuable insight into the structure of these states on a finite volume, their meaning and interpretation in the infinite volume becomes less intuitive as these states become resonances [118, 119]. Furthermore, the systematics required to measure the elastic form factors for unstable particles renders direct experimental determination difficult. What can be determined experimentally are transition form factors where the current transforms an incoming state, i.e. some stable particle, into an outgoing state, the unstable state under consideration. By examining the decay products, one is able to extract the relevant form factor describing the production, or decay, of a resonance. Therefore, we now consider how the variational approach can be utilised for the evaluation of transition form factors. In particular, we shall evaluate the transition form factor relevant to the radiative decay of the ρ meson into a pion.

7.1 Variational Methods for Transitions Elements

As was noted at the end of Section 4.4, to obtain the three-point correlation functions for transitions of the form $\alpha \overset{\mathcal{O}}{\to} \beta$, one simply projects the relevant eigenvectors for eigenstates α and β at the source and sink respectively

$$G_{\mathcal{O}}(\vec{p}', \vec{p}, t_2, t_1; \alpha \to \beta) \equiv v_i^{\beta}(\vec{p}')\, (G_{\mathcal{O}})_{ij}(\vec{p}', \vec{p}, t_2, t_1)\, u_j^{\alpha}(\vec{p})\,.$$

In the case where α and β have the same J^{PC}, it is a simple matter of projecting onto the same matrix of three-point correlators used in the evaluation of the elastic form factors. In general however, α and β need not have the same quantum numbers. Here one must instead consider the three-point correlation function evaluated between source and sink interpolators of differing quantum numbers

$$G_{\mathcal{O}}^{a\to b}(\vec{p}', \vec{p}, t_2, t_1) = \sum_{\vec{x}_2, \vec{x}_1} e^{-i\vec{p}'\cdot\vec{x}_2}\, e^{i(\vec{p}'-\vec{p})\cdot\vec{x}_1}\, \langle\Omega|\chi^b(x_2)\, \mathcal{O}(x_1)\, \bar{\chi}^a(0)|\Omega\rangle\,, \tag{7.1}$$

with a and b labelling the different J^{PC}. To obtain the projected correlators for the transition $\alpha, a \xrightarrow{\mathcal{O}} \beta, b$, we must now work with two variational bases

$$\{\, \chi_i^a \,|\, i = 1, \ldots, n_a \}\,,$$
$$\{\, \chi_i^b \,|\, i = 1, \ldots, n_b \}\,,$$

one for each of the states involved. By solving the eigenvalue problem on each basis separately, we obtain two sets of eigenvectors giving rise to optimised operators for each J^{PC}

$$\phi_a^\alpha(x) = \sum_i (v_a)_i^\alpha \, \chi_i^a(x), \quad \bar{\phi}_a^\alpha(x) = \sum_j \bar{\chi}_j^a(x) \, (u_a)_j^\alpha \,,$$
$$\phi_b^\beta(x) = \sum_i (v_b)_i^\beta \, \chi_i^b(x), \quad \bar{\phi}_b^\beta(x) = \sum_j \bar{\chi}_j^b(x) \, (u_b)_j^\beta \,.$$

We then access the desired three-point correlator for the transition in question by projecting the relevant eigenvectors for source and sink, taken from the relevant bases, onto the $n_a \times n_b$ matrix of three point correlators formed between bases

$$G_{\mathcal{O}}(\vec{p}', \vec{p}, t_2, t_1; \alpha \to \beta) \equiv (v_b)_i^\beta(\vec{p}') \, (G_{\mathcal{O}}^{a \to b})_{ij}(\vec{p}', \vec{p}, t_2, t_1) \, (u_a)_j^\alpha(\vec{p}) \,.$$

Having obtained the projected correlators, isolation of the transition form factors in question is achieved through construction of a suitable ratio, appropriately generalised for transitions. The ratio we work with is one such generalisation of Eq. (4.16)

$$R(p', p; \alpha \to \beta) = \sqrt{\frac{\langle G(\vec{p}', \vec{p}, t_2, t_1; \alpha \to \beta) \rangle \, \langle G(\vec{p}, \vec{p}', t_2, t_1; \beta \to \alpha) \rangle}{\langle G(\vec{p}', t_2; \beta) \rangle \, \langle G(\vec{p}, t_2; \alpha) \rangle}} \,. \tag{7.2}$$

7.2 The Pseudoscalar–Vector Transition

A complete description of the radiative transition between a vector and pseudoscalar meson requires only a single form factor. Expressing the vertex in terms of multipole moments, this form factor is identified as a magnetic dipole ($M1$) transition moment. We therefore choose to label this form factor as $G_{M1}(Q^2)$. For our calculation, we shall use the vertex normalisation of Woloshyn [120]

$$\langle \pi_\alpha(\vec{p}) | J^\mu(0) | \rho_\beta(\vec{p}', s') \rangle = \frac{1}{2\sqrt{E_{\pi_\alpha}(\vec{p}) \, E_{\rho_\beta}(\vec{p}')}} \left(\frac{-ie}{m_{\rho_\beta}} \right) G_{M1}(Q^2) \, \varepsilon^{\mu\delta\sigma\tau} \, p'_\delta \, p_\sigma \, \epsilon_\tau^\beta(p', s') \,, \tag{7.3}$$

where $\epsilon_\tau^\beta(p', s')$ is again a spin-polarisation vector specifying orientation of the ρ meson spin. The corresponding time reversed vertex can be obtained by taking the Hermitian conjugate.

To make contact with the above matrix element, we again begin with the necessary three-point correlation function

$$(G_{\rho\to\pi})^{\mu}_{\nu}(\vec{p},\vec{p}',t_2,t_1;\beta\to\alpha) = \sum_{\vec{x}_2,\vec{x}_1} e^{-i\vec{p}\cdot(\vec{x}_2-\vec{x}_1)}\, e^{-i\vec{p}'\cdot\vec{x}_1} \times \langle\Omega|\, \phi_{\pi}^{\alpha,\vec{p}}(x_2)\, J^{\mu}(x_1)\, \phi_{\rho,\nu}^{\beta,\vec{p}'\,\dagger}(0)\,|\Omega\rangle\,.$$

Applying the completeness identity between the operators gives

$$(G_{\rho\to\pi})^{\mu}_{\nu}(\vec{p},\vec{p}',t_2,t_1;\beta\to\alpha) = \sum_{s'} \frac{e^{-E_{\pi_\alpha}(\vec{p})\,(t_2-t_1)}\, e^{-E_{\rho_\beta}(\vec{p}')\,t_1}}{2\sqrt{E_{\rho_\beta}(\vec{p}')\,E_{\pi_\alpha}(\vec{p})}} \times\langle\Omega|\phi_{\pi}^{\alpha,\vec{p}}(0)|\pi_\alpha(\vec{p})\rangle\,\langle\pi_\alpha(\vec{p})|J^{\mu}(0)|\rho_\beta(\vec{p}',s')\rangle\,\langle\rho_\beta(\vec{p}',s')|\phi_{\rho,\nu}^{\beta,\vec{p}'\,\dagger}(0)|\Omega\rangle\,.$$

Making use of the pseudoscalar and vector operator overlaps, given by Eqs. (6.1) and (6.6), as well as the vertex definition above, reduces this to

$$(G_{\rho\to\pi})^{\mu}_{\nu}(\vec{p},\vec{p}',t_2,t_1;\beta\to\alpha) = \frac{e^{-E_{\pi_\alpha}(\vec{p})\,(t_2-t_1)}\, e^{-E_{\rho_\beta}(\vec{p}')\,t_1}}{4\,E_{\rho_\beta}(\vec{p}')\,E_{\pi_\alpha}(\vec{p})}\,\mathcal{Z}_{\pi}^{\alpha}(\vec{p})\,\mathcal{Z}_{\rho}^{\beta\,\dagger}(\vec{p}') \times\left(\sum_{s'}\epsilon_{\nu}^{\beta}(p',s')\,\epsilon_{\tau}^{\beta\,*}(p',s')\right)\left(\frac{-ie}{m_{\rho_\beta}}\,G_{M1}(Q^2)\,\epsilon^{\mu\delta\sigma\tau}\,p'_{\delta}\,p_{\sigma}\right).$$

Finally, we replace the spin-sum using Eq. (6.7)

$$\sum_{s'}\epsilon_{\nu}(p',s')\,\epsilon_{\tau}^{*}(p',s') = -\left(g_{\nu\tau}-\frac{p'_{\nu}\,p'_{\tau}}{m^2}\right),$$

and by noting that the second term does not contribute with p'_{δ} due to the anti-symmetric properties of the Levi-Civita, we arrive at the general expression describing how the form factor $G_{M1}(Q^2)$ is encoded within the three-point function

$$(G_{\rho\to\pi})^{\mu}_{\nu}(\vec{p},\vec{p}',t_2,t_1;\beta\to\alpha) = \frac{e^{-E_{\pi_\alpha}(\vec{p})\,(t_2-t_1)}\, e^{-E_{\rho_\beta}(\vec{p}')\,t_1}}{4\,E_{\rho_\beta}(\vec{p}')\,E_{\pi_\alpha}(\vec{p})} \times\,\mathcal{Z}_{\pi}^{\alpha}(\vec{p})\,\mathcal{Z}_{\rho}^{\beta\,\dagger}(\vec{p}')\,\left(\frac{-ie}{m_{\rho_\beta}}\,G_{M1}(Q^2)\,\epsilon^{\mu\delta\sigma}{}_{\nu}\,p'_{\delta}\,p_{\sigma}\right).$$

Performing the same procedure on the time-reversed process gives us the corresponding expression

$$(G_{\pi\to\rho})^{\mu}_{\nu}(\vec{p}',\vec{p},t_2,t_1;\alpha\to\beta) = \frac{e^{-E_{\rho_\beta}(\vec{p}')\,(t_2-t_1)}\, e^{-E_{\pi_\alpha}(\vec{p})\,t_1}}{4\,E_{\rho_\beta}(\vec{p}')\,E_{\pi_\alpha}(\vec{p})} \times\,\mathcal{Z}_{\rho}^{\beta}(\vec{p}')\,\mathcal{Z}_{\pi}^{\alpha\,\dagger}(\vec{p})\,\left(\frac{+ie}{m_{\rho_\beta}}\,G_{M1}(Q^2)\,\epsilon^{\mu\delta\sigma}{}_{\nu}\,p'_{\delta}\,p_{\sigma}\right).$$

In order to form the ratio, we require the π and ρ meson two-point correlation functions. These correlators were considered in Section 6.1 with the reduced expressions given by Eqs. (6.2) and (6.8) respectively. Substituting the expressions for the two- and three-point correlators into Eq. (7.2), we arrive at the expression that directly relates the ratio to $G_{M1}(Q^2)$

$$R^{\mu}_{\nu\,\rho\to\pi}(p',p;\beta\to\alpha) = \frac{e\,\epsilon^{\mu\delta\sigma}{}_{\nu}\,p'_{\delta}\,p_{\sigma}}{2\sqrt{E_{\pi_\alpha}(\vec{p})\,E_{\rho_\beta}(\vec{p}')\,\left((p'_{\nu})^2 - m^2_{\rho_\beta}\,g_{\nu\nu}\right)}}\,G_{M1}(Q^2)\,. \qquad (7.4)$$

For this calculation we will use exactly the same set-up as our evaluation of the elastic form factors. In particular, the current 3-momentum is fixed to $\vec{q} = \pm\frac{2\pi}{L}\,\hat{x} \equiv \pm\vec{\xi}$, with current polarization $\mu = 3$. We further choose to fix the vector meson polarization to be $\nu = 2$. Using this arrangement, the term $\epsilon^{\mu\delta\sigma}{}_{\nu}\,p'_{\delta}\,p_{\sigma}$ reduces to $(p'_0\,p_1 - p_0\,p'_1)$. As was done in the evaluation of the elastic form factors, we shall take either the incoming or outgoing state to be at rest. However in the case of a transition, we have the freedom to choose which of the particles is taken to be at rest. Consequently we have two distinct kinematic possibilities (shown here for $\vec{q} = +\vec{\xi}$):

$$\vec{p}' = \vec{\xi},\,\vec{p} = 0 \quad \text{and} \quad \vec{p}' = 0,\,\vec{p} = -\vec{\xi}\,,$$

each of which gives a distinct value in Q^2 due to the difference in the value for the temporal component of the current four-momentum q_0. Applying these kinematics to Eq. (7.4) we arrive at the final expressions used in our determination of the $\rho\to\pi\gamma$ transition form factor

$$e\,G_{M1}(Q^2) = \frac{2m_{\rho_\beta}}{|\vec{q}|}\sqrt{\frac{E_{\rho_\beta}(\vec{q})}{m_{\pi_\alpha}}}R^3_{2\,\rho\to\pi}(\xi,0;\beta\to\alpha)\,,\;\; Q^2 = |\vec{q}|^2 - (E_{\rho_\beta}(\vec{q}) - m_{\pi_\alpha})^2\,;$$

$$e\,G_{M1}(Q^2) = \frac{2m_{\rho_\beta}}{|\vec{q}|}\sqrt{\frac{E_{\pi_\alpha}(\vec{q})}{m_{\rho_\beta}}}R^3_{2\,\rho\to\pi}(0,\xi;\beta\to\alpha)\,,\;\; Q^2 = |\vec{q}|^2 - (m_{\rho_\beta} - E_{\pi_\alpha}(\vec{q}))^2\,,$$

where for the first expression the pion is taken to be at rest while for the second expression the ρ is at rest.

7.3 Results

For this calculation, we use the same framework as was used for the elastic form factors and refer the reader to Section 6.2 for a summary of the simulation details. As outlined at the end of the previous section, our choice of kinematics allows us to evaluate G_{M1} at two distinct values of Q^2. In particular, determinations taken with the pion at rest have time-like $Q^2 < 0$, while those with the ρ meson at rest have space-like $Q^2 > 0$. We therefore have values for G_{M1} on either side of $Q^2 = 0$. In order to compare with experiment and quark model expectations we

(a)

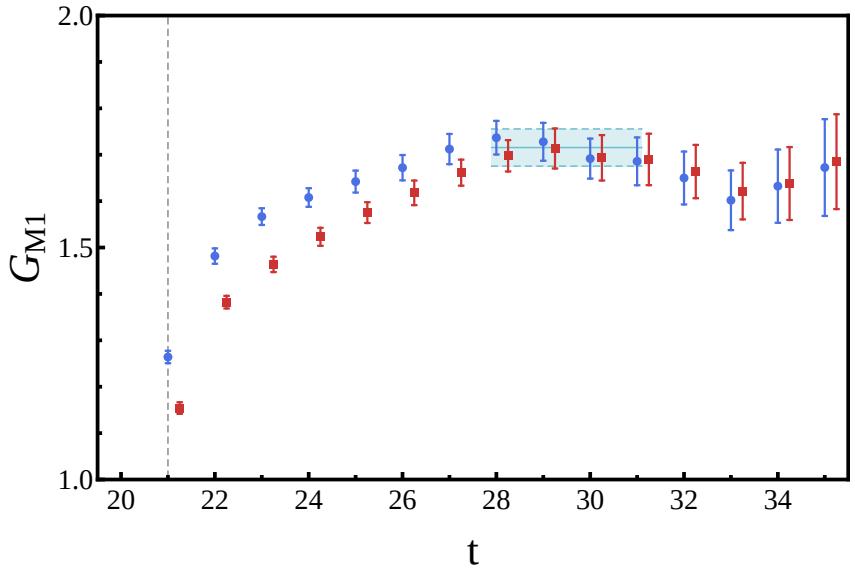

G^u_{M1} with the π meson at rest.

(b)

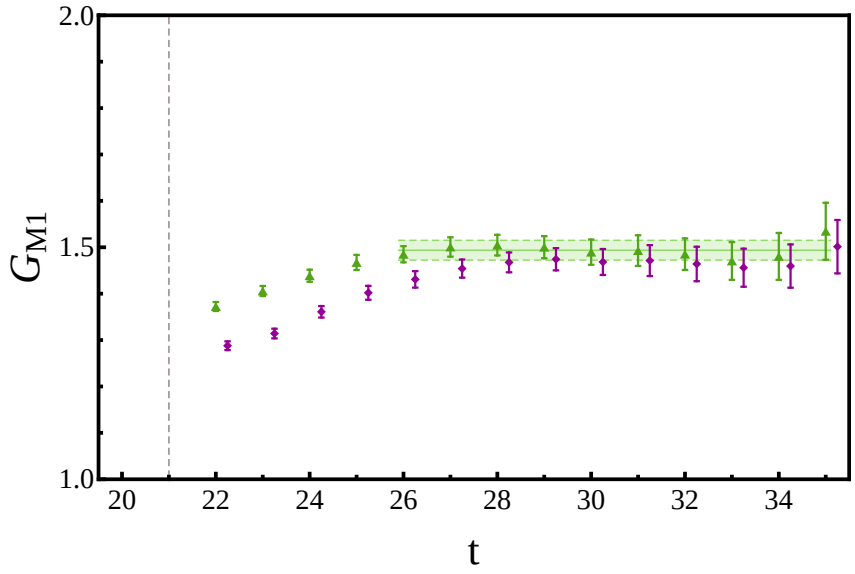

G^u_{M1} with the ρ meson at rest.

Figure 7.1: A comparison of the u-quark contribution to the transition form factor, G^u_{M1}, as a function of Euclidean sink time using the variational approach and the standard single correlator method with smeared source and sink. The results are shown for $m_\pi = 702$ MeV. The two data sets are offset for clarity. The upper figure is for the π meson at rest with the blue circles (●) denoting the results from the variational approach while the red squares (■) illustrate results using the standard single-correlator method. The lower figure is for the ρ meson at rest with the green triangles (▲) denoting the variational method and the purple diamonds (◆) denoting the single-correlator method. The vertical dashed line indicates the position of the current insertion. The fitted value from the variational approach has been included (shaded band) to highlight where the single source approach is consistent with our improved method.

require a determination of $G_{M1}(0)$. To do this we choose to interpolate between our extracted values using a monopole ansatz

$$G_{M1}(Q^2) = \left(\frac{\Lambda^2}{\Lambda^2 + Q^2}\right) G_{M1}(0)\,, \tag{7.5}$$

again motivated by vector meson dominance (VMD) arguments. In these models, interaction with a virtual photon proceeds via neutral vector meson and so the pole mass can be identified as that of the lightest neutral vector mesons, particularly the ρ, i.e. $\Lambda \simeq m_\rho$. Use of VMD hypothesis has been considered in other calculations.The results of Edwards [121], which examine the transition over a range of Q^2 between 0.02-0.6 GeV^2, display behaviour consistent with the VMD hypothesis. Our Q^2 is similar to that of Edwards [121] and so VMD allows for a reasonable estimate of $G_{M1}(0)$.

During the extraction of the quark sector contributions to the form factor, we compared the time-series for the ratio using the correlation matrix approach and the standard single smeared source and sink correlator. For all masses and kinematics, we again find that the correlation matrix method improves the quality of the plateau over the single level of smearing. In particular, the ratio sampling in the time-like region requires significantly more Euclidean time evolution than the corresponding ratio sampling the space-like region. We note that in this case the ρ carries the momentum and the pion is at rest. Figure 7.1 highlights this comparison for a single quark mass.

Once more we present the Euclidean time-series and subsequent fits for the form factor at all quark masses and kinematic arrangements in Appendix B.

We shall now consider the quark sector contributions for the transition form factor. As was outlined in Section 4.2.1, the anti-quark sector contribution is evaluated through considerations of charge conjugation. Evaluating this contribution in this way, we need to account for any signs associated with the charge conjugation properties of the bilinear in the meson interpolator. For the elastic case, the in and out states are the same and so both source and sink operators will pick up a sign and thus drop out. In this case however, the bilinears for the π and ρ mesons transform differently and so we have that the anti-quark sector is equal in magnitude to the quark sector contribution, however differs in sign. Without this sign, we note that under exact isospin, all neutral states with $I_3 = 0$ would not undergo radiative transitions due to the complete cancellation between the quark sectors.

In Fig. 7.2 we present our results for the extracted values for the u-quark sector contribution to the form factor, G^u_{M1}, as well as the corresponding interpolations used to extract $G^u_{M1}(0)$. Here we choose to label these as the quark sector contributions to the positive-charge eigenstate of the corresponding iso-triplet. That is, the quark contribution is labelled as the u-quark sector while the anti-quark contribution is labelled as the d-quark sector. However, as the anti-quark contribution is equal in magnitude with opposite sign, $G^d_{M1} = -G^u_{M1}$, we choose

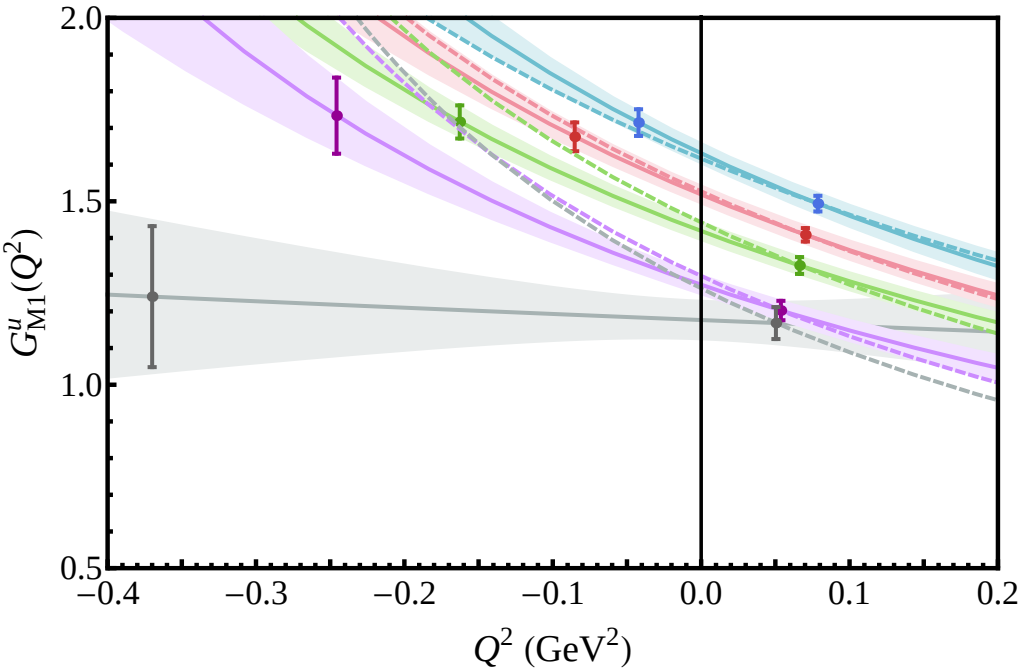

Figure 7.2: The quark sector contributions for the transition form factor, $G^{\mathrm{u}}_{M1}(Q^2)$ for both time-like and space-like Q^2. Each color corresponds to a different value of m_π, with blue the heaviest and masses getting lighter as we read down. For each mass we have access to two values of Q^2 stemming from the freedom to choose which hadron is as rest. The solid line and coloured bands are the resulting monopole parametrisation extracted from the two data points, allowing us access obtain a value for $G^u_{M1}(0)$. We also include a VMD estimate, dashed line, obtained from using the right positive Q^2 data only, with ρ meson mass used as the monopole mass Λ.

to show the quark contribution only. The quark sector contributions are for quarks of unit-charge. We note that the spread of Q^2 sampled is much larger in the time-like region due to the increasing Q_0-component stemming from the Goldstone nature of the pion. In the space-like region, we see this effect is suppressed when the momentum is carried by the pion. This tight grouping of Q^2 values shows a clear decrease in the value of G^u_{M1} as the quark masses become light.

In the time-like region, the most striking feature is the significantly small value obtained for the lightest mass. As discussed in Section 6.3, examination of the projected two-point function appears consistent with a single particle state. We shall note that the plateau for this particular extraction of G^u_{M1} differed in nature to those at heavier masses. Based upon the $\chi^2_{\rm dof}$, one is able to fit much earlier, however this is likely the result of a significant increase in the uncertainty of G^u_{M1} at early time-slices. Guided by the fit-windows at heavier masses we choose to fit at later times, however it is certainly possible that we simply do not have sufficient statistics and so obtain a value for G^u_{M1} that is suppressed. Another possibility is that we are sampling too far into the time-like region for the VMD hypothesis to hold. Therefore this result may suggest that this process is suppressed at large time-like momentum transfers. As a check of the potential impact that this may have on the extracted value of $G^u_{M1}(0)$, we compare our results with the VMD estimate obtained using space-like data and the ρ meson mass as the monopole mass. This result is shown as the dashed line in Fig. 7.2. In Fig. 7.3 we show the monopole masses extracted from our analysis. We also include the corresponding ρ meson masses and find that they compare reasonably well at large quark masses, but diverge in the light quark regime. Indeed, at the lightest mass $\Lambda \simeq 0$. This draws the monopole ansatz into question deep in the time-like regime. Thus to connect to experiment we also work with results in the space-like regime ($Q^2 > 0$) and employ VMD.

We now consider the full hadronic transition form factor. As was noted earlier, for this transition the quark and anti-quark sector contributions are of equal magnitude and opposite sign and so the charge weighted form factor for the $\rho^+ \to \pi^+\gamma$ transition is given by

$$\begin{aligned} G_{M1}(Q^2) &= \frac{2}{3} G^u_{M1}(Q^2) + \frac{1}{3}(-G^u_{M1}(Q^2)) \\ &= \frac{1}{3} G^u_{M1}(Q^2)\,. \end{aligned}$$

Table 7.1 summarises our lattice results. In Fig. 7.4 we present our results for $G_{M1}(0)$. We also include the non-relativistic quark model (NRQM) expectation of Ref. [122] and the available experimental data. Due to the different choice of normalisation for this matrix element, we match conventions via the decay width. The relevant expression for the decay width using our choice of normalisation [120] is

$$\Gamma_{\rho\to\pi\gamma} = \frac{1}{3}\,\alpha\,\frac{|\vec{q}|^3}{m_\rho^2}\,|G_{M1}(0)|^2\,, \tag{7.6}$$

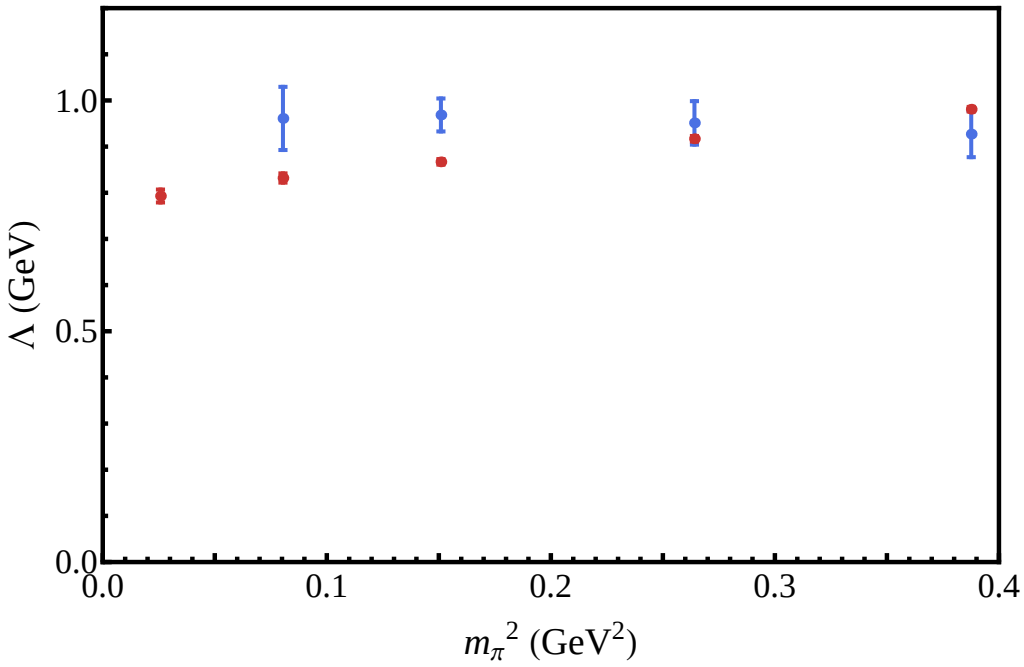

Figure 7.3: Monopole mass Λ (●), obtained from monopole ansatz as suggested by Vector Meson Dominance (VMD) hypothesis. The corresponding ρ meson mass (●) is included to test the VMD hypothesis. The monopole mass for the lightest point is not included as the extracted value for $\Lambda^2 \simeq 0$ stemming from the low value for $G_{M1}(Q^2)$ in the time-like region.

Table 7.1: Lattice results for the charge-weighted form factor G_{M1} of the $\rho^+ \to \pi^+\gamma$ transition for the two available Q^2-values for each pion mass.

κ	m_π (GeV)	m_ρ (GeV)	Q^2 (GeV^2)	$G_{M1}(Q^2)$
0.13700	0.6226(9)	0.981(5)	-0.042(5)	0.572(12)
			0.078(3)	0.498(7)
0.13727	0.5145(9)	0.917(6)	-0.085(5)	0.559(13)
			0.070(3)	0.470(6)
0.13754	0.3884(9)	0.867(6)	-0.163(6)	0.572(15)
			0.066(3)	0.442(8)
0.13770	0.2848(11)	0.832(10)	-0.246(10)	0.578(35)
			0.054(6)	0.401(9)
0.13781	0.1613(31)	0.793(14)	-0.370(17)	0.413(64)
			0.050(9)	0.389(15)

where the photon 3-momentum is evaluated in the ρ meson rest frame

$$|\vec{q}| = \frac{m_\rho^2 - m_\pi^2}{2m_\rho}\,.$$

Using this expression we are able to evaluate $G_{M1}(0)$ for experimental measurements of the decay width. We include the PDG average [105] as well as the three experimental measurements [123–125] used in its evaluation. For the quark model, the choice of normalisation used in Ref. [122] results in the following expression for the decay width

$$\Gamma_{\rho\to\pi\gamma} = \frac{2}{3}\alpha|\vec{q}|^3\left(\frac{E_\pi}{m_\rho}\right)\sum_q |\langle\,\rho\,|\frac{\mu_q e_q \sigma_q}{e}|\,\pi\,\rangle|^2\,.$$

As discussed in Ref. [122], by using SU(6) quark and anti-quark flavour combinations, the sum evaluates to

$$\sum_q |\langle\,\rho\,|\frac{\mu_q e_q \sigma_q}{e}|\,\pi\,\rangle|^2 = \frac{2}{9}\frac{\mu_{ud}^2}{e^2}\,,$$

where the light-quark magnetic moment is

$$\mu_{ud} = \frac{e}{2\,m_{ud}}\,.$$

Matching with Eq. (7.6), this gives rise to the following expression

$$G_{M1}(0) = \frac{2}{3}\sqrt{m_\rho E_\pi}\,\frac{\mu_{ud}}{e}\,.$$

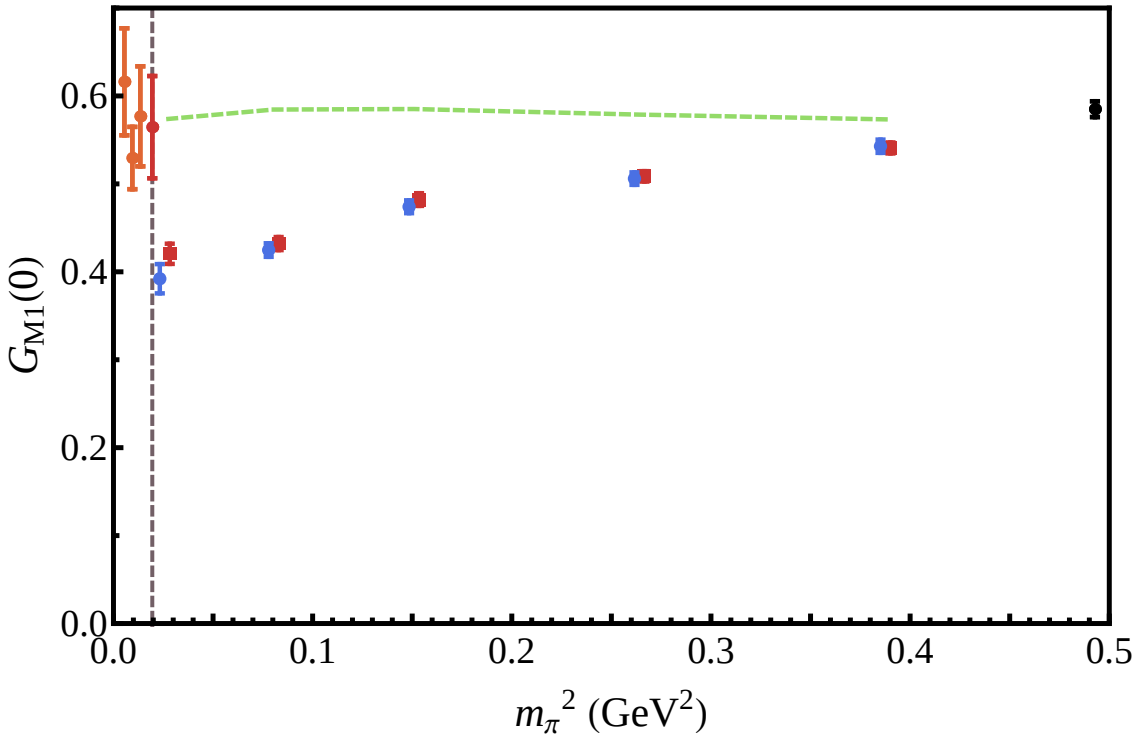

Figure 7.4: Results for the full hadronic transition moment, $G_{M1}(0)$, extracted using both space and time-like Q^2 values (●) and using the space-like values only and invoking the VMD hypothesis (■). We include the available experimental extractions (●) ordered from left to right by year of publication [123–125]. We also include the PDG average (●) obtained from this data [105]. The experimental data are offset for readability, with the PDG average aligned at the physical point indicated by the vertical dashed line. The dashed green line is the non-relativistic quark model expectation of Ref. [122] as discussed herein. We also include the result of Shultz et al. [97] (●) which determines this moment for a single heavy quark mass.

For the quark moment, μ_{ud}, we use a constituent quark mass that varies linearly in m_π^2

$$m_{ud} = a + b\, m_\pi^2 \,,$$

with a and b fixed such that the constituent quark has a mass of 330 MeV at the physical point and 510 MeV at the SU(3) symmetric point, as determined in Ref. [105] using the magnetic moments μ_p, μ_n and μ_Λ.

Beginning with our results at the heaviest values of m_π, we find that our lattice data is close to the quark model expectation. Furthermore the observed trend in the data suggests consistency with increasing quark mass where we would expect the quark model expectation to hold. The trend in the data also appears consistent with the determination of Ref. [97]. As we move down to the lighter masses there is a clear downwards trend in the lattice data, as was also observed

in our previous quenched study [126] [1]. In contrast to this the quark model result shows little variation with m_π. In the light quark regime, we do not expect the quark model to necessarily hold for this transition. Unlike heavier systems such as bottomium and charmonium decays, the quarks in both the π and ρ meson systems are highly relativistic. Furthermore, the pion itself is a Goldstone mode of QCD stemming from the underlying chiral symmetry of the theory. Though we can in principle treat the quarks relativistically [127, 128], the inability to properly describe the chiral behaviour of the pion is a fundamental shortfall of all constituent quark models and may certainly lead to deviations in the chiral limit.

Comparison with the experimental determination shows a notable deviation, with the lattice data sitting around 33% lower than the experimental value. In Fig. 7.4 we also include the values obtained using VMD with the space-like data only and find that significant differences persist. However, we note that our calculation is incomplete. Unlike the elastic form factors for which disconnected contributions are necessarily zero [45, 108], such contributions are present for meson transitions that involve a change in G-parity [97]. As discussed in the previous chapter, under charge-conjugation the "C-even" two-point function and the "C-odd" disconnected loop give rise to a relative sign between the $\{U\}$ and $\{U^*\}$ configurations and so cancel exactly [45] in the ensemble average. For transitions involving a change in G-parity, the two-point function is now "C-odd" and so combining with the disconnected loop gives rise to a common sign between the $\{U\}$ and $\{U^*\}$ configurations resulting in a non-zero quantity [97, 108]. Furthermore, if one neglects disconnected s-quark contributions, the charge weight factors between the connected contributions and the disconnected contributions are equal

$$\begin{aligned} G_{M1} &= q_u\, G_{M1}^{\text{con.}} + q_{\bar{d}}\, (-G_{M1}^{\text{con.}}) + q_u\, G_{M1}^{\text{dis.}} + q_d\, G_{M1}^{\text{dis.}} \\ &= \left(\frac{2}{3} - \frac{1}{3}\right) G_{M1}^{\text{con.}} + \left(\frac{2}{3} - \frac{1}{3}\right) G_{M1}^{\text{dis.}} \\ &= \frac{1}{3}\, G_{M1}^{\text{con.}} + \frac{1}{3}\, G_{M1}^{\text{dis.}}\,. \end{aligned}$$

Thus the discrepancy between our results and the experimental value suggest that disconnected contributions are likely to play an important role in fully describing this transition. One would also expect such contributions to become increasing important with decreasing quark mass. This expectation complements the observation that our results are consistent with quark model expectations at heavier masses, however deviate as we move to light-quark regime.

Another important aspect that warrants further consideration is the fact that the ρ meson is ultimately a resonant state. The nature of resonant states

[1] We note that in this proceedings, there was an error in converting the experimental decay widths to our definition of the form factor $G_{M1}(0)$. The lattice data however is correct and consistent with results presented herein. Comparison with experiment for Ref. [126] should be done with the value presented here.

on the lattice is significantly different to that of continuum due to the lack of a continuous distribution of momentum modes and so to properly make connection with the continuum expectation, one must suitably evolve the lattice determinations to the infinite volume to properly account for the differences in the underlying multi-particle interactions. Understanding exactly how to do this in general is an area of current interest to the community and only very recently has a framework been presented to handle $1 \to 2$ body processes required to properly describe this transition [118, 119, 129, 130]. In fully addressing this aspect, it is important to also consider the role of $\pi\pi$ scattering states in the ρ meson correlation matrix to ensure a complete isolation of QCD eigenstates on the finite volume.

7.4 Summary

In this chapter we utilised the variational approach to examine the radiative decay of the ρ meson in the light quark-mass regime. The calculated transition moment, $G_{M1}(0)$, was found to be consistent with quark model expectations at heavy masses. However we have discovered an important quark mass dependence. Our results in the light quark regime sit low in comparison with experimental determinations, suggesting important disconnected contributions to this process. These results warrant a more comprehensive investigation of this process. Any future work should aim to focus on the inclusion of disconnected contributions, multi-particle contributions and finite volume effects so as to allow for the proper evolution of the lattice determination to the infinite-volume. Understanding the role these systematics play in this calculation may provide important insights into topical transition amplitudes such as $N^* \to N\gamma^*$ and $\Delta^{(*)} \to N\gamma^*$ transitions, and those central to the search for exotic hadron states [131].

Chapter 8

Negative Parity Electromagnetic Form Factors

A look at the PDG baryon summary tables clearly highlights that the overwhelming majority of observed resonant states are excitations of the nucleon, denoted N^*. This is not surprising given that within the standard model, the proton is the only stable hadron and so experimentally the simplest target to operate with. Over the past decade, ongoing efforts at a number of facilities, notably Mainz, Bonn, MIT-Bates and Jefferson Lab [132] have produced a rich body of data on the $N^* \to N\gamma$ and $\Delta^* \to N\gamma$ transition amplitudes. With access to such high-quality experimental data, examination of these transition amplitudes using lattice QCD presents an excellent opportunity to connect the experimental data directly to QCD and in turn shed some insight into how resonant state properties emerge from QCD. However, before we delve into the transition elements we shall first consider the simpler problem of determining the elastic form factors for a nucleon excitation.

The lightest nucleon excitation, the Roper resonance ($N^*(1440)$), is of particular interest as its mass lies lower than the first negative parity excitation, the $N^*(1535)$, a feature which cannot be explained consistently using constituent quark models. Consequently, there has been on going effort within lattice spectroscopy studies to observe a positive parity excitation lower in energy than the lowest negative parity excitation. Such an ordering has yet to be observed and recent Hamiltonian effective field theory studies indicate that the Roper has not yet been seen on the lattice [133]. We shall therefore focus instead on the next nucleon resonance, the $N^*(1535)$. As the $N^*(1535)$ is the lowest lying negative parity nucleon state one could in principle use standard techniques to perform the calculation. However, the small mass gap between this state and the nearby $N^*(1650)$ complicates the calculation. Using standard techniques one cannot properly disentangle these states and so one would encounter severe excited state contamination. The variational approach gives us a means to separate these contributions.

In this chapter, we shall do exactly this. In Section 8.1 we begin by considering how one can access the two- and three-point correlation functions relevant for negative parity baryon states. This is followed by Section 8.2 where we take a look at the negative parity nucleon spectrum obtained using the PACS-CS

ensembles. Section 8.3 describes how we extract the electromagnetic form factors for the negative parity nucleon states followed by the presentation of our results. We conclude the chapter in Section 8.4 with a brief summary.

8.1 Accessing Negative Parity States on the Lattice

Two-point Functions

To understand how negative parity states can be accessed on the lattice, we need to understand the complete structure of the baryon correlator. Equipped with some baryon interpolator, χ, which itself has known parity transformation properties, we consider the baryon correlator

$$G(\vec{p},t) = \sum_{\vec{x}} e^{-i\vec{p}\cdot\vec{x}} \, \langle \Omega | \chi(x) \, \bar{\chi}(0) | \Omega \rangle \, . \tag{8.1}$$

As was outlined in Section 5.1, because the interpolators are spinors, the baryon correlator is a 4×4 matrix coupling all spinor components $\bar{\chi}$ with all those of χ. Consequently, to analyse the correlation function for a given state we must first project out the relevant contributions using some projection operator Γ,

$$G(\vec{p},t;\Gamma) = \mathrm{Tr}\left[\Gamma \, G(\vec{p},t)\right] \, .$$

In order to identify a suitable projection operator, we need to understand how the desired terms are encoded within the complete baryon correlator.

Following the now standard procedure of inserting completeness, operator translation and selecting Euclidean time, we can reduce Eq. (8.1) to the familiar form for our correlation function,

$$\begin{aligned} G(\vec{p},t) = \sum_{\alpha^+,s} & e^{-E_{\alpha^+}(\vec{p})\,t} \, \langle \Omega | \chi(0) | \alpha^+, p, s \rangle \, \langle \alpha^+, p, s | \bar{\chi}(0) | \Omega \rangle \\ & + \sum_{\alpha^-,s} e^{-E_{\alpha^-}(\vec{p})\,t} \, \langle \Omega | \chi(0) | \alpha^-, p, s \rangle \, \langle \alpha^-, p, s | \bar{\chi}(0) | \Omega \rangle \, , \end{aligned}$$

where we have separated the sum over eigenstates into those with positive and negative parity respectively. Now due to the underlying structure of the spinor algebra, the interpolator χ, which is itself a spinor, can couple to both positive and negative parity states. Selecting $\chi = \chi^+$ transforming under parity as

$$\chi^+ \to +\gamma_0 \, \chi^+ \, ,$$

the operator overlap factors can be expressed as

$$\begin{aligned} \langle \Omega | \chi^+(0) | \alpha^+, p, s \rangle &= \mathcal{Z}_{\alpha^+}(\vec{p}) \sqrt{\frac{m_{\alpha^+}}{E_{\alpha^+}(\vec{p})}} \, u_{m_{\alpha^+}}(p,s) \, , \\ \langle \Omega | \chi^+(0) | \alpha^-, p, s \rangle &= \mathcal{Z}_{\alpha^-}(\vec{p}) \sqrt{\frac{m_{\alpha^-}}{E_{\alpha^-}(\vec{p})}} \, \gamma_5 \, u_{m_{\alpha^-}}(p,s) \, , \end{aligned}$$

where $u_{m_i}(p,s)$ is standard Dirac spinor, with the label m_i identifying the associated mass for corresponding state. Substituting these overlaps into our expanded expression for the correlator gives

$$G_+(\vec{p},t) = \sum_{\alpha^+} e^{-E_{\alpha^+}(\vec{p})\,t}\, \mathcal{Z}_{\alpha^+}(\vec{p})\, \bar{\mathcal{Z}}_{\alpha^+}(\vec{p})\, \frac{m_{\alpha^+}}{E_{\alpha^+}(\vec{p})} \left(\sum_s u_{m_{\alpha^+}}(p,s)\, \bar{u}_{m_{\alpha^+}}(p,s) \right) - \sum_{\alpha^-} e^{-E_{\alpha^-}(\vec{p})\,t}\, \mathcal{Z}_{\alpha^-}(\vec{p})\, \bar{\mathcal{Z}}_{\alpha^-}(\vec{p})\, \frac{m_{\alpha^-}}{E_{\alpha^-}(\vec{p})}\, \gamma_5 \left(\sum_s u_{m_{\alpha^-}}(p,s)\, \bar{u}_{m_{\alpha^-}}(p,s) \right) \gamma_5 \,,$$

which can be reduced further using the spin-sum

$$\sum_s u_{m_i}(p,s)\, \bar{u}_{m_i}(p,s) = \left(\frac{\not{p} + m_i}{2m_i} \right) \,,$$

to give

$$G_+(\vec{p},t) = \sum_{\alpha^+} \frac{e^{-E_{\alpha^+}(\vec{p})\,t}}{2\,E_{\alpha^+}(\vec{p})}\, \mathcal{Z}_{\alpha^+}(\vec{p})\, \bar{\mathcal{Z}}_{\alpha^+}(\vec{p})\, \left(\not{p} + m_{\alpha^+} \right) + \sum_{\alpha^-} \frac{e^{-E_{\alpha^-}(\vec{p})\,t}}{2\,E_{\alpha^-}(\vec{p})}\, \mathcal{Z}_{\alpha^-}(\vec{p})\, \bar{\mathcal{Z}}_{\alpha^-}(\vec{p})\, \left(\not{p} - m_{\alpha^-} \right) \,,$$

where we note that the γ_5 have been pulled through the $\left(\not{p} + m\right)$ term for the negative parity states. In Section 5.1 we noted that the energy for the positive parity baryon state (mass if we take $\vec{p} = 0$) can be isolated using the projection operator

$$\Gamma_0 = \left(\frac{\gamma_0 + I}{4} \right) = \frac{1}{2} \begin{pmatrix} I & 0 \\ 0 & 0 \end{pmatrix} \,.$$

Applying this projector to the above expression for the baryon correlator, we find the following terms for positive and negative parity states respectively

$$\begin{aligned} \mathrm{Tr}\left[\Gamma_0 \, \left(\not{p} + m \right) \right] &= (E + m) \,, \\ \mathrm{Tr}\left[\Gamma_0 \, \left(\not{p} - m \right) \right] &= (E - m) \,. \end{aligned}$$

Evidently, if we look in the traditional upper-left quadrant of the Dirac matrix by projecting with Γ_0, we can see that χ^+ interpolators couple strongly to positive parity states and weakly to negative parity states. The same argument carries over to the use of χ^- operators transforming under parity as

$$\chi^- \to -\gamma_0 \chi^- \,.$$

Here the operator overlaps are

$$\begin{aligned} \langle \Omega | \chi^-(0) | \alpha^+, p, s \rangle &= \mathcal{Z}_{\alpha^+}(\vec{p}) \sqrt{\frac{m_{\alpha^+}}{E_{\alpha^+}(\vec{p})}}\, \gamma_5\, u_{m_{\alpha^+}}(p,s) \,, \\ \langle \Omega | \chi^-(0) | \alpha^-, p, s \rangle &= \mathcal{Z}_{\alpha^-}(\vec{p}) \sqrt{\frac{m_{\alpha^-}}{E_{\alpha^-}(\vec{p})}}\, u_{m_{\alpha^-}}(p,s) \,. \end{aligned}$$

Working through the algebra and using the same projection operator Γ_0, one finds that χ^- operators couple strongly to negative parity states and weakly to positive parity states.

However, an important observation is that we can obtain a χ^- operator from a χ^+ operator through

$$\chi^-(x) = \gamma_5 \, \chi^+(x) \, .$$

Consequently, the correlator formed from $\chi^- \bar{\chi}^-$ can be re-expressed as

$$\begin{aligned} G_-(\vec{p},t) &= \sum_{\vec{x}} e^{-i\vec{p}\cdot\vec{x}} \, \langle \Omega | \chi^-(x) \, \bar{\chi}^-(0) | \Omega \rangle \\ &= -\sum_{\vec{x}} e^{-i\vec{p}\cdot\vec{x}} \, \langle \Omega | \gamma_5 \, \chi^+(x) \, \bar{\chi}(0) \, \gamma_5 | \Omega \rangle \\ &= -\gamma_5 \left(\sum_{\vec{x}} e^{-i\vec{p}\cdot\vec{x}} \, \langle \Omega | \chi^+(x) \, \bar{\chi}^+(0) | \Omega \rangle \right) \gamma_5 \\ &= -\gamma_5 \, G_+(\vec{p},t) \, \gamma_5 \, . \end{aligned}$$

Applying the Γ_0 projection operator, we can see that it is possible to isolate the negative parity states from the correlator formed from $\chi^+ \bar{\chi}^+$ by using a modified projection operator,

$$\begin{aligned} G_-(\vec{p},t;\Gamma_0) &= \mathrm{Tr} \left[\Gamma_0 \, (-\gamma_5 G_+(\vec{p},t) \gamma_5) \right] \\ &= \mathrm{Tr} \left[(-\gamma_5 \, \Gamma_0 \, \gamma_5) \, G_+(\vec{p},t) \, \right] \\ &= \mathrm{Tr} \left[\Gamma_0^{--} \, G_+(\vec{p},t) \, \right] \, , \end{aligned}$$

where

$$\Gamma^{--} = -\gamma_5 \, \Gamma \, \gamma_5 \, .$$

The superscript $--$ reflects the parity transition properties of the source and sink operators. This notation will be useful in considering abnormal parity transitions in the following chapter. We can interpret the use of the modified projector on $G_+(\vec{p},t)$ as mapping the spinors in the operator couplings from,

$$\begin{aligned} + : \quad u(p,s) \quad &\rightarrow \quad \gamma_5 \, u(p,s) \\ - : \quad \gamma_5 \, u(p,s) \quad &\rightarrow \quad u(p,s) \, , \end{aligned}$$

leading to strong couplings for the negative parity states and weak couplings for the positive parity states, consistent with $G_-(\vec{p},t)$. An alternate interpretation can be arrived at through consideration of

$$\begin{aligned} \Gamma_0^{--} &= -\gamma_5 \left(\frac{\gamma_0 + I}{4} \right) \gamma_5 \\ &= \left(\frac{\gamma_0 - I}{4} \right) \\ &= -\frac{1}{2} \begin{pmatrix} 0 & 0 \\ 0 & I \end{pmatrix} \, , \end{aligned}$$

which highlights that the negative parity states couple strongly to the lower components of the interpolators and so one finds the correlation function of the negative parity state in the lower-right quadrant of the Dirac matrix.

Three-point Functions

Having examined the case of the two-point correlator in some detail, we shall now turn our attention to the three-point correlator

$$G(\vec{p}', \vec{p}, t_2, t_1) = \sum_{\vec{x}_2, \vec{x}_1} e^{-i\vec{p}'\cdot\vec{x}_2}\, e^{i(\vec{p}'-\vec{p})\cdot\vec{x}_1}\, \langle\Omega|\chi(x_2)\,\mathcal{O}(x_1)\,\bar{\chi}(0)|\Omega\rangle\,. \tag{8.2}$$

Once more, inserting completeness between our operator pairs, appealing to operator translation and finally selecting Euclidean-time, we arrive at the expanded form for the three-point correlator,

$$\begin{aligned}
G(\vec{p}', \vec{p}, t_2,&t_1) = \\
&\sum_{\alpha^+,\beta^+} e^{-E_{\beta^+}(\vec{p}')\,(t_2-t_1)}\, e^{-E_{\alpha^+}(\vec{p})\,t_1}\, \langle\Omega|\chi(0)|\beta^+\rangle\,\langle\beta^+|\mathcal{O}(0)|\alpha^+\rangle\,\langle\alpha^+|\bar{\chi}(0)|\Omega\rangle \\
+ &\sum_{\alpha^+,\beta^-} e^{-E_{\beta^-}(\vec{p}')\,(t_2-t_1)}\, e^{-E_{\alpha^+}(\vec{p})\,t_1}\, \langle\Omega|\chi(0)|\beta^-\rangle\,\langle\beta^-|\mathcal{O}(0)|\alpha^+\rangle\,\langle\alpha^+|\bar{\chi}(0)|\Omega\rangle \\
+ &\sum_{\alpha^-,\beta^+} e^{-E_{\beta^+}(\vec{p}')\,(t_2-t_1)}\, e^{-E_{\alpha^-}(\vec{p})\,t_1}\, \langle\Omega|\chi(0)|\beta^+\rangle\,\langle\beta^+|\mathcal{O}(0)|\alpha^-\rangle\,\langle\alpha^-|\bar{\chi}(0)|\Omega\rangle \\
+ &\sum_{\alpha^-,\beta^-} e^{-E_{\beta^-}(\vec{p}')\,(t_2-t_1)}\, e^{-E_{\alpha^-}(\vec{p})\,t_1}\, \langle\Omega|\chi(0)|\beta^-\rangle\,\langle\beta^-|\mathcal{O}(0)|\alpha^-\rangle\,\langle\alpha^-|\bar{\chi}(0)|\Omega\rangle\,,
\end{aligned} \tag{8.3}$$

where we have again separated the sums explicitly into positive and negative parity states respectively. For clarity we have suppressed the momentum and spin labels on the bras and kets. Having noted that we can access all combinations of interpolators χ^+ and χ^- by projecting with the relevant projection operator, our goal is to identify those operators that allow us to isolate the matrix elements of interest. Taking our interpolators χ to transform as χ^+ we note that the correlation function obtained from χ^- interpolators can be obtained by post-multiplying with $-\gamma_5$ for the source and pre-multiplying by γ_5 for the sink. In projecting out the desired components, we can again appeal to cyclicity of the trace in order to construct modified projectors that allow us to isolate the various matrix elements with given parity combination. These modified projectors are

$$\begin{aligned}
+ \to + &: \quad \Gamma^{++} = \Gamma\,, \\
+ \to - &: \quad \Gamma^{-+} = \Gamma\gamma_5\,, \\
- \to + &: \quad \Gamma^{+-} = -\gamma_5\Gamma\,, \\
- \to - &: \quad \Gamma^{--} = -\gamma_5\Gamma\gamma_5\,,
\end{aligned}$$

where our notation follows the tradition of source on the right and sink on the left, namely $\Gamma^{(\text{sink})(\text{source})}$. By using the required projector for a given transition, all operator overlaps that weight the desired matrix element in Eq. (8.3) are parametrised as

$$\langle\Omega|\chi^{+}(0)|\alpha^{i},p,s\rangle = \mathcal{Z}^{i}_{\alpha}(\vec{p})\sqrt{\frac{m_i}{E_i(\vec{p})}}\,u_{m_i}(p,s)\,,$$

as the γ_5 factors that appear for negative-parity states have been moved to the projector.

8.2 Negative Parity Nucleon Spectrum

The evaluation of the negative parity spectrum on the PACS-CS ensembles was presented in Ref. [104], so here we shall simply present a summary of their calculation and results.

In this work, the variational basis was constructed from the local nucleon interpolators

$$\begin{aligned}
\chi_1(x) &= \epsilon^{abc}\left(u^{aT}(x)\,C\gamma_5\,d^{b}(x)\right)Iu^{c}(x)\,,\\
\chi_2(x) &= \epsilon^{abc}\left(u^{aT}(x)\,C\,d^{b}(x)\right)\gamma_5 u^{c}(x)\,,\\
\chi_4(x) &= \epsilon^{abc}\left(u^{aT}(x)\,C\gamma_5\gamma_0\,d^{b}(x)\right)Iu^{c}(x)\,,
\end{aligned}$$

coupled with some level of source/sink smearing. Their choice of smearing levels is identical to those summarised in Table 5.1. We note that each of these local nucleon interpolators has a unique Dirac structure giving rise to different spin-flavour combinations. In particular, $\chi_1(x)$ and $\chi_4(x)$ contain scalar di-quark interpolators while $\chi_2(x)$ holds a vector di-quark interpolator. For their analysis, the ideal choice of variational parameters $(t_0,\delta t)$ was found to be $(18,2)$. In forming their nucleon spectrum, the authors considered the various combinations of interpolating structures. The results between χ_1, χ_2 and χ_2, χ_4 were found to be consistent, while the χ_1, χ_4 analysis revealed states not present in the other analyses. Within all three choices the lower portion of the spectrum was consistent. As we are only interested in the lowest negative parity nucleon states, we shall only consider the spectrum using χ_1 and χ_2 allowing us to construct an 8×8 correlation matrix. The resulting spectrum below 3 GeV is presented in Fig. 8.1.

As was found in Ref. [104], we obtain two close eigenstates between 1.5-2.0 GeV. The results at the lightest quark mass are consistent with the experimentally measured masses for the $N^{*}(1535)$ and $N^{*}(1650)$. We observe a reordering of states for the second heaviest quark mass. As was highlighted in Refs. [64, 104], without tracking eigenvectors across quark masses, one can easily miss-tag eigenstates based on their apparent ordering. Between 2 and 3 GeV we

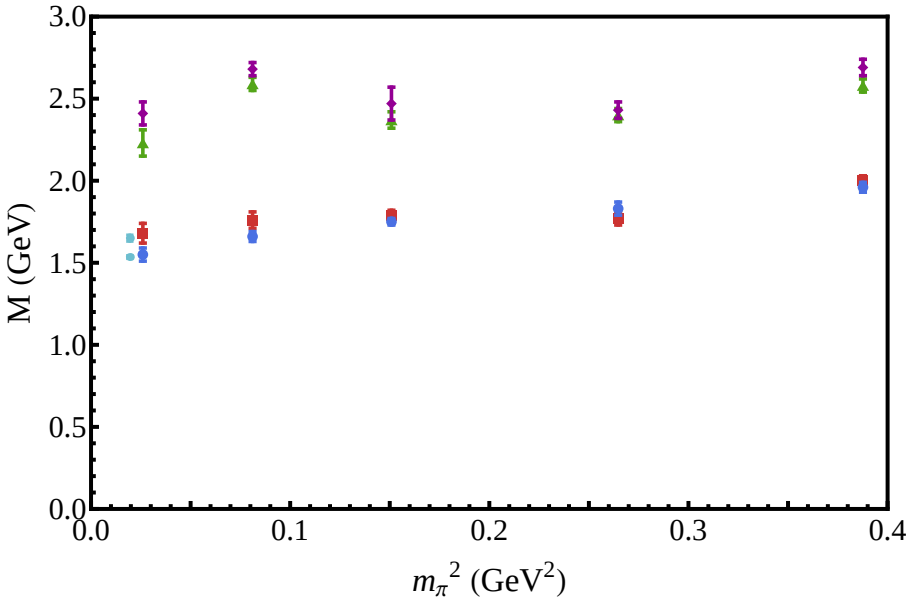

Figure 8.1: Spectrum observed in the negative parity nucleon ($N^{1/2^-}$) channel obtained using χ_1, χ_2 basis of operators as described in Ref. [104]. The light blue data points at the far left are the experimentally observed $N^*(1535)$ and $N^*(1650)$, with the masses taken from the PDG summary tables [105].

observe another pair of eigenstates, displaying similar behaviour to the lowest eigenstates. Within constituent quark models, the $N^*(1535)$ and $N^*(1650)$ are understood to be admixtures of spin-$1/2$ and spin-$3/2$ nucleon states coupled to angular momentum $\ell = 1$. This leads to two near degenerate eigenstates, with the small energy splitting stemming from spin-dependent forces. In Ref. [104] it was noted that the lowest eigenstates both have large contributions from χ_1 and χ_2 interpolators. As these interpolators carry different di-quark structures, large overlap with both interpolators suggest an admixture of spin states.

For both of the lowest lying negative parity nucleon states, we examine $\log(G)$ to ensure that we have single state dominance at the electromagnetic current insertion time $t_1 = 21$ and identify the time windows over which we can examine the form factors. The energies extracted from the identified fit-windows are compared against the dispersion relation for a single particle. These dispersion plots are presented in Figs. 8.2 and 8.3 for the first and second negative-parity eigenstates respectively. For the first non-trivial momentum relevant to the calculations presented in this chapter, we find reasonable agreement between the eigenstate energy and the dispersion relation across all quark masses, with the exception of the lightest mass where we observe a significant decrease in the energy for the lightest eigenstate when the boost is applied. This may be the result of cross-parity contamination at finite momentum whereby the ground state nucleon dominates the correlator at larger Euclidean time. Consequently we do not consider this mass in the form factor analysis.

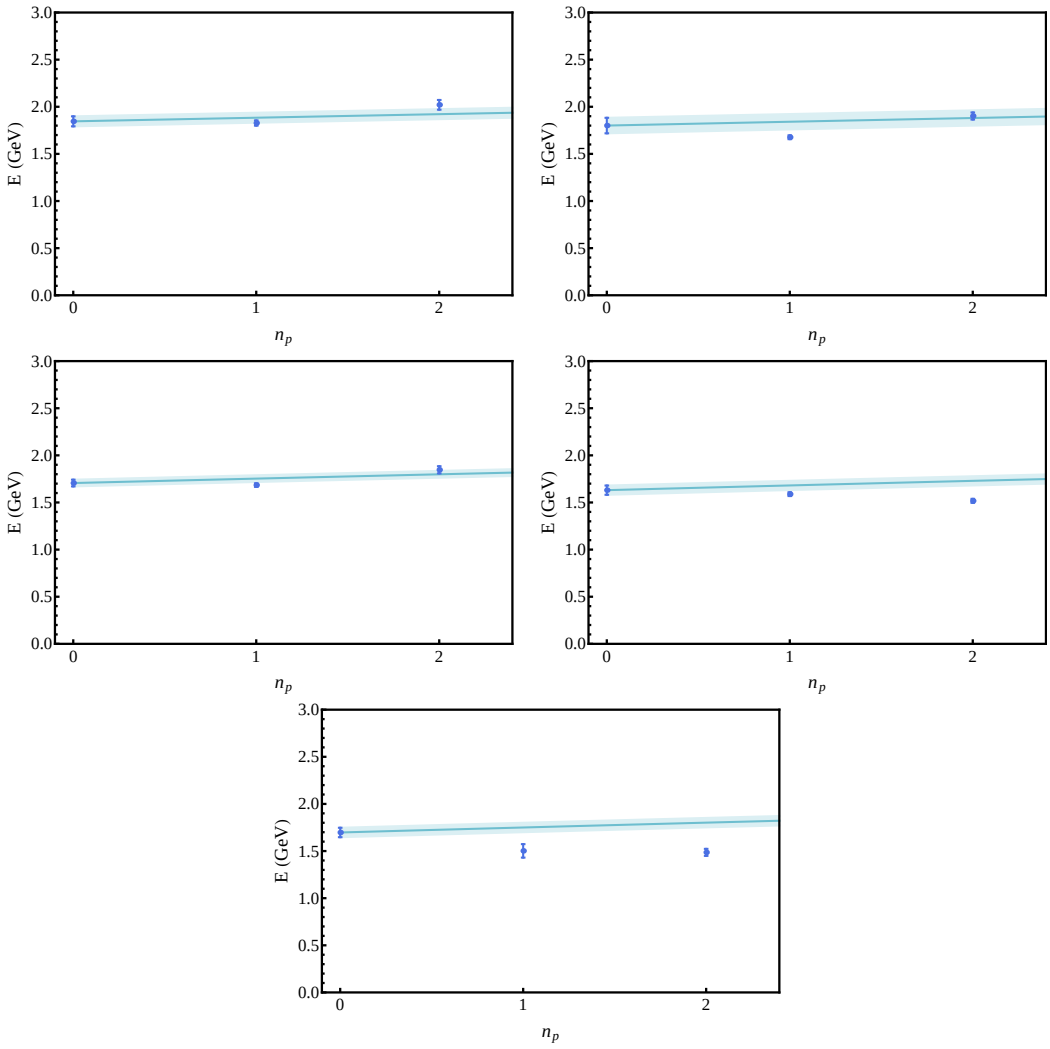

Figure 8.2: Extracted eigenstate energies for the first negative parity nucleon against the single particle dispersion expectation. The bottom axis is the centre-of-mass momentum in units of the minimum available momentum $\frac{2\pi}{L}$. The direction of decreasing quark mass is from left to right and down the page.

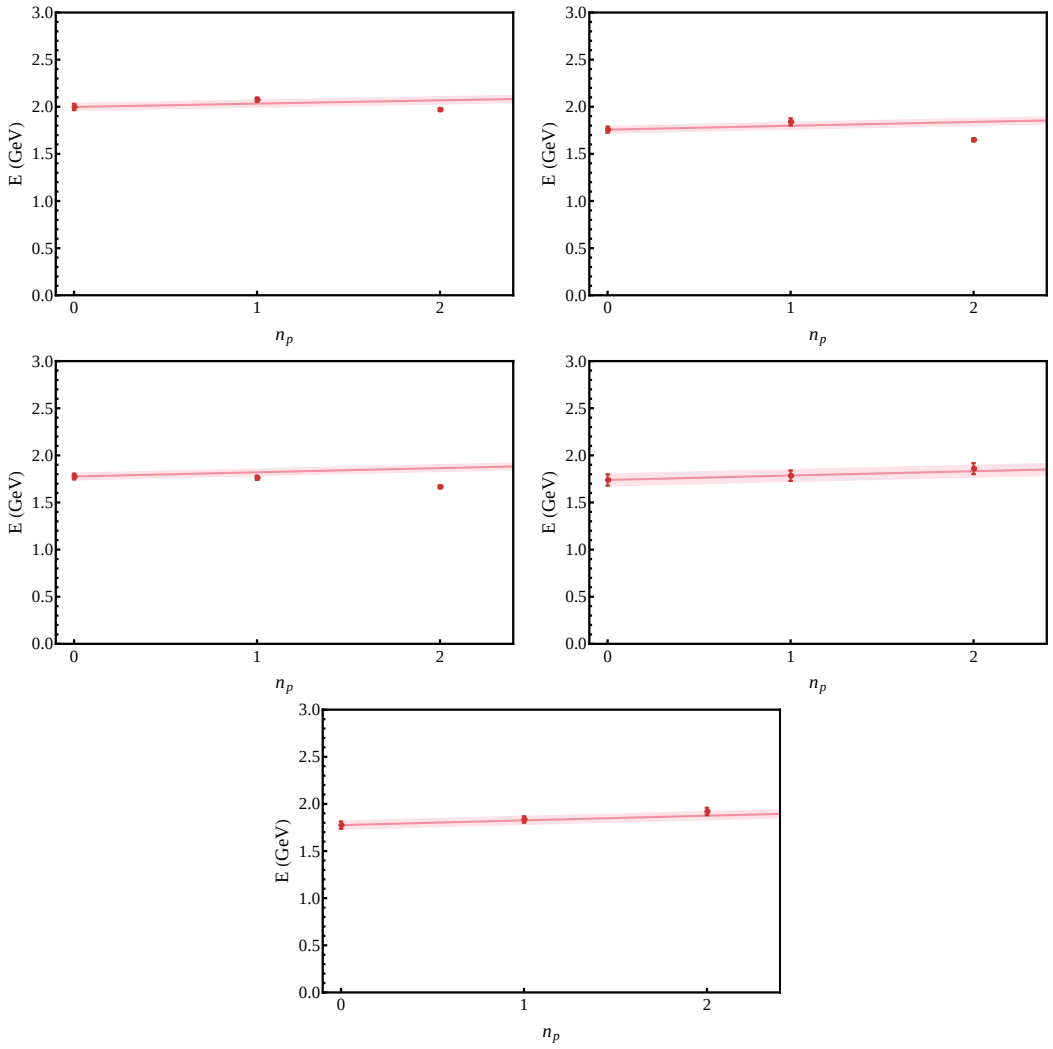

Figure 8.3: Extracted eigenstate energies for the second negative parity nucleon against the single particle dispersion expectation. The bottom axis is the centre-of-mass momentum in units of the minimum available momentum $\frac{2\pi}{L}$. The direction of decreasing quark mass is from left to right and down the page.

8.3 Electromagnetic Form Factors

To evaluate the negative parity nucleon electromagnetic form factors we consider the elastic matrix element,

$$\langle\, N^*(p',s') \,|\, J^\mu \,|\, N^*(p,s) \,\rangle\,.$$

As our nucleons are spin-$1/2$ states, this matrix element can be expressed as

$$\langle\, N^*(p',s') \,|\, J^\mu \,|\, N^*(p,s) \,\rangle = \left(\frac{M^2}{E(\vec{p})E(\vec{p}')}\right)^{1/2} \bar{u}(p',s') \left(\gamma^\mu\, F_1(Q^2) + i\frac{\sigma^{\mu\nu}q_\nu}{2M}\, F_2(Q^2)\right) u(p,s)\,,$$

where $F_1(Q^2)$ and $F_2(Q^2)$ are the so-called Dirac and Pauli Form Factors respectively. These are in turn related to the Sachs Electric and Magnetic form factors

$$\begin{aligned} G_E(Q^2) &= F_1(Q^2) - \frac{Q^2}{(2M)^2}F_2(Q^2)\,,\\ G_M(Q^2) &= F_1(Q^2) + F_2(Q^2)\,, \end{aligned}$$

which describe the distribution of charge and magnetisation within our nucleon states.

As this vertex decomposition is the same as that for the nucleon, isolation of the form factors is well established. Here we choose to follow the approach outlined in Refs. [42, 55], suitably adapted for negative parity baryons. As we are evaluating the full baryon correlator using χ^+ nucleon operators, this amounts to using the negative parity projectors, defined in Section 8.1. We choose to take either the incoming or outgoing state to be at rest. For such kinematics, one finds that the Sachs form factors G_E and G_M can be extracted through the following terms [42, 55]

$$\begin{aligned} G_E(Q^2) &= \overline{R}^0(\vec{q},0;\Gamma_0^{--},\Gamma_0^{--};\alpha)\,,\\ |\epsilon_{ijk}q^i|\,i\,G_M(Q^2) &= (E_q+M)\,\overline{R}^k(\vec{q},0;\Gamma_j^{--},\Gamma_0^{--};\alpha)\,, \end{aligned}$$

where

$$\Gamma_0^{--} = -\gamma_5\,\Gamma_0\,\gamma_5 \quad \text{and} \quad \Gamma_j^{--} = -\gamma_5\,\Gamma_j\,\gamma_5\,,$$

with

$$\Gamma_0 = \frac{1}{2}\begin{pmatrix} I & 0\\ 0 & 0\end{pmatrix} \quad \text{and} \quad \Gamma_j = \frac{1}{2}\begin{pmatrix} \sigma^j & 0\\ 0 & 0\end{pmatrix}\,,$$

and $\overline{R}$ is the reduced ratio

$$\overline{R}^\mu(\vec{p}',\vec{p};\Gamma',\Gamma;\alpha) = \left(\frac{2\,E(\vec{p})}{E(\vec{p})+M}\right)^{1/2}\left(\frac{2\,E(\vec{p}')}{E(\vec{p}')+M}\right)^{1/2} R^\mu(\vec{p}',\vec{p};\Gamma',\Gamma;\alpha)\,.$$

Evaluation the three-point correlation function is done using the same set of SST-propagators used in the evaluation of the meson form factors of chapters 6 and 7. In particular our quark fields are inserted at $t_0 = 16$ relative to the fixed boundary condition at $t = 0$ and the current at $t_1 = 21$. For the current we use an $\mathcal{O}(a)$-improved conserved vector current as described in Section 3.4.2. The current 3-momentum $\vec{q}$ is fixed in the x-direction with magnitude $|\vec{q}| = \frac{2\pi}{L}$. We use both $+\vec{q}$ and $-\vec{q}$, as required for the construction of our ratio as well as use of the U^*-trick. The current is polarised with $\mu = 3, 4$. We evaluate correlators for the four heaviest quark masses with the statistics outlined in Table 6.1.

In evaluating the form factors we consider the contribution from each individual quark-sector separately, with each sector normalised to give the quarks unit charge. The u-quark sector of the proton and the d-quark sector of the neutron are composed of two valence quarks and so we refer to these as the doubly-represented quark sector. Correspondingly, the d-quark sector of the proton and u-quark sector of the neutron are composed of a single valence quark and so we refer to this as the singly-represented quark sector. In constructing the baryon form factor from these quark sectors, we take the charge and quark-number weighted sum of all the quark sector contributions. For the proton-like states this amounts to

$$G^{p^*} = 2 \times \frac{2}{3} \times G^{\text{doub}} + 1 \times \left(-\frac{1}{3}\right) \times G^{\text{sing}}, \tag{8.4}$$

while for the neutron-like states we have

$$G^{n^*} = 2 \times \left(-\frac{1}{3}\right) \times G^{\text{doub}} + 1 \times \frac{2}{3} \times G^{\text{sing}}. \tag{8.5}$$

In Fig. 8.4 we show an example of the form factor plateaus for G_E and G_M. We note that due to the similar masses between these two states, we are essentially probing the same value of Q^2. Consequently, comparison of the plateaus in these figures highlights some notable similarities and differences between the form factors of these two states. Beginning with the electric form factor, we find that both states display very similar values for both quark sectors. Comparing the quark sectors for either state, we can see that the singly-represented quark sector is slightly larger than the doubly-represented quark sector. For the magnetic form factor, the doubly-represented quark sectors are of similar value, however we observe markedly different values for the singly-represented quark. In particular, the first eigenstate has a change in sign from the doubly-represented quark sector to the singly-represented quark sector, while for the second eigenstate there is no change in sign.

As was done in chapter 6 for the meson form factors, we perform shifts in Q^2 to ensure that the variations observed in the form factors between states and quark mass are not due to variations in the Q^2 associated with the change in mass

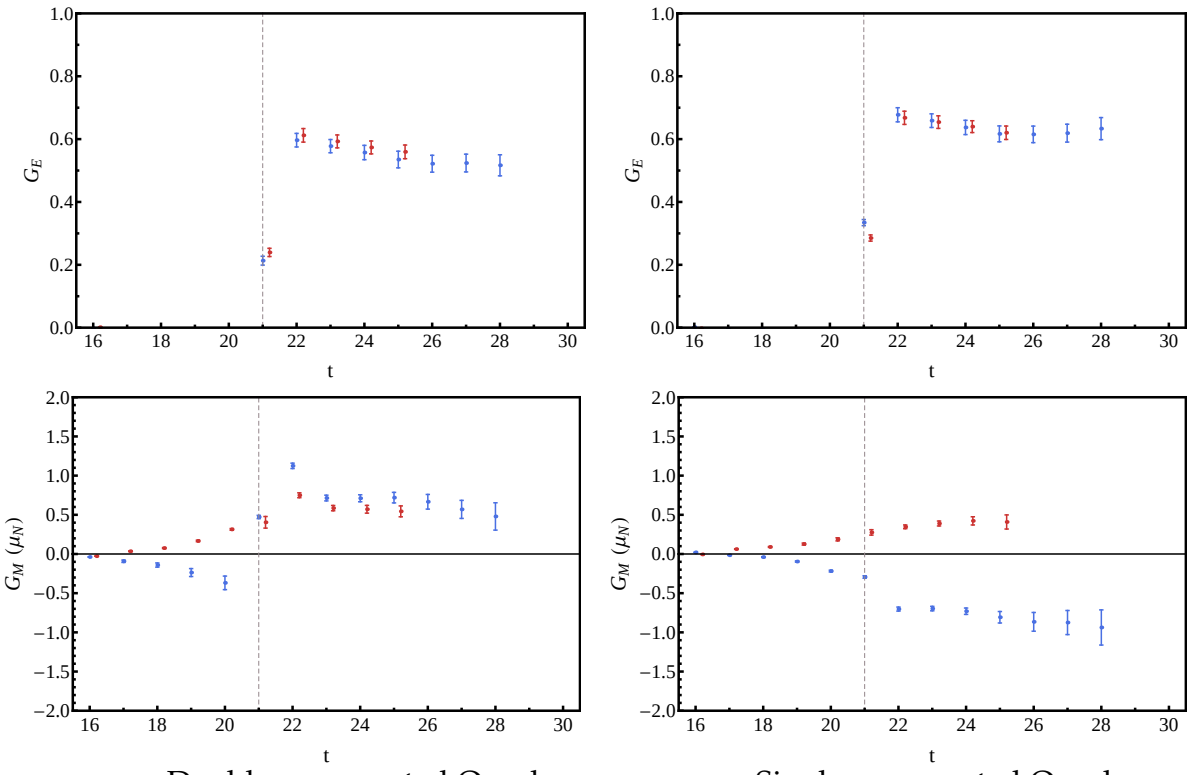

Figure 8.4: An example of the electromagnetic form factors as a function of Euclidean sink time for the first two negative parity nucleon eigenstates. Within each figure, the blue dataset (●) is for the first negative parity eigenstate while the red dataset (●) is for the second eigenstate. These results are obtained with $m_\pi = 570$ MeV. The figures on the left are for the doubly-represented quark sector while those on the right are for the singly-represented quark. Both quark sectors are normalised to single quarks of unit charge. The top figures show the electric form factor G_E while the bottom figures show the magnetic form factor G_M. We find similar values for the electric form factor in both quark sectors, however for the magnetic form factor the singly-represented quark contribution differs in sign between the two states suggesting very different spin configurations for these eigenstates. The vertical dashed line indicates the position of the current insertion.

of the eigenstate. In the case of baryons, we use a dipole form to describe the low Q^2 behaviour of the form factor [42, 134]

$$G_i(Q^2) = \left(\frac{\Lambda^2}{\Lambda^2 + Q^2}\right)^2 G_i(Q^2 = 0)\,,$$

where Λ is determined from the electric form factor using $G_E(0) = 1$, as required by charge conservation for each quark sector having unit charge. Though this choice may not necessarily be a good description of the complete Q^2 evolution for the form factor of an excited baryon, the required shifts in Q^2 are small. We choose to shift the data to $Q^2 = 0.16$ GeV^2 to minimise the shift for the lighter masses considered, with the largest shift around 0.018 GeV^2 occurring at the heaviest quark mass.

In Figs. 8.5 and 8.6 we show the quark sector contributions to G_E and G_M at $Q^2 = 0.16$ GeV^2 for the two lightest negative parity nucleon states. To provide some context to these values, we also include the corresponding quantities for the ground state nucleon. Beginning with the electric form factor we can see that both eigenstates display similar values for each quark sector, with the exception of the lightest quark mass considered. Here we observe a substantial increase in G_E for both quark sectors of the second eigenstate. Comparing the values for the negative parity states with the ground state, we find that for the heaviest three masses, G_E is considerably smaller that of the nucleon suggesting these states are significantly larger is size.

Turning our attention to the magnetic form factor, the most striking feature is the difference in sign between the singly-represented quark sectors. For the lower negative-parity eigenstate, the signs are consistent with that of the nucleon. Within both states, the doubly-represented quark sector is similar in value and displays a slight increase with increasing mass. Across all masses, the value is smaller than the doubly-represented quark sector of the nucleon by $\sim 0.5\,\mu_N$. For the singly-represented quark sectors, the lowest eigenstate displays a value larger in magnitude to that in the nucleon while the heavier eigenstate it is slightly smaller. For the singly-represented quark sector, there appears to be less variation than in the doubly-represented quark sector.

Recently, there have been a handful of model calculations of the magnetic moments for the lightest negative parity baryons [135–139]. In order to facilitate a comparison with these determinations, we need to take our results at finite Q^2 to $Q^2 = 0$. Once more we will make an assumption of common scaling between the electric and magnetic form factors for each quark sector such that the magnetic moment for each quark sector is extracted through

$$\mu = \frac{G_M(Q^2)}{G_E(Q^2)}\,.$$

In Fig. 8.7 we present the magnetic moments for the $1/2^+$ (proton) and $1/2^-$ (neutron) isospin states for the two lightest negative parity nucleon eigenstates

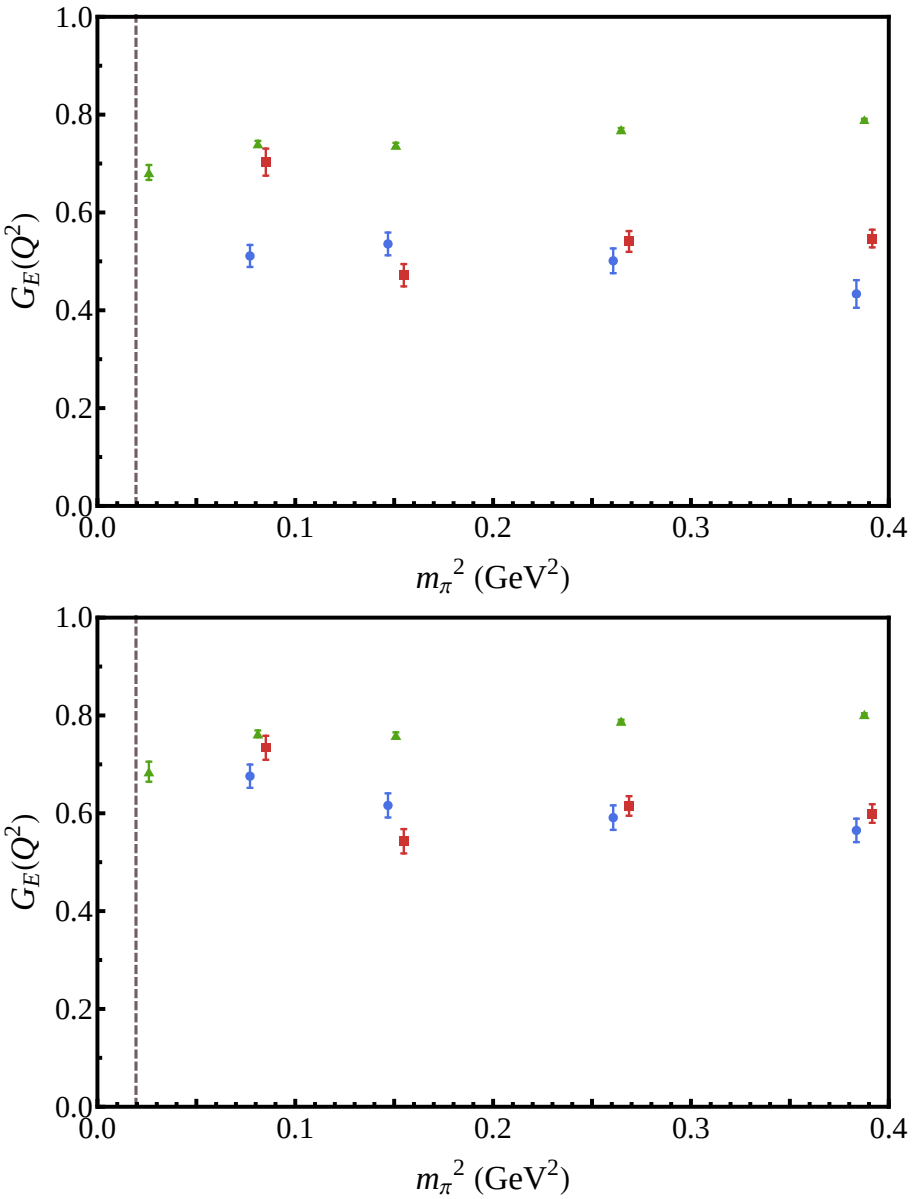

Figure 8.5: The unit-charge quark sector contributions to the electric form factor G_E of the first (●) and second (■) negative-parity nucleon eigenstates at the common value $Q^2 = 0.16$ GeV^2. The green points (▲) are the corresponding values for the ground state nucleon for comparison. The top figure illustrates results for the doubly-represented quark sector while the bottom figure illustrates those for the singly-represented quark sector. The vertical dashed line represents the physical point.

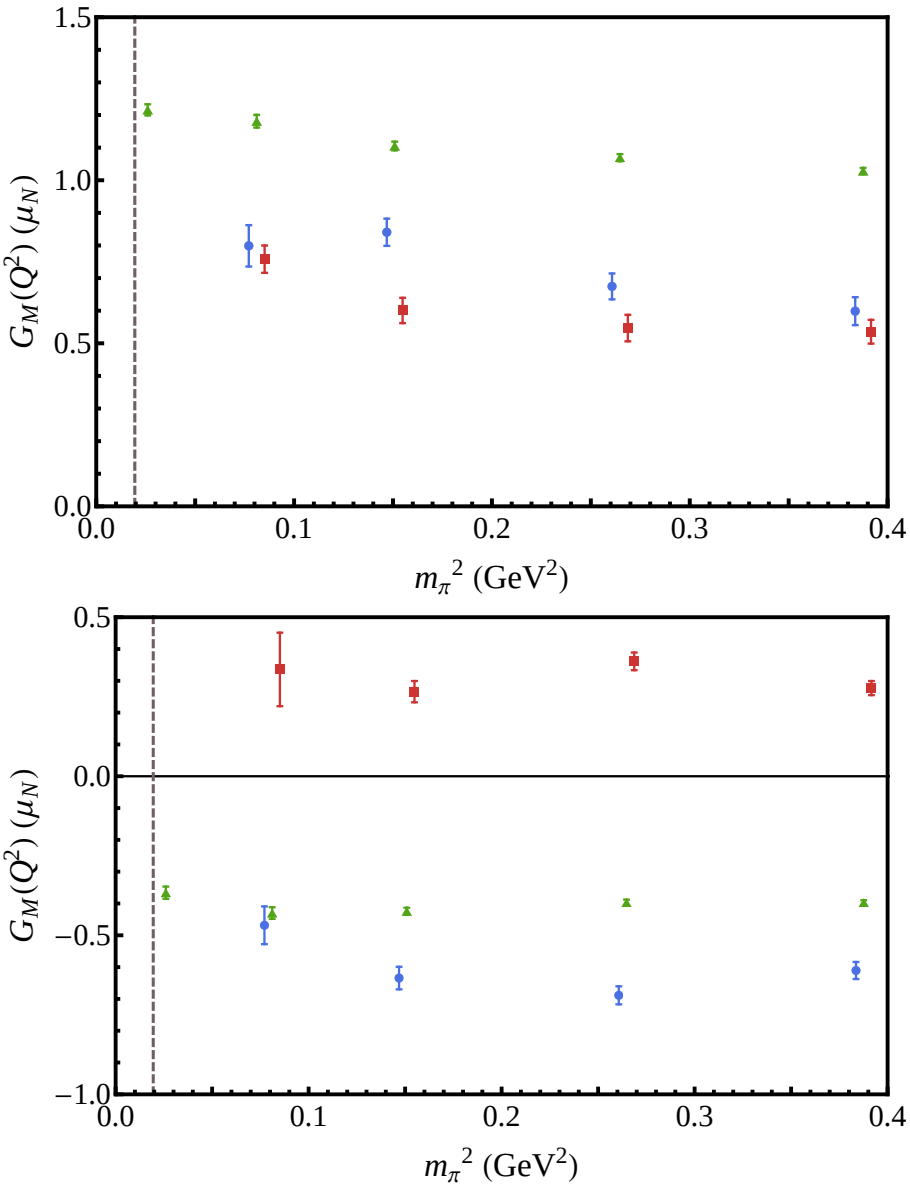

Figure 8.6: The unit-charge quark sector contributions to the magnetic form factor G_M of the first (●) and second (■) negative-parity nucleon eigenstates at the common value $Q^2 = 0.16$ GeV^2. The green points (▲) are the corresponding values for the ground state nucleon. The top figure illustrates results for the doubly-represented quark sector while the bottom figure illustrates those for the singly-represented quark sector. The vertical dashed line represents the physical point.

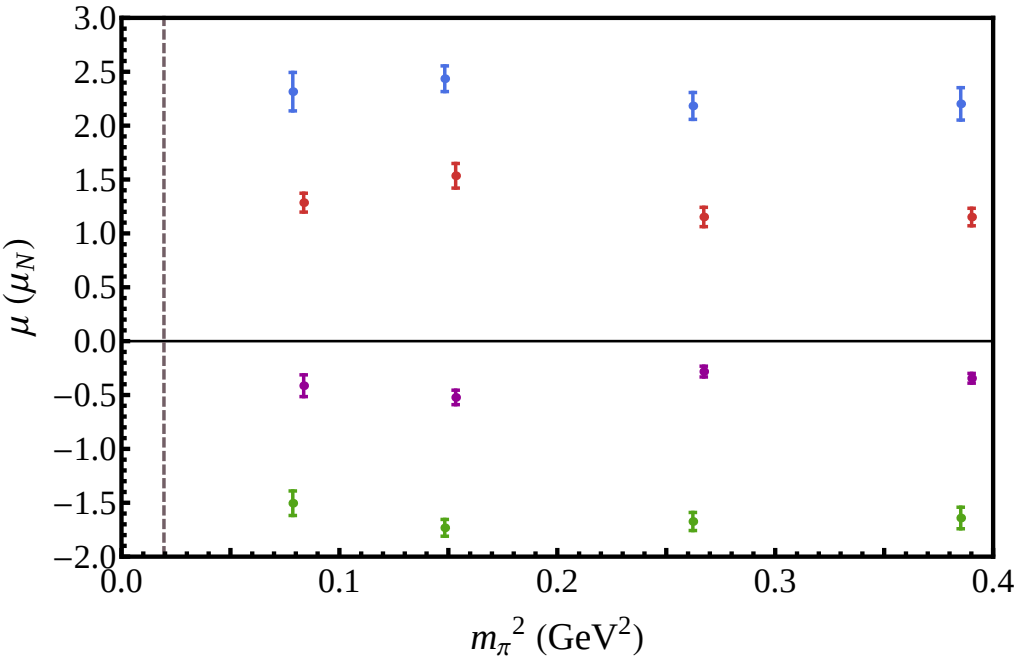

Figure 8.7: Magnetic moments for the $^1/_2^+$ (proton) and $^1/_2^-$ (neutron) isospin states for the two lightest negative parity nucleon eigenstates, obtained assuming common quark-sector scaling for G_E and G_M. In order to compare with model expectations we identify our eigenstates with the experimentally observed states via our negative parity spectrum, presented in Fig. 8.1. With this identification, we have $\mu_{p^*(1535)}$ (●), $\mu_{n^*(1535)}$ (●), $\mu_{p^*(1650)}$ (●) and $\mu_{n^*(1650)}$ (●). The grey dashed line represents the physical point.

Table 8.1: Comparison of the magnetic moments predicted by various model calculations and our lattice extraction. Our determination compares well for the $N^*(1535)$ nucleon state, however we obtain a different ordering for $\mu_{p^*(1650)}$ and $\mu_{n^*(1650)}$.

	$\mu_{p^*(1535)}$	$\mu_{n^*(1535)}$	$\mu_{p^*(1650)}$	$\mu_{n^*(1650)}$
CQM [135]	1.89	-1.28	0.11	0.95
CQM [136]	1.9	-1.3	0.1	1.0
χCQM [136]	1.6	-1.0	0.0	0.7
χCQM [137]	2.085	-1.570	-0.286	0.984
LCSR [138]	1.4	-0.54	-	-
EH [139]	1.24	-0.84	0.12	0.74
Our Result	2.32(18)	-1.50(11)	1.29(9)	-0.41(10)

obtained using Eqs. (8.4) and (8.5) and the magnetic moments for each quark sector. All states display little variation across all of the quark masses considered.

In Table 8.1 we compare model determinations with our lattice extraction for the lightest mass considered. Qualitatively our results for the lowest eigenstate compare well to the model calculations for both proton and neutron moments for the $N^*(1535)$, though slightly larger in magnitude.

For our heavier eigenstate our values are at odds with the quark model expectation. The quark model results suggest a neutron moment of $\sim$ +1 μ_N which is significantly larger in value than the corresponding proton moment. We find moments qualitatively similar to the lighter eigenstate, though somewhat smaller in magnitude.

In order to obtain a moment for the heavier eigenstate consistent with the quark model results, we would require quark sector contributions of 1.2 μ_N for the doubly-represented quark sector and 2.7 μ_N for the singly-represented quark sector. Our results for G_M at $Q^2 = 0.16$ GeV^2 are consistent in that we require both contributions to be positive. However, we observe the doubly-represented quark sector contribution to be larger than the singly-represented quark sector contribution at this value of Q^2.

This significant discrepancy calls our identification of the second negative parity state as the $N^*(1650)$ into question. This result indicates the second state is more likely a different finite-volume meson-baryon dressing of a bare state associated with the $N^*(1535)$. In the Hamiltonian effective field theory calculation of Ref. [133] our lowest lying state is described well by a bare state with a strong πN dressing. Our second state is described well by the same bare state but with a significant ηN dressing in the finite volume. Similar results are seen for the JLab led Hadron Spectrum Collaboration negative parity spectrum obtained on a smaller (2 fm)^3 lattice volume, thus testing the the finite-volume predictions of the model [133].

While the magnetic moments have not been calculated in the Hamiltonian model, the charge neutrality of the η meson will result in smaller moments. For example, $p^* \to n^*\pi^+$ is likely to make an important contribution to the p^* magnetic moment on the lattice. A similar pattern of moments is seen in Table 8.1 with the moment attributed to the $N^*(1650)$ suppressed in magnitude. This lends further support to our second state being attributed to the $N^*(1535)$ in the finite volume of the lattice. As such, state identification on the finite volume of the lattice presents an interesting challenge of unanticipated difficulty.

8.4 Summary

In this chapter we carefully examined the baryon correlator in order to understand how positive and negative parity eigenstate contributions are contained within. Through this examination, we have developed a general strategy for accessing both two- and three-point correlation functions for both positive and negative parity states, as well as transition elements between the various parity eigenstates, whereby the desired contributions are isolated through the selection of the relevant parity projection operator applied to the baryon correlator formed from χ^+ interpolators.

This framework was then utilised to examine the electromagnetic form factors for the lightest two negative parity nucleon eigenstates on the PACS-CS ensembles. We observed very similar behaviour between the two eigenstates for the electric form factor G_E, which in comparing with the ground state nucleon were observed to be considerably smaller suggesting these states are significantly larger in size. For the magnetic form factor G_M, we find that the doubly-represented quark sector is consistent between the two eigenstates. However for the singly-represented quark sector the values differ in both sign and magnitude.

In constructing p^* and n^* magnetic moments to compare with model calculations, we find that the first eigenstate gives values that are consistent with the expected values for the $N^*(1535)$ from constituent quark models. The second eigenstate was found to be inconsistent with the expected values for the $N^*(1650)$ raising doubt as to whether this state, which appears consistent in mass with the $N^*(1650)$, is in fact this state. Examination of the spectrum in Ref. [133] using a Hamiltonian effective field theory suggests this second state could be identified as a different finite-volume meson-baryon dressing of a bare state associated with the $N^*(1535)$. This highlights the complexity and difficulty one faces in identifying eigenstates on the finite volume of the lattice.

Chapter 9

Negative Parity Transition Form Factors

In the previous chapter we made use of variational techniques to evaluate the elastic electromagnetic form factors for the lightest negative-parity nucleon states. While such quantities can provide important insight into the underlying structure of these states and inform model calculations, defining and measuring such quantities experimentally present significant challenges. Experimentally the quantities of interest are the transition elements for the electroproduction processes $\gamma^* N \rightarrow N^*$, specifically the transverse and longitudinal helicity amplitudes $\mathcal{A}_{\frac{1}{2}}$ and $\mathcal{S}_{\frac{1}{2}}$.

Previous lattice calculations have focused primarily on the $\Delta \rightarrow N\gamma$ transition. The framework for such a calculation was established in Ref. [140] and subsequently examined comprehensively both in quenched [141, 142] and full QCD [143, 144]. For all of these studies, due to the choice of lattice ensemble parameters, the Δ baryon remains the lightest state in this channel and so this process can be examined using standard techniques. The results of [144] show good qualitative agreement with the experimental data, especially in the value extracted for $E2/M1$ ratio, however the authors outline that discrepancies observed in the exact behaviour of these amplitudes, particularly the $M1$ amplitude, highlight important chiral dynamics to this process.

The only other nucleon transition considered to date has been the $N^*(1440) \rightarrow N\gamma$ transition [145, 146]. However, as yet it is unlikely any group has properly isolated the $N^*(1440)$ on the lattice [133]. Nonetheless, experimental determinations indicate that the sign of the $\mathcal{A}_{\frac{1}{2}}$ transition form factor is negative at low Q^2, contrary to constituent quark models which predict a positive sign. Therefore evaluation of this amplitude may assist in understanding the underlying dynamics of the Roper resonance and the make up of this state, both on the lattice and in the continuum.

A notably absent calculation is the evaluation of the $N^*(1535) \rightarrow N\gamma$ transition. Having outlined how we isolate the correlation functions for negative parity baryons in the previous chapter, we shall now consider the extraction of the transition form factors for such states. We begin in Section 9.1 with the presentation of a general framework through which one can determine $N^* \rightarrow N\gamma$ transition amplitudes for all choices and combinations of parity, all from the same

baryon correlator. In Section 9.2 we utilise this framework to examine the $\mathcal{A}_{\frac{1}{2}}$ and $\mathcal{S}_{\frac{1}{2}}$ form factors of the first two negative parity nucleon eigenstates and then conclude with a summary in Section 9.3.

9.1 Generalised Nucleon Transition Vertices

Experimentally the quantities of interest are the transverse and longitudinal helicity amplitudes $\mathcal{A}_{\frac{1}{2}}$ and $\mathcal{S}_{\frac{1}{2}}$

$$\mathcal{A}_{\frac{1}{2}} = \sqrt{\frac{2\pi\alpha}{K}}\frac{1}{e}\langle\, N^*, s_z' = {}^1\!/_2{}^+ \,|\, \epsilon_\mu^{(+)} J^\mu \,|\, N, s_z = {}^1\!/_2{}^- \,\rangle\,,$$
$$\mathcal{S}_{\frac{1}{2}} = \sqrt{\frac{2\pi\alpha}{K}}\frac{1}{e}\frac{|\vec{q}|}{Q}\langle\, N^*, s_z' = {}^1\!/_2{}^+ \,|\, \epsilon_\mu^{(0)} J^\mu \,|\, N, s_z = {}^1\!/_2{}^+ \,\rangle\,,$$

where e is the magnitude of the electron's charge, α the electromagnetic fine structure constant and $Q = \sqrt{Q^2}$. Here ϵ_μ represents the polarization of the incoming virtual photon, with $|\vec{q}|$ the photon's 3-momentum in the N^* rest frame and $K = \frac{M^2-m^2}{2M}$. We identify M with the resonance N^* and m with the nucleon N. These amplitudes can in turn be related to matrix elements with the familiar form

$$\langle N^*, p', s'|\, J^\mu \,|N, p, s\rangle \;= e\,\left(\frac{M\,m}{E'(\vec{p}')\,E(\vec{p})}\right)^{1/2}\,\bar{u}_{(M)}(p', s')\,\Gamma(p', p)\,u_{(m)}(p, s)\,,$$

which parametrises the interaction via a different choice of Lorentz covariant structures and consequently a different set of form factors. We shall note that all spinors in this and subsequent expressions are regular Dirac spinors. Here the subscript, $u_{(\xi)}$, labels the mass of the state for which the spinor describes. A convenient choice of parametrisation is that first presented in Ref. [147] and nicely summarised in Refs. [148, 149], which allows us to express the normal-parity (${}^1\!/_2{}^+ \to {}^1\!/_2{}^+$) transition as

$$\langle N^*, p', s'|J^\mu(0)|N, p, s\rangle = e\,\left(\frac{M\,m}{E'(\vec{p}')\,E(\vec{p})}\right)^{1/2}\,\bar{u}_{(M)}(p', s')\,\tilde{J}^\mu\,u_{(m)}(p, s)\,, \qquad (9.1)$$

and abnormal-parity (${}^1\!/_2{}^+ \to {}^1\!/_2{}^-$) transition

$$\langle N^*, p', s'|J^\mu(0)|N, p, s\rangle = e\,\left(\frac{M\,m}{E'(\vec{p}')\,E(\vec{p})}\right)^{1/2}\,\bar{u}_{(M)}(p', s')\,\tilde{J}^\mu\,\gamma_5\,u_{(m)}(p, s)\,, \qquad (9.2)$$

with

$$\tilde{J}^\mu = -\left[q^2\,\gamma^\mu - \not{q}\,q^\mu\right]\,G_1(Q^2) - \left[(P\cdot q)\,\gamma^\mu - \not{q}\,P^\mu\right]\,G_2(Q^2)\,,$$

and $P = \frac{1}{2}(p' + p)$. Using this decomposition, the helicity amplitudes can be expressed in terms of G_1 and G_2 as

$$\mathcal{A}_{\frac{1}{2}}(Q^2) = b_+ \left[2Q^2\, G_1(Q^2) - (M^2 - m^2)\, G_2(Q^2)\right] ,$$
$$\mathcal{S}_{\frac{1}{2}}(Q^2) = b_+ \frac{|\vec{q}|}{\sqrt{2}} \left[2\,(M + m)\, G_1(Q^2) + (M - m)\, G_2(Q^2)\right] ,$$

for normal transitions, and

$$\mathcal{A}_{\frac{1}{2}}(Q^2) = b_- \left[2Q^2\, G_1(Q^2) - (M^2 - m^2)\, G_2(Q^2)\right] ,$$
$$\mathcal{S}_{\frac{1}{2}}(Q^2) = -b_- \frac{|\vec{q}|}{\sqrt{2}} \left[2\,(M - m)\, G_1(Q^2) + (M + m)\, G_2(Q^2)\right] ,$$

for abnormal transitions, with

$$b_\pm = e\sqrt{\frac{E \mp m}{8\, m\, K}} .$$

Another popular choice of parametrisation is to express the vertex in terms of Pauli-Dirac-like form factors $F_1^*(Q^2)$ and $F_2^*(Q^2)$. Taking

$$F_1^*(Q^2) = Q^2\, G_1(Q^2)$$
$$F_2^*(Q^2) = -\frac{(M^2 - m^2)}{2}\, G_1(Q^2) .$$

one can re-express the transition matrix elements [149] as

$$\langle N^*, p', s'|J^\mu(0)|N, p, s\rangle = e \left(\frac{M\, m}{E'(\vec{p}')\, E(\vec{p})}\right)^{1/2} \bar{u}_{(M)}(p', s')\, \Gamma_i^\mu(p', p)\, u_{(m)}(p, s) ,$$

with

$$\Gamma_{\rm n}^\mu(p', p) = \left(\gamma^\mu - \frac{\not{q}\, q^\mu}{q^2}\right) F_1^*(Q^2) + \frac{i\sigma^{\mu\nu}\, q_\nu}{M + m}\, F_2^*(Q^2) , \tag{9.3}$$

for normal transitions and

$$\Gamma_{\rm a}^\mu(p', p) = \left(\gamma^\mu - \frac{\not{q}\, q^\mu}{q^2}\right) \gamma_5\, F_1^*(Q^2) + \frac{i\sigma^{\mu\nu}\, q_\nu}{M - m}\, \gamma_5\, F_2^*(Q^2) . \tag{9.4}$$

for abnormal transitions. We note that our choice of normalisation for the F_2^* form factor in the abnormal transition vertex differs from the common choice [150, 151] by a factor of $\left(\frac{M-m}{M+m}\right)$. However, the absence of parity doubling in the low-lying energy eigenstates of QCD admit this formalism. The advantage of our normalisation is apparent if we consider the expressions for the helicity amplitudes in term of the Dirac and Pauli form factors, namely

$$\mathcal{A}_{\frac{1}{2}}^\pm(Q^2) = 2\, b_\pm \left[F_1^*(Q^2) + F_2^*(Q^2)\right] ,$$
$$\mathcal{S}_{\frac{1}{2}}^\pm(Q^2) = \pm\frac{\sqrt{2}\, b_\pm\, (M \pm m)\, |\vec{q}|}{Q^2} \left[F_1^*(Q^2) - \tau_\pm\, F_2^*(Q^2)\right] ,$$

where

$$b_{\pm} = \sqrt{\frac{Q^2 + (M \mp m)^2}{8\,m\,(M^2 - m^2)}}\,,$$

and

$$\tau_{\pm} = \frac{Q^2}{(M \pm m)^2}\,,$$

with the $\pm$ label indicating the parity of the resonant nucleon state. Compare this to the choice of Refs. [150, 151]

$$\begin{aligned}
\mathcal{A}^{-}_{\frac{1}{2}}(Q^2) &= 2\,b_{-}\,\left[F_1^*(Q^2) + \frac{M-m}{M+m}\,F_2^*(Q^2)\right]\,,\\
\mathcal{S}^{-}_{\frac{1}{2}}(Q^2) &= -\frac{\sqrt{2}\,b_{-}\,(M+m)\,|\vec{q}|}{Q^2}\,\left[\frac{M-m}{M+m}\,F_1^*(Q^2) - \tau_{+}\,F_2^*(Q^2)\right]\,,
\end{aligned}$$

we can see that for our choice the helicity amplitudes are proportional to generalisations of the Sachs electric and magnetic form factors

$$\begin{aligned}
G_E^*(Q^2) &= F_1^*(Q^2) - \frac{Q^2}{(M \pm m)^2}\,F_2^*(Q^2)\,,\\
G_M^*(Q^2) &= F_1^*(Q^2) + F_2^*(Q^2)\,,
\end{aligned}$$

while such an identification is not possible using the normalisation of Refs. [150, 151] due to a relative factor of $\left(\frac{M-m}{M+m}\right)$ between F_1^* and F_2^*. In our analysis we shall use the decompositions given by Eqs. (9.3) and (9.4).

Having suitably parametrised the desired matrix elements and subsequently related the corresponding form factors to the helicity amplitudes $\mathcal{A}_{\frac{1}{2}}$ and $\mathcal{S}_{\frac{1}{2}}$, we shall now consider how these quantities are encoded in the three-point correlation function. For this we will begin with the eigenstate projected three-point correlation function, equipped with the correct parity selector as outlined in Section 8.1,

$$\begin{aligned}
G^{\mu}_{\alpha^i\to\beta^j}(p', p, t_2, t_1; (\Gamma')^{ji}) = \sum_{\vec{x}_2,\vec{x}_1} e^{-i\vec{p}'\cdot\vec{x}_2}\,e^{+i(\vec{p}'-\vec{p})\cdot\vec{x}_1}\\
\times\,\mathrm{Tr}\left[(\Gamma')^{ji}\,\langle\Omega|\phi^{\beta^j,\vec{p}'}(x_2)\,J^{\mu}(x_1)\,\bar{\phi}^{\alpha^i,\vec{p}}(0)|\Omega\rangle\right]\,. \qquad (9.5)
\end{aligned}$$

Here the i, j labels denote an element of $\{+,-\}$ indicating the parity of the associated nucleon state. As discussed in Section 8.1, the parity selectors are defined as

$$\begin{aligned}
\Gamma^{++} &= \Gamma\,,\\
\Gamma^{-+} &= \Gamma\gamma_5\,,\\
\Gamma^{+-} &= -\gamma_5\Gamma\,,\\
\Gamma^{--} &= -\gamma_5\Gamma\gamma_5\,.
\end{aligned}$$

Following the standard arguments of inserting completeness, invoking operator translation and the selection of Euclidean time, this expression reduces to the familiar form

$$G^{\mu}_{\alpha^i\to\beta^j}(p',p,t_2,t_1;(\Gamma')^{ji}) = e^{-E_{\beta j}(\vec{p}')\,(t_2-t_1)}\,e^{-E_{\alpha^i}(\vec{p})\,t_1} \times \mathrm{Tr}\left[(\Gamma')^{ji}\ \langle\Omega|\phi^{\beta j,\vec{p}'}(0)|\beta^j,p',s'\rangle \times \langle\beta^j,p',s'|J^{\mu}(0)|\alpha^i,p,s\rangle\ \langle\alpha^i,p,s|\bar{\phi}^{\alpha^i,\vec{p}}(0)|\Omega\rangle\right] . \quad (9.6)$$

Using our formalism for parity selection, we parametrise all baryon operator overlap factors as

$$\langle\Omega|\phi^{\alpha^i,\vec{p}}(0)|\alpha^i,p,s\rangle = \mathcal{Z}^{\alpha}_i(\vec{p}')\sqrt{\frac{m_{\alpha^i}}{E_{\alpha^i}(\vec{p})}}\,u_{(m_{\alpha^i})}(p,s)\,.$$

Substituting these overlap factors into Eq. (9.6) we have,

$$G^{\mu}_{\alpha^i\to\beta^j}(p',p,t_2,t_1;(\Gamma')^{ji}) = e^{-E_{\beta j}(\vec{p}')\,(t_2-t_1)}\,e^{-E_{\alpha^i}(\vec{p})\,t_1}\ \left(\frac{M_{\beta j}\,m_{\alpha^i}}{E_{\beta^j}(\vec{p}')\,E_{\alpha^i}(\vec{p})}\right)\ \mathcal{Z}^{\beta j}(\vec{p}')\,\bar{\mathcal{Z}}^{\alpha^i}(\vec{p}) \times \mathrm{Tr}\left[(\Gamma')^{ji}\ \left(\sum_{s'} u_{\beta j}(p',s')\,\bar{u}_{\beta j}(p',s')\right)\ \Gamma^{\mu}(p',p)\ \left(\sum_{s} u_{\alpha^i}(p,s)\,\bar{u}_{\alpha^i}(p,s)\right)\right] ,$$

which upon applying the spin-sum identities reduces to

$$G^{\mu}_{\alpha^i\to\beta^j}(p',p,t_2,t_1;(\Gamma')^{ji}) = e^{-E_{\beta j}(\vec{p}')\,(t_2-t_1)}\,e^{-E_{\alpha^i}(\vec{p})\,t_1}\ \left(\frac{\mathcal{Z}^{\beta^j}(\vec{p}')\,\bar{\mathcal{Z}}^{\alpha^i}(\vec{p})}{4\,E_{\beta^j}(\vec{p}')\,E_{\alpha^i}(\vec{p})}\right) \times \mathrm{Tr}\left[(\Gamma')^{ji}\ \left(\not{p}'+M_{\beta^j}\right)\ \Gamma^{\mu}(p',p)\ \left(\not{p}+m_{\alpha^i}\right)\right] . \quad (9.7)$$

The trace within the above expression is a linear combination of the form factors and it is this term we wish to isolate in our ratio of correlation functions.

For our choice of ratio we require the three-point correlators for both the forwards process $\alpha^i \to \beta^j$ and the reverse process $\beta^j \to \alpha^i$. Applying the same arguments as above to the correlator for the backwards process, we have

$$G^{\mu}_{\beta^j\to\alpha^i}(p,p',t_2,t_1;(\tilde{\Gamma}')^{ij}) = e^{-E_{\alpha^i}(\vec{p})\,(t_2-t_1)}\,e^{-E_{\beta j}(\vec{p}')\,t_1}\ \left(\frac{\mathcal{Z}^{\alpha^i}(\vec{p})\,\bar{\mathcal{Z}}^{\beta^j}(\vec{p}')}{4\,E_{\beta^j}(\vec{p}')\,E_{\alpha^i}(\vec{p})}\right) \times \mathrm{Tr}\left[(\tilde{\Gamma}')^{ij}\ \left(\not{p}+m_{\alpha^i}\right)\ \Gamma^{\mu}(p,p')\ \left(\not{p}'+M_{\beta^j}\right)\right] ,$$

where the tilde on the projection matrix denotes that it is distinct to that used in the forwards process. Using the symmetry property of Eqs. (9.3) and (9.4),

$$\gamma_0\ (\Gamma^{\mu}(p,p'))^{\dagger}\ \gamma_0 = \Gamma^{\mu}(p',p)\,,$$

it is possible to re-express the trace in this correlator as

$$G^{\mu}_{\beta^j\to\alpha^i}(p,p',t_2,t_1;(\tilde{\Gamma}')^{ij}) = e^{-E_{\alpha^i}(\vec{p})\,(t_2-t_1)}\,e^{-E_{\beta^j}(\vec{p}')\,t_1}\,\left(\frac{\mathcal{Z}^{\alpha^i}(\vec{p})\,\bar{\mathcal{Z}}^{\beta^j}(\vec{p}')}{4\,E_{\beta^j}(\vec{p}')\,E_{\alpha^i}(\vec{p})}\right) \times \mathrm{Tr}\left[(\Gamma')^{ji}\,\left(\not{p}'+M_{\beta^j}\right)\,\Gamma^{\mu}(p',p)\,\left(\not{p}+m_{\alpha^i}\right)\right]^{*}, \quad (9.8)$$

provided that we have

$$(\tilde{\Gamma}')^{ij} = \gamma_0\,\left[(\Gamma')^{ji}\right]^{\dagger}\,\gamma_0\,.$$

We shall therefore use this relation as the definition for the necessary choice of projection operator for the correlator describing the backwards process. In the case where $\gamma_0\,(\Gamma')^{\dagger}\,\gamma_0 = \Gamma'$, this relationship reduces to

$$(\tilde{\Gamma}')^{ij} = (\Gamma')^{ij}\ ,$$

for all choices of parity labels i and j. That is to say we can use the same base projection operator, Γ', suitably adjusted for source and sink parities using the parity selectors outlined in Section 8.1.

Having identified the term of interest in the three-point correlator, we now construct the following ratio,

$$R^{\mu}_{\alpha^i\to\beta^j}(p',p;\Gamma',\Gamma;j,i) = \sqrt{\frac{\langle G_{\alpha^i\to\beta^j}(p',p,t_2,t_1;(\Gamma')^{ji})\rangle\,\langle G_{\beta^j\to\alpha^i}(p,p',t_2,t_1;(\Gamma')^{ij})\rangle}{\langle G_{\alpha^i}(p,t_2;(\Gamma)^{ii})\rangle\,\langle G_{\beta^j}(p',t_2;(\Gamma)^{jj})\rangle}}\,,$$

where we note that the ordering of p' and p, as well as the parity label j and i follow the tradition of source on the right and sink on the left. Using the parity selected correlators, both two-point functions that appear in the denominator can be expressed as

$$G_{\alpha^i}(p,t_2;\Gamma_0^{ii}) = e^{-E_{\alpha^i}(\vec{p})\,t_2}\,\mathcal{Z}^{\alpha^i}(\vec{p})\,\bar{\mathcal{Z}}^{\alpha^i}(\vec{p})\,\left(\frac{E_{\alpha^i}(\vec{p})+m_{\alpha^i}}{2\,E_{\alpha^i}(\vec{p})}\right)\,,$$
$$G_{\beta^j}(p',t_2;\Gamma_0^{jj}) = e^{-E_{\beta^j}(\vec{p}')\,t_2}\,\mathcal{Z}^{\beta^j}(\vec{p}')\,\bar{\mathcal{Z}}^{\beta^j}(\vec{p}')\,\left(\frac{E_{\beta^j}(\vec{p}')+M_{\beta^j}}{2\,E_{\beta^j}(\vec{p}')}\right)\,,$$

which substituting into the ratio, along with Eqs. (9.7) and (9.8), gives us

$$R^{\mu}_{\alpha^i\to\beta^j}(p',p;\Gamma',\Gamma;j,i) = \frac{1}{4\,E_{\alpha^i}(\vec{p})\,E_{\beta^j}(\vec{p}')}\left\{\left(\frac{2\,E_{\alpha^i}(\vec{p})}{E_{\alpha^i}(\vec{p})+m_{\alpha^i}}\right)\,\left(\frac{2\,E_{\beta^j}(\vec{p}')}{E_{\beta^j}(\vec{p}')+M_{\beta^j}}\right)\right\}^{1/2} \times \mathrm{Tr}\left[(\Gamma')^{ji}\,\left(\not{p}'+M_{\beta^j}\right)\,\Gamma^{\mu}(p',p)\,\left(\not{p}+m_{\alpha^i}\right)\right]\,.$$

This can be further simplified by using the reduced ratio

$$\overline{R}^{\mu}_{\alpha^i\to\beta^j}(p',p;\Gamma',\Gamma;j,i) = \left(\frac{2\,E_{\alpha^i}(\vec{p})}{E_{\alpha^i}(\vec{p})+m_{\alpha^i}}\right)^{1/2}\,\left(\frac{2\,E_{\beta^j}(\vec{p}')}{E_{\beta^j}(\vec{p}')+M_{\beta^j}}\right)^{1/2}\,R^{\mu}_{\alpha^i\to\beta^j}(p',p;\Gamma',\Gamma;j,i)\,,$$

to give

$$(E_{\alpha^i}(\vec{p}) + m_{\alpha^i})\ \left(E_{\beta^j}(\vec{p}') + M_{\beta^j}\right) \overline{R}^{\mu}_{\alpha^i \to \beta^j}(p', p; \Gamma', \Gamma; j, i) = \\ \mathrm{Tr}\left[(\Gamma')^{ji}\ \left(\not{p}' + M_{\beta^j}\right)\ \Gamma^{\mu}(p', p)\ \left(\not{p} + m_{\alpha^i}\right)\right] .$$

In order to isolate the form factors we can express the trace, which is itself a linear combination of these terms, as a matrix product

$$\mathrm{Tr}\left[(\Gamma')^{ji}\ \left(\not{p}' + M_{\beta^j}\right)\ \Gamma^{\mu}(p', p)\ \left(\not{p} + m_{\alpha^i}\right)\right] \\ = \begin{pmatrix} K_1^{\mu}(p', p; (\Gamma')^{ji}) & K_2^{\mu}(p', p; (\Gamma')^{ji}) \end{pmatrix} \begin{pmatrix} F_1^*(Q^2) \\ F_2^*(Q^2) \end{pmatrix} ,$$

expressed here in terms of the Pauli-Dirac decomposition. The kinematic weights $K_i^{\mu}(p', p; (\Gamma')^{ji})$ are determined by substituting the explicit form for the vertex function in the trace and reducing the product of γ-matrices into expressions involving the incoming and outgoing energies and momenta, the eigenstate masses and the hadron spins via Pauli matrices. These expressions are presented in Appendix C for both normal and abnormal transitions. By expressing each independent determination of $\overline{R}^{\mu}_{\alpha^i \to \beta^j}(p', p; \Gamma', \Gamma; j, i)$ in this way, we can combine the results into a single vector equation

$$\mathbf{R} = \mathbb{K}\,\mathbf{F} ,$$

where $\mathbf{R}$ is a vector containing n independent ratio determinations, $\mathbb{K}$ is an $n \times 2$ matrix of kinematic factors and $\mathbf{F}$ is a vector containing the 2 form factors. Provided we have atleast two linearly independent determinations of $\overline{R}^{\mu}_{\alpha^i \to \beta^j}(p', p; \Gamma', \Gamma; j, i)$, we can solve the linear system by taking the pseudoinverse of $\mathbb{K}$ via the Singular Value Decomposition (SVD) of $\mathbb{K}$, to give

$$\mathbf{F} = \mathbb{K}^{+}\,\mathbf{R} .$$

To express this solution in terms of another choice of form factor decomposition, it is a simple matter of applying the relevant basis transformation matrix relating the two parameterisations. Consequently we can determine the the generalised Sachs form factors and the helicity amplitudes through the following expressions,

$$\mathbf{G} = \begin{pmatrix} G_E^*(Q^2) \\ G_M^*(Q^2) \end{pmatrix} = \begin{pmatrix} 1 & -\frac{Q^2}{(M \pm m)^2} \\ 1 & 1 \end{pmatrix} \mathbb{K}^{+}\,\mathbf{R}$$

$$\mathbf{H} = \begin{pmatrix} \mathcal{S}_{\frac{1}{2}}(Q^2) \\ \mathcal{A}_{\frac{1}{2}}(Q^2) \end{pmatrix} = b_{\pm} \begin{pmatrix} \pm\frac{\sqrt{2}(M \pm m)|\vec{q}|}{Q^2} & 0 \\ 0 & 2 \end{pmatrix} \begin{pmatrix} 1 & -\frac{Q^2}{(M \pm m)^2} \\ 1 & 1 \end{pmatrix} \mathbb{K}^{+}\,\mathbf{R} .$$

9.1.1 Extractions Involving a State at Rest

The method discussed above allows for a general approach to the determination of the transition form factors for an arbitrary choice of incoming and outgoing 3-momentum, current polarisation and hadron spin polarisation. However in the

case where one state is at rest, the expressions reduce remarkably allowing for each helicity amplitude to be sampled independently through a given choice of parameters. As was noted in the case of the $\rho \to \pi\gamma$ transition, we have a choice as to which state is at rest and consequently, we can access to distinct values of Q^2. We shall examine the case of the incoming state is at rest ($\vec{p} = 0, \vec{p}\,' = \vec{q}$) in detail for both temporal and spatial currents and simply quote the result for the outgoing state at rest. We begin with the normal parity transition.

Working from the reduced expressions presented in Appendix C, choosing the temporal current ($\mu = 0$) and projecting with

$$\Gamma' = \Gamma_0 = \frac{1}{2}\begin{pmatrix} I & 0 \\ 0 & 0 \end{pmatrix} ,$$

we have

$$K_1^0(q,0;\Gamma_0^{++}) = \frac{+1}{Q^2}\left\{2m_{\alpha^+}\ (M_{\beta^+} + E_{\beta^+})\ \Big(Q^2 + (M_{\beta^+} - m_{\alpha^+})\ (E_{\beta^+} - m_{\alpha^+})\Big)\right\} ,$$

and

$$K_2^0(q,0;\Gamma_0^{++}) = -\frac{2m_{\alpha^+}\,|\vec{q}|^2}{M_{\beta^+} + m_{\alpha^+}} .$$

By noting that

$$\Big(Q^2 + (M_{\beta^+} - m_{\alpha^+})\ (E_{\beta^+} - m_{\alpha^+})\Big) = (E_{\beta^+} - M_{\beta^+})\ (M_{\beta^+} + m_{\alpha^+}) ,$$

we can rewrite this first expression as

$$\begin{aligned} K_1^0(q,0;\Gamma_0^{++}) &= \frac{2m_{\alpha^+}}{Q^2}\ (E_{\beta^+} + M_{\beta^+})\ (E_{\beta^+} - M_{\beta^+})\ (M_{\beta^+} + m_{\alpha^+}) \\ &= \frac{2m_{\alpha^+}}{Q^2}\,|\vec{q}|^2\ (M_{\beta^+} + m_{\alpha^+}) . \end{aligned}$$

Combining these together we have

$$\begin{aligned} \overline{R}^0_{\alpha^+\to\beta^+}(q,0;\Gamma_0,\Gamma_0;+,+) &= \frac{1}{2m_{\alpha^+}}\,\frac{1}{(E_{\beta^+} + M_{\beta^+})}\,\frac{2m_{\alpha^+}\,|\vec{q}|^2\,(M_{\beta^+} + m_{\alpha^+})}{Q^2} \\ &\qquad \times\left(F_1^*(Q^2) - \frac{Q^2}{(M_{\beta^+} + m_{\alpha^+})^2}\,F_2^*(Q^2)\right) \\ &= \frac{(M_{\beta^+} + m_{\alpha^+})}{(E_{\beta^+} + M_{\beta^+})}\,\frac{|\vec{q}|^2}{Q^2}\,G_E^*(Q^2) \\ &= \frac{(M_{\beta^+} + m_{\alpha^+})}{(E_{\beta^+} + M_{\beta^+})}\,\frac{|\vec{q}|^2}{Q^2}\,\frac{Q^2}{\sqrt{2}\,b_+\,(M_{\beta^+} + m_{\alpha^+})\,|\vec{q}|}\,\mathcal{S}_{\frac{1}{2}}(Q^2) \\ &= \frac{|\vec{q}|}{\sqrt{2}\,b_+\,(E_{\beta^+} + M_{\beta^+})}\,\mathcal{S}_{\frac{1}{2}}(Q^2) \end{aligned}$$

and so we can isolate the $\mathcal{S}^{\frac{1}{2}}$ helicity amplitude through

$$\mathcal{S}_{\frac{1}{2}}(Q_1^2) = \frac{\sqrt{2}\, b_+ \,(E_{\beta^+} + M_{\beta^+})}{|\vec{q}|}\, \overline{R}^0_{\alpha^+\to\beta^+}(q,0;\Gamma_0,\Gamma_0;+,+)\,.$$

If now choose the spatial current ($\mu = k$) and project with

$$\Gamma' = \Gamma_j = \frac{1}{2}\begin{pmatrix}\sigma^j & 0\\ 0 & 0\end{pmatrix}\,,$$

we have

$$K_1^k(q,0;\Gamma_j^{++}) = (-i)\, 2m_{\alpha^+}\, \epsilon_{ijk}\, q^i\,,$$

and

$$K_2^k(q,0;\Gamma_j^{++}) = (-i)\, 2m_{\alpha^+}\, \epsilon_{ijk}\, q^i\,.$$

Combining these together we have

$$\begin{aligned}
\overline{R}^k_{\alpha^+\to\beta^+}(q,0;\Gamma_j,\Gamma_0;+,+) &= \frac{1}{2m_{\alpha^+}}\,\frac{1}{(E_{\beta^+}+M_{\beta^+})}\,(-i)\,2m_{\alpha^+}\,\epsilon_{ijk}\,q^i \\
&\qquad\qquad \times\left(F_1^*(Q^2)+F_2^*(Q^2)\right) \\
&= \frac{-i}{(E_{\beta^+}+M_{\beta^+})}\,\epsilon_{ijk}\,q^i\,G_M^*(Q^2) \\
&= \frac{-i}{(E_{\beta^+}+M_{\beta^+})}\,\epsilon_{ijk}\,q^i\,\frac{1}{2b_+}\mathcal{A}_{\frac{1}{2}}(Q^2) \\
&= \frac{-i}{2\,b_+\,(E_{\beta^+}+M_{\beta^+})}\,\epsilon_{ijk}\,q^i\,\mathcal{A}_{\frac{1}{2}}(Q^2)\,,
\end{aligned}$$

and so we can isolate the $\mathcal{A}^{\frac{1}{2}}$ helicity amplitude through

$$\epsilon_{ijk}\,q^i\,\mathcal{A}_{\frac{1}{2}}(Q_1^2) = +2i\,b_+\,(E_{\beta^+}+M_{\beta^+})\,\overline{R}^k_{\alpha\to\beta}(q,0;\Gamma_j,\Gamma_0;+,+)\,.$$

Using the alternative kinematics, we can isolate $\mathcal{S}^{\frac{1}{2}}$ using

$$\mathcal{S}_{\frac{1}{2}}(Q_2^2) = \frac{\sqrt{2}\, b_+ \,(E_{\alpha^+} + m_{\alpha^+})}{|\vec{q}|}\, \overline{R}^0_{\alpha^+\to\beta^+}(0,q;\Gamma_0,\Gamma_0;+,+)\,,$$

and $\mathcal{A}^{\frac{1}{2}}$ from

$$\epsilon_{ijk}\,q^i\,\mathcal{A}_{\frac{1}{2}}(Q_2^2) = +2i\,b_+\,(E_{\alpha^+}+m_{\alpha^+})\,\overline{R}^k_{\alpha^+\to\beta^+}(0,q;\Gamma_j,\Gamma_0;+,+)\,.$$

For the abnormal parity transitions, we note that the γ_5 in the corresponding vertex function acts to produce analogous expressions to those in the normal parity case, however shifted into the off-diagonal quadrants of the spinor matrix. By projecting out these off-diagonal contributions, we are able to access the helicity amplitudes through expressions analogous to those used in the normal

parity case. Once more we shall demonstrate this for the case where the incoming state is at rest ($\vec{p} = 0, \vec{p}\,' = \vec{q}$) and simply present the results for the alternate kinematics.

Choosing the temporal current ($\mu = 0$) and projecting with $\Gamma' = \Gamma_0$

$$K_1^0(q,0;\Gamma_0^{-+}) = \frac{-1}{Q^2}\left\{2m_{\alpha^+}\,(M_{\beta^-} - E_{\beta^-})\,\left(Q^2 - (M_{\beta^-} + m_{\alpha^+})\,(E_{\beta^-} - m_{\alpha^+})\right)\right\}\,,$$

and

$$K_2^0(q,0;\Gamma_0^{-+}) = \frac{2m_{\alpha^+}\,|\vec{q}|^2}{M_{\beta^-} - m_{\alpha^+}}\,.$$

By noting that

$$\left(Q^2 - (M_{\beta^-} + m_{\alpha^+})\,(E_{\beta^-} - m_{\alpha^+})\right) = -\,(E_{\beta^-} + M_{\beta^-})\,(M_{\beta^-} - m_{\alpha^+})\,,$$

we can rewrite this first expression as

$$\begin{aligned} K_1^0(q,0;\Gamma_0^{-+}) &= -\frac{2m_{\alpha^+}}{Q^2}\,(E_{\beta^-} + M_{\beta^-})\,(E_{\beta^-} - M_{\beta^-})\,(M_{\beta^-} - m_{\alpha^+}) \\ &= -\frac{2m_{\alpha^+}}{Q^2}\,|\vec{q}|^2\,(M_{\beta^-} - m_{\alpha^+})\,. \end{aligned}$$

Combining these together we have

$$\begin{aligned} \overline{R}^0_{\alpha^+\to\beta^-}(q,0;\Gamma_0,\Gamma_0;-,+) &= -\frac{1}{2m_{\alpha^+}}\,\frac{1}{(E_{\beta^-} + M_{\beta^-})}\,\frac{2m_{\alpha^+}\,|\vec{q}|^2\,(M_{\beta^-} - m_{\alpha^+})}{Q^2} \\ &\qquad \times\left(F_1^*(Q^2) - \frac{Q^2}{(M_{\beta^-} - m_{\alpha^+})^2}\,F_2^*(Q^2)\right) \\ &= -\frac{(M_{\beta^-} - m_{\alpha^+})}{(E_{\beta^-} + M_{\beta^-})}\,\frac{|\vec{q}|^2}{Q^2}\,G_E^*(Q^2) \\ &= -\frac{(M_{\beta^-} - m_{\alpha^+})}{(E_{\beta^-} + M_{\beta^-})}\,\frac{|\vec{q}|^2}{Q^2}\,\left(-\frac{Q^2}{\sqrt{2}\,b_-\,(M_{\beta^-} - m_{\alpha^+})\,|\vec{q}|}\right)\,\mathcal{S}_{\frac{1}{2}}(Q^2) \\ &= \frac{|\vec{q}|}{\sqrt{2}\,b_-\,(E_{\beta^-} + M_{\beta^-})}\,\mathcal{S}_{\frac{1}{2}}(Q^2) \end{aligned}$$

and so we can isolate the $\mathcal{S}^{\frac{1}{2}}$ helicity amplitude through

$$\mathcal{S}_{\frac{1}{2}}(Q_1^2) = \frac{\sqrt{2}\,b_-\,(E_{\beta^-} + M_{\beta^-})}{|\vec{q}|}\,\overline{R}^0_{\alpha^+\to\beta^-}(q,0;\Gamma_0,\Gamma_0;-,+)\,.$$

If we now choose the spatial current ($\mu = k$) and project with $\Gamma' = \Gamma_j$, we have

$$K_1^k(q,0;\Gamma_j^{-+}) = (-i)\,2m_{\alpha^+}\,\epsilon_{ijk}\,q^i\,,$$

and

$$K_2^k(q,0;\Gamma_j^{-+}) = (-i)\,2m_{\alpha^+}\,\epsilon_{ijk}\,q^i\,,$$

as we had in the normal parity case. Working through the same steps we find that we can isolate the $\mathcal{A}^{\frac{1}{2}}$ helicity amplitude through

$$\epsilon_{ijk}\, q^i\, \mathcal{A}_{\frac{1}{2}}(Q_1^2) = +2i\, b_-\, (E_{\beta^-} + M_{\beta^-})\, \overline{R}^k_{\alpha^+\to\beta^-}(q, 0; \Gamma_j, \Gamma_0; -, +)\,.$$

In the case of the alternative kinematics, in order to obtain a non-zero contribution one must project out the opposite quadrant and so a modified projector must be used, namely $\gamma_5\ (\Gamma')^{-+}\ \gamma_5 = -\,(\Gamma')^{+-}$. Using these kinematics we isolate $\mathcal{S}^{\frac{1}{2}}$ using

$$\mathcal{S}_{\frac{1}{2}}(Q_2^2) = \frac{\sqrt{2}\, b_-\, (E_{\alpha^+} + m_{\alpha^+})}{|\vec{q}|}\, \overline{R}^0_{\alpha^+\to\beta^-}(0, q; \gamma_5\, \Gamma_0\, \gamma_5, \Gamma_0; -, +)\,,$$

and $\mathcal{A}^{\frac{1}{2}}$ from

$$\epsilon_{ijk}\, q^i\, \mathcal{A}_{\frac{1}{2}}(Q_2^2) = +2i\, b_-\, (E_{\alpha^+} + m_{\alpha^+})\, \overline{R}^k_{\alpha^+\to\beta^-}(0, q; \gamma_5\, \Gamma_j\, \gamma_5, \Gamma_0; -, +)\,.$$

9.2 Negative Parity Nucleon Transition Results

In figures 9.1 and 9.2 we present the Euclidean time-series for $\mathcal{A}_{\frac{1}{2}}$ and $\mathcal{S}_{\frac{1}{2}}$ respectively. Results are illustrated for the first two negative parity eigenstates of chapter 8, undergoing radiative transition to the ground state. Similar to the case of $\rho \to \pi\gamma$, for each eigenstate we have access to two distinct values of Q^2 stemming from the choice for which state is taken to be at rest. The values are presented in Table 9.1. It is immediately apparent from the data that with our choice of kinematics, we are limited to time-like Q^2 only. This ultimately stems from our small value for the 3-momentum transfer, $|\vec{q}| \simeq 0.4$ GeV, which across all quark masses is consistently smaller than the difference in energy between the incoming and outgoing states.

Beginning with the $\mathcal{A}_{\frac{1}{2}}$ amplitude, for each state we observe plateau-like regions for both choices of kinematics. Within both states we find that the doubly-represented and singly-represented quark sectors come with opposite signs. Values are in the range $0.1 - 0.5\,\text{GeV}^{-1/2}$.

To directly compare our quark-sector results with experiment, we consider the PDG values [105] for the photon decay amplitude, $\mathcal{A}_{\frac{1}{2}}(0)$, for both proton and neutron states. In the absence of s-quark contributions, estimates for the expected doubly- and singly-represented quark sector contribution to $\mathcal{A}_{\frac{1}{2}}(0)$ are

$$\begin{aligned} N^*(1535): &\quad \mathcal{A}^{\text{doub}}_{\frac{1}{2}}(0) = 0.153\,\text{GeV}^{-1/2}, \quad \mathcal{A}^{\text{sing}}_{\frac{1}{2}}(0) = 0.265\,\text{GeV}^{-1/2}\,, \\ N^*(1650): &\quad \mathcal{A}^{\text{doub}}_{\frac{1}{2}}(0) = 0.070\,\text{GeV}^{-1/2}, \quad \mathcal{A}^{\text{sing}}_{\frac{1}{2}}(0) = 0.145\,\text{GeV}^{-1/2}\,. \end{aligned}$$

These estimates reflect both connected and disconnected contributions from a given quark flavour. While the magnitude is consistent, it is apparent that the

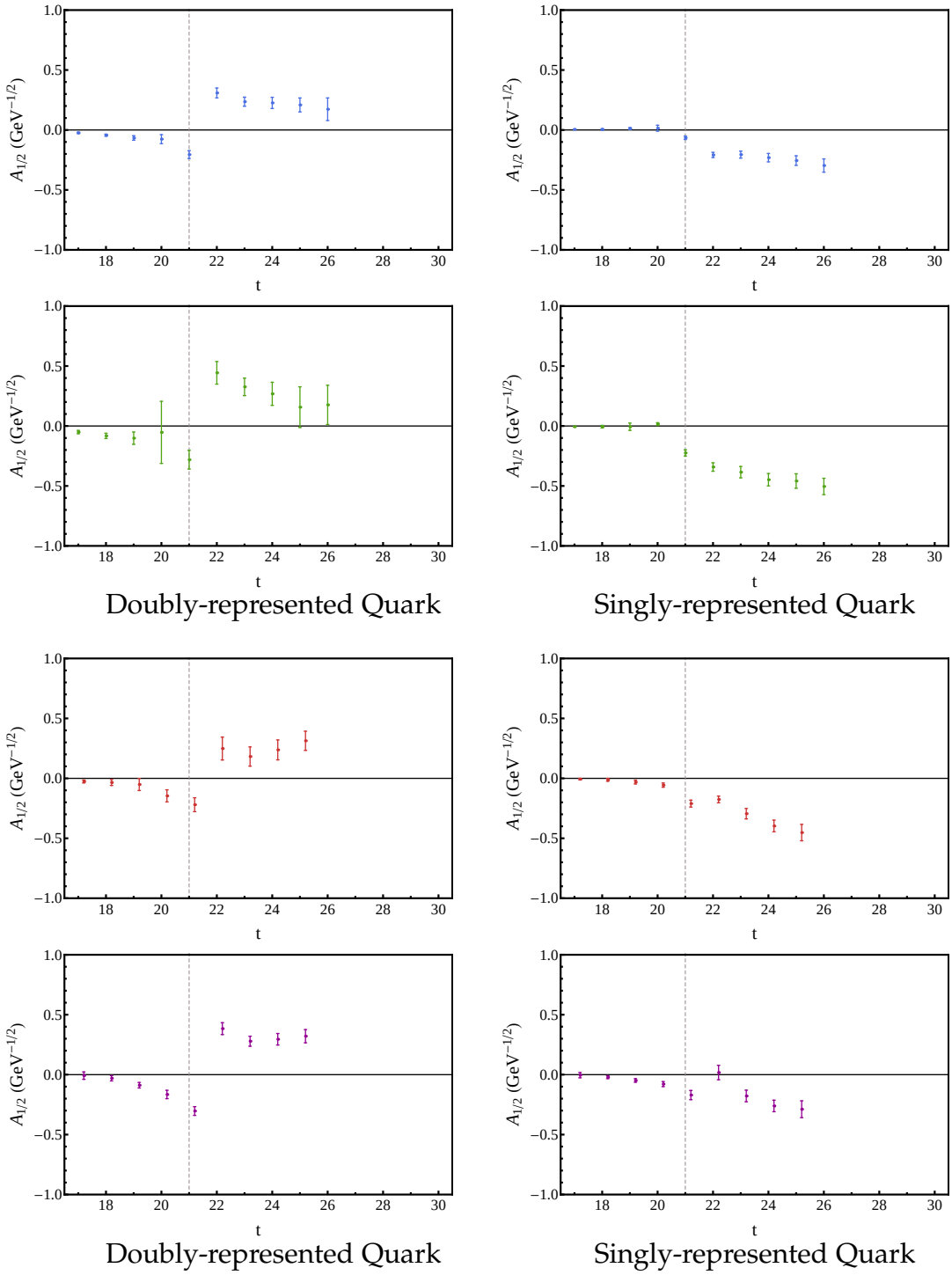

Figure 9.1: An example of the $\mathcal{A}_{\frac{1}{2}}$ helicity amplitude as a function of Euclidean sink time for the first two negative parity nucleon eigenstates. These results are obtained with $m_\pi = 411$ MeV. The upper four figures (●) and (●) are for the first excited nucleon state while the lower four figures (●) and (●) are for the second excited nucleon state. For each eigenstate, the upper figures are evaluated with the N^* at rest while the lower figures with the N at rest. All figures on the left are for the doubly-represented quark sector while those on the right are for the singly-represented quark. Both quark sectors are normalised to unit charge. The vertical dashed line indicates the position of the current insertion.

Table 9.1: The Q^2 values accessed in the our lattice evaluation of the $N^* \to N\gamma$ helicity amplitudes for the two lightest negative parity eigenstates. For each state we are able to access two distinct values for Q^2 stemming from the choice of which state is taken to be at rest. For Q_1^2, the ground state nucleon, N, is at rest, while for Q_2^2, the excited nucleon, N^*, is at rest.

		$N^*(1535)$		$N^*(1650)$	
κ	m_π (MeV)	Q_1^2 (GeV^2)	Q_2^2 (GeV^2)	Q_1^2 (GeV^2)	Q_2^2 (GeV^2)
0.13700	702	-0.110(24)	-0.205(28)	-0.147(29)	-0.246(34)
0.13727	570	-0.095(26)	-0.199(31)	-0.064(28)	-0.162(34)
0.13754	411	-0.135(21)	-0.272(25)	-0.182(36)	-0.328(42)
0.13770	296	-0.089(34)	-0.231(42)	-0.259(64)	-0.431(74)

sign on our singly-represented quark sector is at odds with the experimental determination. Consequently, the value we would extract for the proton $\mathcal{A}_{\frac{1}{2}}$ amplitude would be larger than expected. We note that a previous determination for the helicity amplitudes obtained from light-cone distribution amplitudes [152] for values of $Q^2 \geqslant 1\,\text{GeV}^2$, suggest a value for the $\mathcal{A}_{\frac{1}{2}}$ larger than the experimental value. To make a quantitative comparison would require extractions in the space-like regime and extrapolations to $Q^2 = 0$.

For the $\mathcal{S}_{\frac{1}{2}}$ amplitude, again the results are quite similar between the two eigenstates. Both states give values around $0.1 - 0.2$ GeV$^{-1/2}$ with both quark sectors carrying the same sign. In combining the quark sector results to obtain the proton $\mathcal{S}_{\frac{1}{2}}$ amplitude, we find the value to be positive in the time-like region. The CLAS data for this process [153] shows a definite negative value for this amplitude from $Q^2 = 0 - 4$ GeV^2, however at around 1 GeV^2 there is a definite turning point with the value tending towards 0. If one were to continue this trend into time-like Q^2, the value for the $\mathcal{S}_{\frac{1}{2}}$ would be positive in value.

In comparing the results between the two helicity amplitudes, it appears that the $\mathcal{A}_{\frac{1}{2}}$ amplitude produces a cleaner signal than the corresponding $\mathcal{S}_{\frac{1}{2}}$ amplitude across the majority of simulation parameters considered. Comparing the helicity amplitudes for each state with the corresponding N^* elastic form factors there is a significant decrease in the signal quality, despite one of our states being the ground state nucleon. It is important to note that here we are operating in the time-like region, compared to the elastic case where extractions are necessarily in the space-like region. Our results for the $\rho \to \pi\gamma$ transition, presented in chapter 7, sampled the form factor in both space and time-like regions of Q^2 and showed a marked reduction in the quality of the plateau when sampling in the time-like region.

These results mark the first direct extraction of the helicity amplitudes for the negative parity $N^* \to N\gamma^*$ transition, however the apparent limitation of our results is the fact our extractions lie in the time-like region. In order to compare

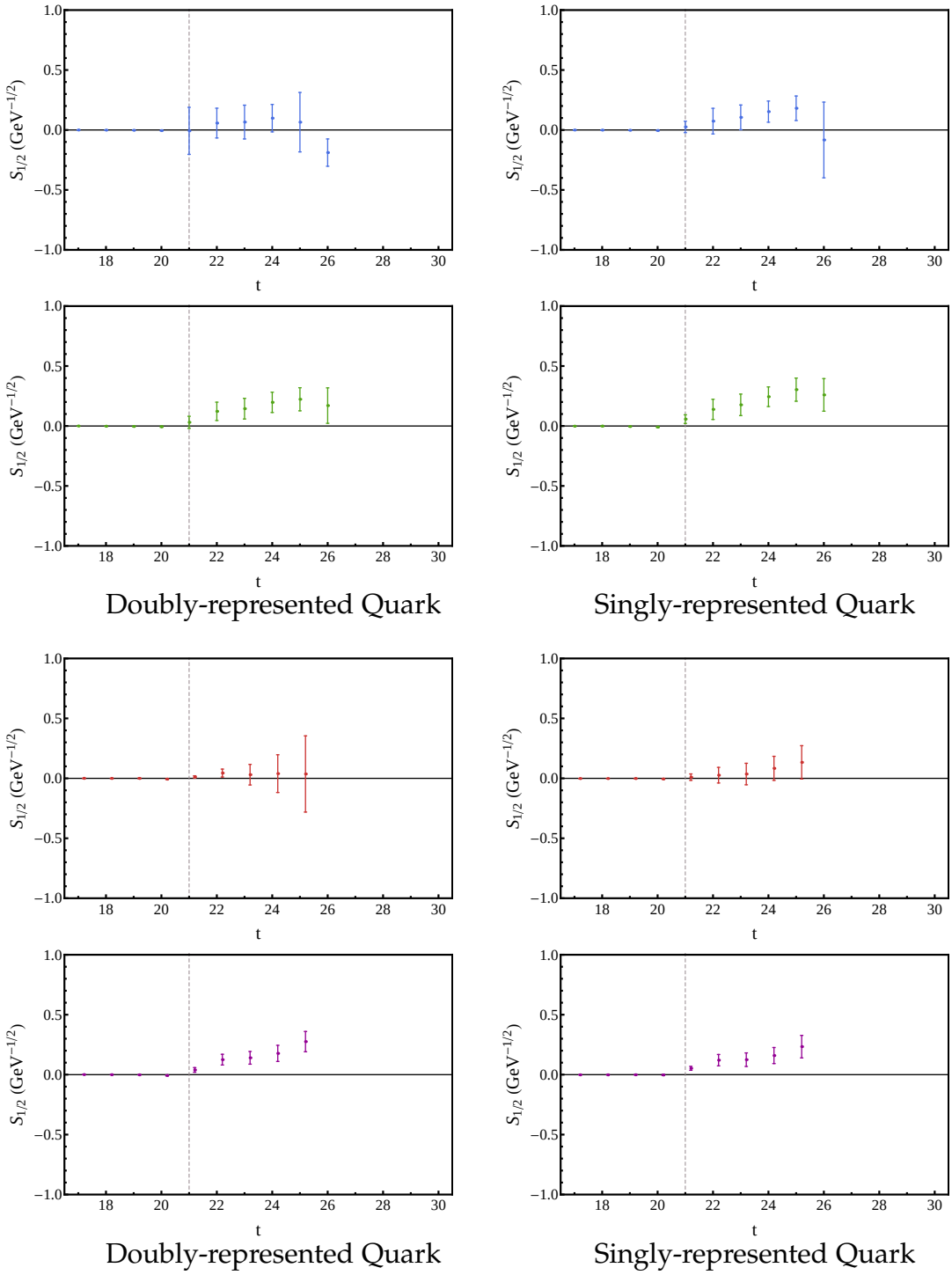

Figure 9.2: An example of the $\mathcal{S}_{\frac{1}{2}}$ helicity amplitude as a function of Euclidean sink time for the first two negative parity nucleon eigenstates. These results are obtained with $m_\pi = 411$ MeV. The upper four figures (●) and (●) are for the first excited nucleon state while the lower four figures (●) and (●) are for the second excited nucleon state. For each eigenstate, the upper figures are evaluated with the N^* at rest while the lower figures with the N at rest. All figures on the left are for the doubly-represented quark sector while those on the right are for the singly-represented quark. Both quark sectors are normalised to unit charge. The vertical dashed line indicates the position of the current insertion.

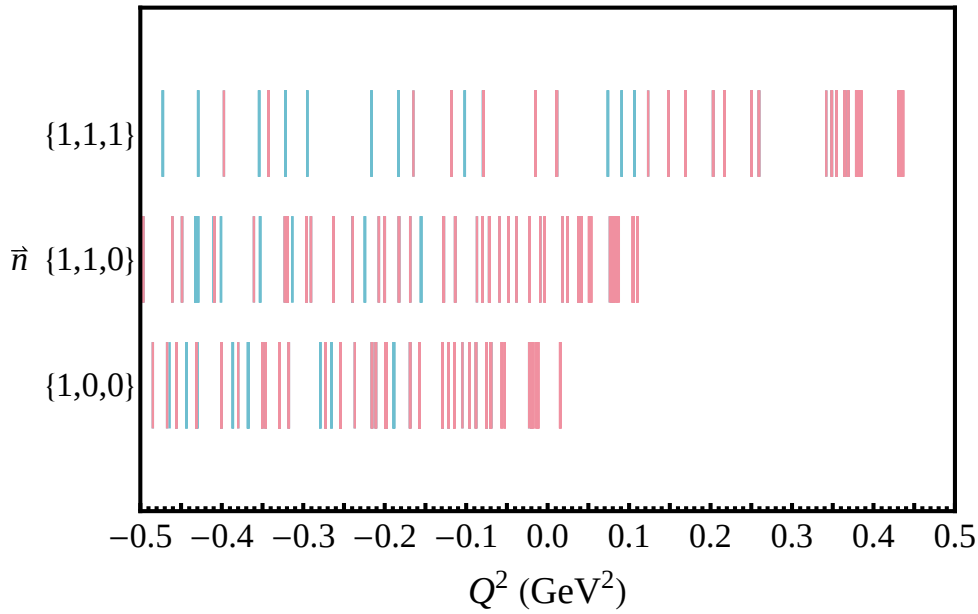

Figure 9.3: The distribution of Q^2 values obtained for various current momenta $\vec{q} = \frac{2\pi}{L}\,\vec{n}$ formed from taking different values for the incoming momentum $\vec{p}$. We consider all possible values of $\vec{p}$ with $|\vec{p}|^2 \leq 10\,\frac{2\pi}{L}$. The blue lines are taking the nucleon excitation, N^*, to be the outgoing state while the red lines are taking the ground state nucleon, N, to be the outgoing state. The values are for $m_\pi =$ 296 MeV with $M = 1.66$ GeV, the mass of the first negative parity nucleon excitation, and $m = 1.07$ GeV, the mass of the ground-state nucleon, for this ensemble.

with the existing experimental data and models, we need extractions in the space-like domain. Extractions with low space-like Q^2 are particularly interesting as as model calculations are sensitive to long-distance physics in describing the amplitudes. As was noted earlier, the limitation in our ability to sample the desired Q^2 stems from the small value for $|\vec{q}|$ when compared with the energy separation between the incoming and outgoing states. For the states of interest here, the mass separation between our states is between 0.5 and 0.7 GeV and so choosing a $|\vec{q}|$ on the upper side of this bound will result in $Q^2 > 0$ when the N^* is taken at rest. However, an alternate method that instead decreases the energy separation is to work in a boosted frame. For the method used in this work whereby the SST inversion is performed via the current rather than the sink, we can access a range of different Q^2 by projecting out different momenta at the sink, to give

$$Q^2 = |\vec{q}|^2 - (E_M(\vec{p}') - E_m(\vec{p}))^2 \tag{9.9}$$
$$= 2\,(E_M(\vec{p}')\,E_m(\vec{p}) - \vec{p}' \cdot \vec{p}) - M^2 - m^2\,, \tag{9.10}$$

where $\vec{p}\,'$ is determined from our choice of the current and source momentum using $\vec{p}\,' = \vec{q} + \vec{p}$. From this expression we can see that space-like Q^2 can be

generated by increasing the incoming momentum $\vec{p}$ while holding the current momentum fixed, or choosing kinematics such that $\vec{p}\,' \cdot \vec{p} < 0$. In Fig. 9.3 we show the resulting Q^2 generated for several choices of $\vec{q}$ and can find that we can obtain a range of space-like Q^2 for relatively small momenta, $\vec{p}$. Unfortunately, candidature time frames prevent an investigation of this idea herein, however it will be a first point of investigation post-submission.

9.3 Summary

Here we have created a formalism for the extraction of the electromagnetic transition form factors for both positive and negative spin-$1/2$ baryons. The formalism enables the description of electroproduction processes for excited nucleon states, $N\gamma^* \to N^*$. Through this framework we outlined how all possible parity transitions could be obtained from the same baryon correlator and was suitably generalised for determinations using arbitrary incoming and outgoing momenta, current polarisation and spin orientations. We then considered explicit extractions relevant to the choice of kinematics utilised in this work.

In examining the $\mathcal{A}_{\frac{1}{2}}$ and $\mathcal{S}_{\frac{1}{2}}$ helicity amplitudes for the abnormal parity transition of the first two negative parity nucleon eigenstates, we observed definite plateau-like behaviour in both channels. However, due to the relatively small value of $|\vec{q}|$ used in our calculation, our extractions were limited to time-like Q^2 limiting our ability to perform a direct comparison with experiment and model calculations. With this in mind, a framework was proposed that would allow for space-like Q^2 values to be examined without the need for increasing $|\vec{q}|^2$.

Chapter 10

Conclusion

In this work we have considered a generalisation of the variational approach, standard to hadron spectroscopy calculations, for use in the determination of hadron structure. As the variational process acts to produce interpolators that couple to individual eigenstates, it allows us to project out the contributions for an individual state or transition from the corresponding three-point correlation function. The appeal of such an approach is two-fold. It provides us with a means of removing and thus controlling the effect of excited state contamination to the determination of ground state properties. Complementary to this, it allows us to disentangle the terms describing excited states properties from the dominant ground state. With this understanding, we go on to consider a range of structure calculations for a variety of hadron states.

We began in chapter 5 with the nucleon axial charge, g_A. The lattice determinations for this quantity have consistently been lower than the experimental determination and it has been suggested that excited state contaminations may play a significant role. Using the variational approach we find that the resulting optimised interpolators provide rapid ground state dominance, allowing for earlier insertion of the current and earlier fit windows, with a corresponding reduction in statistical uncertainties. Through a subsequent comparison of standard single source methods with the variational result, we are able to show that excited state contamination acts to suppress the measured value for g_A when equipped with inadequately tuned sources and sinks.

The following chapter considered the electromagnetic form factors for the ground state π and ρ mesons and their first excitations. Once more we are able to show that use of the variational approach gives rise to improved ground state dominance, discernible through the improved plateau quality and duration. This allows for the selection of both earlier and larger fit windows. Using the variational framework we are able to extract accurate results for the ρ meson form factors in (2+1)-flavour QCD at near physical masses for the first time. Our value for the ρ meson g-factor, $g_\rho = 2.21(8)$, compares well with the experimental determination of Ref. [92], $g_\rho = 2.1(5)$, albeit with significantly smaller uncertainty. For the ρ meson quadrupole form factor, we observe significant chiral curvature with a rapid increase in the magnitude of the quadrupole moment as the quark mass approaches the physical value. The quadrupole moment is found to be negative, consistent with previous lattice determinations.

Through the variational framework, we are also able to perform the first extraction for the electromagnetic form factors of a light meson excitation. For the charge form factor G_C of the π^* and ρ^* mesons, we find the magnitude to be lower than the corresponding ground states, indicating that these states are larger in extent. For the ρ^* meson, we are further able to extract values for the magnetic form factor which are found to be significantly smaller than the ground state ρ meson. Evaluation of the magnetic moments for the ρ and ρ^* mesons give a value for $\mu_{\rho^*}/\mu_\rho = 0.74(9)$ consistent with model determinations.

In chapter 7 we presented a follow-up calculation examining the $\rho \to \pi\gamma$ transition. While there have been some lattice determinations of the corresponding form factor, very few have been with dynamical quarks and none in the light quark regime. In our extraction we are able to obtain values for the transition form factor G_{M1} in both the space-like and time-like Q^2 domain, which in turn allows for the extraction of the transition moment $G_{M1}(0)$. Our results are found to be consistent with quark model expectations for heavy quark masses, however our result for the lightest quark mass is significantly lower than the experimental value. Our results suggest that disconnected sea-quark loop contributions may play a significant role for the complete description of this process and further investigation is warranted.

The remaining two chapters considered the use of the variational approach for the study of nucleon excitations, particularly those in the negative parity channel. Due to the small mass splitting between the $N^*(1535)$ and $N^*(1650)$ in this channel, standard single source methods would encounter severe excited state contamination. Consequently this channel is well suited for the use of the variational approach. Through considerations of the structure of the baryon correlator, we present a framework for accessing both positive and negative parity eigenstate contributions through the selection of appropriate projection operators. With this in mind, we perform a calculation of the electromagnetic form factors for the two lightest negative parity nucleon eigenstates. The electric form factor G_E is found to be similar between both states and comparison with the ground state nucleon show the value to be significantly smaller, indicating these states are considerably larger in extent. For the magnetic form factor G_M, similar values are observed for the doubly-represented quark sector, however for the singly-represented quark sector the values differ in sign, suggesting different spin configuration for these states. To compare with model calculations, we construct estimates for the magnetic moments of the p^* and n^* isospin projections for the two negative parity eigenstates. Our lightest eigenstate gives values consistent with the model estimates for the $N^*(1535)$, however significant discrepancies are observed for the second eigenstate and the model estimates for the $N^*(1650)$. This observation, coupled with the spectrum analysis of Ref. [133], suggest that the eigenstate isolated on the lattice is more likely a finite-volume meson-baryon dressing of the $N^*(1535)$, rather than the $N^*(1650)$. This highlights the challenge involved in identifying states on the lattice. Nonetheless,

determination of the properties of these eigenstates can guide us and provide hints as to the nature of the eigenstates observed on the lattice.

In the final chapter we present a general framework for the determination of the $N\gamma \to N^*$ transition form factors central to the electroproduction processes of excited nucleon states being considered by the experimental programs at Mainz, Bonn, MIT-Bates and Jefferson Lab. Through this framework, we outline how one is able to extract all possible parity transitions from the same baryon correlator. The presentation allows for arbitrary incoming and outgoing momenta, current polarisations and spin orientations. We then perform a determination of the $\mathcal{A}_{\frac{1}{2}}$ and $\mathcal{S}_{\frac{1}{2}}$ helicity amplitudes for the transition of the two lightest negative parity nucleon eigenstates, considered in the preceding chapter, to the ground state nucleon. Between the two states, we observe very similar results for both amplitudes. Unfortunately, due to our choice for the current 3-momentum $|\vec{q}|$, our extractions are limited to the time-like Q^2 domain limiting our ability for a direct comparison with experiment and model calculations. A method was proposed to access space-like Q^2 through considerations of boosted frames; this will be a focus of future investigations.

In summary, we have been able to demonstrate the efficacy of the variational approach in separating out the terms for individual eigenstates. The resulting optimised interpolators allow for improved results for the determination of ground state properties. This method is also the ideal means to study the underlying structure of hadron excitations. Considerations of the negative parity spectrum demonstrate the difficulties associated with state identification and highlight the need to couple the hadron structure calculations presented here with studies of the evolution and make-up of the finite-volume eigenstates. Taking such an approach, we may well have the means to uncover some of the long standing mysteries of the hadron spectrum.

Appendix A

Gamma Matrices

Here we review the representations of the γ-matrices used in this work. In particular we consider the Dirac representation, which is used to facilitate calculations of the γ-matrix algebra at the phenomenological level, and the Sakurai representations which we use in the explicit numerical calculations of our correlation functions.

The defining property for the γ-matrix algebra is that elements satisfy the anti-commutation relation

$$\{\gamma^\mu, \gamma^\nu\} = 2g^{\mu\nu}\,,$$

where $g^{\mu\nu}$ is the metric for the space in question. Generally this algebra is extended to include the matrix γ_5, which satisfies

$$\{\gamma_5, \gamma^\nu\} = 0\,.$$

From these matrices one is able to construct a basis that spans the space of 4×4 spinor matrices

$$\left\{\mathbb{I}, \gamma^\mu, \sigma^{\mu\nu}|_{\mu>\nu}\,, \gamma^\mu\gamma_5, \gamma_5\right\}\,,$$

where $\sigma^{\mu\nu} = \frac{i}{2}[\gamma^\mu, \gamma^\nu]$.

Dirac Representation

The Dirac representation,

$$\gamma_0 = \begin{pmatrix} I_2 & 0 \\ 0 & -I_2 \end{pmatrix}, \quad \gamma_i = \begin{pmatrix} 0 & \sigma_i \\ -\sigma_i & 0 \end{pmatrix},$$

satisfies the Clifford algebra for Minknowski metric (signature (+ - - -)),

$$\{\gamma^\mu, \gamma^\nu\} = 2g^{\mu\nu}.$$

For this metric we define $\gamma_5 = \frac{i}{4!}\epsilon_{\mu\nu\sigma\tau}\gamma^\mu\gamma^\nu\gamma^\sigma\gamma^\tau$, which in this representation takes the explicit form

$$\gamma_5 = \begin{pmatrix} 0 & I_2 \\ I_2 & 0 \end{pmatrix}.$$

Useful definitions and properties

$$\gamma_0^2 = I_4 \tag{A.1}$$
$$\gamma_i^2 = -I_4 \tag{A.2}$$
$$\gamma_5^2 = I_4 \tag{A.3}$$

$$\gamma_0^\dagger = \gamma_0 \tag{A.4}$$
$$\gamma_i^\dagger = -\gamma_i \tag{A.5}$$
$$\gamma_5^\dagger = \gamma_5 \tag{A.6}$$

$$\gamma_0\gamma_\mu^\dagger\gamma_0 = \gamma_\mu \tag{A.7}$$

$$C = i\gamma_0\gamma_2 \tag{A.8}$$
$$C^\dagger = C^{-1} = C^T = -C \tag{A.9}$$

Sakurai Representation

The Sakurai representation,

$$\gamma_4 = \begin{pmatrix} I_2 & 0 \\ 0 & -I_2 \end{pmatrix}, \quad \gamma_i = \begin{pmatrix} 0 & -i\sigma_i \\ i\sigma_i & 0 \end{pmatrix},$$

satisfies the Clifford algebra for the Euclidean metric,

$$\{\gamma^\mu, \gamma^\nu\} = 2\delta^{\mu\nu}.$$

For this metric we define $\gamma_5 = \frac{1}{4!}\epsilon_{\mu\nu\sigma\tau}\gamma^\mu\gamma^\nu\gamma^\sigma\gamma^\tau$, which in this representation takes the explicit form

$$\gamma_5 = -\begin{pmatrix} 0 & I_2 \\ I_2 & 0 \end{pmatrix}.$$

Useful definitions and properties

$$\gamma_\mu^2 = I_4 \tag{A.10}$$
$$\gamma_5^2 = I_4 \tag{A.11}$$

$$\gamma_\mu^\dagger = \gamma_\mu \tag{A.12}$$
$$\gamma_5^\dagger = \gamma_5 \tag{A.13}$$

$$C = \gamma_4\gamma_2 \tag{A.14}$$
$$C^\dagger = C^{-1} = C^T = -C \tag{A.15}$$

Appendix B

Form Factor Plateaus

Here we present the figures showing the Euclidean time series and corresponding fits for the electromagnetic form factors examined in the work. The error analysis of the correlation function ratios is performed via a second order, single-elimination jackknife, with the χ^2 per degree of freedom (χ^2_{dof}) obtained from the covariance matrix fits. We perform a series of fits of the ratio after the current insertion at t_1. By examining the χ^2_{dof} we are able to establish a valid window through which we may fit in order to extract our observables.

B.1 Light Meson Form Factors

π meson Sachs Charge Form Factor

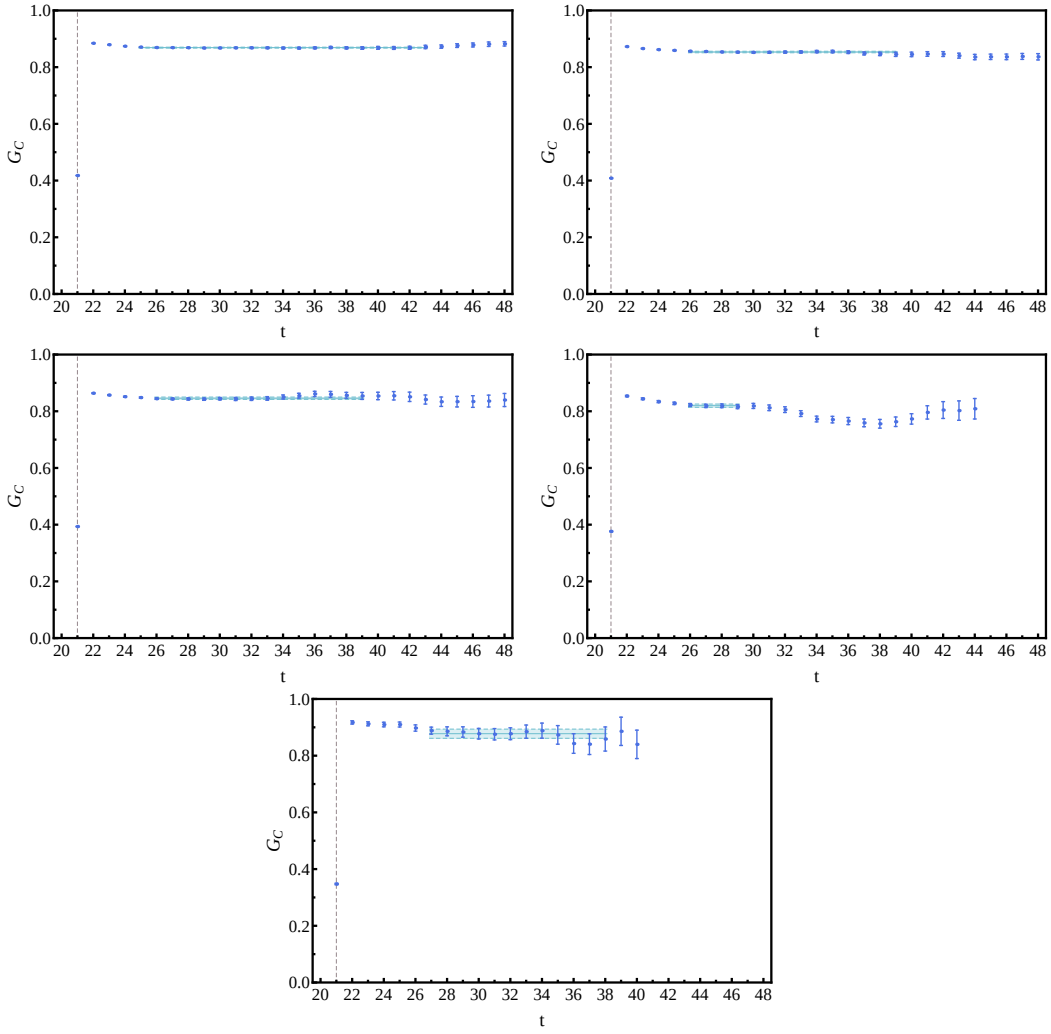

Figure B.1: The quark sector results for the π meson charge form factor G_C. The dashed line represents the time-slice at which the current is inserted. The direction of decreasing quark mass is left to right and down the page.

π^* meson Sachs Charge Form Factor

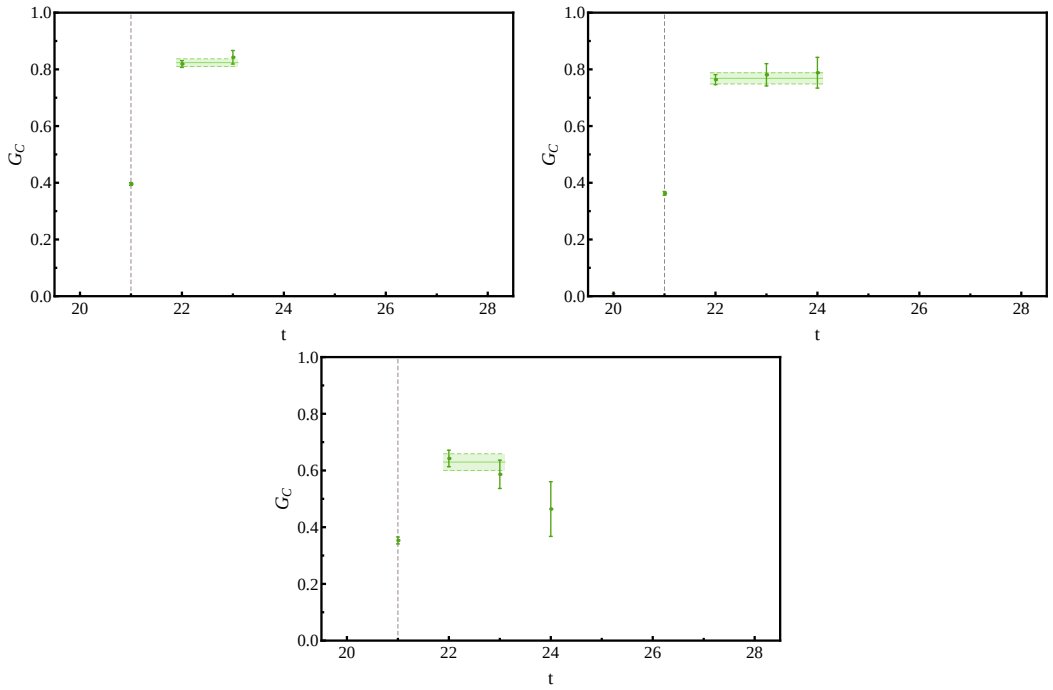

Figure B.2: The quark sector results for the π^* meson charge form factor G_C. The dashed line represents the time-slice at which the current is inserted. The direction of decreasing quark mass is left to right and down the page.

ρ meson Sachs Charge Form Factor

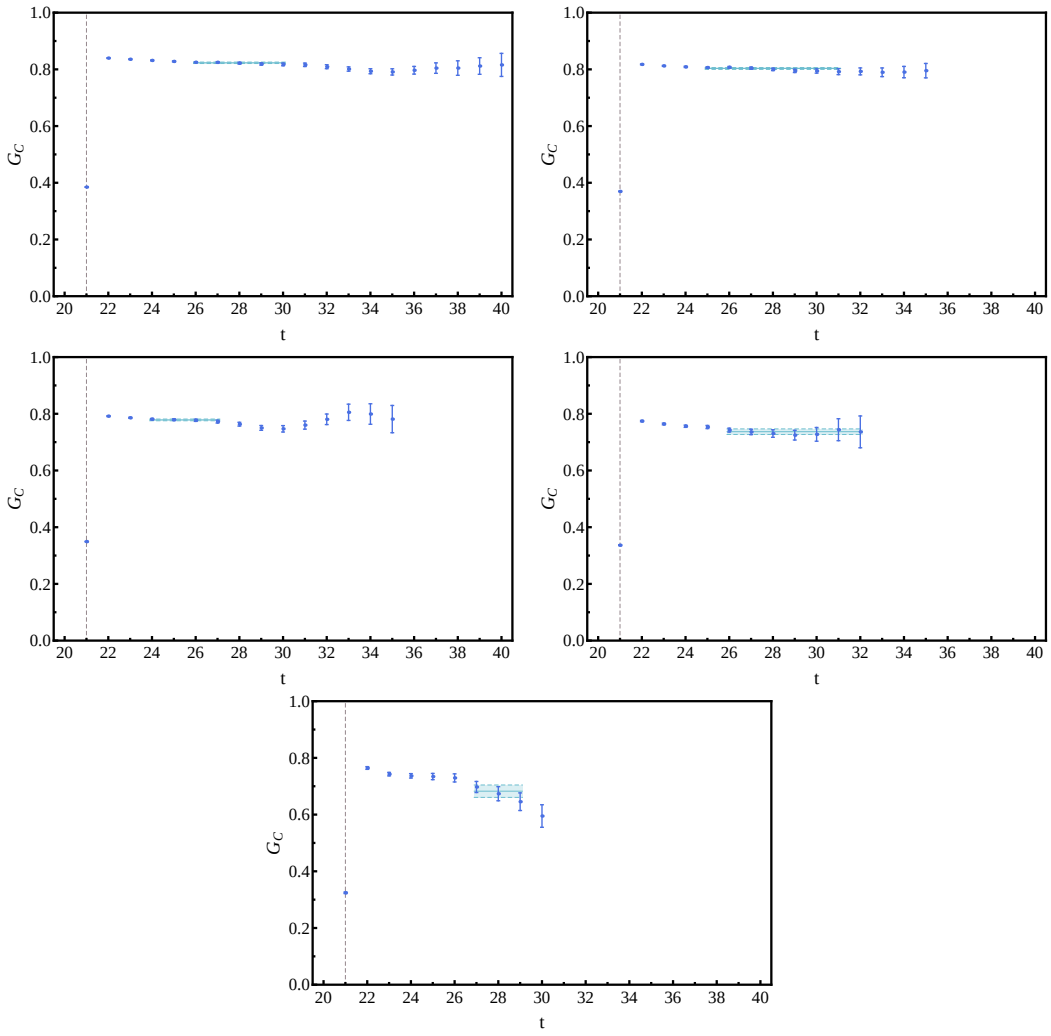

Figure B.3: The quark sector results for the ρ meson charge form factor G_C. The dashed line represents the time-slice at which the current is inserted. The direction of decreasing quark mass is left to right and down the page.

ρ^* meson Sachs Charge Form Factor

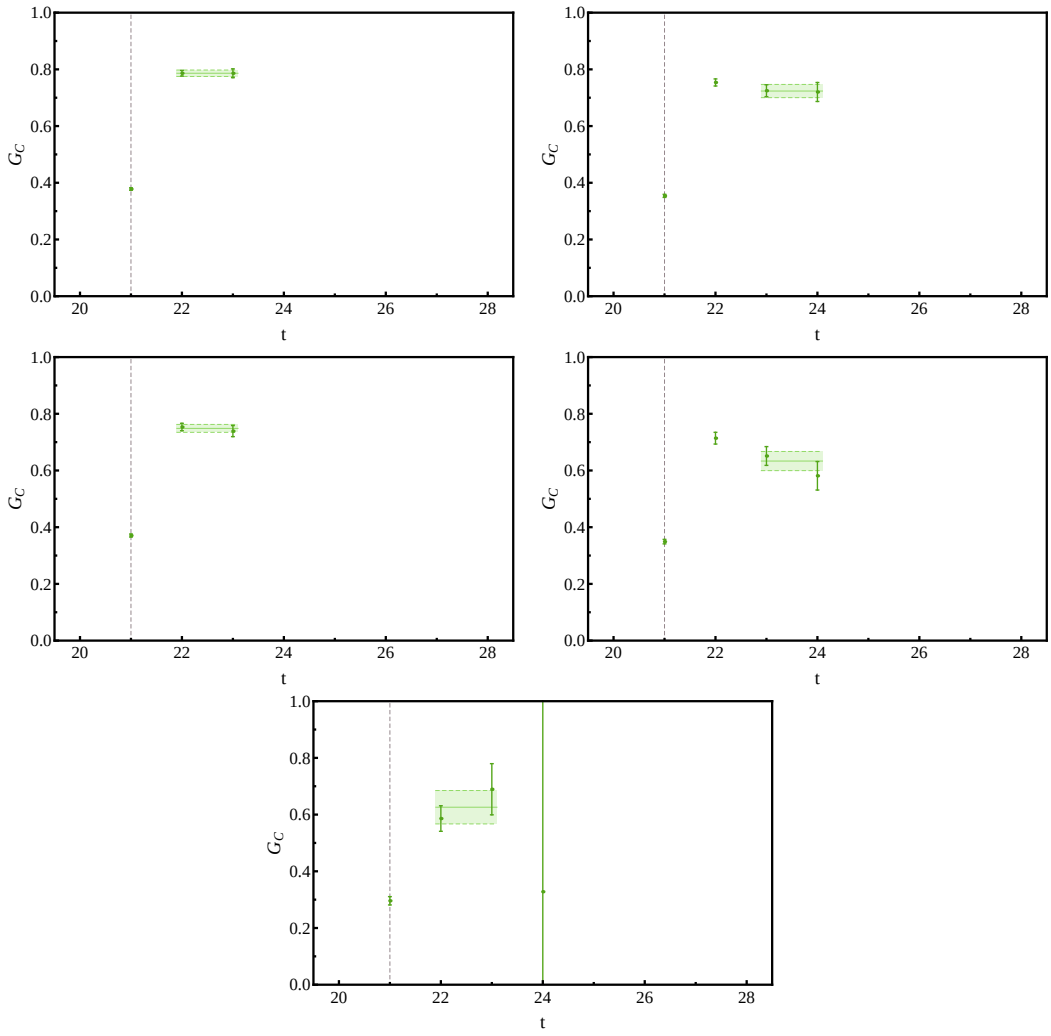

Figure B.4: The quark sector results for the ρ^* meson charge form factor G_C. The dashed line represents the time-slice at which the current is inserted. The direction of decreasing quark mass is left to right and down the page.

ρ meson Sachs Magnetic Form Factor

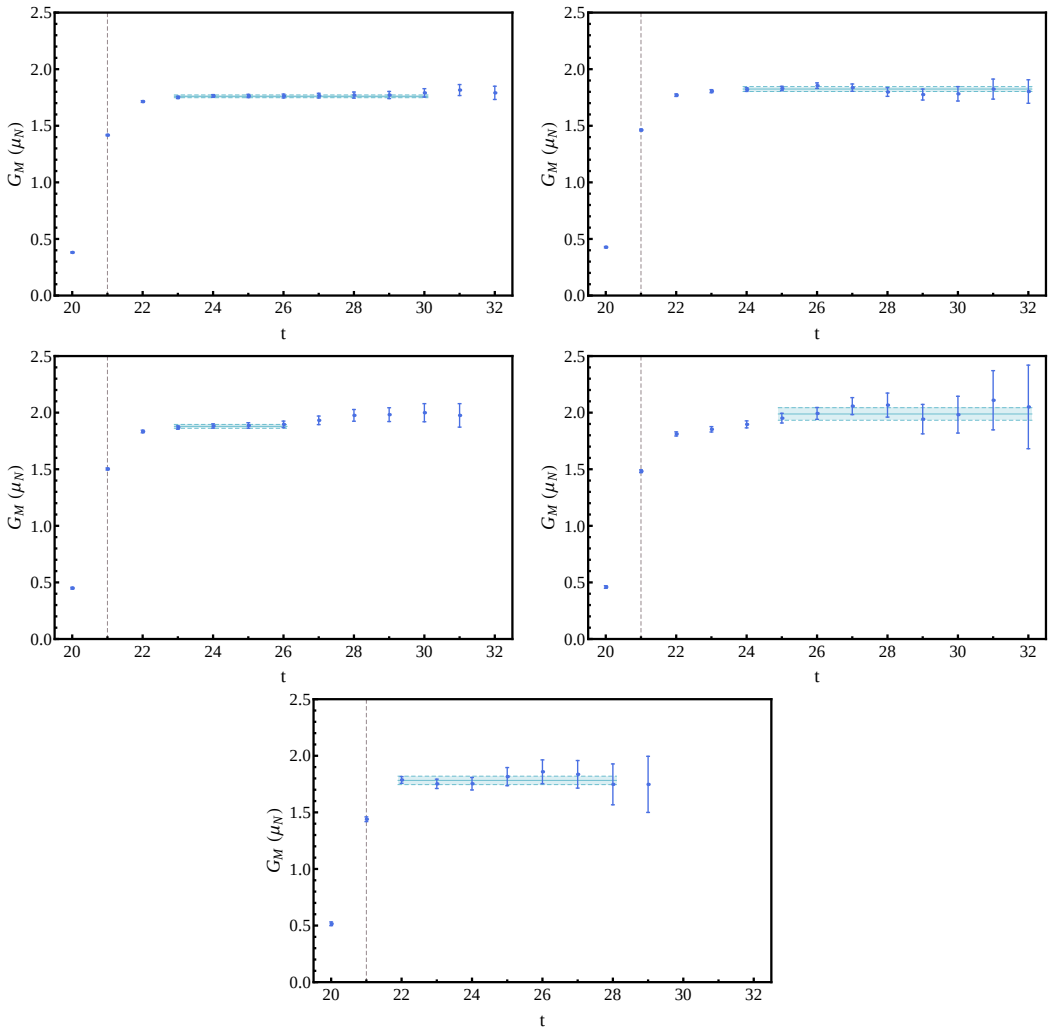

Figure B.5: The quark sector results for the ρ meson magnetic form factor G_M. The dashed line represents the time-slice at which the current is inserted. The direction of decreasing quark mass is left to right and down the page.

ρ^* meson Sachs Magnetic Form Factor

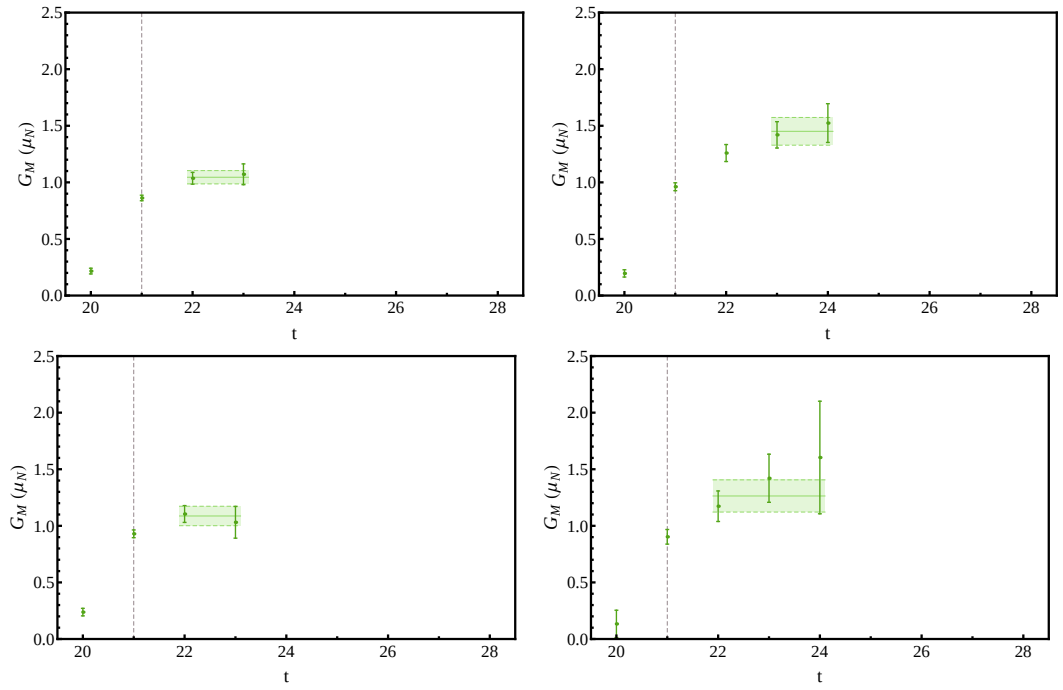

Figure B.6: The quark sector results for the ρ^* meson magnetic form factor G_M. The dashed line represents the time-slice at which the current is inserted. The direction of decreasing quark mass is left to right and down the page.

ρ meson Sachs Electric Quadrupole Form Factor

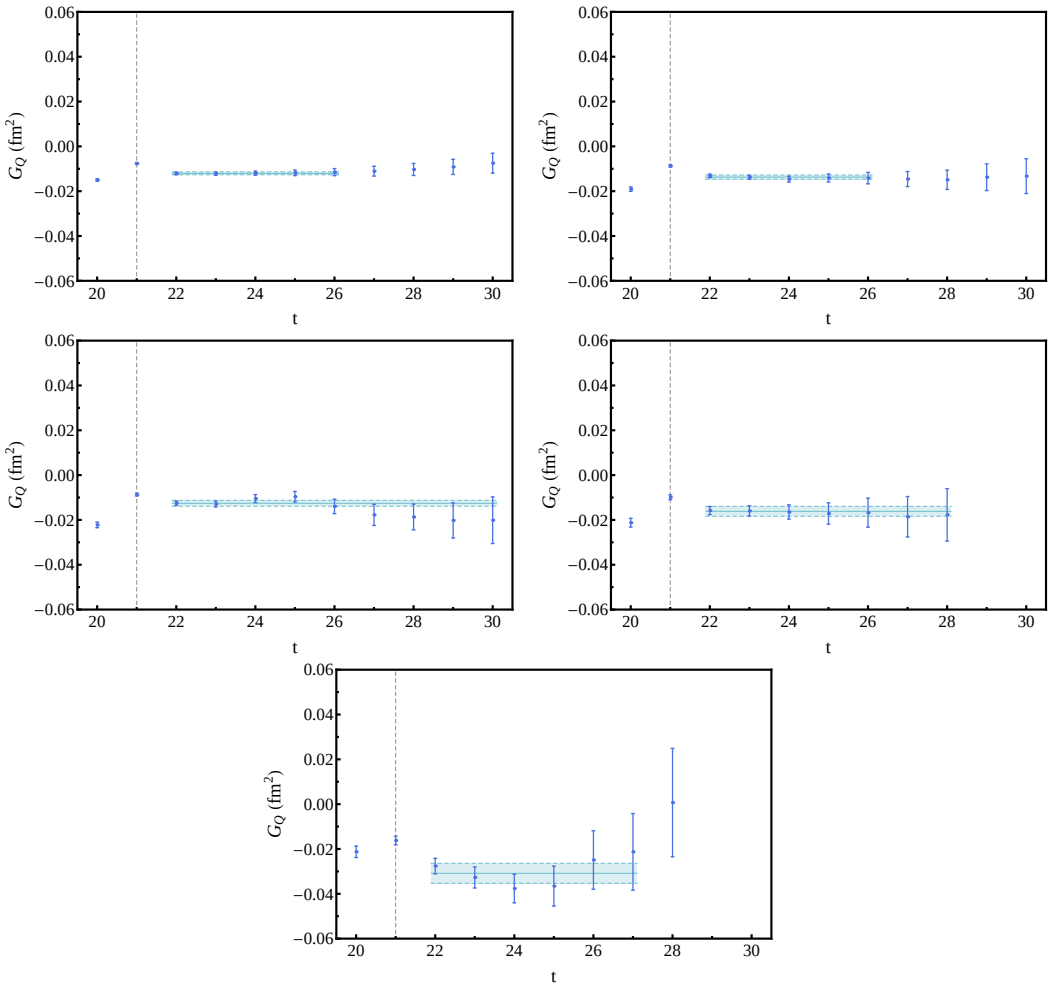

Figure B.7: The quark sector results for the ρ meson quadrupole form factor G_Q. The dashed line represents the time-slice at which the current is inserted. The direction of decreasing quark mass is left to right and down the page.

B.2 Light Meson Transition Form Factors

$\rho \to \pi\gamma$ Transition Form Factor (π at rest)

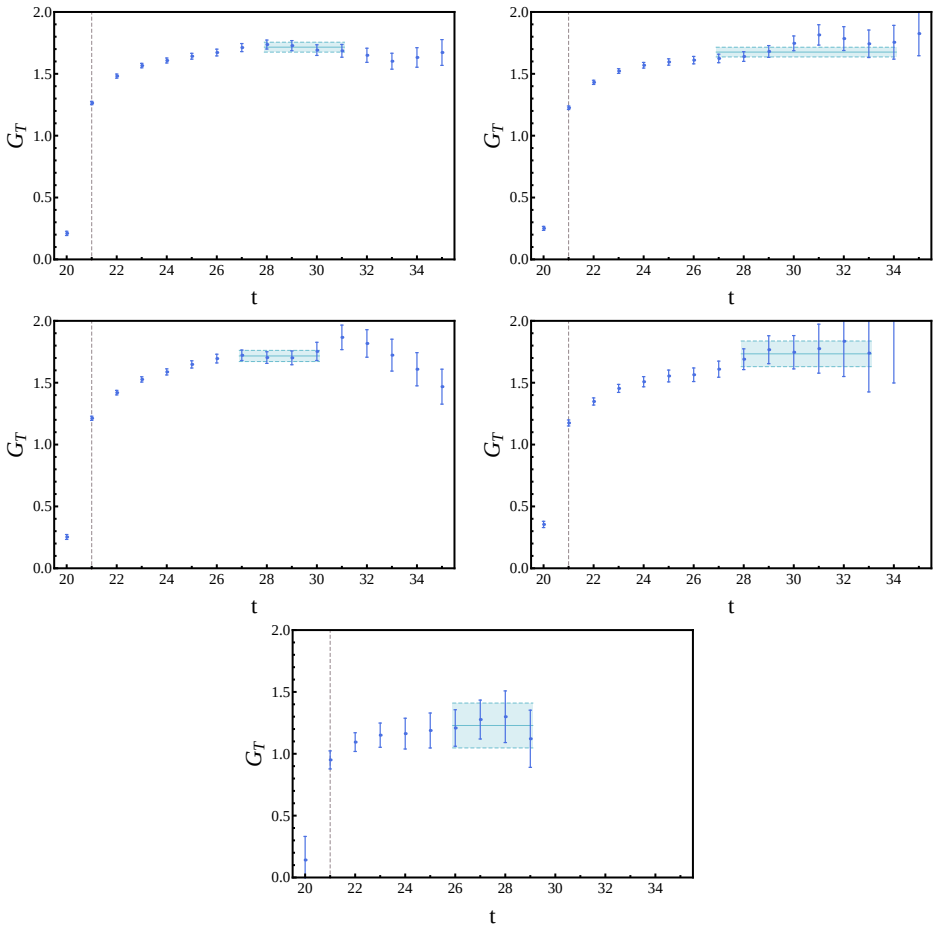

Figure B.8: The quark sector results for the $\rho \to \pi\gamma$ transition form factor G_{M1}, evaluated with the π meson at rest. The dashed line represents the time-slice at which the current is inserted. The direction of decreasing quark mass is left to right and down the page.

$\rho \to \pi\gamma$ Transition Form Factor (ρ at rest)

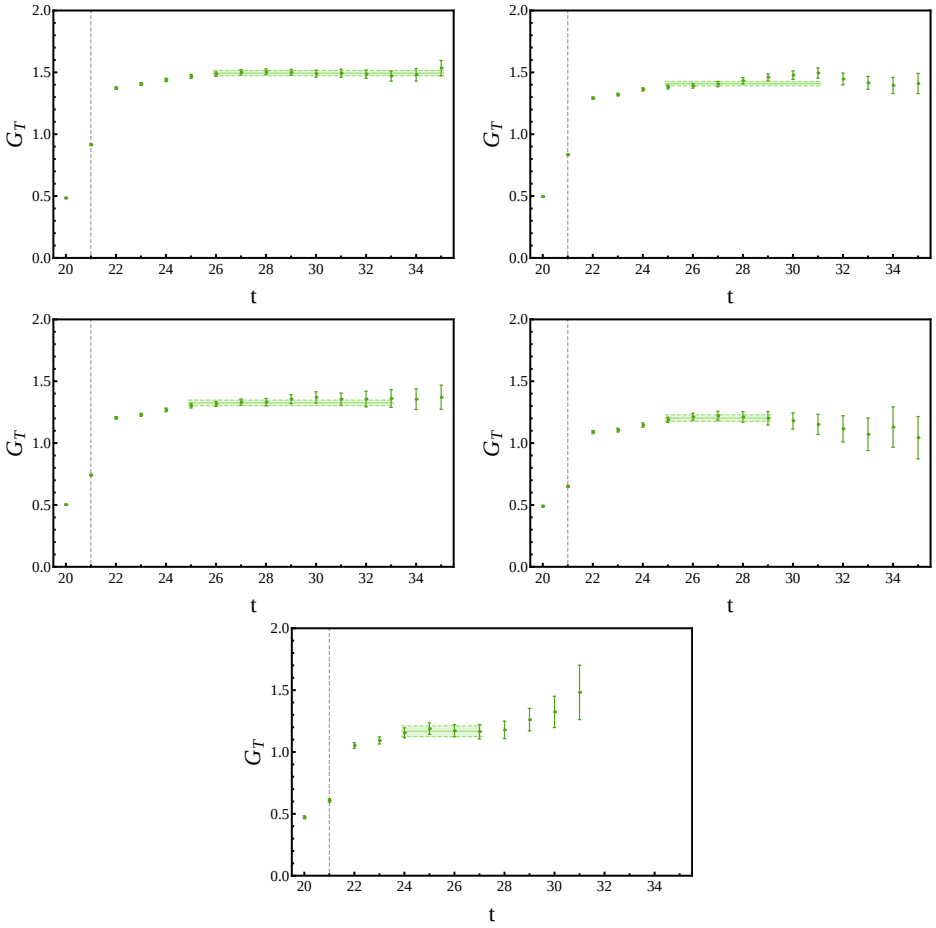

Figure B.9: The quark sector results for the $\rho \to \pi\gamma$ transition form factor G_{M1}, evaluated with the ρ meson at rest. The dashed line represents the time-slice at which the current is inserted. The direction of decreasing quark mass is left to right and down the page.

B.3 Negative Parity Nucleon Form Factors

Sachs Electric Form Factor for the 1st Negative Parity Eigenstate

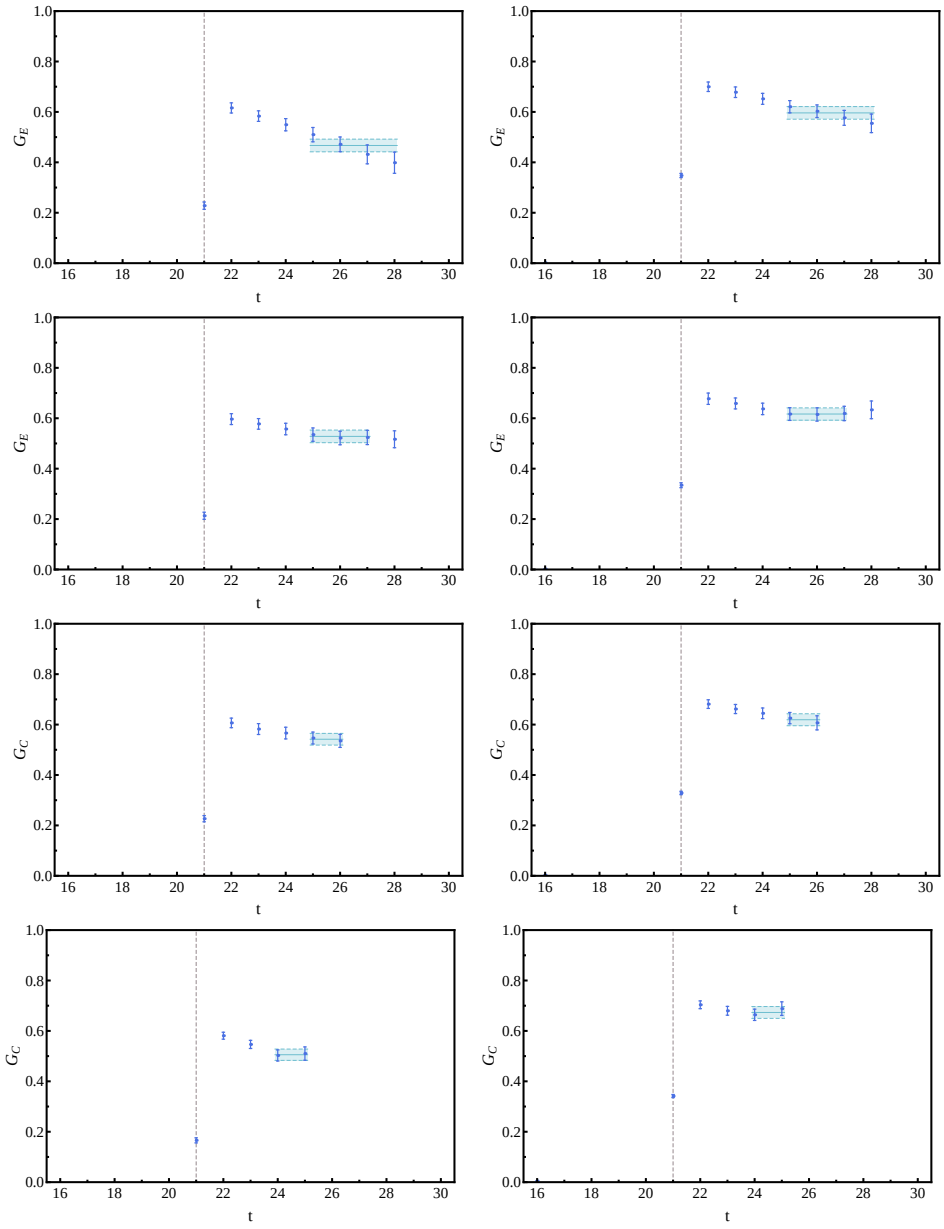

Figure B.10: The quark sector results for the electric form factor G_E of the first negative parity nucleon eigenstate. The doubly-represented quark sector is presented on the left and the singly-represented quark sector on the right. The dashed line represents the time-slice at which the current is inserted. The direction of decreasing quark mass is the page.

Sachs Electric Form Factor for the 2nd Negative Parity Eigenstate

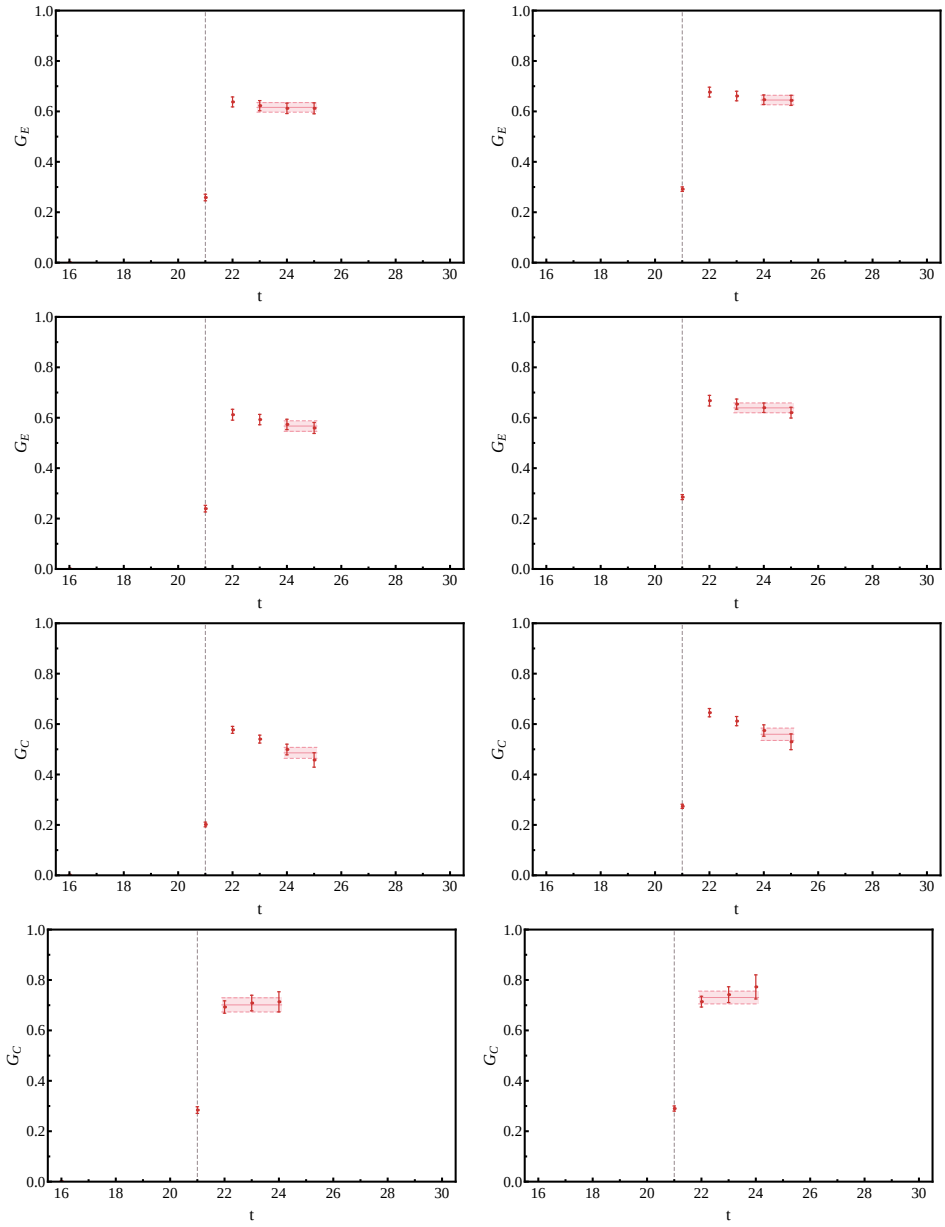

Figure B.11: The quark sector results for the electric form factor G_E of the second negative parity nucleon eigenstate. The doubly-represented quark sector is presented on the left and the singly-represented quark sector on the right. The dashed line represents the time-slice at which the current is inserted. The direction of decreasing quark mass is down the page.

Sachs Magnetic Form Factor for the 1st Negative Parity Eigenstate

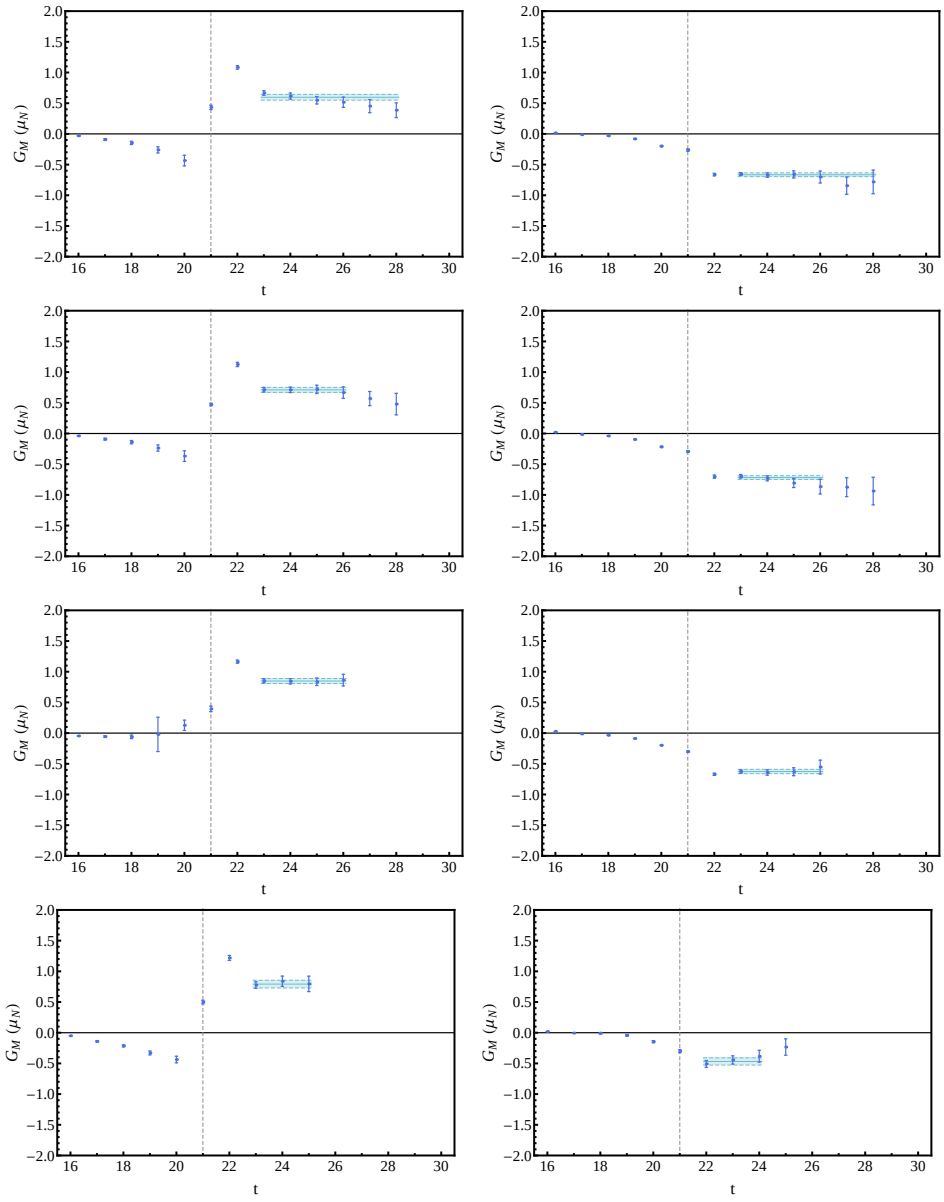

Figure B.12: The quark sector results for the magnetic form factor G_M of the first negative parity nucleon eigenstate. The doubly-represented quark sector is presented on the left and the singly-represented quark sector on the right. The dashed line represents the time-slice at which the current is inserted. The direction of decreasing quark mass is down the page.

Sachs Magnetic Form Factor for the 2nd Negative Parity Eigenstate

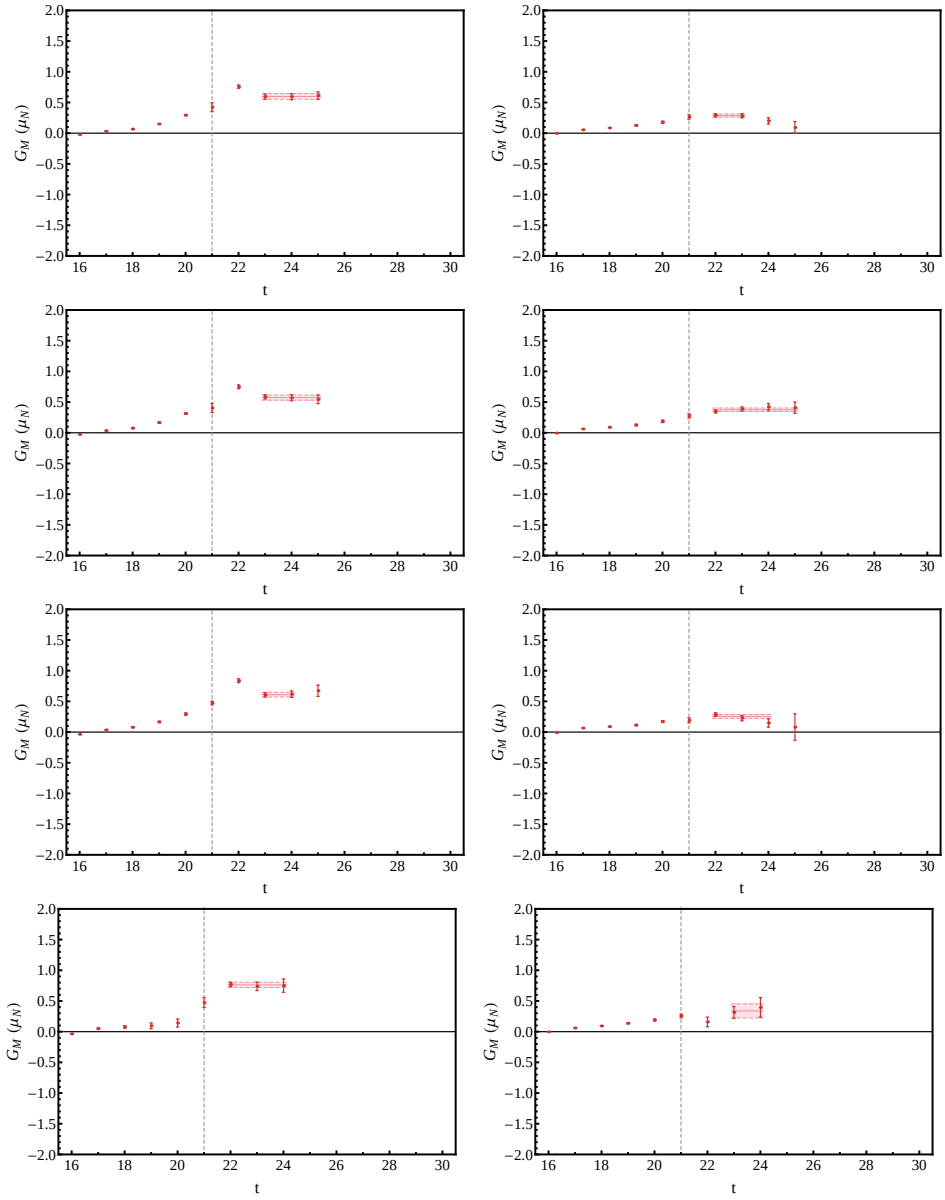

Figure B.13: The quark sector results for the magnetic form factor G_M of the first negative parity nucleon eigenstate. The doubly-represented quark sector is presented on the left and the singly-represented quark sector on the right. The dashed line represents the time-slice at which the current is inserted. The direction of decreasing quark mass is down the page.

Appendix C

Full Expressions for the Nucleon Transition Matrix Elements

Here we provide the reduced expressions for the γ-matrix products found within the trace required for the nucleon transition elements. In particular, we express the products as

$$\left(\not{p}' + M_{\beta^j}\right) \Gamma^\mu(p',p) \left(\not{p} + m_{\alpha^i}\right) = \mathbb{X}^\mu(p',p) F_1^*(Q^2) + \mathbb{Y}^\mu(p',p) F_2^*(Q^2)\,. \tag{C.1}$$

Consequently, the kinematic factors that form the elements of the kinematic weight matrix $\mathbb{K}$ (discussed in section 9.1), are given via the following traces

$$\begin{aligned} K_1^\mu(p',p;(\Gamma')^{ji}) &= \mathrm{Tr}\left[(\Gamma')^{ji}\,\mathbb{X}^\mu(p',p)\right]\,, \\ K_2^\mu(p',p;(\Gamma')^{ji}) &= \mathrm{Tr}\left[(\Gamma')^{ji}\,\mathbb{Y}^\mu(p',p)\right]\,. \end{aligned}$$

Due to the underlying block 2×2 structure of the γ-matrices, we choose to present $\mathbb{X}^\mu(p',p)$ and $\mathbb{Y}^\mu(p',p)$ in a 2×2 block form, with each term $\mathbb{X}^\mu_{ab}(p',p)$ implicitly multiplied by the 2×2 identity matrix.

C.1 Normal Parity Transition Elements

These elements are formed from the vertex function for normal parity-transitions ($\pm\to\pm$) given by Eq. (9.3).

For the temporal component of the current ($\mu=0$):

$$\begin{aligned} \mathbb{X}^0_{11}(p',p) = \frac{+1}{Q^2}\big\{&(m+E)\,(M+E')\left(Q^2+(M-m)\,(E'-E)\right) \\ &+\left(\vec{p}\,'\cdot\vec{p}+i\,\vec{p}\,'\cdot(\vec{p}\times\vec{\sigma})\right)\left(Q^2-(M-m)\,(E'-E)\right)\big\}\,, \end{aligned}$$

$$\begin{aligned} \mathbb{X}^0_{12}(p',p) = \frac{+1}{Q^2}\big\{&(m-E)\left(Q^2-(M-m)\,(E'-E)\right)(\vec{p}\,'\cdot\vec{\sigma}) \\ &-(M+E')\left(Q^2+(M-m)\,(E'-E)\right)(\vec{p}\cdot\vec{\sigma})\big\}\,, \end{aligned}$$

$$\mathbb{X}^0_{21}(p',p) = \frac{+1}{Q^2}\left\{(m+E)\left(Q^2+(M-m)(E'-E)\right)(\vec{p}\,'\cdot\vec{\sigma}) \right. \\ \left. -(M-E')\left(Q^2-(M-m)(E'-E)\right)(\vec{p}\cdot\vec{\sigma})\right\},$$

$$\mathbb{X}^0_{22}(p',p) = \frac{-1}{Q^2}\left\{(m-E)(M-E')\left(Q^2-(M-m)(E'-E)\right) \right. \\ \left. +(\vec{p}\,'\cdot\vec{p}+i\,\vec{p}\,'\cdot(\vec{p}\times\vec{\sigma}))\left(Q^2+(M-m)(E'-E)\right)\right\};$$

$$(M+m)\,\mathbb{Y}^0_{11}(p',p) = -(m+E)(\vec{q}\cdot\vec{p}\,'-i\,\vec{p}\,'\cdot(\vec{p}\times\vec{\sigma}))+(M+E')(\vec{q}\cdot\vec{p}+i\,\vec{p}\,'\cdot(\vec{p}\times\vec{\sigma})),$$

$$(M+m)\,\mathbb{Y}^0_{12}(p',p) = +(\vec{q}\cdot\vec{p})(\vec{p}\,'\cdot\vec{\sigma})+(\vec{q}\cdot\vec{p}\,')(\vec{p}\cdot\vec{\sigma})+((m-E)(M+E')-\vec{p}\,'\cdot\vec{p})(\vec{q}\cdot\vec{\sigma}),$$

$$(M+m)\,\mathbb{Y}^0_{21}(p',p) = +(\vec{q}\cdot\vec{p})(\vec{p}\,'\cdot\vec{\sigma})+(\vec{q}\cdot\vec{p}\,')(\vec{p}\cdot\vec{\sigma})+((m+E)(M-E')-\vec{p}\,'\cdot\vec{p})(\vec{q}\cdot\vec{\sigma}),$$

$$(M+m)\,\mathbb{Y}^0_{22}(p',p) = +(m-E)(\vec{q}\cdot\vec{p}\,'-i\,\vec{p}\,'\cdot(\vec{p}\times\vec{\sigma}))-(M-E')(\vec{q}\cdot\vec{p}+i\,\vec{p}\,'\cdot(\vec{p}\times\vec{\sigma})).$$

For the spatial component of the current ($\mu = i$):

$$\mathbb{X}^i_{11}(p',p) = +(m+E)\,p'_i+(M+E')\,p_i-i\,(m+E)(\vec{p}\,'\times\vec{\sigma})_i+i\,(M+E')(\vec{p}\times\vec{\sigma})_i \\ +\frac{(M-m)}{Q^2}\left((m+E)(M+E')-\vec{p}\,'\cdot\vec{p}-i\,\vec{p}\,'\cdot(\vec{p}\times\vec{\sigma})\right)q_i,$$

$$\mathbb{X}^i_{12}(p',p) = -(\vec{p}\cdot\vec{\sigma})\,p'_i-(\vec{p}\,'\cdot\vec{\sigma})\,p_i+((m-E)(M+E')+\vec{p}\,'\cdot\vec{p})\,\sigma_i+i\,(\vec{p}\,'\times\vec{p})_i \\ -\frac{(M-m)}{Q^2}\left((m-E)(\vec{p}\,'\cdot\vec{\sigma})+(M+E')(\vec{p}\cdot\vec{\sigma})\right)q_i,$$

$$\mathbb{X}^i_{21}(p',p) = +(\vec{p}\cdot\vec{\sigma})\,p'_i+(\vec{p}\,'\cdot\vec{\sigma})\,p_i-((m+E)(M-E')+\vec{p}\,'\cdot\vec{p})\,\sigma_i-i\,(\vec{p}\,'\times\vec{p})_i \\ +\frac{(M-m)}{Q^2}\left((m+E)(\vec{p}\,'\cdot\vec{\sigma})+(M-E')(\vec{p}\cdot\vec{\sigma})\right)q_i,$$

$$\mathbb{X}^i_{22}(p',p) = +z\,(m-E)\,p'_i+(M-E')\,p_i-i\,(m-E)(\vec{p}\,'\times\vec{\sigma})_i+i\,(M-E')(\vec{p}\times\vec{\sigma})_i \\ +\frac{(M-m)}{Q^2}\left((m-E)(M-E')-\vec{p}\,'\cdot\vec{p}-i\,\vec{p}\,'\cdot(\vec{p}\times\vec{\sigma})\right)q_i;$$

$$
\begin{aligned}
(M+m)\,\mathbb{Y}^i_{11}(p',p) = &-(m+E)\,(E'-E)\,(p'_i - i(\vec{p}\,'\times\vec{\sigma})_i) + (\vec{q}\cdot\vec{p})\,p'_i \\
&+ (M+E')\,(E'-E)\,(p_i + i(\vec{p}\times\vec{\sigma})_i) - (\vec{q}\cdot\vec{p}\,')\,p_i \\
&+ i\,(\vec{p}\,'\cdot\vec{\sigma} + \vec{p}\cdot\vec{\sigma})\,(\vec{p}\,'\times\vec{p})_i - i\,((m+E)\,(M+E') - \vec{p}\,'\cdot\vec{p})\,(\vec{q}\times\vec{\sigma})_i\,,
\end{aligned}
$$

$$
\begin{aligned}
(M+m)\,\mathbb{Y}^i_{12}(p',p) = &+ i\,(M+m)\,(\vec{p}\,'\times\vec{p})_i + (E'-E)\,(\vec{p}\,'\cdot\vec{\sigma})\,p_i + (E'-E)\,(\vec{p}\cdot\vec{\sigma})\,p'_i \\
&+ (m-E)\,(\vec{q}\cdot\vec{\sigma})\,p'_i - (M+E')\,(\vec{q}\cdot\vec{\sigma})\,p_i - (m-E)\,(\vec{q}\cdot\vec{p}\,')\,\sigma_i \\
&+ (M+E')\,(\vec{q}\cdot\vec{p})\,\sigma_i + (E'-E)\,((m-E)\,(M+E') - \vec{p}\,'\cdot\vec{p})\,\sigma_i\,,
\end{aligned}
$$

$$
\begin{aligned}
(M+m)\,\mathbb{Y}^i_{21}(p',p) = &- i\,(M+m)\,(\vec{p}\,'\times\vec{p})_i + (E'-E)\,(\vec{p}\,'\cdot\vec{\sigma})\,p_i + (E'-E)\,(\vec{p}\cdot\vec{\sigma})\,p'_i \\
&- (m+E)\,(\vec{q}\cdot\vec{\sigma})\,p'_i + (M-E')\,(\vec{q}\cdot\vec{\sigma})\,p_i + (m+E)\,(\vec{q}\cdot\vec{p}\,')\,\sigma_i \\
&- (M-E')\,(\vec{q}\cdot\vec{p})\,\sigma_i + (E'-E)\,((m+E)\,(M-E') - \vec{p}\,'\cdot\vec{p})\,\sigma_i\,,
\end{aligned}
$$

$$
\begin{aligned}
(M+m)\,\mathbb{Y}^i_{22}(p',p) = &+ (m-E)\,(E'-E)\,(p'_i - i(\vec{p}\,'\times\vec{\sigma})_i) + (\vec{q}\cdot\vec{p})\,p'_i \\
&- (M-E')\,(E'-E)\,(p_i + i(\vec{p}\times\vec{\sigma})_i) - (\vec{q}\cdot\vec{p}\,')\,p_i \\
&- i\,(\vec{p}\,'\cdot\vec{\sigma} + \vec{p}\cdot\vec{\sigma})\,(\vec{p}\,'\times\vec{p})_i - i\,((m-E)\,(M-E') + \vec{p}\,'\cdot\vec{p})\,(\vec{q}\times\vec{\sigma})_i\,.
\end{aligned}
$$

C.2 Abnormal Parity Transition Elements

These elements are formed from the vertex function for abnormal parity-transitions ($\mp \to \pm$) given by Eq. (9.4).

For the temporal component of the current ($\mu = 0$):

$$
\begin{aligned}
\mathbb{X}^0_{11}(p',p) = \frac{+1}{Q^2}\,\big\{&(m+E)\,\big(Q^2 - (M+m)\,(E'-E)\big)\,(\vec{p}\,'\cdot\vec{\sigma}) \\
&+ (M+E')\,\big(Q^2 + (M+m)\,(E'-E)\big)\,(\vec{p}\cdot\vec{\sigma})\big\}\,,
\end{aligned}
$$

$$
\begin{aligned}
\mathbb{X}^0_{12}(p',p) = \frac{+1}{Q^2}\,\big\{&(m-E)\,(M+E')\,\big(Q^2 + (M+m)\,(E'-E)\big) \\
&- (\vec{p}\,'\cdot\vec{p} + i\,\vec{p}\,'\cdot(\vec{p}\times\vec{\sigma}))\,\big(Q^2 - (M+m)\,(E'-E)\big)\big\}\,,
\end{aligned}
$$

$$
\begin{aligned}
\mathbb{X}^0_{21}(p',p) = \frac{-1}{Q^2}\,\big\{&(m+E)\,(M-E')\,\big(Q^2 - (M+m)\,(E'-E)\big) \\
&- (\vec{p}\,'\cdot\vec{p} + i\,\vec{p}\,'\cdot(\vec{p}\times\vec{\sigma}))\,\big(Q^2 + (M+m)\,(E'-E)\big)\big\}\,,
\end{aligned}
$$

$$
\begin{aligned}
\mathbb{X}^0_{22}(p',p) = \frac{+1}{Q^2}\,\big\{&(m-E)\,\big(Q^2 + (M+m)\,(E'-E)\big)\,(\vec{p}\,'\cdot\vec{\sigma}) \\
&+ (M-E')\,\big(Q^2 - (M+m)\,(E'-E)\big)\,(\vec{p}\cdot\vec{\sigma})\big\}\,;
\end{aligned}
$$

$$(M-m)\,\mathbb{Y}^0_{11}(p',p) = -\,(\vec{q}\cdot\vec{p})\,(\vec{p}\,'\cdot\vec{\sigma}) - (\vec{q}\cdot\vec{p}\,')\,(\vec{p}\cdot\vec{\sigma}) + ((m+E)\,(M+E') + \vec{p}\,'\cdot\vec{p})\,(\vec{q}\cdot\vec{\sigma})\ ,$$

$$(M-m)\,\mathbb{Y}^0_{12}(p',p) = -\,(m-E)\,(\vec{q}\cdot\vec{p}\,' - i\,\vec{p}\,'\cdot(\vec{p}\times\vec{\sigma})) - (M+E')\,(\vec{q}\cdot\vec{p} + i\,\vec{p}\,'\cdot(\vec{p}\times\vec{\sigma}))\ ,$$

$$(M-m)\,\mathbb{Y}^0_{21}(p',p) = +\,(m+E)\,(\vec{q}\cdot\vec{p}\,' - i\,\vec{p}\,'\cdot(\vec{p}\times\vec{\sigma})) + (M-E')\,(\vec{q}\cdot\vec{p} + i\,\vec{p}\,'\cdot(\vec{p}\times\vec{\sigma}))\ ,$$

$$(M-m)\,\mathbb{Y}^0_{22}(p',p) = -\,(\vec{q}\cdot\vec{p})\,(\vec{p}\,'\cdot\vec{\sigma}) - (\vec{q}\cdot\vec{p}\,')\,(\vec{p}\cdot\vec{\sigma}) + ((m-E)\,(M-E') + \vec{p}\,'\cdot\vec{p})\,(\vec{q}\cdot\vec{\sigma})\ .$$

For the spatial component of the current ($\mu = i$):

$$\begin{aligned}\mathbb{X}^i_{11}(p',p) = &+\,(\vec{p}\cdot\vec{\sigma})\,p'_i + (\vec{p}\,'\cdot\vec{\sigma})\,p_i + ((m+E)\,(M+E') - \vec{p}\,'\cdot\vec{p})\,\sigma_i - i\,(\vec{p}\,'\times\vec{p})_i \\ &- \frac{(M+m)}{Q^2}\,((m+E)\,(\vec{p}\,'\cdot\vec{\sigma}) - (M+E')\,(\vec{p}\cdot\vec{\sigma}))\,q_i\ ,\end{aligned}$$

$$\begin{aligned}\mathbb{X}^i_{12}(p',p) = &+\,(m-E)\,p'_i - (M+E')\,p_i - i\,(m-E)\,(\vec{p}\,'\times\vec{\sigma})_i - i\,(M+E')\,(\vec{p}\times\vec{\sigma})_i \\ &+ \frac{(M+m)}{Q^2}\,((m-E)\,(M+E') + \vec{p}\,'\cdot\vec{p} + i\,\vec{p}\,'\cdot(\vec{p}\times\vec{\sigma}))\,q_i\ ,\end{aligned}$$

$$\begin{aligned}\mathbb{X}^i_{21}(p',p) = &+\,(m+E)\,p'_i - (M-E')\,p_i - i\,(m+E)\,(\vec{p}\,'\times\vec{\sigma})_i - i\,(M-E')\,(\vec{p}\times\vec{\sigma})_i \\ &+ \frac{(M+m)}{Q^2}\,((m+E)\,(M-E') + \vec{p}\,'\cdot\vec{p} + i\,\vec{p}\,'\cdot(\vec{p}\times\vec{\sigma}))\,q_i\ ,\end{aligned}$$

$$\begin{aligned}\mathbb{X}^i_{22}(p',p) = &-\,(\vec{p}\cdot\vec{\sigma})\,p'_i - (\vec{p}\,'\cdot\vec{\sigma})\,p_i - ((m-E)\,(M-E') - \vec{p}\,'\cdot\vec{p})\,\sigma_i + i\,(\vec{p}\,'\times\vec{p})_i \\ &+ \frac{(M+m)}{Q^2}\,((m-E)\,(\vec{p}\,'\cdot\vec{\sigma}) - (M-E')\,(\vec{p}\cdot\vec{\sigma}))\,q_i\ ;\end{aligned}$$

$$\begin{aligned}(M-m)\,\mathbb{Y}^i_{11}(p',p) = &-\,i\,(M-m)\,(\vec{p}\,'\times\vec{p})_i - (E'-E)\,(\vec{p}\,'\cdot\vec{\sigma})\,p_i - (E'-E)\,(\vec{p}\cdot\vec{\sigma})\,p'_i \\ &+ (m+E)\,(\vec{q}\cdot\vec{\sigma})\,p'_i + (M+E')\,(\vec{q}\cdot\vec{\sigma})\,p_i - (m+E)\,(\vec{q}\cdot\vec{p}\,')\,\sigma_i \\ &- (M+E')\,(\vec{q}\cdot\vec{p})\,\sigma_i + (E'-E)\,((m+E)\,(M+E') + \vec{p}\,'\cdot\vec{p})\,\sigma_i\ ,\end{aligned}$$

$$\begin{aligned}(M-m)\,\mathbb{Y}^i_{12}(p',p) = &-\,(m-E)\,(E'-E)\,(p'_i - i(\vec{p}\,'\times\vec{\sigma})_i) - (\vec{q}\cdot\vec{p})\,p'_i \\ &- (M+E')\,(E'-E)\,(p_i + i(\vec{p}\times\vec{\sigma})_i) + (\vec{q}\cdot\vec{p}\,')\,p_i \\ &- i\,(\vec{p}\,'\cdot\vec{\sigma} + \vec{p}\cdot\vec{\sigma})\,(\vec{p}\,'\times\vec{p})_i - i\,((m-E)\,(M+E') - \vec{p}\,'\cdot\vec{p})\,(\vec{q}\times\vec{\sigma})_i\ ,\end{aligned}$$

$$
\begin{aligned}
(M-m)\,\mathbb{Y}^i_{21}(p',p) = &+ (m+E)\,(E'-E)\,(p'_i - i(\vec{p}\,'\times\vec{\sigma})_i) - (\vec{q}\cdot\vec{p})\,p'_i \\
&+ (M-E')\,(E'-E)\,(p_i + i(\vec{p}\times\vec{\sigma})_i) + (\vec{q}\cdot\vec{p}\,')\,p_i \\
&+ i\,(\vec{p}\,'\cdot\vec{\sigma} + \vec{p}\cdot\vec{\sigma})\,(\vec{p}\,'\times\vec{p})_i - i\,((m+E)\,(M-E') - \vec{p}\,'\cdot\vec{p})\,(\vec{q}\times\vec{\sigma})_i\,,
\end{aligned}
$$

$$
\begin{aligned}
(M-m)\,\mathbb{Y}^i_{22}(p',p) = &+ i\,(M-m)\,(\vec{p}\,'\times\vec{p})_i - (E'-E)\,(\vec{p}\,'\cdot\vec{\sigma})\,p_i - (E'-E)\,(\vec{p}\cdot\vec{\sigma})\,p'_i \\
&- (m-E)\,(\vec{q}\cdot\vec{\sigma})\,p'_i - (M+E')\,(\vec{q}\cdot\vec{\sigma})\,p_i + (m-E)\,(\vec{q}\cdot\vec{p}\,')\,\sigma_i \\
&+ (M-E')\,(\vec{q}\cdot\vec{p})\,\sigma_i + (E'-E)\,((m-E)\,(M-E') + \vec{p}\,'\cdot\vec{p})\,\sigma_i\,.
\end{aligned}
$$

Appendix D

Papers by the Author

Journal Articles

[1] F. M. Stokes, W. Kamleh, D. B. Leinweber, M. S. Mahbub, B. J. Menadue and B. J. Owen, *Parity-expanded variational analysis for non-zero momentum*, *submitted to Phys. Rev. D*, [arXiv:1302.4152 [hep-lat]].

[2] B. J. Owen, W. Kamleh, D. B. Leinweber, M. S. Mahbub and B. J. Menadue, *Transition of $\rho \to \pi\gamma$ in lattice QCD*, Phys. Rev. D **92**, no. 3, 034513 (2015) [arXiv:1505.02876 [hep-lat]].

[3] A. L. Kiratidis, W. Kamleh, D. B. Leinweber and B. J. Owen, *Lattice baryon spectroscopy with multi-particle interpolators*, Phys. Rev. D **91**, no. 11, 094509 (2015) [arXiv:1501.07667 [hep-lat]].

[4] B. Owen, W. Kamleh, D. Leinweber, B. Menadue and S. Mahbub, *Light Meson Form Factors at near Physical Masses*, Phys. Rev. D **91**, no. 7, 074503 (2015) [arXiv:1501.02561 [hep-lat]].

[5] J. M. M. Hall, W. Kamleh, D. B. Leinweber, B. J. Menadue, B. J. Owen, A. W. Thomas and R. D. Young, *The Lambda 1405 is an anti-kaon–nucleon molecule* Phys. Rev. Lett. **114**, no. 13, 132002 (2015) [arXiv:1411.3402 [hep-lat]].

[6] B. J. Owen, J. Dragos, W. Kamleh, D. B. Leinweber, M. S. Mahbub, B. J. Menadue and J. M. Zanotti, *Variational Approach to the Calculation of gA*, Phys. Lett. B **723**, 217 (2013) [arXiv:1212.4668 [hep-lat]].

[7] J. M. M. Hall, D. B. Leinweber, B. J. Owen and R. D. Young, *Finite-volume corrections to charge radii*, Phys. Lett. B **725**, 101 (2013) [arXiv:1210.6124 [hep-lat]].

Conference Proceedings

[1] B. Owen, W. Kamleh, D. Leinweber, S. Mahbub and B. Menadue, *Electromagnetic matrix elements for negative parity nucleons*, PoS LATTICE **2014**, 159 (2015), [arXiv:1412.4432 [hep-lat]].

[2] J. M. M. Hall, W. Kamleh, D. B. Leinweber, B. J. Menadue, B. J. Owen, A. W. Thomas and R. D. Young, *On the Structure of the Lambda 1405*, PoS LATTICE **2014**, 094 (2015), [arXiv:1411.3781 [hep-lat]].

[3] B. J. Owen, W. Kamleh, D. B. Leinweber, M. S. Mahbub and B. J. Menadue, *Probing the proton and its excitations in full QCD*, PoS LATTICE **2013**, 277 (2014), [arXiv:1312.0291 [hep-lat]].

[4] B. J. Menadue, W. Kamleh, D. B. Leinweber, M. S. Mahbub and B. J. Owen, *Electromagnetic Form Factors for the $\Lambda(1405)$*, PoS LATTICE **2013**, 280 (2014), [arXiv:1311.5026 [hep-lat]].

[5] B. Owen, W. Kamleh, D. B. Leinweber, S. Mahbub and B. Menadue, *Correlation matrix methods for excited meson form factors in full QCD*, PoS LATTICE **2012**, 173 (2012).

[6] B. Owen, W. Kamleh, D. Leinweber, A. El Bakry and P. Moran, *Light meson transition form factors on the lattice*, PoS LATTICE **2012**, 254 (2012).

[7] B. J. Menadue, W. Kamleh, D. B. Leinweber, M. S. Mahbub and B. J. Owen, *Electromagnetic form factors of the Lambda(1405) in (2+1)-flavour lattice QCD*, PoS LATTICE **2012**, 178 (2012).

Bibliography

[1] S. Durr, Z. Fodor, J. Frison, C. Hoelbling, R. Hoffmann, et al., *Ab-Initio Determination of Light Hadron Masses*, Science **322**, 1224 (2008), 0906.3599.

[2] G. Aad et al. (ATLAS Collaboration), *Observation of a new particle in the search for the Standard Model Higgs boson with the ATLAS detector at the LHC*, Phys.Lett. **B716**, 1 (2012), 1207.7214.

[3] S. Chatrchyan et al. (CMS Collaboration), *Observation of a new boson at a mass of 125 GeV with the CMS experiment at the LHC*, Phys.Lett. **B716**, 30 (2012), 1207.7235.

[4] Y. Ne'eman, *Derivation of strong interactions from a gauge invariance*, Nucl.Phys. **26**, 222 (1961).

[5] M. Gell-Mann, *Symmetries of baryons and mesons*, Phys.Rev. **125**, 1067 (1962).

[6] M. Gell-Mann, *A Schematic Model of Baryons and Mesons*, Phys.Lett. **8**, 214 (1964).

[7] O. Greenberg, *Spin and Unitary Spin Independence in a Paraquark Model of Baryons and Mesons*, Phys.Rev.Lett. **13**, 598 (1964).

[8] F. Close, *An Introduction to Quarks and Partons* (1979).

[9] N. Isgur and G. Karl, *Hyperfine Interactions in Negative Parity Baryons*, Phys.Lett. **B72**, 109 (1977).

[10] N. Isgur and G. Karl, *Positive Parity Excited Baryons in a Quark Model with Hyperfine Interactions*, Phys.Rev. **D19**, 2653 (1979).

[11] R. L. Jaffe, *Multi-Quark Hadrons. 1. The Phenomenology of (2 Quark 2 anti-Quark) Mesons*, Phys.Rev. **D15**, 267 (1977).

[12] R. Aaij et al. (LHCb collaboration), *Observation of the resonant character of the $Z(4430)^-$ state*, Phys.Rev.Lett. **112**, 222002 (2014), 1404.1903.

[13] C.-N. Yang and R. L. Mills, *Conservation of Isotopic Spin and Isotopic Gauge Invariance*, Phys.Rev. **96**, 191 (1954).

[14] K. G. Wilson, *Confinement of Quarks*, Phys.Rev. **D10**, 2445 (1974).

[15] H. B. Nielsen and M. Ninomiya, *Absence of Neutrinos on a Lattice. 1. Proof by Homotopy Theory*, Nucl.Phys. **B185**, 20 (1981).

[16] H. B. Nielsen and M. Ninomiya, *Absence of Neutrinos on a Lattice. 2. Intuitive Topological Proof*, Nucl.Phys. **B193**, 173 (1981).

[17] H. B. Nielsen and M. Ninomiya, *No Go Theorem for Regularizing Chiral Fermions*, Phys.Lett. **B105**, 219 (1981).

[18] P. H. Ginsparg and K. G. Wilson, *A Remnant of Chiral Symmetry on the Lattice*, Phys.Rev. **D25**, 2649 (1982).

[19] H. Rothe, *Lattice gauge theories: An Introduction*, World Sci.Lect.Notes Phys. **43**, 1 (1992).

[20] K. Symanzik, *Continuum Limit and Improved Action in Lattice Theories. 1. Principles and ϕ^4 Theory*, Nucl.Phys. **B226**, 187 (1983).

[21] K. Symanzik, *Continuum Limit and Improved Action in Lattice Theories. 2. O(N) Nonlinear Sigma Model in Perturbation Theory*, Nucl.Phys. **B226**, 205 (1983).

[22] M. Luscher and P. Weisz, *On-Shell Improved Lattice Gauge Theories*, Commun.Math.Phys. **97**, 59 (1985).

[23] Y. Iwasaki, *Renormalization Group Analysis of Lattice Theories and Improved Lattice Action. II. Four-dimensional non-Abelian SU(N) gauge model* (2011), `1111.7054`.

[24] S. Aoki et al. (PACS-CS Collaboration), *2+1 Flavor Lattice QCD toward the Physical Point*, Phys.Rev. **D79**, 034503 (2009), `0807.1661`.

[25] C. Gattringer and C. B. Lang, *Quantum chromodynamics on the lattice*, Lect.Notes Phys. **788**, 1 (2010).

[26] B. Sheikholeslami and R. Wohlert, *Improved Continuum Limit Lattice Action for QCD with Wilson Fermions*, Nucl.Phys. **B259**, 572 (1985).

[27] S.-J. Dong and K.-F. Liu, *Stochastic estimation with Z(2) noise*, Phys.Lett. **B328**, 130 (1994), `hep-lat/9308015`.

[28] G. S. Bali, S. Collins, and A. Schafer, *Effective noise reduction techniques for disconnected loops in Lattice QCD*, Comput.Phys.Commun. **181**, 1570 (2010), `0910.3970`.

[29] M. Peardon et al. (Hadron Spectrum Collaboration), *A Novel quark-field creation operator construction for hadronic physics in lattice QCD*, Phys.Rev. **D80**, 054506 (2009), `0905.2160`.

[30] S. Gusken, *A Study of smearing techniques for hadron correlation functions*, Nucl.Phys.Proc.Suppl. **17**, 361 (1990).

[31] R. Babich, R. C. Brower, M. A. Clark, G. T. Fleming, J. C. Osborn, et al., *Exploring strange nucleon form factors on the lattice*, Phys.Rev. **D85**, 054510 (2012), 1012.0562.

[32] G. S. Bali et al. (QCDSF Collaboration), *Strangeness Contribution to the Proton Spin from Lattice QCD*, Phys.Rev.Lett. **108**, 222001 (2012), 1112.3354.

[33] A. Abdel-Rehim, C. Alexandrou, M. Constantinou, V. Drach, K. Hadjiyiannakou, et al., *Disconnected quark loop contributions to nucleon observables in lattice QCD*, Phys.Rev. **D89**, 034501 (2014), 1310.6339.

[34] C. W. Bernard, T. Draper, G. Hockney, and A. Soni, in *Lattice Gauge Theory: A Challenge in Large Scale Computing*, NATO Sci.Ser.B **140** (1986).

[35] S. Dinter, C. Alexandrou, M. Constantinou, V. Drach, K. Jansen, et al., *Precision Study of Excited State Effects in Nucleon Matrix Elements*, Phys.Lett. **B704**, 89 (2011), 1108.1076.

[36] M. Luscher, R. Narayanan, P. Weisz, and U. Wolff, *The Schrodinger functional: A Renormalizable probe for non-Abelian gauge theories*, Nucl.Phys. **B384**, 168 (1992), hep-lat/9207009.

[37] M. Della Morte et al. (ALPHA Collaboration), *Non-perturbative quark mass renormalization in two-flavor QCD*, Nucl.Phys. **B729**, 117 (2005), hep-lat/0507035.

[38] S. Aoki et al. (PACS-CS collaboration), *Non-perturbative renormalization of quark mass in $N_f = 2 + 1$ QCD with the Schroedinger functional scheme*, JHEP **1008**, 101 (2010), 1006.1164.

[39] G. Martinelli, C. Pittori, C. T. Sachrajda, M. Testa, and A. Vladikas, *A General method for nonperturbative renormalization of lattice operators*, Nucl.Phys. **B445**, 81 (1995), hep-lat/9411010.

[40] M. Gockeler, R. Horsley, H. Oelrich, H. Perlt, D. Petters, et al., *Nonperturbative renormalization of composite operators in lattice QCD*, Nucl.Phys. **B544**, 699 (1999), hep-lat/9807044.

[41] G. Martinelli, C. T. Sachrajda, and A. Vladikas, *A Study of 'improvement' in lattice QCD*, Nucl.Phys. **B358**, 212 (1991).

[42] S. Boinepalli, D. Leinweber, A. Williams, J. Zanotti, and J. Zhang, *Precision electromagnetic structure of octet baryons in the chiral regime*, Phys.Rev. **D74**, 093005 (2006), hep-lat/0604022.

[43] J. Sakurai, *Advanced Quantum Mechanics* (Addison-Wesley Publishing Company, 1967).

[44] T. Draper, R. Woloshyn, W. Wilcox, and K.-F. Liu, *Electromagnetic Form-factors of Hadrons*, Nucl.Phys.Proc.Suppl. **9**, 175 (1989).

[45] T. Draper, R. Woloshyn, W. Wilcox, and K.-F. Liu, *The Pion Form-factor in Lattice QCD*, Nucl.Phys. **B318**, 319 (1989).

[46] B. Lasscock, J. N. Hedditch, D. B. Leinweber, W. Melnitchouk, A. W. Thomas, et al., *Search for the pentaquark resonance signature in lattice QCD*, Phys.Rev. **D72**, 014502 (2005), hep-lat/0503008.

[47] C. Alexandrou, J. O. Daldrop, M. Dalla Brida, M. Gravina, L. Scorzato, et al., *Lattice investigation of the scalar mesons $a_0(980)$ and κ using four-quark operators*, JHEP **1304**, 137 (2013), 1212.1418.

[48] J. Hedditch, W. Kamleh, B. Lasscock, D. Leinweber, A. Williams, et al., 1^{-+} *exotic meson at light quark masses*, Phys.Rev. **D72**, 114507 (2005), hep-lat/0509106.

[49] D. Mohler, *Review of lattice studies of resonances*, PoS **LATTICE2012**, 003 (2012), 1211.6163.

[50] J. J. Dudek, R. G. Edwards, M. J. Peardon, D. G. Richards, and C. E. Thomas, *Toward the excited meson spectrum of dynamical QCD*, Phys.Rev. **D82**, 034508 (2010), 1004.4930.

[51] R. G. Edwards, J. J. Dudek, D. G. Richards, and S. J. Wallace, *Excited state baryon spectroscopy from lattice QCD*, Phys.Rev. **D84**, 074508 (2011), 1104.5152.

[52] M. S. Mahbub, W. Kamleh, D. B. Leinweber, and A. G. Williams, *Searching for low-lying multi-particle thresholds in lattice spectroscopy*, Annals Phys. **342**, 270 (2014), 1310.6803.

[53] W. Detmold, *Multi-hadron systems in lattice QCD*, Eur.Phys.J. **A49**, 83 (2013).

[54] W. Detmold, *Nuclear Physics from Lattice QCD*, Lect.Notes Phys. **889**, 153 (2015).

[55] D. B. Leinweber, R. Woloshyn, and T. Draper, *Electromagnetic structure of octet baryons*, Phys.Rev. **D43**, 1659 (1991).

[56] J. N. Hedditch et al., *Pseudoscalar and vector meson form-factors from lattice QCD*, Phys.Rev. **D75**, 094504 (2007), hep-lat/0703014.

[57] C. Michael, *Adjoint Sources in Lattice Gauge Theory*, Nucl.Phys. **B259**, 58 (1985).

[58] M. Luscher and U. Wolff, *How to Calculate the Elastic Scattering Matrix in Two-dimensional Quantum Field Theories by Numerical Simulation*, Nucl.Phys. **B339**, 222 (1990).

[59] S. Basak, R. Edwards, G. Fleming, U. Heller, C. Morningstar, et al., *Group-theoretical construction of extended baryon operators in lattice QCD*, Phys.Rev. **D72**, 094506 (2005), hep-lat/0506029.

[60] S. Basak et al. (Lattice Hadron Physics Collaboration (LHPC)), *Clebsch-Gordan construction of lattice interpolating fields for excited baryons*, Phys.Rev. **D72**, 074501 (2005), hep-lat/0508018.

[61] J. J. Dudek, R. G. Edwards, B. Joo, M. J. Peardon, D. G. Richards, et al., *Isoscalar meson spectroscopy from lattice QCD*, Phys.Rev. **D83**, 111502 (2011), 1102.4299.

[62] M. Peardon et al. (Hadron Spectrum Collaboration), *A Novel quark-field creation operator construction for hadronic physics in lattice QCD*, Phys.Rev. **D80**, 054506 (2009), 0905.2160.

[63] D. S. Roberts, W. Kamleh, and D. B. Leinweber, *Nucleon Excited State Wave Functions from Lattice QCD*, Phys.Rev. **D89**, 074501 (2014), 1311.6626.

[64] M. S. Mahbub, W. Kamleh, D. B. Leinweber, P. J. Moran, and A. G. Williams, *Structure and Flow of the Nucleon Eigenstates in Lattice QCD*, Phys.Rev. **D87**, 094506 (2013), 1302.2987.

[65] H. W. Lin, *Lattice Hadron Structure: Applications within and beyond QCD*, PoS **LATTICE2012**, 013 (2012).

[66] H.-W. Lin, *Recent progress on nucleon structure with lattice QCD*, Int.J.Mod.Phys.Conf.Ser. **25**, 1460039 (2014).

[67] J. Green, *Hadron Structure from Lattice QCD* (2014), 1412.4637.

[68] S. Sasaki, K. Orginos, S. Ohta, and T. Blum (RIKEN-BNL-Columbia-KEK Collaboration), *Nucleon axial charge from quenched lattice QCD with domain wall fermions*, Phys.Rev. **D68**, 054509 (2003), hep-lat/0306007.

[69] R. Edwards et al. (LHPC Collaboration), *The Nucleon axial charge in full lattice QCD*, Phys.Rev.Lett. **96**, 052001 (2006), hep-lat/0510062.

[70] A. Ali Khan et al., *Axial coupling constant of the nucleon for two flavours of dynamical quarks in finite and infinite volume*, Phys.Rev. **D74**, 094508 (2006), hep-lat/0603028.

[71] P. Hägler et al. (LHPC Collaborations), *Nucleon Generalized Parton Distributions from Full Lattice QCD*, Phys.Rev. **D77**, 094502 (2008), 0705.4295.

[72] H.-W. Lin and K. Orginos, *First Calculation of Hyperon Axial Couplings from Lattice QCD*, Phys.Rev. **D79**, 034507 (2009), 0712.1214.

[73] T. Yamazaki et al. (RBC+UKQCD Collaboration), *Nucleon axial charge in 2+1 flavor dynamical lattice QCD with domain wall fermions*, Phys.Rev.Lett. **100**, 171602 (2008), 0801.4016.

[74] H.-W. Lin, T. Blum, S. Ohta, S. Sasaki, and T. Yamazaki, *Nucleon structure with two flavors of dynamical domain-wall fermions*, Phys.Rev. **D78**, 014505 (2008), 0802.0863.

[75] J. Bratt et al. (LHPC Collaboration), *Nucleon structure from mixed action calculations using 2+1 flavors of asqtad sea and domain wall valence fermions*, Phys.Rev. **D82**, 094502 (2010), 1001.3620.

[76] C. Alexandrou et al. (ETM Collaboration), *Axial Nucleon form factors from lattice QCD*, Phys.Rev. **D83**, 045010 (2011), 1012.0857.

[77] D. Pleiter et al. (QCDSF/UKQCD Collaboration), *Nucleon form factors and structure functions from N(f)=2 Clover fermions*, PoS **LATTICE2010**, 153 (2010), 1101.2326.

[78] N. L. Hall, A. W. Thomas, R. D. Young, and J. M. Zanotti, *Volume Dependence of the Axial Charge of the Nucleon* (2012), 1205.1608.

[79] S. Capitani et al., *The nucleon axial charge from lattice QCD with controlled errors*, Phys.Rev. **D86**, 074502 (2012), 1205.0180.

[80] R. Horsley, Y. Nakamura, A. Nobile, P. Rakow, G. Schierholz, et al., *Nucleon axial charge and pion decay constant from two-flavor lattice QCD*, Phys.Lett. **B732**, 41 (2014), 1302.2233.

[81] T. Bhattacharya, S. D. Cohen, R. Gupta, A. Joseph, H.-W. Lin, et al., *Nucleon Charges and Electromagnetic Form Factors from 2+1+1-Flavor Lattice QCD*, Phys.Rev. **D89**, 094502 (2014), 1306.5435.

[82] S. Capitani, M. Della Morte, G. von Hippel, B. Jager, B. Knippschild, et al., *Excited state systematics in extracting nucleon electromagnetic form factors*, PoS **LATTICE2012**, 177 (2012), 1211.1282.

[83] B. Brandt, S. Capitani, M. Della Morte, D. Djukanovic, J. Gegelia, et al., *Form factors in lattice QCD*, Eur.Phys.J.ST **198**, 79 (2011), 1106.1554.

[84] J. Bulava, M. Donnellan, and R. Sommer, *On the computation of hadron-to-hadron transition matrix elements in lattice QCD*, JHEP **1201**, 140 (2012), 1108.3774.

[85] L. Maiani, G. Martinelli, M. Paciello, and B. Taglienti, *Scalar Densities and Baryon Mass Differences in Lattice QCD With Wilson Fermions*, Nucl.Phys. **B293**, 420 (1987).

[86] M. G. Beckett, B. Joo, C. M. Maynard, D. Pleiter, O. Tatebe, et al., *Building the International Lattice Data Grid*, Comput.Phys.Commun. **182**, 1208 (2011), 0910.1692.

[87] M. S. Mahbub, W. Kamleh, D. B. Leinweber, P. J. Moran, and A. G. Williams (CSSM Lattice collaboration), *Roper Resonance in 2+1 Flavor QCD*, Phys.Lett. **B707**, 389 (2012), 1011.5724.

[88] D. S. Roberts, W. Kamleh, D. B. Leinweber, M. S. Mahbub, and B. J. Menadue, *Accessing High Momentum States In Lattice QCD*, Phys.Rev. **D86**, 074504 (2012), 1206.5891.

[89] T. Maurer, T. Burch, L. Y. Glozman, C. Lang, D. Mohler, et al., *Axial charges of excited nucleons from CI-fermions* (2012), 1202.2834.

[90] G. Lopez Castro and A. Mariano, *Determination of the Δ^{++} magnetic dipole moment*, Phys.Lett. **B517**, 339 (2001), nucl-th/0006031.

[91] M. Kotulla, J. Ahrens, J. Annand, R. Beck, G. Caselotti, et al., *The Reaction $\gamma p \to \pi^0 \gamma' p$ and the magnetic dipole moment of the $\Delta^+(1232)$ resonance*, Phys.Rev.Lett. **89**, 272001 (2002), nucl-ex/0210040.

[92] D. G. Gudiño and G. T. Sánchez, *Determination of the magnetic dipole moment of the ρ meson* (2013), 1305.6345.

[93] W. Andersen and W. Wilcox, *Lattice charge overlap. 1. Elastic limit of π and ρ mesons*, Annals Phys. **255**, 34 (1997), hep-lat/9502015.

[94] C. Alexandrou, P. de Forcrand, and A. Tsapalis, *Probing hadron wave functions in lattice QCD*, Phys.Rev. **D66**, 094503 (2002), hep-lat/0206026.

[95] M. Gurtler et al. (QCDSF Collaboration), *Vector meson electromagnetic form factors*, PoS **LATTICE2008**, 051 (2008).

[96] F. X. Lee, S. Moerschbacher, and W. Wilcox, *Magnetic moments of vector, axial, and tensor mesons in lattice QCD*, Phys.Rev. **D78**, 094502 (2008), 0807.4150.

[97] C. J. Shultz, J. J. Dudek, and R. G. Edwards, *Excited meson radiative transitions from lattice QCD using variationally optimized operators*, Phys.Rev. **D91**, 114501 (2015), 1501.07457.

[98] K. J. Kim and Y.-S. Tsai, *Magnetic Dipole and Electric Quadrupole Moments of $W^{\pm}$ Meson*, Phys.Rev. **D7**, 3710 (1973).

[99] R. Arnold, C. E. Carlson, and F. Gross, *Polarization Transfer in Elastic electron Scattering from Nucleons and Deuterons*, Phys.Rev. **C23**, 363 (1981).

[100] S. J. Brodsky and J. R. Hiller, *Universal properties of the electromagnetic interactions of spin one systems*, Phys.Rev. **D46**, 2141 (1992).

[101] A. W. Thomas and W. Weise, *The Structure of the Nucleon* (2001).

[102] R. Arnold, P. E. Bosted, C. Chang, J. Gomez, A. Katramatou, et al., *Measurement of Elastic electron Scattering from the Proton at High Momentum Transfer*, Phys.Rev.Lett. **57**, 174 (1986).

[103] B. J. Menadue, W. Kamleh, D. B. Leinweber, and M. S. Mahbub, *Isolating the $\Lambda(1405)$ in Lattice QCD*, Phys.Rev.Lett. **108**, 112001 (2012), 1109.6716.

[104] M. S. Mahbub, W. Kamleh, D. B. Leinweber, P. J. Moran, and A. G. Williams (CSSM Lattice Collaboration), *Low-lying Odd-parity States of the Nucleon in Lattice QCD*, Phys.Rev. **D87**, 011501 (2013), 1209.0240.

[105] J. Beringer et al. (Particle Data Group), *Review of Particle Physics (RPP)*, Phys.Rev. **D86**, 010001 (2012).

[106] C. Gattringer, L. Y. Glozman, C. Lang, D. Mohler, and S. Prelovsek, *Derivative sources in lattice spectroscopy of excited mesons*, Phys.Rev. **D78**, 034501 (2008), 0802.2020.

[107] G. P. Engel, C. Lang, M. Limmer, D. Mohler, and A. Schafer (BGR [Bern-Graz-Regensburg] Collaboration), *Meson and baryon spectrum for QCD with two light dynamical quarks*, Phys.Rev. **D82**, 034505 (2010), 1005.1748.

[108] J. J. Dudek, R. G. Edwards, and D. G. Richards, *Radiative transitions in charmonium from lattice QCD*, Phys.Rev. **D73**, 074507 (2006), hep-ph/0601137.

[109] A. Badalian and Y. Simonov, *Magnetic moments of mesons*, Phys.Rev. **D87**, 074012 (2013), 1211.4349.

[110] J. de Melo and T. Frederico, *Covariant and light front approaches to the ρ meson electromagnetic form-factors*, Phys.Rev. **C55**, 2043 (1997), nucl-th/9706032.

[111] M. Bhagwat and P. Maris, *Vector meson form factors and their quark-mass dependence*, Phys.Rev. **C77**, 025203 (2008), nucl-th/0612069.

[112] T. Aliev, A. Ozpineci, and M. Savci, *Magnetic and quadrupole moments of light spin-1 mesons in light cone QCD sum rules*, Phys.Lett. **B678**, 470 (2009), 0902.4627.

[113] H. Roberts, A. Bashir, L. Gutierrez-Guerrero, C. Roberts, and D. Wilson, *π- and ρ-mesons, and their diquark partners, from a contact interaction*, Phys.Rev. **C83**, 065206 (2011), 1102.4376.

[114] M. Pitschmann, C.-Y. Seng, M. J. Ramsey-Musolf, C. D. Roberts, S. M. Schmidt, et al., *Electric dipole moment of the ρ-meson*, Phys.Rev. **C87**, 015205 (2013), 1209.4352.

[115] D. Djukanovic, E. Epelbaum, J. Gegelia, and U.-G. Meissner, *The magnetic moment of the ρ-meson*, Phys.Lett. **B730**, 115 (2014), 1309.3991.

[116] C. S. Mello, A. Nunes da Silva, J. de Melo, and T. Frederico, *Electromagnetic form factors for spin-1 particles with the light-front*, Nucl.Phys.Proc.Suppl. **251-252**, 62 (2014).

[117] T. D. Lee, *Minimal Electromagnetic Interaction and C, T Noninvariance*, Phys. Rev. **140**, B967 (1965).

[118] V. Bernard, D. Hoja, U. Meissner, and A. Rusetsky, *Matrix elements of unstable states*, JHEP **1209**, 023 (2012), 1205.4642.

[119] R. A. Briceño, M. T. Hansen, and A. Walker-Loud, *Multichannel $1 \to 2$ transition amplitudes in a finite volume*, Phys.Rev. **D91**, 034501 (2015), 1406.5965.

[120] R. Woloshyn, *Vector Meson Radiative Decay in Lattice QCD*, Z.Phys. **C33**, 121 (1986).

[121] R. G. Edwards (Lattice Hadron Physics Collaboration), *Electromagnetic hadronic form-factors*, Nucl.Phys.Proc.Suppl. **140**, 290 (2005), hep-lat/0409119.

[122] P. J. O'Donnell, *Radiative decays of mesons*, Rev.Mod.Phys. **53**, 673 (1981).

[123] T. Jensen, D. Berg, C. Chandlee, S. Cihangir, T. Ferbel, et al., *Radiative Decay Width of the ρ^- Meson*, Phys.Rev. **D27**, 26 (1983).

[124] J. Huston, D. Berg, C. Chandlee, S. Cihangir, B. Collick, et al., *Measurement of the Resonance Parameters and Radiative Width of the ρ^+*, Phys.Rev. **D33**, 3199 (1986).

[125] L. Capraro, P. Levy, M. Querrou, B. Van Hecke, M. Verbeken, et al., *The ρ Radiative Decay Width: A Measurement at 200-GeV*, Nucl.Phys. **B288**, 659 (1987).

[126] B. Owen, W. Kamleh, D. Leinweber, A. El Bakry, and P. Moran, *Light meson transition form factors on the lattice*, PoS **LATTICE2012**, 254 (2012).

[127] N. Barik, P. Dash, and A. Panda, *Radiative decay of mesons in an independent quark potential model*, Phys.Rev. **D46**, 3856 (1992).

[128] N. Barik and P. Dash, *Radiative decay of light and heavy mesons*, Phys.Rev. **D49**, 299 (1994).

[129] A. Agadjanov, V. Bernard, U.-G. Meissner, and A. Rusetsky, *A framework for the calculation of the $\Delta N\gamma$ transition form factors on the lattice*, Nucl.Phys. **B886**, 1199 (2014), 1405.3476.

[130] R. A. Briceño and M. T. Hansen, *Multichannel 0-to-2 and 1-to-2 transition amplitudes for arbitrary spin particles in a finite volume* (2015), 1502.04314.

[131] J. Dudek, R. Ent, R. Essig, K. Kumar, C. Meyer, et al., *Physics Opportunities with the 12 GeV Upgrade at Jefferson Lab*, Eur.Phys.J. **A48**, 187 (2012), 1208.1244.

[132] L. Tiator, D. Drechsel, S. Kamalov, and M. Vanderhaeghen, *Electromagnetic Excitation of Nucleon Resonances*, Eur.Phys.J.ST **198**, 141 (2011), 1109.6745.

[133] Z.-W. Liu et al. (2015), private communication.

[134] S. Boinepalli, D. Leinweber, P. Moran, A. Williams, J. Zanotti, et al., *Precision electromagnetic structure of decuplet baryons in the chiral regime*, Phys.Rev. **D80**, 054505 (2009), 0902.4046.

[135] W.-T. Chiang, S. N. Yang, M. Vanderhaeghen, and D. Drechsel, *Magnetic dipole moment of the $S_{11}(1535)$ from the gamma $p \to \gamma\eta p$ reaction*, Nucl.Phys. **A723**, 205 (2003), nucl-th/0211061.

[136] J. Liu, J. He, and Y. Dong, *Magnetic moments of negative-parity low-lying nucleon resonances in quark models*, Phys.Rev. **D71**, 094004 (2005).

[137] N. Sharma, A. Martinez Torres, K. Khemchandani, and H. Dahiya, *Magnetic moments of the low-lying $1/2^-$ octet baryon resonances*, Eur.Phys.J. **A49**, 11 (2013), 1207.3311.

[138] T. Aliev and M. Savci, *Magnetic moments of negative-parity baryons in QCD*, Phys.Rev. **D89**, 053003 (2014), 1402.4609.

[139] I. Narodetskii and M. Trusov, *Magnetic moments of negative parity baryons from the effective Hamiltonian approach to QCD*, JETP Lett. **99**, 57 (2014), 1311.2407.

[140] D. B. Leinweber, T. Draper, and R. Woloshyn, *Baryon octet to decuplet electromagnetic transitions*, Phys.Rev. **D48**, 2230 (1993), hep-lat/9212016.

[141] C. Alexandrou, P. de Forcrand, T. Lippert, H. Neff, J. W. Negele, et al., *$N \to \Delta$ electromagnetic transition form-factors from lattice QCD*, Phys.Rev. **D69**, 114506 (2004), hep-lat/0307018.

[142] C. Alexandrou, P. de Forcrand, H. Neff, J. W. Negele, W. Schroers, et al., *The $N \to \Delta$ electromagnetic transition form-factors from lattice QCD*, Phys.Rev.Lett. **94**, 021601 (2005), hep-lat/0409122.

[143] C. Alexandrou, G. Koutsou, H. Neff, J. W. Negele, W. Schroers, et al., *Nucleon to delta electromagnetic transition form factors in lattice QCD*, Phys.Rev. **D77**, 085012 (2008), 0710.4621.

[144] C. Alexandrou, G. Koutsou, J. Negele, Y. Proestos, and A. Tsapalis, *Nucleon to Delta transition form factors with $N_F = 2+1$ domain wall fermions*, Phys.Rev. **D83**, 014501 (2011), 1011.3233.

[145] H.-W. Lin, S. D. Cohen, R. G. Edwards, and D. G. Richards, *First Lattice Study of the $N \to P_{11}(1440)$ Transition Form Factors*, Phys.Rev. **D78**, 114508 (2008), 0803.3020.

[146] H.-W. Lin and S. D. Cohen, *Roper Properties on the Lattice: An Update*, AIP Conf.Proc. **1432**, 305 (2012), 1108.2528.

[147] R. Devenish, T. Eisenschitz, and J. Korner, *Electromagnetic NN^* Transition Form-Factors*, Phys.Rev. **D14**, 3063 (1976).

[148] I. Aznauryan, V. Burkert, and T.-S. Lee, *On the definitions of the $\gamma^* N \to N^*$ helicity amplitudes* (2008), 0810.0997.

[149] I. Aznauryan and V. Burkert, *Electroexcitation of nucleon resonances*, Prog.Part.Nucl.Phys. **67**, 1 (2012), 1109.1720.

[150] G. Ramalho and M. Pena, *A covariant model for the $\gamma N \to N(1535)$ transition at high momentum transfer*, Phys.Rev. **D84**, 033007 (2011), 1105.2223.

[151] G. Ramalho and K. Tsushima, *A simple relation between the $\gamma N \to N(1535)$ helicity amplitudes*, Phys.Rev. **D84**, 051301 (2011), 1105.2484.

[152] V. Braun, M. Gockeler, R. Horsley, T. Kaltenbrunner, A. Lenz, et al., *Electroproduction of the $N^*(1535)$ resonance at large momentum transfer*, Phys.Rev.Lett. **103**, 072001 (2009), 0902.3087.

[153] I. Aznauryan et al. (CLAS Collaboration), *Electroexcitation of nucleon resonances from CLAS data on single pion electroproduction*, Phys.Rev. **C80**, 055203 (2009), 0909.2349.